Investigating spatial variation in the surface and atmosphere of Pluto through stellar occultations and PSF photometry

by

Amanda Marie Zangari

Submitted to the Department of Earth, Atmospheric, and Planetary Sciences
in partial fulfillment of the requirements for the degree of

Doctor of Philosophy

at the

MASSACHUSETTS INSTITUTE OF TECHNOLOGY

June 2013

Author .....
Department of Earth, Atmospheric, and Planetary Sciences
April 17, 2013

Certified by .....
Richard P. Binzel
Professor of Planetary Sciences, Margaret MacVicar Faculty Fellow
Thesis Supervisor

Certified by .....
Michael J. Person
Research Scientist, Department of Earth, Atmospheric and Planetary Sciences
Thesis Supervisor

Accepted by .....
Robert van der Hilst
Schlumberger Professor of Earth and Planetary Sciences,
Head of Department of Earth, Atmospheric and Planetary Sciences

Investigating spatial variation in the surface and atmosphere of Pluto through stellar occultations and PSF photometry

by

Amanda Marie Zangari

Submitted to the Department of Earth, Atmospheric, and Planetary Sciences
on April 17, 2013, in partial fulfillment of the
requirements for the degree of
Doctor of Philosophy

Abstract

Stellar occultations provide a high-resolution view of a single chord through Pluto's atmosphere. This thesis presents three projects related to stellar occultation observations of Pluto. The first project concerns the ground testing of the High-speed Imaging Photometer for Occultations (HIPO), a camera aboard the Stratospheric Observatory For Infrared Astronomy (SOFIA). Differential photometry was found to be reliable to one part in 10^4. The second project is a modern determination of the light ratio of Charon and Pluto, essential for predicting future occultations. The final project considers twenty years worth of Pluto stellar occultation results, including new measurements using HIPO, and determines whether temperature asymmetries can be seen in fits for the upper atmosphere. These measurements allow the first Earth-based assessment of Pluto's geographic temperature distribution. Included is a description of the extensive test modeling to determine the boundary selection methods for the upper atmosphere for each differently-shaped light curve. The temperature asymmetries or lack thereof, are considered in the context of time of day, average insolation and surface features in the vicinity of the area near the occultation half-light radius. No clear correlation was found for any of the three metrics, suggesting that Pluto's atmosphere is spatially isothermal.

Thesis Supervisor: Richard P. Binzel
Title: Professor of Planetary Sciences, Margaret MacVicar Faculty Fellow

Thesis Supervisor: Michael J. Person
Title: Research Scientist, Department of Earth, Atmospheric and Planetary Sciences

Acknowledgments

First and foremost, I would like to thank the late James L. Elliot for starting me on this path. I did not realize how precious the time I spent working with him was until it was too late.

Secondly, I would like to thank Michael J. Person and Richard P. Binzel for the shouldering the burden of surprise graduate student, and allowing me continue the work I had started with Jim. Their patience with me, especially during our weekly meetings, has been incredible. I especially appreciate that they allowed me to drop everything for about six weeks to read every paper on Pluto I could get my hands on (at this point, I should note that, this research has made use of NASA's Astrophysics Data System Bibliographic Services, without which the project that would later become Chapter 2 would have be much more difficult). Equally valuable was their impatience, without which I would not be here today with a full-sized thesis.

In addition to academic support, social support was provided by the many wonderful friends I have met during my time here at MIT, including but not limited to Elisabeth, Jon, Andy, Moritz, Katja, Tobi, Jenny, Sonia, Jason, Rahul, Jeremy, Brandon, Alex, Sukrit, Courtney, Bekki and Allison. Special thanks also goes to my tolerant roommates, Arghavan, David, Will and Albert, and the Ashdown Housemasters, Terry and Ann, and Yuriy and Katie for making my home away from home so great.

Finally, I would like to thank my family for their love and support: Mom, Dad, Melissa, Rebecca, Rob and Grandma.

Contents

List of Figures

List of Tables

Chapter 1

Introduction

1.1 A brief history of Pluto science and stellar occultations

When Pluto was discovered in 1930, it was merely an unresolvable dot, similar in appearance to an asteroid. Even today, the pictures from the Hubble Space Telescope can barely resolve hints of Pluto's changing surface. Challenging to observe, our knowledge of Pluto has changed time and again as scientists have discovered more and more about this cold, dark, yet fascinating world. Originally, Pluto was thought to be much more massive than it is, but its size was constantly revised downwards until the first accurate measurements were made in the 1980s (Marcialis, 1997). Today we know that Pluto's diameter is about 1000 km smaller than that of our moon.

The first attempts to measure Pluto's brightness over time were made by Baade (1934). While Baade did not use these brightness changes to determine a rotation period for Pluto, he did measure brightness changes over several nights. Unfortunately, the night-to-night magnitude differences Baade measured were approximately the same size as his precision (Dessler & Russell, 1980; Tholen & Buie, 1997). It would be over two decades, after Pluto had re-emerged from the the peak of southern hemisphere summer[1] in the late 1940s (Stern & Mitton, 2005a) before an answer was found.

[1]Throughout this document, I will refer to the hemisphere visible from Earth and receiving sunlight at the time of Pluto's discovery up through the mutual events of the late 1980s as the

Over a single night, Pluto's brightness did not appear to change. Rather, Walker & Hardie (1955) found that Pluto rotates very slowly, and the cycle of brightening and dimming repeated itself once every 6.39 days. As Pluto's long shadowed northern hemisphere began to shift into view and Pluto accelerated towards its equinox, the difference between the dimmest and brightest points became even more pronounced. It was discovered that Pluto had highly variegated surface features: the second most dramatic variations of any other round object in the Solar System (Tholen & Buie, 1997). In 1978, Pluto's moon, Charon, was first spotted, and Pluto was found to be doubly tidally locked to a formidable body with over half its diameter.

After several unsuccessful search attempts (Stern et al., 1991; Stern, 2003; Nicholson & Gladman, 2006), two additional moons were discovered using the Hubble Space Telescope in 2005 (Weaver et al., 2006), with a fourth found in 2011 (Showalter et al., 2011), and a fifth found in 2012 (Showalter et al., 2012)[2]. Pluto also evolved from being labeled as a planet to being placed in a novel category called "dwarf planet", and is now considered the most interesting among many bodies in a region of space known as the Kuiper Belt. While Pluto strolls around the sun along its deep space route once every 248 years, its surface and atmosphere are dynamically interacting on much shorter time scales. After receding from its closest approach to the sun, Pluto's atmospheric pressure doubled in size in just fourteen years (Elliot et al., 2003b). However, in a few decades Pluto's atmopshere has been predicted to disappear entirely (Terrile et al., 1997). Recent models by Young (2013) have imminent collapse as one of three possible paths Pluto's atmosphere could take, depending on the atmospheric thermal inertia and the degree of volatile exchange between the dark and light hemispheres. At one extreme: atmospheric collapse, at the other, a permanent supply of volatiles in the northern hemisphere.

While technological advances such as CCD cameras, HST, large telescopes, adap-

southern hemisphere, making the currently-visible hemisphere the northern hemisphere. The reasons for this will be discussed at length in Chapter 2, which is solely devoted to the proper usage of these designations.

[2]To be fair to those who failed to detect Nix, Hydra and P5: the locations and brightnesses of these moons were on the other side of the detection limits placed by previous searches. P4 was later found in the Nix and Hydra discovery images, obscured by diffraction spikes.

tive optics, computing power and airborne telescopes such as the KAO and SOFIA have driven many discoveries, gaining knowledge about Pluto requires a fair bit of cleverness. The most striking example is the wealth of data derived from the "mutual events" in the late 1980s, when Earth-based astronomers could watch Pluto and Charon passing in front of each other, thereby enabling scientists to derive accurate sizes, colors and orbits for the two bodies. Cleverness also allows blurry images from HST to become surface maps; it finds novel ways of obscuring Pluto and Charon's light to locate the smaller bodies which would be otherwise drowned out by the brighter members in the system. Stellar occultations probe Pluto's atmosphere at higher resolution than any picture that can be taken from Earth.

In two years, everything we know about Pluto and Charon will be revolutionized. On July 14, 2015, after nine long years of travel, the New Horizons spacecraft will make a fast flyby of Pluto, creating a single, detailed portrait of this ice world. Our knowledge of Pluto will be divided into two periods: before New Horizons, and after New Horizons. Of the long journey, Pluto researcher Marc Buie has complained that nine years is not enough time to calibrate and publish all of the data that have been observed in advance of the spacecraft's arrival. After that time, New Horizons' many discoveries will take precedence, and currently unpublished work may be lost to the sands of time. The Charon-Pluto light ratio project, described in Chapter 4, is one such example of a project that had been pushed aside in favor of new data, despite its usefulness in other areas.

After all is said and done, even if a second space mission to Pluto were approved on July 15, 2015, it would take decades for humanity to build the craft and for it to arrive at Pluto. The data from New Horizons will provide only a snapshot of Pluto. Thus the techniques pioneered before New Horizons will be all that remain to follow-up with this dynamic world. This thesis mainly concerns itself with stellar occultations, a technique that has provided a long baseline of information on Pluto, and which will have a continuing vital role in the post-New Horizons era.

An *occultation* is said to occur when a large body passes in front of a small one. In our case, Pluto is the big object, and a star is the little object, not in the absolute

sense, but in terms of angular diameter, or the object's apparent size as seen from Earth. The opposite of an occultation is a *transit*– a small object passing in front of a larger one. The most recent notable example in our Solar System was the June 2012 transit of Venus. Outside our Solar System, transits have led to the discovery of many of the known extra-solar planets.

Most particularly, transits and occultations are responsible for the greatest fraction of our knowledge about Pluto and Charon. During the period in the late 1980s, known as the mutual events, as Pluto transitioned from being south-pole-on as seen from Earth to north-pole on, Charon and Pluto alternately blocked each other, allowing the best measurements of the sizes of those two objects. In addition, Charon probed different latitudes during successive transits, marking out Pluto's polar caps, and the fact that Pluto and Charon are different colors (Binzel & Frueh, 1986). When Charon was fully blocked by Pluto, Pluto's spectrum can be observed without interference, allowing it to be determined that Pluto and Charon have different compositions (Sawyer et al., 1987).

Much useful scientific information can be derived from stellar occultations. One of two things happen when a body passes in front of a star: the light is either extinguished sharply or gradually. If it is the latter, an atmosphere refracted the starlight around the planet's limb. Thanks to spectroscopic observations that hinted at the presence of gaseous methane (Fink et al., 1980), it was not a complete surprise that when Pluto passed in front of a star on June 9, 1988, the light dimmed gradually, and did not just wink away. What *was* puzzling was that the light began to dim gradually, but then disappeared more sharply, repeating the reverse of this pattern when Pluto unblocked the star. The unusual light curve from this occultation can be seen in Figure 6-2 on page 159. This unique "knee" shape seen in the 1988 light-curve did not appear again in 2002, the next time Pluto occultations were observed. Fortunately, there were four years, not fourteen until the next occultation observations, but no Pluto occultation since 1988 has had with such a drastic knee. Since 2006, an occultation by Pluto has been observed on Earth at least once in each calendar year (Elliot et al., 2007; Olkin et al., 2007; Buie et al., 2009; Young et al., 2009, 2010;

Person et al., 2010; Pasachoff et al., 2011; Person et al., 2012; Sicardy et al., 2012).

Anything can happen in fourteen years, but what if location, not occultation year was responsible for the different shapes of Pluto's light curve, and any asymmetry between sides? Understanding this variability in stellar occultation profiles has been a major unsolved problem over the past three decades of Pluto science. This thesis attempts to solve this long-standing problem by investigating how much influence the location on Pluto where an occultation is observed affects that profile. In Chapters 5-7, I seek to solve this problem. Chapter 5 and 6 follow intra light curve variability by looking at measurements of the temperature of Pluto's upper atmosphere. Chapter 5 seeks to set limitations on what sort of light curve measurements are feasible by using model light-curves to determine how to define the extent of the upper atmosphere, as well as quantify what the minimum quality standards for a light curve should be. Additionally, I investigate at the effects of an erroneous occultation chord impact parameter on occultation temperature difference results. Using Chapter 5's criterion, Chapter 6 takes the Pluto occultation light curves that make the cut, and using the upper atmospheric selection method outlined, fits temperature differences for each light curve.

Chapter 7 takes these temperature differences and considers them in the context of surface location on Pluto. A longitude and latitude are calculated for each immersion and emersion location pair. Each pair is then compared with its temperature difference in view of the amount of light received/season, time of day, and map of surface features.

While calculating locations on a map may seem like a straightforward process, coordinates on Pluto are anything but. In the course of preparing Chapter 7, I came across several inconsistencies and contradictions in the way that Pluto coordinates are defined in the literature. Chapter 2 seeks to bring some order to the Pluto coordinate system by providing a framework to compare different papers accurately. I will also highlight errors and some mistakes to avoid so that Pluto location measurements can be properly merged.

Maps of Pluto's surface are not just useful after the fact for occultations– they

play an important role in occultation predictions. Because Pluto and Charon appear to be a single blob at all but the best sites on Earth, the contribution of Charon's light needs to be accounted for to know the precise position of Pluto. Because Pluto's surface is dynamic and because Pluto and Charon are different colors, I will present data in Chapter 4 that calculates the Charon-Pluto light ratio and compares it against data taken decades earlier.

As I will describe in Section 1.2, occultation observations are not necessarily a sure thing. Out of eighteen occultation observations I have attempted, only two have resulted in an occultation. In many cases, weather in the form of wind, clouds or rain prevented data from being collected. In other cases, I was not in the path of the occultation, sometimes by design in the case of uncertain KBO predictions. In other cases, the predicted occultation path had changed substantially in the months between the telescope application process and observing.

Airborne astronomy seeks to solve both the weather and the path problems. Clouds? Fly above them. Outdated prediction? Bring the telescope elsewhere. In 2010, I was fortunate enough to work with Ted Dunham and Georgi Mandushev on a series of stability tests for the High-Speed Imaging Photometer for Occultations (HIPO), an instrument aboard the Stratospheric Observatory for Infrared Astronomy (SOFIA). A necessary part of instrument commissioning is testing the instrument's reliability against changes in physical conditions that might been seen inside an airplane, such as changing cabin temperature. Less than a year after testing, HIPO was installed and data of an occultation were collected in June 2011. These occultation results form an integral part of the asymmetry data set in Chapter 6. Hopefully, these HIPO stellar occultations will be only the first of many that continue to improve our understanding of Pluto an its atmosphere, both before and after its visit by New Horizons.

Thus, this thesis approaches new scientific knowledge of Pluto in an end-to-end manner. State-of-the-art tools must be developed and verified (Chapter 3), accurate predictions for where occultations may be observed must be enabled (Chapter 4), and occultation observations must be successful (Section 1.2). Analysis of spatial

dependencies requires precise determination of Pluto's coordinate system (Chapter 2). Analysis of the occultation profiles to deduce temperature values is the subject of Chapter 6. Finally, Chapter 7 will bring new insights to atmospheric profile variability and implications for Pluto's global characteristics.

1.2 Stellar occultation event observations

Over the past six years, I have observed (or rather attempted to observe) no fewer than eighteen stellar occultation and transit events, some by Pluto and some by other solar system bodies. All but one of these observations occurred during my tenure as a graduate student at MIT. What follows is a discussion of events, as well as lessons learned. A complete list of events can be found in Table 1.2.

Occultation observing can be quite stressful. There is only one chance to observe an event. Generally, anything that can go wrong does. Some events are more difficult than others. The trickiest events occur either right after sunset or as the occultation star is rising, leaving just minutes to locate the proper place on the sky and begin imaging

2007-03-18 Pluto "P445.3"

My long string of failures to observe a stellar occultation began in March 2007 with an event by Pluto[3]. As part of an effort led by Leslie Young of SwRI, I had accompanied Jeff Regester to Apache Point Observatory to help install a PHOT camera on the 1-m telescope along with Jon Holtzman, a Professor at New Mexico State University. On the event day, the sky had become increasingly cloudy, despite spectacularly clear weather on the days prior to the occultation. The occultation was to occur in the early morning. While waiting, we spent time confirming the pointing on various bright stars, but as the clouds rolled in, even a nearby sixth-magnitude star was not visible. We had not found the field, and the time to observe the occultation was beginning. As occultation time drew nearer, we made a blind jump to the occultation field coordinates. The clouds opened for just an instant, but it was sufficient to see that the Pluto field matched the one seen the previous evening. It was enough. Unfortunately, Pluto was obscured by clouds throughout the entire hour surrounding the event. I did learn how to proceed with intermittently cloudy weather before the beginning of the occultation time. I would later use this information four years later

[3]Data from this occultation, known as P445.3, will be examined in Chapters 6 and 7.

for an occultation in May 2011.

2009-03-04 Nix

In March of 2009, I attempted a remote observation of a stellar occultation by Nix with the IRTF alongside fellow lab-mates Elisabeth Adams and Matthew Lockhart. The occultation was predicted to be near Hawaii, but as the orbits of Pluto's smallest satellites are highly uncertain, so was the shadow path. Unfortunately, clouds prevented observations of any kind. Observations were made with MORIS (Gulbis et al., 2011) and SpeX (Rayner et al., 2003).

2009-10-09 (55636) 2002 TX_{300}

The failure to observe a stellar occultation by (55636) 2002 TX_{300} was actually a success. I was stationed at Lick Observatory with Katie Morzinsky and Bryant Grigsby, 1512 km North of the actual centerline. While our group did not wish to miss the occultation, such a large path error would have indicated a massive prediction failure.

After much internal debating about which model to use, the MIT Planetary Astronomy Lab predicted that the occultation would cross the Earth just 499 kilometers south of Mauna Kea Observatory. Nearly correct at 21 km north of MKO, the occultation was observed at Haleakala and the Mauna Kea Mid Level (really the parking lot at the visitor's center). As the first large-scale targeted observation of any Kuiper Belt Object occultation, the MIT group stationed observers at 18 observatories from 41°N to 44°S, for a total distance of 5920 km. The average station density was 328 km, and poor weather occurred at 7 stations. The KBO turned out to have a radius of 143± 5km, much smaller than predicted (Elliot et al., 2010). Jim Elliot described the successful dual observations of such as small KBO as the "second luckiest" occultation event that he had been involved with (Elliot, 2009).

Our observations were made by mounting a POETS (Souza et al., 2006) on the then-130-year-old Crossley Telescope. Described as "piece of junk"[4] and under a threat of closure that is now a reality, the Crossley 36-inch telescope is a manually

[4] `http://www.ucolick.org/public/telescopes/crossley.html`

operated telescope. Getting anything beyond a naked-eye star centered in the field proved to be a matter of luck and skill. Two things allowed for successful observations with this difficult telescope. The first was receiving ample evenings prior to the occultation event to practice and learn with the Crossley and to find the field. The second was having an occultation-capable camera. As a frame-transfer camera with nearly instantaneous readout, the POETS instrument is ideal for star-hopping due to its video mode. High-resolution star charts of up to 1° can be downloaded from the STSci Digitized Sky Survey[5], Katie and I found a naked eye star– ϵ And– within 1° of the KBO, and we created extensive finder charts between that star and the field, marked with intermediate stars. After two nights of getting used to the telescope, but not finding the field, the star-hop method worked beautifully. On our fourth and final observing night, we found the field immediately, and gathered an extensive pre-event baseline that was later used for a satellite search (Jensen-Clem et al., 2011). The Crossley would not be my last experience on a manual telescope: I later used star-hopping for field testing the 2011 (20000) Varuna occultation.

2010-07-04 Pluto

In July 2010, Pluto occulted a 15 magnitude star. I accompanied Jim Elliot to Las Campanas observatory to use MagIC on the Clay telescope. While the initial predicted path started within 100 km away, the final path was roughly one radius away (Zuluaga, 2013). Unfortunately, high winds prevented opening of the telescope. Small telescopes in South Africa and Namibia had some observing successes, these events are mentioned briefly in Chapter 6.

(28978) Ixion

In July 2010, the MIT PAL's event watch-list included a possible occultation of an 11.5 magnitude star by (28978) Ixion. This bright star had been identified in catalog searches but the occultation path was predicted to be slightly north of the Earth. Earlier predictions had a path that started on the Earth in South America, then

[5]`http://archive.stsci.edu/cgi-bin/dss_form`

jumped off the Earth over North America, but returned to hover over Massachusetts, shortly after sunset before leaving the Earth again. The combination of the ease of observing at Wallace, large event uncertainty and stellar brightness made it a perfect longshot attempt. The weather at Wallace Observatory cooperated, and I was able to obtain the field on the 24" shortly after sunset. No occultation was seen.

2011-02-10 (20000)Varuna

In February 2011, I traveled to Palmer, Alaska to observe an occultation by KBO (20000) Varuna using a 24-inch reflecting telescope hand-built by Jim Egger. Like the Crossley, it was a manual telescope. While I was prepared to use the same star-hopping techniques (and had practiced them at Wallace observatory that previous December), the weather was cloudy on the occultation day and all observing days prior. As no other site observed an occultation, it is unknown where the path went.

2011-05-22 Pluto

In May 2011, I observed perhaps one of the most frustrating cloud-related misses at Vassar College's 32-inch telescope with Professor Fred Chromey. Like in 2007, the night of the Pluto occultation was only clear enough to briefly check the pointing. We moved blindly to Pluto, and recorded images of clouds until a brief hole proved that the field was correct. Soon after, the clouds cleared fully, and pre-event observations began. The clouds returned and remained for the duration of the occultation observations except for a roughly one minute window, about ten minutes after predicted mid-time. The cloud hole seen before our event did travel east, and hovered over Williams College, enabling successful observation there.

2011-06-23 Pluto/Charon

In June 2011, I traveled to Cairns, Australia, for the first of three occultation attempts with Joe Brimacombe at Coral Towers Observatory. Pluto and Charon were predicted to occult the same star, with Charon situated slightly to Pluto's north. The observatory had been located south of an occultation path that had shifted south a

few weeks before the event, eventually shifting north again, and settling over Hawaii and the southwestern United States. While the occultation field had been successfully acquired, intermittent clouds interrupted observing. As Cairns was too far south of the path, no event was seen. However, several telescopes did observe this occultation, including the Stratospheric Observatory For Infrared Astronomy (Person et al., 2013).

2011-06-27 Pluto/Hydra

The second of the three June 2011 events was another dual Pluto occultation, this time with moon Hydra. Hydra was originally predicted to occult the star from somewhere over Australia, with Pluto passing slightly more northward. While it was technically "dry season" in June for tropical northern Queensland, that evening there was sprinkling rain despite a half-clear sky. As the very light rain continued, we were not sure if the rain would get worse and damage the camera and/or we would get electrocuted. Thus we made the agonizing decision to shut the telescope down. As rain prevailed throughout the eastern hemisphere that night, the occultation was not observed anywhere, killing the opportunity to observe two Pluto occultations less than one Pluto day apart.

2011-06-29 (10199) Chariklo

The third and final of the three June 2011 events I attempted at Cairns was a an occultation by centaur (10199) Chariklo. Unforuntately, clouds skunked the third occultation's observations.

2011-07-25 Charon

This event was observed with a group of MIT PAL summer students at Wallace observatory. Multiple telescopes were put into service: we had two 14" telescopes in the shed and 16" which had SBIG CCD cameras for general observing, while the 24" telescope was outfitted with a POETS camera. While POETS had worked for the previous night's testing, the power supply no longer worked the next day.

Fortunately, the POETS power controls only the camera cooling. However, without its cooling, the camera's dark current was calculated to be too strong to perceive Pluto. A variable power supply found in the observatory's lab bench was rigged to feed power to camera, but that did not work. Imaging did go smoothly in the shed no occultation was observed.

2011-11-30 (2060) Chiron

In November of 2011, I had my first successful observation of an occultation: an occultation by (2060) Chiron in 2011. This occultation was observed remotely using MORIS and SPEX on the IRTF. Narrow jet-like features emanating from Chiron were seen. These light curves were written up in Ruprecht (2013).

2011-12-07 (136108)Haumea

Attempts to observe a rare occultation by Haumea of a dim 17 magnitude star in December 2011 proved rather frustrating. Mattthew Lockhart and I had traveled to Tonantzintla Observatory in San Andrés Cholula. While the occultation did not happen until the the early morning, Haumea had only risen enough to be reached by the telescope just minutes before the mid-time. East of the observatory is the capital city of Puebla, and due to light pollution, it was never established whether the field had been properly reached. No other observatory successfully observed an occultation.

2012-01-02 (20000) Varuna

In January of 2012, I traveled with a POETS to Sendai, Japan to observe an occultation of (20000) Varuna at Sendai Astronomical Observatory. Here, we mounted the camera to a stationary Nasmyth port ordinarily used with an eyepiece for public observing. While the field would rotate as the stars traveled across the sky, the fast imaging cadence made this problem irrelevant. While the field was located successfully, and observations were made, intermittent clouds appeared during the event,

including the mid-time. Other observations were met with a similar fate, and Varuna's actual occultation path was again unknown.

2012-06-06 Transit of Venus

On June 6 2012 (UT), Venus transited the sun for the last time this century. Noting that the weather in New England was unlikely to produce a visible transit, I flew to Flagstaff, Arizona for successful visual observation of the transit.

2012-06-14 Pluto

In June 2012, I traveled with POETS to my alma mater, Wellesley College, to observe a stellar occultation by Pluto with Professor Stephen Slivan, and his summer student, Alyssa Sokal. Unfortunately, the weather did not cooperate. Successful observations from nearby observatories confirm that no occultation passed over Wellesley College.

2012-09-09 Pluto

Like the (2060) Chiron event in 2011, my second occultation observing success occurred remotely, this time using the MONET North 1.2-m telescope at McDonald Observatory. The was to occur shortly after sunset, after rain and connection problems had reduced the previous practice night to a mere few minutes of imaging. Cloudy weather had plagued other observatories surrounding McDonald: but radar images of the sky showed clouds moving in a circular patten around McDonald with the eye in the storm. Despite the clear sky, bad seeing and inexperience caused me to spend too much time on the focus. While the whole occultation was observed, there are only a few baseline images prior to the occultation, save for a handful focus images.

2012-10-02 Pluto

I took the helm of MONET North in October 2012 after a telescope scheduling conflict was generously sorted out in our favor. Again, the weather and telescope cooperated

much better, and experience and superior seeing allowed for smooth focusing. However, no occultation was seen as the path traveled (as predicted) over South America.

Table 1.1. Summary of occultation observation efforts made by the author

Date	Object	Telescope	Location	Other Observers	Result
2007-03-17	Pluto	1-m	Apache Point Observatory, NM	Jeff Regester and Jon Holtzman	clouds
2009-03-04	Nix	3-m IRTF	Mauna Kea Observatory, HI	Elisabeth Adams and Matthew Lockhart	clouds
2009-10-08	(55636) 2002 TX_{300}	36-inch Crossley	Lick Observatory, CA	Katie Morzinsky, Bryant Grigsby	data taken, but out of path
2010-07-04	Pluto	6.5-m Clay	Las Campanas Observatory, Chile	Jim Elliot	winds too high to open telescope
2010-07-19	(28978) Ixion	24-inch	Wallace Astrophysical Observatory, Westford, MA	-	no occultation
2011-02-10	(2000) Varuna	24-inch	The Egger Observatory, Palmer AK	Jim Egger	clouds
2011-05-22	Pluto	32-inch	Vassar College Observatory, Poughkeepsie, NY	Fred Chromey	clouds
2011-06-23	Pluto/Charon	14-inch	Coral Towers Observatory, Cairns, QLD, Australia	Joe Brimacombe	partly cloudy; out of path
2011-06-27	Pluto/Hydra	14-inch	Coral Towers Observatory, Cairns, QLD, Australia	Joe Brimacombe	clouds/rain
2011-06-29	(10199) Chariklo	14-inch	Coral Towers Observatory, Cairns, QLD, Australia	Joe Brimacombe	clouds
2011-07-25	Charon	24-inch, 16-inch, 14-inch x2	Wallace Astrophysical Observatory, Westford, MA	Summer 2010 crew	no occultation + equipment failure
2011-11-30	(2060) Chiron	3-m IRTF	Mauna Kea Observatory, HI	Amanda Bosh, Michael Person	**success**
2011-12-07	(136108) Haumea	1-m	Tonantzintla, PUE, Mexico	Matt Lockhart, Santiago Torres, Barbara Pichardo Silva	light pollution
2012-01-02	(20000) Varuna	1.3-m	Sendai Astronomical Observatory	Masahiro Koshikawa, Suguru Araki	clouds
2012-06-06	Venus	visual, Nikon D40	Flagstaff, Arizona	-	**success**
2012-06-14	Pluto	24-inch Sawyer	Wellesley College Observatory	Alyssa Sokal	clouds
2012-09-09	Pluto	1.2-m MONET North	McDonald Observatory	-	**success**
2012-10-02	Pluto	1.2-m MONET North	McDonald Observatory	-	no occultation

Chapter 2

Coordinates on Pluto

2.1 Background information

In Chapter 7, I will discuss asymmetries of Pluto occultation light curves as compared with surface features on Pluto. To correlate location with surface feature, one must first calculate the longitude and latitude of the half-light radius for each occultation chord, and then translate that information atop a map of Pluto's surface. For that, I needed some maps of Pluto. I requested and received two maps of Pluto from Henry Throop, along with instructions to check their orientation in GEOVIZ, the New Horizons encounter planning tool:[1]

> Enclosed are several versions. Pick your favorites. I don't know that the geometry is consistent, but if you compare to each other and the GV output, then you'll be able to figure out which way is up, etc. (Throop, 2012)

When I looked at the maps (see Figure 2-1), I noticed that the U-shaped feature in the albedo map (top) seemed inverted when displayed in the composition map (center). I suspected it might be upside down in GEOVIZ too. To make a long story short, it was upside down, but I had difficulty finding information to convince Henry

[1] `http://soc.boulder.swri.edu/nhgv/gv.php`

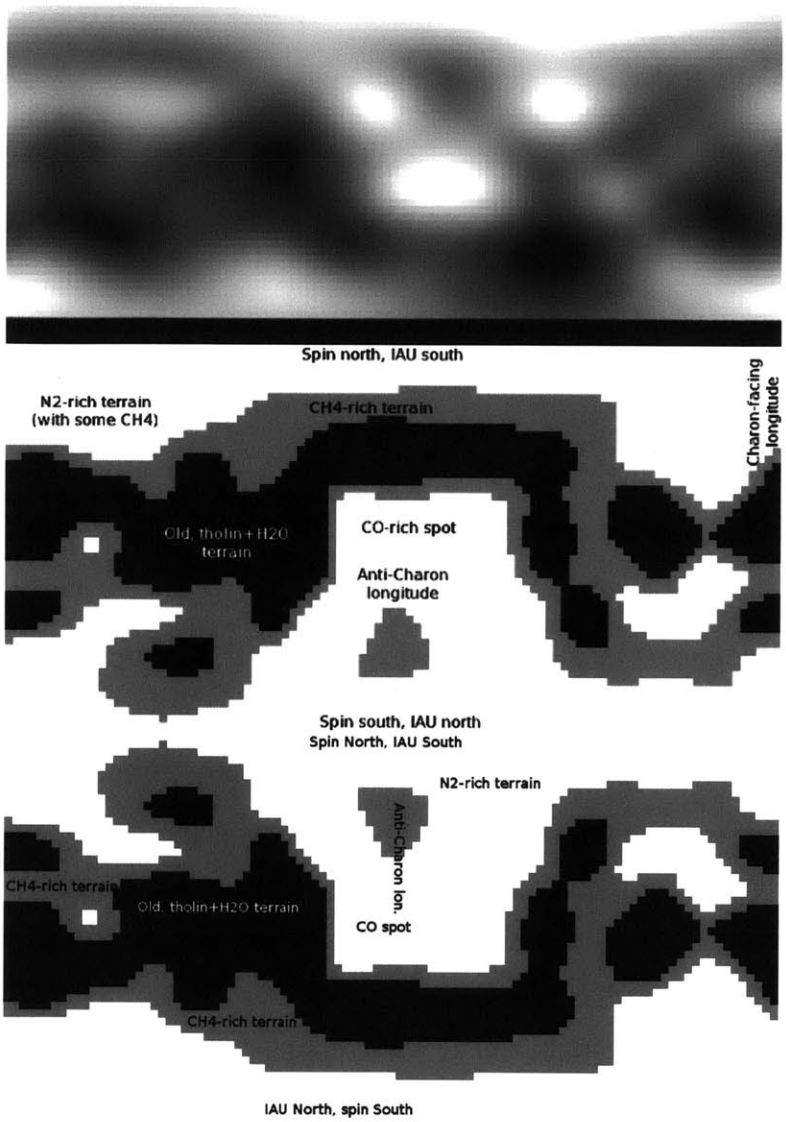

Figure 2-1: Original maps provided by Henry Throop as oriented in GEOVIZ. The pole facing Earth is oriented upwards. The albedo map (top) is properly oriented, while the lower composition map (center) was found to be upside down. The properly oriented map is below. The top map was published in Stern et al. (1997) while an unannotated version of the lower map was published in Grundy & Buie (2001).

Throop of that fact.[2] It wasn't until a week into poring through the literature that I was able to find the original published version of the composition map (Grundy & Buie, 2001) and prove that it was in fact upside down. By that point, it was clear to me that the map was not the only mistake related to Pluto coordinates, but a symptom of a larger problem. I spent the next several weeks delving deeper into the issue.

Simply put, is Pluto is right-side up and rotating backwards, or upside down and rotating in the usual direction (counter-clockwise)? Does one define Pluto's "North Pole" as the pole that is north of the ecliptic or the pole that represents the direction of the vector of Pluto's angular momentum? On Earth, these two poles are the same. With Pluto, these two poles differ, as do the poles of Uranus and Venus (Seidelmann et al., 2007).

2.2 Cartographic coordinate conventions

2.2.1 Two IAU conventions

The following is the IAU definition for the pole of a *Major planet.*

> Planetographic coordinates are defined by guiding principles contained in a resolution passed at the fourteenth General Assembly of the IAU in 1970. These guiding principles state that:
>
> 1. The rotational pole of a planet or satellite which lies on the north side of the invariable plane will be called north, and northern latitudes will be designated as positive.
> 2. The planetographic longitude of the central meridian, as observed from a direction fixed with respect to an inertial system, will increase with time. The range of longitudes shall extend from 0° to 360° (Archinal et al., 2011b).

[2] In the end it was found that the program used to add the additional labels to the composition map flipped the .gif file along the Y-axis relative to how the original IDL program wrote the file.

The IAU's 2006 redefinition of Pluto as a dwarf planet meant that these rules did not necessarily apply to Pluto any longer. As a new category, scientists could choose whether to use the major planet rules or follow the guidelines for coordinates on asteroids. Here are the IAU's rules for dwarf planets:

> Taking all of this into account, our recommendation is that longitudes on dwarf planets, minor planets, their satellites, and comets should be measured positively from 0 to 360 degrees using a right-hand system from a designated prime meridian. The origin is the center of mass, to the extent known. (Archinal et al., 2011b)

Because Pluto's right-hand rule pole is not above the ecliptic, this decision reversed both longitude and latitude. The North pole was swapped with the South pole, and longitude changed from planetographic (sub-Earth longitude increasing as seen from Earth) to planetocentric (sub-Earth longitude decreasing as seen from Earth). Despite its adoption in 2009, and publication of the new rules in 2011, no paper had (as of 2012) recognized the new decision. However, many scientists had been using the right-hand rule in publications for years[3].

As there are now two possible IAU systems, using the moniker "IAU" is ambiguous. Throughout this chapter, I will refer to the IAU *major planet* definition, which applied to Pluto until 2006 as the **Ecliptic North, Increasing Longitude System** or **ENLon+**. I will refer to the IAU definition for *dwarf planets* as the **Right-Hand Rule, Decreasing Longitude System** or **RHRLon-**. Outside this chapter, all coordinates will be specified as RHRLon-.

2.2.2 A third system: phase

Before the adoption of sub-Earth longitude for Pluto, rotational phase was commonly used to describe the time of day. Rotational phase runs from 0 to 1. An epoch that denotes the zero of rotation period is usually provided with the period and phase measurement.

[3]e.g. `http://www.boulder.swri.edu/~buie/pluto/maptoys.html`

Table 2.1. Pluto pole determinations by the IAU throughout time.

Meeting Year	Pole α_0	Pole δ_0	W	$\dot{W}$	Publication
1979	305	5	360[a]	−56.367	Davies et al. (1980)
1982	311	4.00	360	−56.364000	Davies et al. (1983)
1985	311.63	4.18	252.66[b]	−56.3640000	Davies et al. (1986)
1988	311.63	4.18	252.66	−56.3640000	Davies et al. (1989)
1991	313.02	9.09	236.77	−56.3623195	Davies et al. (1992)
1994	313.02	9.09	236.77	−56.3623195	Davies et al. (1996)
1997[c]	-	-	-	-	-
2000	313.02	9.09	236.77	−56.3623195	Seidelmann et al. (2002)
2003[d]	-	-	-	-	Seidelmann et al. (2005)
2006	312.993	6.163	237.305	−56.3625335	Seidelmann et al. (2007)
2009	132.993	−6.163	237.305	56.3625225	Archinal et al. (2011b)
2009 erratum	-	-	302.695	56.3625225	Archinal et al. (2011a)

[a]Zero longitude was defined with respect to the epoch of B1950.0: JED 2433282.5, invariable plane north pole 272°.40, +66°.99.

[b]Zero longitude was defined with respect to the epoch of J2000.0: JD 2451545.0. invariable plane north pole 273°.85 +66°.99

[c]No report exists from the 1997 meeting in Kyoto.

[d]While a report *does* exist for this meeting, it states that no values were redefined. Thus, they were not reprinted.

The two most common places to define the zero point of Pluto's rotational phase are light-curve minimum (see Figure 2-2), and greatest northern elongation of Charon (see Figure 2-3). By a coincidence that Richard P. Binzel states that astronomers have largely "gotten over", these two points are off by just a few hours (Binzel, 2012).

The system (along with RHR for the north pole) was commonly used for publications about the mutual events, where 0.25 denoted a transit by Charon ("inferior event") and 0.75 noted a occultation by Pluto ("superior event").

It is inappropriate the note phase in degrees. Unlike sub-Earth longitude, rotational phase does not take into account observer position and time of year– phase and sub-Earth longitude are analogous to sidereal and solar days.

2.2.3 Twelve possible coordinate conventions to eight

Altogether, there are twelve possible configurations to report Pluto coordinates: three latitude (Ecliptic North, RHR North, or none), and four longitude (Increasing, Decreasing, Phase [all Epochs] or none). Omitting the dual non-mention of longitude and

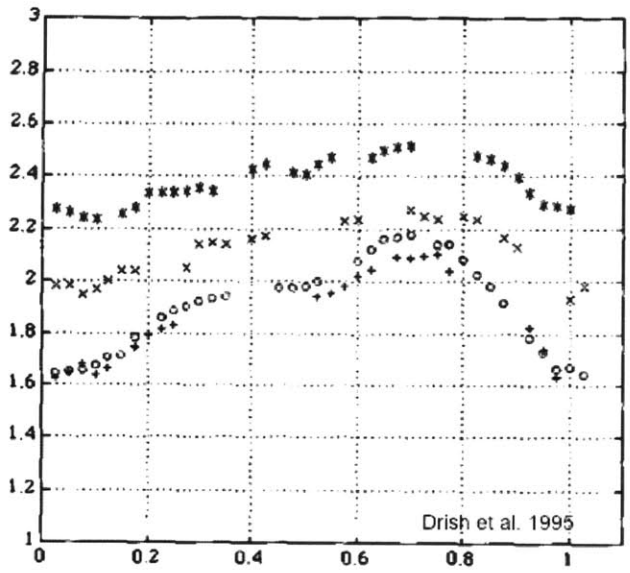

FIG. 2b. The normalized disk-integrated lightcurves for 1954 (*), 1964 (x), 1981 (+), and 1986 (o). These data are used directly by MLI and are normalized to the interval [0, π]. Regions in rotational phase where there are gaps have corresponding rows in the H matrix set to zero.

Drish et al. 1995

Figure 2-2: Pluto's light curve in time, plotted using a rotational phase system with zero at minimum light, a location that coincidently corresponds to Charon's greatest northern elongation. Figure reproduced from Drish et al. (1995).

latitude– the vast majority of papers published about Pluto do not go into specifics about surface location at all– leaves eleven possible conventions. Usually, only one set of rules is used. For example, ecliptic north is usually seen with increasing longitude and if a paper that uses the right-hand rule mentions sub-Earth longitude, it will be decreasing longitude. Phase was only *ever* paired with the RHR pole. There are some exceptions: some papers will mention both conventions. See Figure 2-4 for advice on converting between conventions.

2.3 History of Pluto's obliquity

For over two decades after Pluto's discovery, Pluto's light-curve was unknown. In the 1950s, it was discovered that Pluto varied by 0.1 magnitude over 6.39 days (Walker & Hardie, 1955). Shortly before that time period, Pluto was nearly pole-on as see from the Earth. Pluto's light curve, which is produced by albedo variations and not

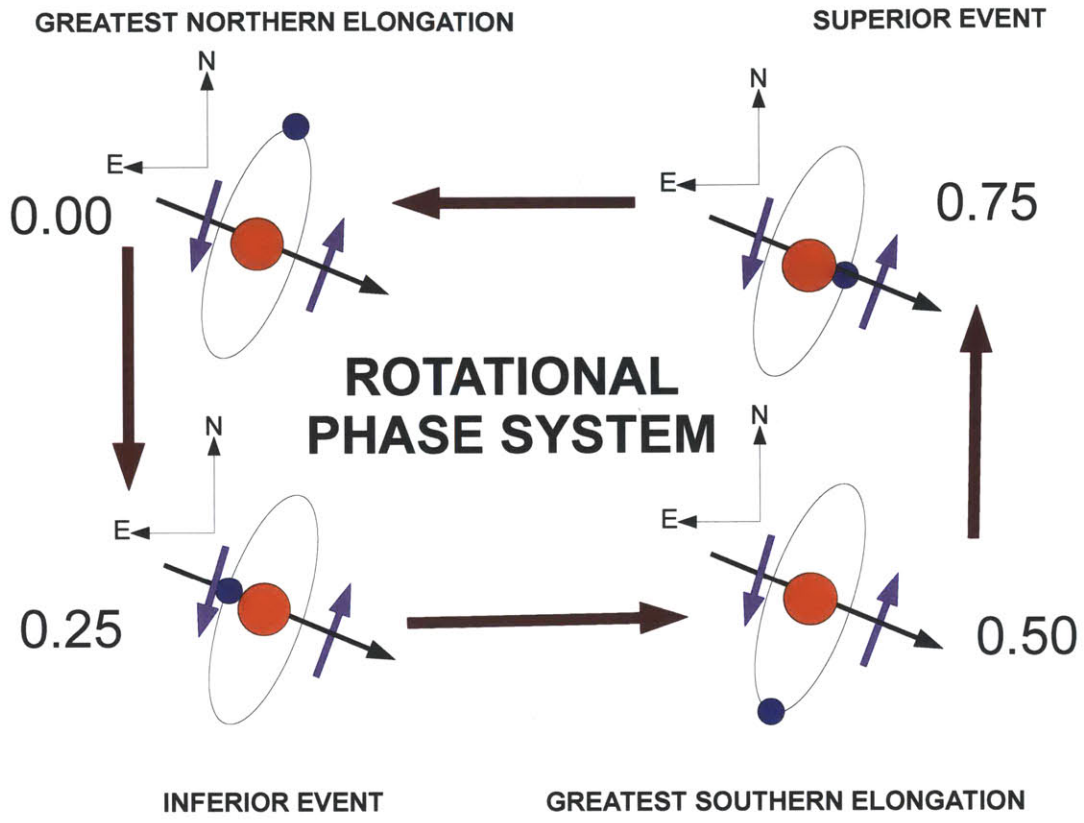

Figure 2-3: Rotational phase system as defined by Charon's orbital revolution. In the 1980s, the epoch of rotational phase was readjusted to have a zero point at the greatest northern elongation of Charon. Coincidently, the greatest northern elongation lines up very nearly to light-curve minimum, the original phase definition.

an oblong shape, was at its most dramatic when seen edge-on during the mutual events from 1985 to 1990. Andersson & Fix (1973) published the first paper about Pluto's obliquity. Pluto's pole was later found to be slightly out of the range first given (Marcialis, 1997).

In 1978, Charon was discovered, and found revolve to around Pluto with the same period as its rotation (Christy & Harrington, 1978). From Charon, Pluto's pole position and rotational direction was established by the IAU, choosing the pole to be north of the invariable plane (Davies et al., 1980). Since then, Pluto's pole position has been updated to reflect the following: the change from B1950 to J2000.0, the zero to be at Pluto sub-Charon longitude, some precision adjustments and finally, the redefinition of Pluto's pole to follow the new dwarf planet rules (see Table 2.1).

Green=Right Hand Rule ; Red= Ecliptic North/Increasing; Yellow=Rotational Phase

	No long No phase	Long --	Long ++	Rotational Phase
No Pole		:-)	360-long	360-360(phase-0.25)
RHR North	:-)	:-)	360-long	360-360(phase-0.25)
Ecliptic North	-lat	-lat	-lat 360-long	-lat 360-360(phase-0.25)

Figure 2-4: Instructions for converting between conventions to reach the Right-Hand Rule, Decreasing Longitude (RHRlon-) convention. The columns show the four longitude possibilities, while the rows show the three possible latitude conventions. Boxes show the appropriate formula.

2.4 The survey

2.4.1 Survey goals and scope

With the following goals in mind, I conducted a survey of Pluto literature from the late 1970s until June 2012, and made a catalog of which coordinate system was used:

- To provide background research for this document.
- To make a catalogue of many papers and write which convention they use for easy reference.
- To seek out other abnormalities in Pluto coordinates.
- To properly merge occultation paper information.
- To make an informed choice of coordinate systems for this work.

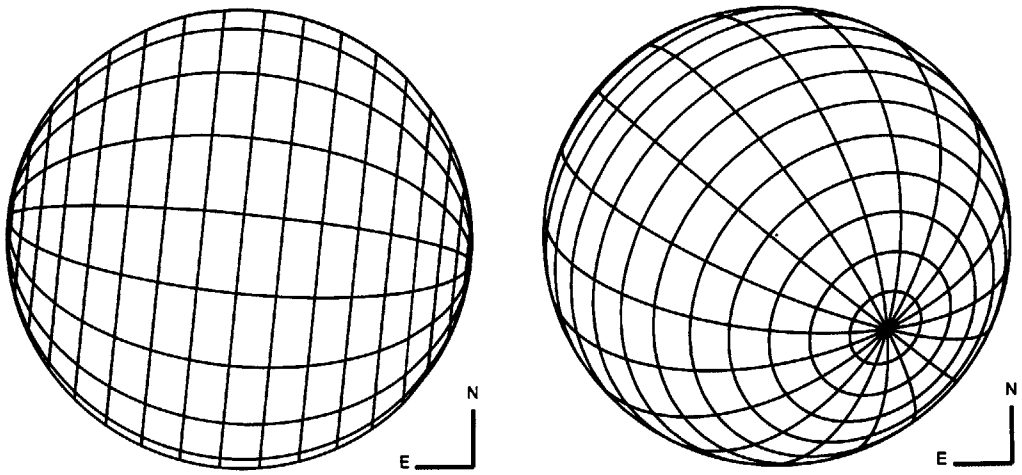

Figure 2-5: Sub-Earth view of Pluto on June 9, 1988 (left) and July 14, 2015 (right) oriented North up, East left as frequently seen on the sky. Since the mutual events in the late 1980s, the same face of Pluto has been visible, and will be for another century. Pluto rotates counter-clockwise around the currently visible pole, and its angular momentum vector points in the same direction.

Querying Harvard's Astrophysical Data System (ADS)[4] with Pluto entered in the "title" search field, I received about 1700 hits, approximately 800 of which made it into my survey. I only selected works that had an "E" or "F" link, which indicated that a full text version of the paper was available online. Some conferences, such as the European Planetary Science Congress or EPSC have full two-page abstracts. Older meeting abstracts, were originally typed, mailed and pasted together. Thus ADS includes them as scans with full text links, and thus those were included. Thus, AAS or DPS abstracts were not part of the survey, unless the abstract was scanned. Major books on Pluto were found offline. If available online and linked to ADS, I located several PhD theses. Book reviews (usually about books about Pluto) and introductory articles– the sort that would accompany a *Nature* paper– were included. If an article was clearly not about Pluto, I simply skipped it. For example, I ignored articles about Plutonic Rocks, or code package named PLUTO.

[4] `http://adsabs.harvard.edu/abstract_service.html`

2.4.2 Coordinate survey methods

I skimmed each paper to determine what coordinate system was used. If optical character recognition existed for the paper, I would search for the key phrases "sub-Earth longitude", "sub-Earth latitude", North, South, East, West, rotational phase and pole. If a table of measurements of Pluto was included, I looked to consecutive measurements to determine whether longitude was increasing or decreasing.

Often, papers did not directly state outright which conventions were used. If that was the case, the longitude and latitude were estimated using a JPL ephemeris and the convention was identified. For the north and south poles, it was simply a matter of checking which pole was identified as visible at the time of observation. For example, if a paper describing work after 1989 identified the North Pole as currently visible (see Figure 2-5), the right-hand rule was used.

The convention each paper used was catalogued, and if an error or ambiguity was present, a note was made.

2.4.3 Coordinate survey results

The number of each papers that followed each convention, and the topic of each paper was hand counted (possibly resulting in an error of 1-2 papers for each figure given). For the breakdown of number of papers by convention, see Figure 2-6. The papers that use the RHRLon- system outnumber ENLon+ paper by about 4 to 1. The number of errors and ambiguities that were found (19) is commensurate with the number of papers using the ENlon+ system (21).

Historically, phase and RHR north were used in the 1980s, but were phased out in favor of decreasing longitude by the mid-1990s. After the year 2000, there was resurgence of ENLon+. See Figure 2-8 for more details. Much of the increase in ENLon+ coordinates can be attributed to two topics: Pluto occultations and New Horizons.

Even though no paper has yet acknowledged the IAU's adoption of the right-hand rule, the majority of papers were written using the RHRlon- rules or parts thereof

Green=Right Hand Rule ; Red= Ecliptic North/Increasing; Yellow=Rotational Phase

	No long No phase	Long --	Long ++	Rotational Phase
No Pole		8	2	23
RHR North	37	40	0	7
Ecliptic North	12	0	7	0

Figure 2-6: Number of papers for each convention. The columns show the four longitude possibilities while the rows show the three possible latitude conventions. The 19 papers with errors or ambiguities are not included in this table.

anyway. With the exception of the first two spot models, which use phase (Marcialis, 1988) and Drish et al. (1995), all maps of Pluto follow RHRlon- coordinates. See Figure 2-7. If papers about mutual events chose to use a coordinate system at all, it was RHR north with phase, though later papers focusing on mapping switched to sub-Earth longitude.

2.4.4 Pluto occultations and coordinate systems

As shown in Figure 2-7, the majority of Pluto occultation papers that use coordinates on Pluto follow the ENlon+ system. Only a small handful papers mention particular location on Pluto at all. Most papers discuss occultation prediction, briefly reports success or failures, or refer to latitudes and longitudes on Earth instead. However, the papers associated with P8, particularly Millis et al. (1993), use RHRlon- coordinates as was custom during that time period. It would be a full decade between that work and the next occultation results, which favored the ENlon+ system (Sicardy et al., 2003; Elliot et al., 2003b).

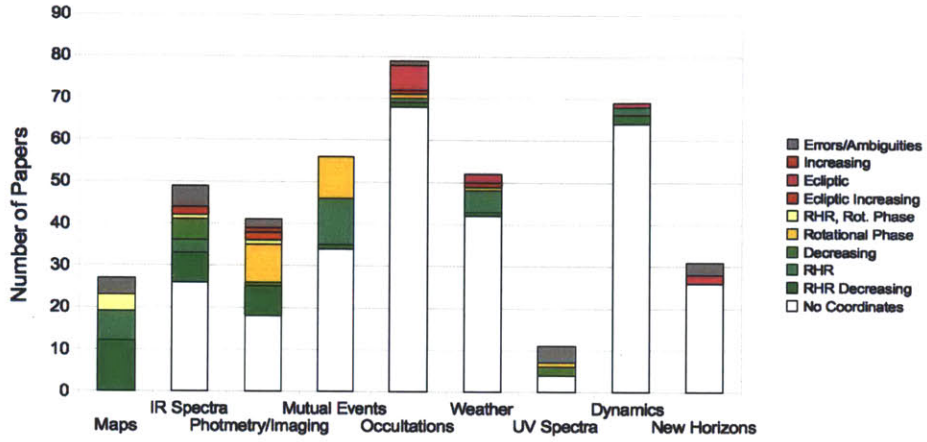

Figure 2-7: Number of papers that use each system sorted by topic. The nine topics shown here have five or more papers that mention coordinates. While a paper could be classified in more than one way, it was only assigned to one topic, thus this graph should be treated as representing general trends only.

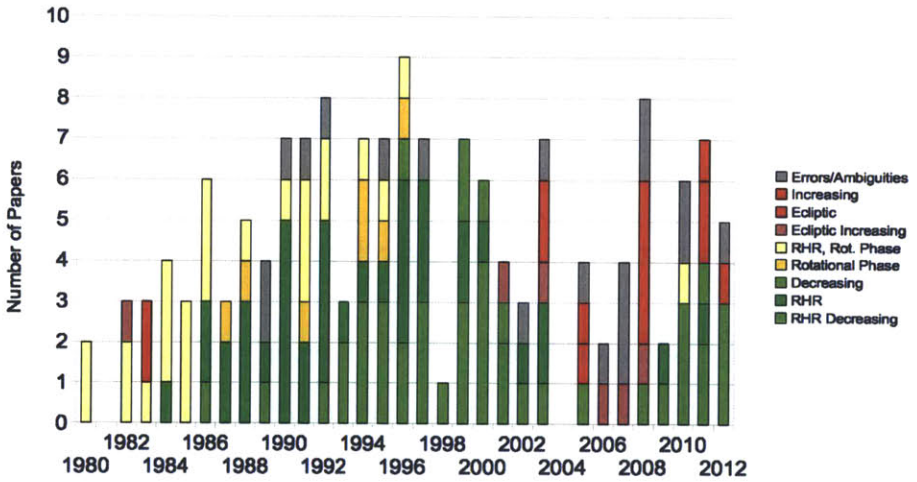

Figure 2-8: Number of papers that use each coordinate system by year published. Note that the obsolete phase convention gives way to RHRlon- by the mid-1990s, and that there is a resurgence of the ENLon+ system after the year 2000. Grey indicates errors or ambiguities found in the literature.

2.4.5 Survey conclusions

The large number of Pluto maps and papers using RHRlon- make it the most important conventions. The publication of surface maps using the RHRlon- convention, and the implicit assumption (that has resulted in many errors) that all coordinate systems are identical has made RHRlon- coordinate the *de facto* system. The additional endorsement of the IAU and the system's popularity among astronomers, simply cements its usefulness. There is no reason to use an unpopular system, simply because it was once favored in 2006. For that reason, all data herein, and all descriptions of Pluto presented elsewhere in this thesis will be presented using RHRlon- coordinates or converted to that system, where applicable.

2.5 Recommendations to avoid errors

When decoding others' papers...

Having looked at over a hundred papers that refer to longitude and latitude, I will offer the following advice for those reading papers to decode which coordinate system is in use:

- **Assume nothing.** Because many papers have mistakes, one should work from the assumption that the information about pole and coordinates may or may not be correct. Instead...
- **Take only times from papers.** It is very possible that the pole position has since been readjusted, not in the sense of which way is north, into a slightly updated position based new observations. Thus longitude and latitude should be recalculated to prevent small error on the order of a degree or so.
- **Hypothesize which pole the author is talking about.** Calculate which pole the author is describing, then check to see that it is correct.
- **Do not assume that the entire paper is consistent. Confirm EVERYTHING.** An individual point could be problematic, or multiple systems could

be used across one work. Many mistakes occur when data are merged.

- **Beware east longitude. Write a program to calculate all conventions for a given time.** "East longitude" could potentially refer to both ecliptic/planetographic coordinates or the right-hand rule, even though east longitude is most frequently used with the right-hand rule. Recalculating points allows for a stronger identification.

When writing papers...

When writing your own papers do the following.

- **ALWAYS include mid-times with data.** This will allow future Plutophiles to recalculate the sub-Earth point when the pole position is improved in the future.

- **If using phase, include an epoch and length of Pluto day.** Even when in fashion, epochs centered on the same calendar date, often differed from each other by a few hundredths of a Julian day. However, phase is obsolete and should be avoided.

- **Mark all permanent night-areas as unavailable on maps.** Because a large portion of Pluto's surface is currently unknowable, marking it as unavailable (as opposed to interpolation) serves as a reminder which pole is currently visible. While a black bar did not prevent all errors, it should have prevented the GEOVIZ error. Unfortunately, no such surface feature exists to sort out longitude.

- **Use "currently visible/RHR" and "Discovery/non-visible/ecliptic" pole to distinguish between the two poles for polar caps.** Dropping the terms north and south allows for a way to tell the poles apart.

- **Use prograde and retrograde to define direction**. The use of prograde or retrotrade can replace east and west in situations when winds are described.

- **Using your own system? Flip other data to match!** It's more confusing to use multiple systems in one paper.

- **Do not invoke the IAU as an unambiguous identifier. Describe what you are doing (RHR: spin north, decreasing), cite quietly.** The IAU way could now refer to both major systems. So far no paper has mentioned the IAU's reversal on Pluto coordinates. Thus "IAU Way" has become synonymous with the Ecliptic system. The best approach is to cite the new paper, but not use the words "IAU".

- **When combining data, RECALCULATE sub-Earth points, even for fully consistent systems (pole drift).** Simply converting between systems is not enough as the pole position has moved by a few degrees several times throughout history.

- **THE RHR POLE IS STRONGLY PREFERRED.** Finally, the right-hand rule system is the best system. New Horizons should adopt it, as it is currently preferred by the IAU, matches the most papers, and is least prone to confusion.

2.6 A final note

On October 9, 2012, the author gave a colloquium on the subject of Pluto coordinates at Southwest Research Institute. The audience included many members of the New Horizons team. While the talk was well-received, it was later confirmed that it was too late in the mission design process for the team to switch coordinate systems for planning purposes. It does seem likely, that a coordinate swap will occur after data are received, and publications will use RHRLon- coordinates.

Chapter 3

Laboratory Testing of the High-speed Imaging Photometer for Occultations (HIPO)

Portions of this document were taken from an internal report on HIPO stability written by the author, as well as a EPSC poster of the same (Zangari et al., 2011).

3.1 Introduction and motivation

3.1.1 Airborne astronomy takes flight

In Section 1.2, I listed the number of occultation and transit events I have attempted to observe over the past six years. Of the eighteen events listed, only three events were successes. Clouds were responsible for nine failures, and wind another. For other events, I was simply outside the path of the occultation. Every occultation provides a unique observational opportunity. Occultations are single events occurring at one time and place in the sky. There are no do-overs.

In Chapters 5 to 7, I will discuss the relationship between the location probed in a stellar occultation and asymmetries seen in the light curves. In Section 5.4.3, I will show that only the best light curves are suitable for asymmetry analysis, leaving a set

of nine light curves. In Chapter 7, these nine light curves will be broken down into categories related to insolation, time of day and surface features, leaving just one or two light curves of each type. The loss of an event has a very strong impact on the aggregate occultation data set.

Observations from an airborne platform have the power to overcome the two of the most common reasons for failing to observe a stellar occultation: weather and an occultation path outside of an observing site. With a telescope and a plane, one can fly above the clouds and into the shadow path.

Airborne astronomy does not solve these problems 100%– poor weather can delay flights, storms can divert planes for landing at other airports, and in the case of 2010 eruptions of an Icelandic volcano, geophysical activity can ground air traffic for days at a time. While the use of an airborne plane does allow adjustments based on last-minute changes in the prediction, the new ideal observing location may not be feasible. Even if a new occultation path is still over the Earth, the path may not be in range of an airport capable of deploying an airborne observing platform, or more frustratingly, the new path is in the middle of international airspace where permission to fly cannot be granted in time, or is unsafe (i.e. a war zone). Owing to the price and organizational efforts required to carry out observations from an airborne platform, observers must be circumspect when deciding for which occultations they will choose to request airborne observations.

From 1974 to 1995, the Kuiper Airborne Observatory flew roughly 80 missions per year over its 21 year history (Haas, 1995), the most well-known of which were in support of stellar occultations. The KAO sought and oberved occultations by Triton (Elliot et al., 1993), Chiron (Elliot et al., 1995), Saturn (Dunham et al., 1989), Pluto (Elliot et al., 1988), Uranus (Elliot et al., 1978) and Mars (Elliot et al., 1977a). Most famously, the rings of Uranus and Pluto's atmosphere were discovered during stellar occultations on the KAO (Elliot et al., 1978, 1988).

In development since the mid-1980s[1], the Stratospheric Observatory for Infrared Astronomy was built to be the successor to the KAO. A modified 747-SP with a

[1] `http://www.sofia.usra.edu/Sofia/history/sofia_history.html`

2.7-m mirror[2], SOFIA boasts the largest telescope mirror to ever be placed in an an aircraft.

3.1.2 Previous airborne occultation instrumentation

For original occultation observations on the KAO, Elliot et al. simply brought aboard the three-channel photometer used for observations of lunar occultations (Elliot et al., 1975, 1977b; Dunham & Elliot, 1983). Prompted by photometric problems, namely scattered background light and seeing disks too large for the aperture of the photoelectric photometer (Dunham & Elliot, 1983), Dunham et al. (1985) decided to try out CCD a camera as a photometer, resulting in the creation of the SNAPSHOT system.

Unlike photomultiplier tubes which cannot read out any slower than 1 second (Dunham & Elliot, 1983), the SNAPSHOT required about 1 second of readout time per image, assuming three 50-pixel subframe boxes were created, and data were only read from those areas.

In 1993, Buie et al. (1993) describes a frame transfer CCD for use in occultations, PCCD. This device later flew aboard the KAO to observe the 9 March 1994 occultation by Chiron (Elliot et al., 1995). Since then, frame transfer CCDs have formed the backbone of occultation systems such as POETS (Souza et al., 2006), an upgrade to MagIC (Osip et al., 2008), and the PHOT system (Young et al., 2011), assuming the expense can be spared (Lockhart et al., 2010).

3.1.3 HIPO

Designed with stellar occultations in mind, the High-speed Imaging Photometer for Occultations is a two-channel optical photometer with two liquid nitrogen-cooled 1k x 1k[3] frame-transfer CCDs that can take up to two GPS-triggered, full, unbinned

[2]Part of the mirror is blocked at any one time so the mirror is typically referred to as a 2.5-m mirror to reflect its true light-collecting area (`http://www.sofia.usra.edu/Sofia/telescope/sofia_tele.html`).

[3]Precise chip dimensions are 1056 x 1030 pixels.

frames per second (Dunham et al., 2008). HIPO contains two parallel, but fully independent CCDs, filter wheels, dewars, electronics boxes, power supplies, and control computers. The optical light is divided by a removable dichroic, which sends light through reimaging optics to each of the two separate CCDs. The "blue channel" can image from 300 nm to 650 nm, while the "red channel" can image from 400 to 1100 nm. HIPO can be co-mounted with the infrared camera, FLITECAM for simultaneous three-channel photometry (Dunham et al., 2004; Dunham, 2003).

Aside from redundancy, multi-color observations will allow users to search for wavelength dependencies in occultation data. Multi-wavelength observations may be essential for determining whether Pluto's lower atmosphere has a haze layer with wave-length dependent refraction or a thermal gradient. Additionally, filtering down an occultation camera will allow for proper determination of the extinction of occultation and field stars, vital for reduction of high-airmass occultations, such as the Pluto occultation observed from Europe in February 2010 (Young, 2011).

However, there is one very good reason to forgo multi-color observations: signal-to-noise. High-cadence observations, which reveal atmospheric waves and precise positioning of the occulting body, are only feasible if enough light is collected to permit them. No piece of optics, whether it is a filter, dichroic or mirror, is 100% efficient. If the blue channel, the red channel, FLITECAM and the Fast Diagnostic Camera (Wolf et al., 2010) are all used to observe an occultation, there will be little light for any single camera. Thus the simplest optical design will allow the maximum number of photons to be collected. HIPO sports an "unfiltered" option for each of its two channels. Additionally, if more light is desired, the dichroic beamsplitter can be removed, sending all its light to the red channel (Dunham et al., 2004).

3.2 HIPO characterization in the lab

In preparation for HIPO commissioning which took place in summer 2011, a series of imaging tests have been undertaken. These tests examine the stability of the differential photometry against temperature changes on the chip, the electronics and

power supply. Determining the limits of HIPO's photometric precision in a laboratory setting is necessary to determine the limits of high-precision airborne exoplanet transit photometry, another important application of HIPO (Gehrz et al., 2010).

3.2.1 Sources of change

With the Kepler mission, "end to end system tests" were designed to ensure the desired precision of 1×10^{-5} was achievable in the "presence of disturbances ... expected in a spacecraft" (Witteborn et al., 2000) . Along the same vein, the HIPO team listed several sources of problems in the airborne environment:

1. Bias and gain instability from various sources
2. Flat field variations with temperature, pressure
3. Imperfect flat field correction
4. Liquid nitrogen boil-off (CCD temperature change, possible position offset too)
5. CCD temperature change
6. CCD controller temperature variation
7. CCD controller power supply temperature change
8. Image motion
9. PSF variability, including focus change, misalignment, aero-optics
10. Atmospheric transmission variation

The goal was to take test data while simulating such disturbances and determine the photometric stability under idealized lab conditions.

At the instrument lab in Flagstaff, Arizona, HIPO was attached to an "integrating sphere" that illuminated a brass shim stock foil plate through which several holes were drilled with a 0.007" diameter twist drill to resemble stars (Dunham, 2013). Our artificial star plate contained nine synthetic stars, with five on the region read out by

the left amplifier, and four on the region read out by the right amplifier. Figure 3-1 shows the layout of each frame. After installation, the star plate remained in place throughout the testing which began in October 2010 until HIPO was transported to Palmdale, CA for commissioning in June 2011 (Dunham, 2013). Throughout this chapter, these artificial stars will be referred to simply as stars. Overscan regions were also included; each amplifier read out a 40 pixel postscan region. HIPO allows the user to select one of many different "DSP codes" to run the camera. DSP code choice determines the read-noise, gain, camera speed and camera dynamic range. For each test, an identical DSP code was used, with the exception of a test where the wrong DSP code was selected for the red camera. The DSP code used had camera gains of 1.7 an 1.6 for the left and right amplifiers of the red channel and 1.7 and 1.67 for the blue channel. It had read noises of 4.9 and 4.6 for the red channel and 4.5 for both amplifiers of the blue channel[4].

For each test, identical imaging times (2s), integrating sphere brightness, filters and star plates were used.

The photometry temperature tests fall into three categories:

Detector temperature tests

For the first detector temperature test, the set point of the CCD temperature for each chip was changed while imaging was taking place. For the second two tests, the two warm dewars were filled with liquid nitrogen. Images were taken during simultaneous chip cool-down.

Controller temperature tests

Each of HIPO's independent CCDs is operated by its own electronics box ("controller"), mounted on opposite side of the HIPO casing. The controller consists of several Leach boards (Leach et al., 1998) that run the camera. Over the course of six separate tests, the temperature of one electronics box was altered. The controller

[4]These gains and read noises were later used for the HIPO observations of an occultation by Pluto in June 2011.

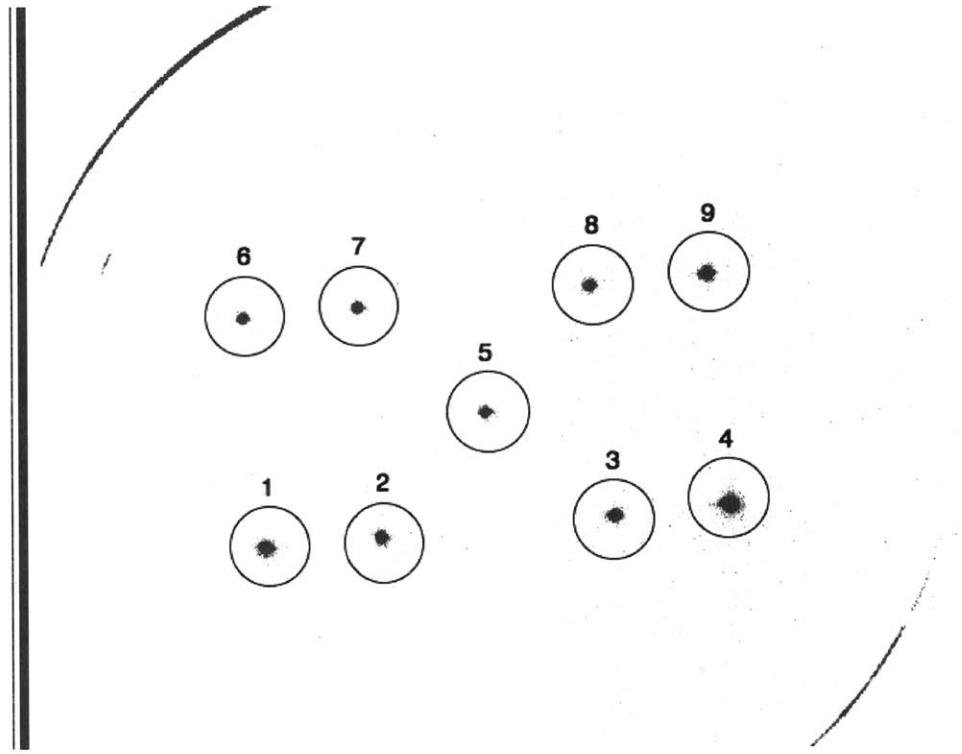

Figure 3-1: Sample HIPO test image with artificial stars labeled. Stars 1, 2, 5, 6, and 7 fall on the left amplifier while stars 3 4, 8 and 9 fall on the right amplifier. This image is from the HIPO blue a23 test.

temperature was raised through insulation with a cardboard box, or lowered with either liquid nitrogen or ice water. In the case of the ice water chilling, the outer plate of the controller box was replaced with a similar-sized plate with metal pipes fastened to the outside. An aquarium pump forced ice water through the pipes from a cooler on the floor, after which point, the spent water was returned to the floor cooler. This test is designed to mimic changes in cabin temperature. Ambient temperature has been known to affect the bias level. After years of observations, it was discovered that the bias level of a camera at the US Naval Observatory in Flagstaff, Arizona fluctuated with the time of year, or rather the temperature changes brought with the changing seasons (Levine, 2010).

Power supply temperature tests

During imaging, the covers were removed from both power supplies, which were cooled using a household fan. Unlike the detector and controller temperature, the power

supply temperature could not be continuously monitored by a probe that reported to the header of each image. Thus the cover was removed from the power supply and a small thermometer was inserted inside the power supply and the temperature was recorded 1. at the beginning of the test, 2. when the cover was removed, 3. when the fan was turned on and 4. at the end of the test.

Tests not described herein

The work below only summarizes HIPO stability test data taken by Georgi Mandushev and Ted Dunham in October 2010 and further data taken in December 2010 by Georgi Mandushev, Ted Dunham and Amanda Zangari. The twelve tests described below do not contain the data taken in July 2010 by Georgi Mandushev, Ted Dunham, Amanda Zangari and Jim Elliot. These previous data included four sessions that included a stability test which ended with imaging on an empty dewar, a second stability test, a detector temperature test and a focus test. In addition to time constraints prohibiting their analysis, these data had other issues. These data featured an earlier, less symmetric star plate from which the stars holes were hastily poked. The first data set was taken when the HIPO programming updated the detector and cold tip temperatures at the start of every imaging sequence, not the start of each data cube, making it impossible to probe temperature-based photometry changes. No overscans were taken for the first two data sets. The cold tip temperature probe was pegged at 39°C. The detector temperature test was repeated in October 2010 and the new test was analyzed here, and the focus test was repeated and analyzed by Matt Sooknah in January 2011 (Sooknah, 2011).

3.2.2 Methods of probing change

For each test, each image was overscan corrected and both the "overscanned" and raw images were analyzed using IRAF[5]'s **imstat**. Several relevant keywords were

[5]IRAF is distributed by the National Optical Astronomy Observatories, which are operated by the Association of Universities for Research in Astronomy, Inc., under cooperative agreement with the National Science Foundation.

Table 3.1: List of test dates, test duration and test purpose. Instrument failures are marked.

Date	Test Code	Purpose	Duration
2010-10-23	a23	Detector Temperature Test	15.5 hours
2010-10-27	a27	Cool Down Test	3.5 hours
2010-10-28	a28 1 of 2	Blue LN Controller Test	2.5 hours
2010-10-28	a28 2 of 2	Cool Down Test	2.5 hours
2010-10-29	a29*	Blue LN Controller Test	3.75 hours
2010-11-30	b30 1 of 2 †	Blue Cold Water Controller Test	4.75 hours
2010-11-30	b30 2 of 2 †	Blue Cold Water Controller Test and Dual LN Fill	4.75 hours
2010-12-01	c01	Red Cold Water Controller Test	14 hours
2010-12-02	c02 1 of 3	Blue Cold Water Controller Test Redo	7 hours
2010-12-02	c02 2 of 3‡	Dual Power Supply Test	3.75 hours
2010-12-02	c02 3 of 3	Blue Power Supply Test	3.75 hours
2010-12-03	c03 3 of 3	Red Power Supply Test	3.75 hours

* The red computer crashed during this test and the system was restarted.
† The open filter was used on the blue system instead of V, and as a consequence, the data are saturated.
‡ The blue computer crashed during the last hour of testing.

extracted from the header. Photometry was performed by **daophot** through IRAF. A template with positions for the 9 stars on the star plate was made for October and another for December using **daofind**. Aperture photometry was performed non-interactively, though each star was re-centered using the centroid option. Apertures of 8, 10 and 15 pixels were used. It was later determined that an aperture of 8 provided the highest signal-to-noise ratio, so an 8-pixel aperture was used in analysis for all tests. Regardless of aperture choice, the median sky was calculated using an annulus of inner radius 25 and outer radius 35. IDL code was written such that the tens of thousand images acquired could be analyzed in an identical fashion.

For each test the following image characteristics were analyzed as variables:

Time

As each test consisted of a series of FITS cubes, time was only written to the header for the first image of each cube. Thus, the cycle time was used to calculate a start

time for each individual frame. For our purposes, we converted time to UT hours, but represented minutes and seconds as decimal values.

Cube position

The position of a frame within an image cube was added to the image header after each frame was split from its FITS cube into an individual image. Position within an imaging sequence matters, as the first image within a cube will be exposed for longer than the proceeding images, as the first GPS-triggered readout occurs at the beginning of the second image.

Every star on the first image of every cube differed from every other image in the cube in instrumental magnitude by 5 millimag and was thrown out before analysis. **HIPO observers should plan on not using the first image in a cube.** For the left amplifier on both the red and blue sides, the average *background counts* of the last overscan-corrected image in a cube were lower by a fraction of an ADU, an effect not visible in the instrumental magnitudes. Thus, the last image of each cube was not discarded.

A more-detailed analysis of cube position against photometry or astrometry was not performed.

Background

The image background is comprised of the bias and the dark current and is affected by the read noise. In addition to the light from the nine artificial stars, arcs of light from the sides of the star plate also reached the chip.

IRAF's **imstat** package was used to determine the background on each chip. The chips were divided into sections that contained the whole of the left amplifier and the whole of the right amplifier. These sections also included the drop off in light at the bottom of the chip as well as the stray light from the star plate and the stars themselves. For each section, the mean, "midpt", standard deviation and mode were calculated, though only the mean was used for analysis purposes.

The mean background values were calculated for the overscan regions as well as

the light collecting regions. The data were also overscan corrected, and the corrected mean background was also calculated.

A change in background could be caused by three things: a change in the electronics offset, a change in the amount of dark current, and a change in intensity of the sensitivity to light.

Detector temperature

With HIPO, the set chip temperature is maintained by a balance between a heater, and liquid nitrogen, which boils at -196°C. Each of HIPO's two CCDs has its own liquid nitrogen dewar. The "hold time" of the dewar is roughly 25 hours (Dunham et al., 2008). The typical flight duration of SOFIA is 8-10 hours[6]. For the HIPO CCDs, -120°C was chosen as the ideal operating temperature. A detector that is too warm will have dark current. Chip temperature is recorded in the header at the start of each cube.

Chip temperature fluctuations can come in many forms. For instance, the chip temperature can begin to cool again after the warm dewars have been filled. The temperature can be set to a cooler temperature than the current chip temperature. The temperature can be set to a warmer temperature than the current chip temperature. The liquid nitrogen can fully evaporate and the chip temperature will rise towards ambient (one of the July 2010 tests, not reported here, was designed to measure the effects of a warming dewar).

We performed three tests to probe photometric stability over temperature changes. The first test featured controlled warming of the chip in five degree increments. For the second and thirds tests, data were taken after liquid nitrogen had been added to a "warm", but not ambient temperature dewar. On all other tests, the chip temperature remained constant.

[6]http://www.sofia.usra.edu/Science/FAQ/index.html

Controller temperature

Like detector temperature, the temperature of the controller is written to the header at the beginning of each image cube.

The temperature of the controller was modified in three ways. First, the nozzle of the dewar used to supply the HIPO dewars was opened slightly and liquid nitrogen was sprayed directly onto the controller box. During one test temperature dropped by about 3 degrees over 3 minutes. Less drastically, a custom plate with pipes alongside it allowed cold water, often containing ice, to be pumped near the controller. Here the temperature change was roughly 3 degrees over 30 minutes. The final attempt at modifying the controller temperature was via insulation– a cardboard box was placed over the electronics box to little effect.

Individual star data

The primary data products from the photometry were X and Y[7] coordinates of the centers of each star, along with its the sky-subtracted flux. Each star was identified as being a part of a specific amplifier– the left (stars 1, 2, 5, 6, 7) or the right (stars 3, 4, 8, 9). Figure 3-1 shows the layout of the stars on the HIPO chips.

As comparing one star to another would be cumbersome with 9! combinations, the brightest two stars on each amplifier, star 1 for the left and star 4 for the right amplifier were compared using the remaining stars on their respective amplifier. Star 4 was the brightest star overall.

Instrumental magnitudes

While **daophot** can output instrumental magnitudes, they had to be recalculated from the flux because the provided precision of a millimag proved insufficient. Thus instrumental magnitudes were calculated using the following formula used by **daophot**:

$$mag = zmag - 2.5 * \log_{10}(flux/exptime). \tag{3.1}$$

[7]The X direction is the serial direction, while the Y direction is parallel.

Here *zmag* is set to 25.

For simplicity's sake, we sum the fluxes on the left amplifier (stars 1, 2, 5, 6, 7) and the right amplifier (stars 3, 4, 8, 9) and convert these sums into instrumental magnitudes. Instrumental magnitudes are magnitudes of the star compared against no flux above background on the detector. We sum the fluxes of the stars on each amplifier and plot instrumental magnitudes based on the sum of the fluxes for the stars on the left (left) and right (right) amplifiers. As the left amplifier contained five stars as opposed to the right amplifier's four stars, the right amplifier received more flux.

In the field, the instrumental magnitudes reflect the absolute brightness of the stars on the chip. Changes indicate either changes in gain or absolute changes in the source itself.

Differential magnitudes

It may be possible that the differential magnitude of stars located on two different amplifiers may not be constant. Sooknah (2011) chose not to perform cross-amplifier comparisons because "the two amplifiers have slightly different gain and read noise values." However, restricting star observations to a single side of the chip defeats the purpose of having two amplifiers– the chip might as well be cut in half to achieve the gains in speed by not forcing a one amplifier to read the whole chip. Thus, cross-amplifier comparisons are made herein.

To avoid complication with comparing all 9 stars, we consider three different differential scenarios. First, we compare the magnitude of the brightest star on the left amplifier (1) with magnitude calculated from the sum flux of all the other stars on the amplifier (2, 5, 6, 7). Second, we compare the magnitude of the brightest star on the right amplifier (4) with magnitude calculated from the sum flux of all the other stars on the amplifier (3,8,9). Finally, we compare the magnitude calculated from the sum flux of all the stars on the left amplifier with the magnitude of the sum flux of all the stars on the right amplifier.

Ideally, as the stars are illuminated by a single source of constant light, and

their brightnesses are dependent on the the size of the holes in the foil, differential magnitude should always be constant.

Group standard deviation and signal-to-noise

The sample standard deviation of the differential magnitudes was taken for each of the three comparisons: left amplifier, right amplifier, and left vs right amplifier. With the exception of the temperature stepping test, standard deviations were taken of groups in half-hour increments. For the temperature test, groups were divided up by chip temperature. We also calculated the signal-to-noise for each cube, using mean relative flux between the left and right amplifiers and its standard deviation.

Allan deviation

Theoretically, the more points data points that are collected, the closer a sample mean gets to the actual mean, and the standard deviation of that mean decreases. However, noise in the electronics will set a limit to infinite precision being reached. To measure the stability of the photometry in time, we look at a modified version of the *Allan deviation*, $\sigma_y(\tau)$. Like the standard deviation, the Allan deviation is used to describe the noise of a system, but instead of summing the deviations from the mean, the Allan deviation sums the differences of consecutive points. The Allan variance, $\sigma_y^2(\tau)$, is defined to be:

$$\sigma_y^2(\tau) = \frac{1}{2(M-1)} \sum_{i=1}^{M-1} [y_{i+1} - y_i]^2 \tag{3.2}$$

where τ is the time interval over which an individual point is averaged, and y is a deviation from a frequency. Here we substitute the concept of frequency deviation ($\frac{\Delta f}{f}$) for differential magnitude. Mathematically, these two concepts are equivalent, as the differencing would cancel out the calculation of the deviation from a common designated frequency. Division by that common frequency will alter the Allan variance by the equivalent of multiplying by a coefficient that would remain constant for every τ. However, while the value of the Allan deviation specifies the precision of a

measurement, the more important number is the τ at which the Allan variance stops decreasing according to a specific power law (Riley, 2008).

To split groups into blocks spanning time τ, we pay special note to the timestamp each image receives. We could merely group n images together, however, these groups may span time gaps in the data, which could possibly be quite large. There are three sources of these time gaps: downtime between image cubes, gaps where a bias was taken or data that were removed due to the amplifier issues[8]. To account for these gaps, we bin by time, taking the first image, and binning in units of time between two successive cubes (here $2s$). Each bin has a start time and an end time– images with a timestamp at or after the start time or before the end time are placed into that binning group. A mean and standard deviation of these images are taken without regard to the number of images in the binning group. Gaps will cause some binning groups have 0 images and are ignored in the differencing. As the length of time each binning group spans (τ) increases, the number of empty bins decreases.

We plot τ versus $\sigma_y(\tau)$ on a log-log plot. As τ increases, the Allan deviation should appear to decrease linearly on the log-log axes: the more points one places into a bin, the smaller the noise becomes. If the noise were completely gaussian, one could bin an increasingly large number of points and the noise would become increasingly smaller at a rate proportional to the square root of the number of points, and the linear improvement on the log-log plot would continue indefinitely. After a certain time, other factors come into play and prevent further noise reduction. For example, the source being measured is not constant or the ability of the equipment to register a constant signal has deteriorated. Instead of white noise, measurements could instead be dominated by flicker noise, drift, or a random walk.

The turn-offs for the Allan deviations were measured by hand by clicking on the graph at the approximate location of the turn-off. These hand measurements are accurate to 0.1 in log time and 0.05 in log magnitudes. See Figure 3-2 for an example of an Allan turnoff.

[8]For a few tests, unusual background features appeared in the left amplifier of the blue chip. These issues were documented in the larger report (Zangari, 2011). The blue controller Leach board experienced an age-related failure a few months after testing, and was replaced (Collins, 2011).

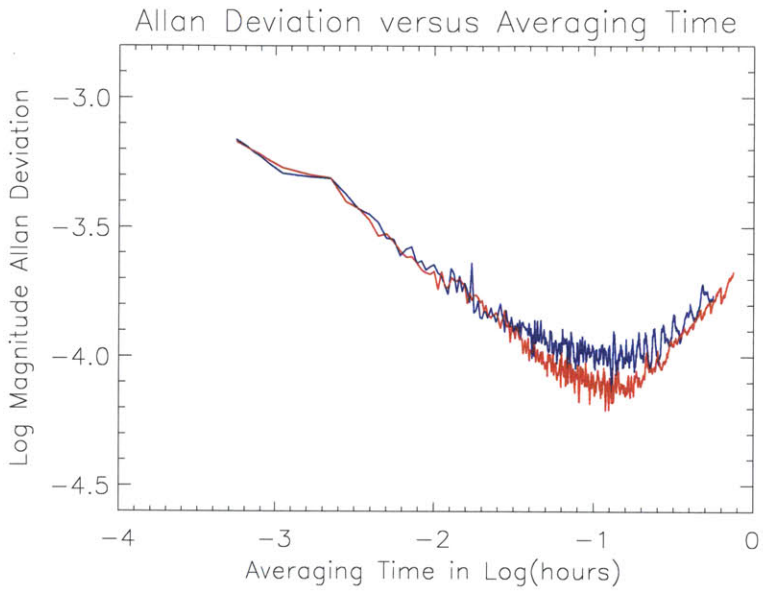

Figure 3-2: Allan deviation versus averaging time for the red channel and the blue channel of differential photometry data from the dual power supply temperature test. At first, as the photometry was binned, the Allan deviation improved. However, when binning size increased to beyond $10^{-0.9}$ hours (**about 7.5 minutes**), the Allan deviation turns off sharply, indicating that external factors had begun to affect the photometry, and the maximum achievable precision is roughly 0.0001 magnitude. These results represent data taken using both amplifiers and are from one of the twelve tests described herein.

Astrometry

Photometry was performed for each star using **daophot**, non-interactively. Starting coordinates were determined for each chip and set of sessions, that is to say blue October tests, blue December tests, red October tests and red December tests. IRAF was allowed to refit the centroid for each individual image using the automatic functions in **daophot**.

The X,Y deviation from the average position was calculated for each star and the stars were compared as a group. Additionally, the individual x and y position change in time was calculated for a single star, star 3 (chosen arbitrarily).

3.2.3 HIPO temperature test results

Each data set was analyzed for changes in each the above variables caused by changes in the chip, controller and power supply temperatures. Group standard deviations and group signal-to-noise proved to be insensitive to any of the three temperature fluctuations, so no significant conclusions could be drawn.

Star position, instrumental magnitude and differential magnitudes were all found to be correlated with detector temperature and controller temperature. Overall, cross-amplifier differential magnitude comparisons were more greatly affected by controller temperature changes. See Table 3.2 for a list of basic quantitative instrument limits.

In the case of the power supply temperature tests, removing the cover of the power supply had little affect on the photometry, though the recorded temperature inside the power supply dropped by 2°C. However, when the fan was turned on different photometry and star position responded slightly, as did controller temperature. It is likely that the fan, which was aimed under the HIPO instrument circulated air to the controllers and cooled their temperatures. This test was later repeated in January 2011 and a "computer fan" was used to cool the power supply. No controller temperatures are quoted with these results (Sooknah, 2011). A smaller fan may not direct as much air elsewhere.

The following is a list of more-specific test results:

1. Once the detector temperature had reached its set point, it remained within a 0.6° range throughout all tests.

2. When the detector transitioned from cooling or warming to maintaining a set temperature, the controller temperature briefly spiked downwards or upwards. There is a corresponding bump in background temperatures and instrumental magnitudes.

3. Detector temperature correlates with both X and Y position, but Y motion is drastically dependent on detector temperature. A 0.5 pixel change in Y position correlated with a 15°C change.

Table 3.2: Summary of the most crucial quantitative HIPO test results:

Situation	Result
Red cool down times -105°C to -120°C	1 hour 6 minutes
Blue cool down times -105°C to -120°C	1 hour 14 minutes.
Typical maximum averaging time (single amplifier)	>10 minutes (300 Images @ 2s)
Typical maximum averaging time (double amplifier)	> 7.5 minutes (225 images @2s)
Absolute best averaging time	> 55 minutes (c01, red side)
Typical best binned differential photometry lab precision	< 0.0001 mag
Absolute best binned differential photometry lab precision	< 0.00003 mag (c01, red side)
Deviation of overscan corrected background	1 ADU
Absolute "stellar" centroid motion	< 1 pixel in unstable situations, location dependent
Absolute change in magnitude for 20 degree temperature change	0.04 mag
Typical unbinned lab differential photometry standard deviation	0.001 mag
Differential magnitude drift	0.002 mag

4. Controller temperature was found to be highly correlated with overscan-corrected background counts on the red chip as well as X position of the stars on the blue chip.

5. Interrupting imaging to take a 50-frame bias cube caused a drop in background levels by 1 ADU, from which the recovery took 3 cubes (90 images). This effect was still apparent after overscan correction. If biases are deemed unnecessary for testing purposes, it is probably best that imaging be performed without them.

6. In test c01, when a new imaging sequence was started, the background counts on the blue chip left amplifier dropped by 10 ADU.

7. As photometry was performed by subtracting a median sky annulus, the drop in background seen immediately after the biases were taken does not affect the photometry. This lack of photometric change in the face of background change

suggests that differences in detector or controller temperature change either the gain or the sensitivity of the chip to light and not artifacts of a poor photometry algorithm.

8. Millimag-level systematic effects were seen for both changes in detector temperature and changes in controller temperature. These effects were larger for detector temperature changes.

9. Photometric precision on the order of a few millimag is consistent from test to test. With the exception of the red a28 1 of 2 data in which a different DSP code was used, all tests had a signal-to-noise ratios between 1300 and 1400. The signal-to-noise for HIPO blue and HIPO red matched within error bars.

10. **The average Allan turn-off was measured to be greater than 10 minutes for single amplifier data and greater than 7 minutes for comparisons of the left and right amplifiers.** At 2 seconds per image, up to 300 images could be included in this average (there is a break of 4 seconds between 2 second cubes of 60).

11. The differential magnitudes calculated between the left and right amplifiers always had the best Allan deviation to start (more photons, lower standard deviation), but turned off from the power law after fewest points had been averaged because the different amplifiers responded differently to stimuli.

12. Typically, adding an overscan correction did not improve the Allan deviation. However, overscan correction of the red right amplifier during c01 (the cold water *red* controller test) improved the Allan deviation such that averaging times of *over an hour* were possible before turn-off. This was the longest test after the detector temperature test, and contained a long period of little stimuli.

13. Astrometric effects caused by stimuli manifested themselves in a simliar way for all stars. For instance, if the detector temperature decreased, all stars would move upward in Y on the chip. If controller temperature decreased, all stars

would move in the positive X direction for the blue chip. The relative amount that each star moved differed from star to star (usually top center stars moved to the least), but on the whole, each star's centroid followed a similar-shaped, albeit stretched or shrunken, path.

14. Filling the red liquid nitrogen dewar during imaging caused the stellar centroids on the red side move approximately three-quarters of a pixel in both directions. Such a large change was not seen while the blue dewar was being filled.

15. Filling the liquid nitrogen dewars did cause a millimag level hiccough in instrumental magnitudes and differential magnitudes between the two amplifiers. This hiccough lasted for the duration of the filling.

16. For the power supply test, there was no noticeable change in the photometry, astrometry or background when a single cover was removed. The power supply temperature decreased by 1-3°C. When the fan was turned on, both controller temperatures dropped and effects were observed. Turning on the fan did not affect the power supply alone.

3.3 Recommendations for users

The following recommendations were made for users, based on test results:

1. In the detector temperature test, and in the two cool down tests, the red chip was found to cool more quickly than the blue chip. During the temperature tests, the blue camera took 9 minutes more than the red camera to cool from -105°C to -120°C. For the a27 cool down test, it took 6 minutes more for the blue camera to cool from -100°C to -120°C, and 6 minutes more the second time around for a28 2 of 2. **Observers who are waiting for the cameras to cool before imaging should know that the red will finish first.**

2. When cooling, the camera will overshoot the set point by a few degrees (about 3°). After the camera warms from this overshoot to 0.5°C below the set point,

the image background will have stabilized. **Observers should consider the data after that time as stable.**

3. The first image of every cube differed from every other image in the cube in instrumental magnitude by 5 millimag and was thrown out before analysis. **HIPO observers should plan on not using the first image in a cube.** For the left amplifiers only, the average *background counts* of the last overscan-corrected image in a cube were lower by a fraction of an ADU, an effect that did not alter the instrumental magnitudes.

4. The overscan correction brought the mean background level to a constant value that remained within an ADU on all tests, though the resulting background was still affected by detector and controller temperature. **Thus, the overscan values can be used as a diagnostic tool to identify data that may have been affected by temperature variations in the controller or detector OR times at which the amplifier was producing bad images.**

5. When a series of cubes is started, the detector temperature, while near the set point, stabilizes to a constant temperature within a half-hour of the program restarting. **It is recommended that for a program involving continuous, precise imaging, imaging commence 30 minutes before usable data are desired.**

6. Instrumental magnitudes on each amplifier did not increase or decrease by equal amounts when the controller temperature was altered. **For exoplanet transit observations requiring high precision, a single amplifier should be used to avoid millimag-level effects related to differing reactions to stimuli from each amplifier, even at the expense of cadence.** As millimag precision is not required for occultation work, and long averaging times will not be necessary, **it should be fine to use both amplifiers for occultation work.**

7. During the a29 blue controller test, an insulating box was put on the blue

controller for 10 minutes. The controller was in still the process of recovering from a previous liquid nitrogen attack, so the temperature increase seen was likely unrelated. This test should be repeated. As it took 45 minutes for the controller to reach its original temperature, **one should wait at least one hour for the instrument to recover from the liquid nitrogen blasts.**

8. When ice water was used to cool the controller over a period of hours, heat loss spread to the entire instrument and the opposite controller's temperature began to cool as well, albeit at a delayed time. **Thus, blasting the instrument with liquid nitrogen is best for testing purposes, as the cooling effect is localized.**

9. The blue chip, especially the left amplifier, was the most robust than the red chip against changes in detector temperature (0.01 magnitude for blue versus 0.02 magnitude for red). However, the left blue amplifier exhibited large fluctuations in background counts or the bottom third of the amplifier, possibly due to a failing Leach board, which was replaced before the June 2011 commissioning (Collins, 2011). **If for some reason only one camera can be used, the red is the best choice.**

10. The differential magnitude standard deviations became smaller if more stars (and thus more counts) were included in the calculation. The precision reached by these tests is likely limited by the number of stars involved in the calculation of the differential magnitudes. **A star plate with more holes should be able to give even more precise laboratory measurements.**

11. For the red chip, the right amplifier had later Allan turnoffs and smaller Allan deviations than the left amplifier. **If one amplifier should be used on the red chip, the right should be chosen.**

12. **For the blue chip, the left amplifier performed better for detector temperature change tests, but on the other tests, one amplifier wasn't definitively better. Both blue amplifiers experienced failure states.**

Future work

- A laboratory test should be conducted to ensure that the sealed HIPO is truly light tight against room lights.
- Though it contained a 7 hour period with a constant CCD temperature and no interruptions to the controller or power supply, the a23 test was not a true stability test. As Allan turn-offs were not measurable, a true stability test, on the order of 15 hours or more should occur.
- For the red chip a28 1 of 2, the wrong DSP code was selected. Instead of a drop in background counts, a rise in background counts occurred. A clear guide to DSP code and object noise should be made.
- For symmetry purposes, a controller test in which the controller is warmed should be devised and carried out. This test should not occur at the same time the controller is undergoing or recovering from a cooling test. It is unlikely the test would say anything unique that the cooling test and the detector temperature test did not.
- The power supply tests should be redone in such a way that attempts to cool the power supply do not also cool both controllers.
- Another test should occur where the dewar is filled during testing to test the robustness of the blue camera (the blue stars were saturated because no filter was used). As astrometry is not a priority, preliminary results suggest refilling the dewar while imaging is preferable to risking warm up.

3.4 HIPO takes off

On June of 2011, HIPO took its first commissioning flights on SOFIA. Along with the FDC, the HIPO instrument successfully observed an occultation by Pluto on June 23, 2011. These data will be seen in Chapters 6 and 7. While other tests were performed using HIPO, the data represent actual conditions one might expect, and

provide excellent comparison between the lab and field. We are now able to see what changes in controller temperature are caused by the environment as well as examine how steady SOFIA really is.

Like every alt-az telescope, SOFIA must track in altitude, azimuth and rotate with the field. Unlike Magellan, for which instruments must be able to flip the full 360°, SOFIA can only support a 3° rotation before the pointing must jump. Ergo, it is impossible to view a field for an extended period of time, though a half-hour occultation cube can fit solely into a single pointing.

The PC20110623 event was observed as one half-hour cube of 1800 images in blue (1 frames per second) and 3600 images in red (2 frames per second). As a result, the controller and detector temperatures could not be monitored during the observation. For each image, however, coordinates of the 11 comparison stars that comprised the light curve could be extracted. As the chip was binned 3x3 for occultation observations, we correct the coordinates to fill out the full chip. See Figure 3-3 for the motion of the stars during the occultation cube. Overall, for one half hour, the stars move about 10 pixels on the sky.

If one reconsiders Figure 3-3, we see that there is some distortion between the relative locations of the same red and blue stars, especially along the Y axis. The camera fields of view are not identical: The red camera field of view is 5.58′ while the blue is 5.66′, which provides one explanation.

These computations do not reflect the optimal tracking conditions with SOFIA. Ted Dunham writes:

> [...] The in-air pointing was done with FFI (Fine Field Imager) tracking. The FDC can track, but not when taking data as it was during the occultation. The FFI is a small (~10") telescope mounted on the side of the SOFIA telescope and there are known differential pointing shifts between it and the focal plane. [...] One spot in the field can be held reasonably well fixed. We also intend to implement a HIPO self-guiding capability to improve this (Dunham, 2011).

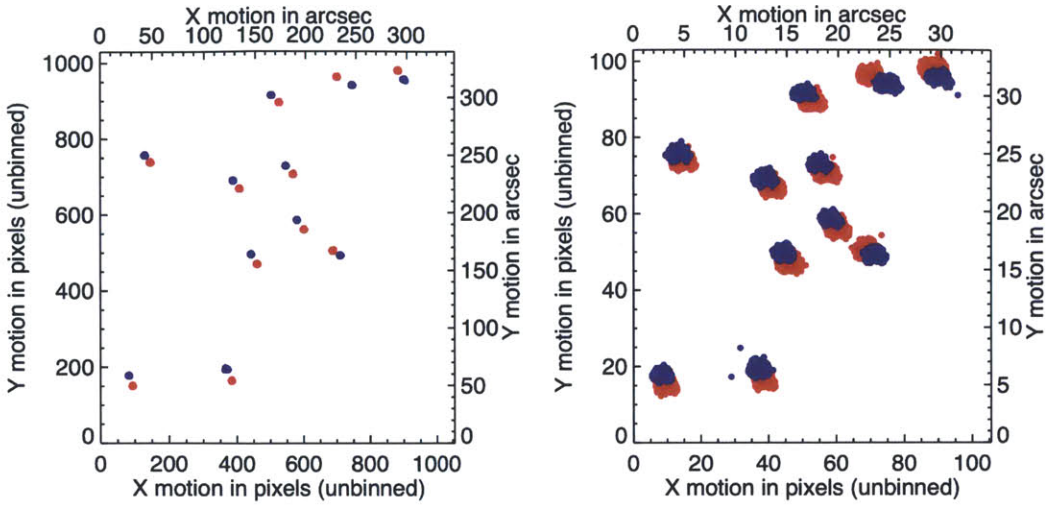

Figure 3-3: Left: Unbinned positions of comparison stars from 30 minute stellar occultation cube taken on 2011 June 23. Right: Zoomed-in plot of star positions to show shape of motion. Stars have been shifted to fit on one graph, but arranged to match their original locations. In lab, temperature changes cause motion of less than 1 pixel!

Thus we are not yet looking at the best of HIPO pointing. Meanwhile, we see that the changes we do observe dwarf the one pixel centroid motion caused by filling the dewar, the most drastic effect observed in the lab. Hopefully, HIPO will be used to observe many more occultations.

Chapter 4

The Charon-Pluto Light Ratio

4.1 Introduction

In 1978, James Christy was examining photographic plates taken of Pluto from the 1.55-m refractor at the US Naval Observatory, when he noticed a bulge coming from Pluto, visible on specific nights, sometimes to the north, other times to the south. He found that the bulge moved around Pluto with a period identical to Pluto's rotation (Christy & Harrington, 1978). The bulge was due to, of course, Pluto's largest moon, Charon: half Pluto's diameter, tidally locked and so close to Pluto that the system barycenter lies outside of Pluto itself (Dobrovolskis et al., 1997). However, not everyone immediately believed that Charon was real: after originally being skeptical of Charon's existence, Derral Mulholland (1978) published an article conceding that Charon could exist. Even then, Charon was not officially accepted by the IAU as Pluto's moon until definitive proof of its existence was provided in 1985 (Marsden, 1986), with the first mutual event observations (Binzel et al., 1985), despite an occultation detecting Charon in 1980 (Walker, 1980).

At perihelion, Pluto was undergoing mutual events, but at Charon's greatest northern elongation and greatest southern elongation, Pluto and Charon were 0.94″ apart on the sky at 29.7 AU from the sun[1]. Charon's orbit is considered, within er-

[1]This calculation, and all others in this thesis, were made by the author using the JPL ephemeris, PLU 022 and DE405.

rors, to be perfectly circular (Buie et al., 2012), however, its ellipsoidal appearance is due to its tilt as seen from Earth. In 2011, over two decades since perihelion and the end of mutual events, Pluto and Charon, then 32.0 AU from the sun, were 0.88″ apart in the sky at maximum separation. Charon's orbit plane has opened up considerably as seen from Earth. At minimum separation, Charon and Pluto are now 0.64″ apart.

While a slight bulge may be visible in a CCD image, Charon is only separate from Pluto in the best seeing conditions, available at a few sites on Earth, such as Mauna Kea or Las Campanas Observatory, both of which routinely see sub-arcsecond seeing. While the astrometric images used for Pluto occultation predictions are taken from good sites, Charon may not necessarily be resolved. Charon's contribution to Pluto's light offsets the position of Pluto's location, so a static light ratio that attributes a certain percentage of light to Charon and Pluto is uniformly applied to each image. However, it is important that this ratio be accurate: with a 19571.4 ± 4.0 km semi-major axis for Charon (Buie et al., 2006), a difference in light ratio of 1% corresponds to approximately 196 km of occultation shadow track on Earth's surface.

The Charon-Pluto light ratio is not uniform in color, and in time. For one, Pluto has the second highest albedo variations in the Solar System, after Iapetus (Tholen & Buie, 1997). Its light curve amplitude is on the order of 0.3 magnitude. Charon's light curve is flatter. Additionally, Pluto and Charon are not the same color: Binzel (1988) found that Charon was darker and bluer than Pluto. Spectra show that their compositions are completely different.

Sawyer et al. (1987) obtained separate visible spectra of Pluto and Charon during a superior mutual event in which Pluto occulted and completely blocked Charon. As the only body visible, a pure spectrum of Pluto could be subtracted from the mixed spectra of the two bodies, leaving Charon's contribution only. The authors found Charon's visible spectrum is relatively featureless, while Pluto has a large methane band at 890 nm and smaller methane bands at 730, 790, 840, and 860 nm. Pluto's spectrum brightens with increasing wavelength, while Charon's spectrum remains relatively flat, and is neutrally colored. Today, separate spectra can be obtained with adaptive optics, or in good seeing, such as the measurements by Verbiscer et al.

(2007). However, instead of visible light, most new spectra cover the more interesting infrared range, where Charon shows water absorption bands and ammonium, while Pluto shows signs of carbon monoxide and nitrogen as well as methane.

There are two major methods for performing photometry on stellar objects: aperture photometry and PSF photometry. Aperture photometry was used to test the HIPO data in Chapter 3. The brightness of the pixels inside an area on the image, often circular and known as the "aperture", is summed, and the average background sky level is removed to derive the net flux, which can be directly compared against other stars or converted into instrumental magnitude. Aperture photometry makes no distinction between the object of interest and any other object that may fall within the aperture, especially the light of nearby stars. PSF photometry fits a model stellar profile to the intensity and location for a group of stars, iterating until an agreeable match is found for the entire group via non-linear least squares. The final models are subtracted from the image. PSF photometry is ideal for crowded fields and overlapping stars, but many astronomers avoid it due to its labor-intensive nature.

From the ground, the disk of Pluto is not resolvable. At Pluto's current distance (about 32 AU from the sun), its angular diameter just $0.11''$ wide, too small to be resolved in even the best Magellan seeing, which could be something like $0.2''$. The best LDSS-3 images acquired for this project had $0.46''$ seeing. Thus Pluto's stellar appearance permits PSF photometry.

For this project, data were acquired from March 2011 to May 2012 using LDSS-3 on the Clay telescope. Through these data, we seek to answer the following questions to aid in occultation predictions: Has the Charon-Pluto light ratio changed from previous observations? How does the light ratio change with filter? How does ground-based PSF photometry compare with data from the Hubble Space Telescope? Does the light ratio change significantly with Pluto's rotation? Ultimately, the goal of the light ratio is to feed into occultation predictions, from which scientific analysis on Pluto follows. While astrometric data taken for occultations are obtained at high-quality observing sites, separate PSFs for Pluto and Charon are not fit. Instead, a static light ratio is used, and Charon is assumed to reside at a particular location.

4.2 Previous observations of separate photometry

This is not the first attempt to use PSF photometry to resolve the ratio between Charon and Pluto brightness. Several attempts were made in early 1990s. Bosh et al. (1992) used the IRTF to calculate light ratios for the J, H and K bands. Young et al. (1994) used PSF models to calculate the relative mass using B filter data only (though more images were taken). Jones et al. (1988) calculate the light ratio for a single image in the B and I filters.

Perfect separation of Pluto and Charon can be easily achieved using the Hubble Space Telescope. However, HST time is rare, expensive and difficult to get[2].

The HST was used by Marc Buie in 1992-1993 and 2002-2003 to collect fully resolved B and V filter separate light curves using HST's 'F435/F439' and 'F555' bandpasses (Buie et al., 1997, 2010a). The resulting, previously published, light curves have been converted to Charon-Pluto differences and are plotted in Figure 4-1. The observations track each other fairly well in the intervening decade. These observations do not cover the redder range of the spectrum, which comprises most astrometry imaging, as well as open occultation observations, which have effective wavelengths closer to R than B and V, which have been traditionally used to observe Pluto.

Using the 1992-1993 observations, Buie et al. (1997) attempted to calculate the *opposition effect*, a linear increase in an object's brightness with decreasing solar phase angle. Buie found linear phase coefficients of 0.0294±0.0011 mag/deg for Pluto and 0.0866±0.0078 mag/deg for Charon. Thus, as the solar phase of the Pluto-Charon system decreases, Charon should appear brighter relative to Pluto without any surface changes occurring in the system. At that time, no phase angle smaller than 0.5° was seen. Buie ponders the lack of *opposition surge*, the extreme, non-linear brightening at ultra-small phase angles, and notes the existence of such a surge could not be

[2]Mark Showalter related his experiences applying for time to use HST to look at Pluto at a New Horizons Team meeting that the author attended in January 2012. A few years after the discovery of Nix and Hydra (using HST), Mark Showalter proposed a novel method to search for debris in the Pluto system. The time allocation committee rejected the proposal and informed Showalter that it was in the bottom quartile of all proposals received. After intervention on Showalter's behalf, the time was granted, and Showalter went on to discover P4, and in the following year P5.

ruled out until Pluto crosses the ecliptic in 2018. In 2002, HST sampled Pluto at solar phase as as small as 0.316°. This time, Buie et al. (2010a) found a strong, color-dependent opposition surge for Charon. Buie estimates a 0.2 magnitude change in brightness for 0.5° to 0° in V, but a 0.25 change in B magnitude over the same angle range, fitting a Hapke-based model (Hapke, 1993) for each event. Such a surge was not seen for Pluto, and Buie finds phase coefficients of 0.0355 mag/deg (V) and 0.0392 mag/deg (B) are better fits for the new Pluto data. However, he cautions that these observations represent the beginning of a non-linear trend, one for which he does not have enough ultra-low solar phase angle data to quantify.

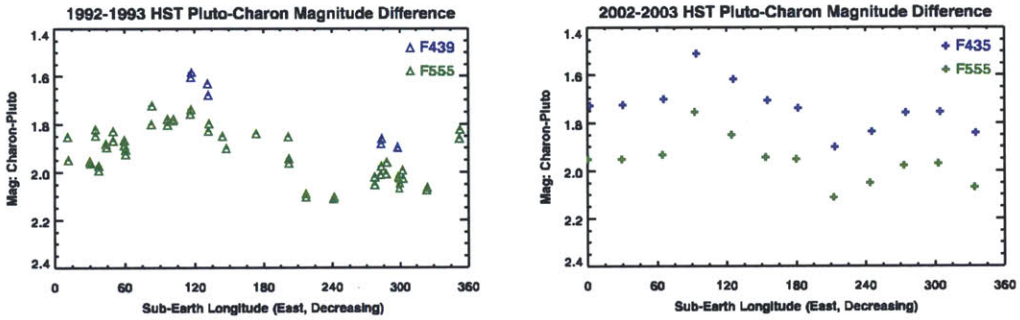

Figure 4-1: Left: Charon-Pluto magnitude difference vs sub-Earth longitude using previously published 1992-1993 data from Buie et al. (1997) in B and V equivalent filters. Right: Visit-averaged Charon-Pluto magnitude difference vs sub-Earth longitude using previously published 2002-2003 data from Buie et al. (2010a) in B and V equivalent filters. Both curves are plotted using decreasing longitude. Increasing Charon brightness relative to Pluto is up. The 2002-2003 HST data are directly compared against LDSS-3 data in Figure 4-9. Curves are not corrected for solar phase angle.

4.3 Status of past MagIC light ratio observations

During the prediction process for P131.1, an occultation that occurred in August 2002, it was found that there were periodic residuals between the ephemerides and Pluto's position (Clancy et al., 2005). A regular observing campaign was undertaken to observe the Charon-Pluto light ratio. Prior to the observations in 2011 made by the author, Pluto was observed roughly annually at Magellan between 2001 and 2006 using MagIC (Osip et al., 2004) on the Magellan telescopes at Las Campanas

Observatory. MagIC originally consisted of a 2k by 2k SITe CCD chip, centered in the focal plane. In September 2007, after these observations were completed, MagIC was upgraded to include an frame transfer e2V chip with a smaller field of view, but fast readout. The original chip was not removed, but instead, the dual chips were co-mounted, each offset from the center of the focal plane (Osip et al., 2008). MagIC was eventually removed from its permanent home on a folded port, to the Nasmyth port on the Clay telescope. A few observations were taken of Pluto using the SITe chip with the upgraded MagIC in 2010, as part of engineering in prep for the PC20100704 occultation observations. However, these images were never examined. In January 2011, MagIC was removed from the Clay, and has not be used since.

Over the years, several attempts have been made to analyze the backlog of MagIC data. The first sets were analyzed by Kelly Clancy, and were presented at a 2003 IAU meeting (Clancy et al., 2005). While the presentation and its results are preserved on the the MIT Planetary Astronomy Labs' servers, it is not immediately apparent which files comprise the presented results and which do not. Later PSF fitting work was also done by Susan Benecchi, Emily Kramer, Jim Elliot and Michael Person. In total, there are at least nine different versions of the data. Each version includes some dates, though not others, and not necessarily the same frames on each night. All of the initial fitting was performed with uncalibrated data. Later, a sub-set of the earliest images were calibrated, and work began on them anew. The data sets differ as to whether Charon's position was left fixed or an available parameter to be fit. Each fitting attempt does not necessarily exhaust all images taken on a particular night. Work was abandoned when observations of a Charon occultation in 2005 (C313.2) and a Pluto occultation in 2006 (P384.2) took precedence. Jim Elliot suggested that the group use 0.15 as a constant Charon-Pluto ratio (a magnitude difference of 2.06), and no further work had been done (Person, 2013).

4.4 LDSS-3 vs MagIC

Initially, Jim Elliot and I hoped to continue the light ratio project using the MagIC instrument, and we applied for Spring 2011 observing time in Fall 2010. However, in January 2011, MagIC was scheduled to be removed from the Magellan telescope to make way for LDSS-3, an imaging spectrograph that took over MagIC's former port. We obtained time to use LDSS-3, though the instrument has several characteristics that make observing, data quality and reduction paradigm very different from the MagIC observations.

For one, the MagIC SITe camera boasts a pixel-scale of 0.069″/pix with total FOV of 2.36 arcminutes (Kern et al., 2008). LDSS-3 has a pixel scale of 0.1889″/pix (Muchaey & Gladders, 2011). In excellent seeing, the PSF will become very close to being under-sampled on LDSS-3. Because the same amount of light would be spread over nine pixels, MagIC can expose for longer before saturation, increasing signal-to-noise of each item. While exposing at LDSS-3's minimum of 1 second, the maximum peak signal above background was just under 30,000 ADU (r′, FWHM=2.85. The LDSS-3 manual states that LDSS-3 is linear within 1% to 40,000, but linearity has not been tested. Accidental overexposure in good seeing is a reasonable risk.

The LDSS-3 shutter speed is such that its manual suggests a minimum exposure time of 10 seconds for flat field images. LDSS-3 has re-imagining optics, there is a strong increase in FWHM with distance from the center of the focal plane.

MagIC's four amplifiers read out in 23s for an unbinned image (Kern et al., 2008). In fast mode (used for all observations), LDSS-3 will read out in 43s, with a shorter time if a region of interest is used. For a program that relies on many short images, LDSS-3's duty cycle is appallingly inefficient.

MagIC is also superior to LDSS-3 due to its dual filter wheel: it contains both the Sloan u′, g′, r′, i′ and z′ as well as the Harris BVRI filter set (in addition to a VR filter that was not used). LDSS-3 has only a Harris B and Sloan g′, r′, i′, z′ (in addition to a VR filter that was not used). The transmission curves for LDSS-3 are displayed in Figure 4-2.

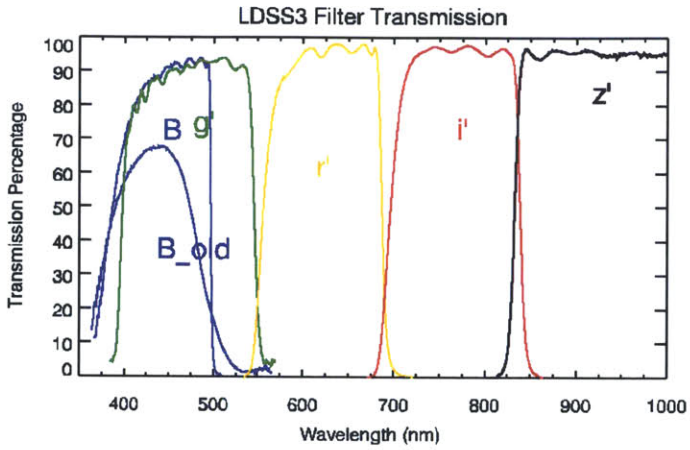

Figure 4-2: Transmission curves of filters used for 2011-2012 observations with LDSS-3. Data compiled from Las Campanas Observatory (2007). The "B_old" filter was inserted in place of the normal B filter for nights 3 and 4. Because the B light ratio measurements from nights 4 and 6 overlap within their respective error bars (see Figure 4-7), these two filters will be treated as essentially interchangeable. However, I will point out which nights contain B_old as necessary.

LDSS-3 did boast one significant advantage over MagIC: its 5″ field of view, over MagIC's 2.36″ field. The larger field provided two principal advantages. Firstly, there was a wider range of model stars available to select from to form a PSF. Secondly, the entire run's fields were contained in a single frame, allowing for simultaneous observing of Pluto in addition to making a definitive identification of the stars whose light was found to be enmeshed with Pluto and Charon on another morning's observations.

Examining Pluto fields for stars on off-nights was a crucial part of getting accurate PSF fits. One reason for the increase in frequency of stellar occultation observations (e.g. fourteen years between the P8 and P126/P131.1, P384.2 four years later, then at least one occultation observed every year since), is the rise in stellar density. For the past several years Pluto has been passing through the galactic plane. For the period ranging from 2008 to 2015, the two years with the highest peak stellar density are 2011 and 2012 (Assafin et al., 2010). Thus, every night's field needed to be carefully examined for stellar contamination, making LDSS-3's large field very helpful.

4.5 New observations with LDSS-3

Observing time on the Magellan telescope was granted through the MIT TAC for a total of eleven separate nights in four sessions between March 2011 and May 2012. The nights were assigned based on telescope availability, without regard to Pluto sub-Earth longitude, solar phase or proximity to other nearby stars. All eleven nights were completely clear, though one night (20120529) had such bad seeing (average of 3 arcsec) that a reduction was not attempted[3]. That night is omitted from the results, leaving a total of 10 nights. Table 4.1 lists the date, time, seeing, and number of images successfully fit per filter for each morning's observation. Each night was assigned a night number. These numbers are consecutive, except for night 5, which falls temporally between nights 8 and 9, and was accidentally skipped. The degree of stellar interference with Pluto is noted in the column "crowding" and can be examined visually in Figure 4-4.

For each night, there was approximately one hour of observing time near the end of the night, plus additional time during twilight. For each filter, a minimum of five images were taken of Pluto and Charon per night. Observations of Landolt standard stars were taken before and after the science images in weather that appeared photometric. For the first year's observations, the Landolt fields were defocused so that the Landolt stars would not saturate the telescope field of view. In 2012, the same field stars were observed, but instead, the fields were not defocused so that "Stetson" standards could be used[4]. If any observing time remained before the morning sun brightened the sky, the use of the telescope was divided between obtaining additional images of Pluto or obtaining images of potential Pluto occultation fields. These fields included fields for PC20110522, PC20110623, PH20110627, PC20120909, PC20121002, and Haumea 20111207, events that the author later attempted (see Section 1.2).

[3]Immediately after, the telescope was closed due to high winds, which persisted well into the following evening, but miraculously died down in time for the 20120530 observations.

[4]Lists of Landolt and Stetson standards can be found at `http://www.cfht.hawaii.edu/ObsInfo/Standards/Landolt/` and `http://www3.cadc-ccda.hia-iha.nrc-cnrc.gc.ca/community/STETSON/standards/`. All observations included star L109-381.

With the exception of nights 5, and 9, all observations were made while was Pluto was rising. Only night 9's observations were made at low airmass. A dither pattern was maintained over the course of the first night. However, this pattern was dropped after the first evening, as moving the telescope between images severely hindered the efficiency of both the observing and reduction processes.

Table 4.1: Summary of 2011 and 2012 LDSS-3 Charon-Pluto light ratio observations

Night	UT Date	UT time	Solar phase	Crowding	Seeing (arcsec)	Sub-Earth long.[1]	B	g'	r'	i'	z'
0	20110307	8:39 - 9:05	1.66	yes	0.46 to 1.07	131-130	4	6	5	4	6
1	20110308	8:38 - 9:13	1.67	yes	0.57 to 1.04	75-73	5	7	5	5	7
2	20110309	8:37 - 9:11	1.68	yes	0.69 to 1.26	18-15	3	9	5	5	5
3	20110319	8:30 - 8:57	1.76	no	0.64 to 1.08	175-174	5	5	5	5	3
4	20110320	8:39 - 9:05	1.77	yes	0.55 to 1.25	118-117	5	6	5	5	5
6	20120228	8:41 - 9:03	1.53	yes	0.73 to 1.20	324-322	4	1	7	9	4
7	20120229	8:24 - 9:08	1.54	yes	0.68 to 1.20	111-110	7	5	7	7	8
8	20120301	8:33 - 9:24	1.56	yes	0.74 to 1.22	55-53	7	4	8	7	7
5	20120530	9:22 - 9:52	0.89	no	0.73 to 1.26	359-356	8	7	8	8	8
9	20120531	6:53 - 7:22	0.90	no	0.52 to 0.99	273-272	8	9	7	8	8

1. Sub-Earth longitude on Pluto is defined as having a zero at the sub-Charon point and decreasing in time.

4.6 Data reduction, PSF fitting, data quality

4.6.1 Image calibration

The process for reducing LDSS-3 data is different enough from the usual standard image calibration steps that I will take the time to describe it in some detail. LDSS-3 comprises a single chip with a dual amplifier that reads into two separate FITS[5] files. Each file contains an overscan region located in what would be the center of the field. Thus, the overscan region must be removed to join the two images, one of which must be reoriented to reconstruct the full field of view. This process was carried out using an IDL script provided by Susan Benecchi. The script merged and overscan corrected the images, simply subtracting the average overscan value from the entire image. While the full field of LDSS-3 is 8′, the field is vignetted into a circular pattern. To avoid erroneous detection of stars within the vignetted area and unnecessary computational intensity, during the stitching process, the images were also trimmed down to an inscribed rectangle, leaving approximately 5′ field of view. In 2012, a subframe of this same area was created to save readout time. The images were also flat-corrected using twilight flats, if not obtained on the same night observations were made, obtained during that two or three night run.

4.6.2 PSF fitting

Each image was PSF fit using IRAF's **daophot** package (Stetson et al., 1990). For each pointing and filter combination, the image with the best seeing (which was calculated by measuring the FWHM of Pluto using IRAF's **imexam** tool) was fit interactively using an intensive 28-step process that combined custom IDL scripts and IRAF's routines, enumerated in detail in Appendix A.

The very first step in PSF fitting is to identify field sources with **daofind** and perform aperture photometry with **phot** to get an input position and brightness for each star. Of crucial importance to the starting list is the value for sky background.

[5]FITS, or Flexible Image Transport System, is the standard file type for astronomical images.

Extreme care must be taken such that the residual light does not enter the sky annulus, so that the brightest stars are properly subtracted. Once the star list is complete, PSF fitting can begin.

Analogous to aperture size and sky radius, the **daophot** PSF fitting algorithm takes two numbers that define the boundaries of the fitting routine. The first number, `psfrad`, is the radius of the stellar PSF that will be created. One wants the radius to comprise the point at which the star light disappears into the background (the size of a stellar PSF is infinite), but be small enough so that the stellar PSF fits do not become unnecessarily computationally intensive. The second number, `fitrad`, determines the radius that will be relevant to determining the brightness of each profile. Generally, it is advisable to set the `fitrad` to be comparable to the FWHM. However, in this case, the `fitrad` was set to 3.4 pixels (0.64″) to avoid contribution from Charon , the minimum separation of the two. The `psfrad` was set to 21 to accommodate the rough maximum radius of a bright star on an image with a FWHM between 6 and 7 (1.1 to 1.3″), which represented the worst seeing conditions seen in this study. The consequences of an oversized `psfrad` are slower processing times, and a wider identification radius for neighboring stars. See Figure 4-3 for all illustration of `fitrad` and `psfrad`.

When PSF fitting, a model star is fit to the location and intensity of each object in the frame. Multiple groups of stars are fit simultaneously. The model star is typically derived from stars in the field. With LDSS-3, the FWHM of the field stars increased with distance from the center of the image, so a second-order "variable" PSF was used. Second-order PSFs require a large number of stars. Mathematically, the minimum is 6, but Davis (1994) recommends 18 stars to reach a high enough SNR and sample the different parts of the image. Several custom programs were written in IDL to systematically wade through the hundreds of potential stars and the neighboring stars associated with them.

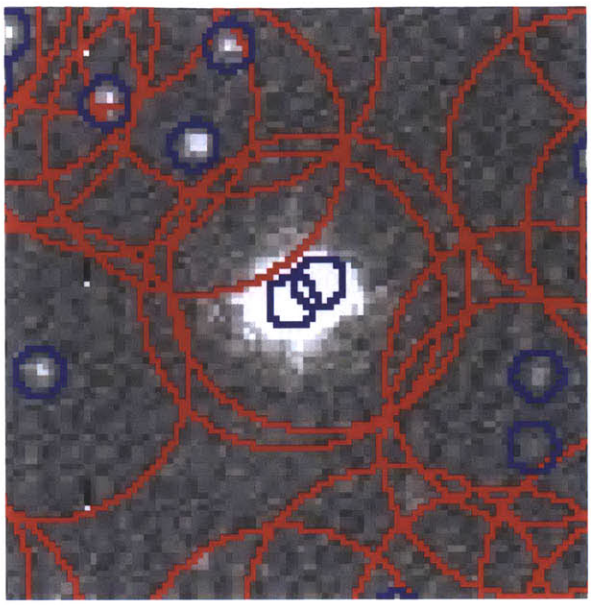

Figure 4-3: `Daophot` fitting radii. Pluto and Charon (center) with a `fitrad` of 3.4 pixels marked in blue and a `psfrad` of 21 pixels marked in red. IRAF determines the brightness of a star using the pixels inside `fitrad`, though the stellar PSF model extends to all pixels inside `psfrad`. A typical choice for `fitrad` is FWHM+0.1 pixels, though here a `fitrad` of 3.4 was chosen based on a minimum separation between Pluto and Charon of 0.64″with an LDSS-3 plate scale of 0.1899″/pixel. The `psfrad` is meant to extend to the limit at which a star's light blends in with the noise.

Star selection, model star selection and neighbor identification

All LDSS-3 images were fit using the following protocol. The image with the best seeing for each filter/pointing was selected as a model image.

Stars in the field were identified by **daophot**'s **daofind** algorithm. The algorithm requires the user to set the approximate FWHM of the image, and based on background noise, set a detection threshold. If the threshold is set too high, many dim stars are missed, while if it is set too low, the algorithm begins to identify noise as stars, while missing out on the dim stars all the same! A large number of stars will slow down the PSF fitting algorithms. False identification of noise as stars, especially if these "stars" are close to a potential model star, can cause the unnecessary rejection of an otherwise suitable model star. Instead, I aimed the star detection threshold to identify all non-dim stars. Dim stars around the Pluto-Charon area were added by hand, as were stars that were not detected, but known to be interfering with Pluto

or Charon based on images of the field from other nights during the run. Unless the seeing was exceptional, Charon was often not automatically detected by **daofind**. Rather, a pointer in its approximate location, often further away from Pluto, was added manually, using the location of Charon from a previous fit of Pluto alone.

Potential PSF models stars were identified using the IRAF routine **pstselect**. **Pstselect** will identify the brightest stars in an image that have no brighter neighboring stars within `psfrad`+`fitrad`+1.0 as candidate PSF stars. Here, the 200 brightest stars meeting this criteria were selected. A program written by the author went through **pstselect**'s list and eliminated stars that had neighbors of ANY brightness within 3.1*`fitrad`[6].

The radial profiles remaining stars (usually about 120), were examined for quality, and eliminated on the basis of large neighbors between the two regions (but not dimmer ones), clear presence of a double star missed by **daofind**, or star with a profile near a bad column or cosmic ray. If an adequate number of stars were found among the brightest stars, the dimmest stars remained. From that 30-50 were left, and the first PSF was made. This first PSF was applied to the stars used to form it, the PSF stars' neighbors and the "friends of neighbors"[7]. Neighboring stars are found to be within 1.5*`psfrad`+2.0*`fitrad`+1.0, where friends of neighbors have centers within 2.0*`fitrad`+1.0 of a neighbor. Every star was examined to see if additional dim neighbors were not identified, or the the star was unsuitable for PSF subtraction, again because it was a double, or contained odd residuals. Poor stars were eliminated, and missing neighbor stars were added to the image star list. After the addition of neighbor stars, the PSF stars were rechecked to see if any of the stars had newly identified neighbors within 3.1*`fitrad`. Stars that did were removed. Using the new PSF from the remaining stars, the neighbor stars were then subtracted from the PSF stars. A third and final PSF was created from the main stars, without neighbors.

[6]The PSF stars have neighboring stars subtracted. However, the `psfrad` for the neighbor subtraction is equal to the distance of the nearest neighbor minus `fitrad`. This number is always smaller than `psfrad` for the full image. Bright neighbors closer than 3.0*`fitrad` to a PSF star will have a minimum radius so tiny that they lose only their cores, defeating the purpose of neighbor subtraction.

[7]A technical term, defined in IRAF manuals for the PSF fitting task.

This PSF was then used to model every star in the image. After all model PSFs were subtracted, the area around Pluto and Charon was examined for any important missing stars.

Once the image's PSF subtraction was deemed adequate, the lists of stars, PSF model stars, and PSF model neighbors were used to non-interactively fit PSFs for any other images with the same pointing and filter. The other images have stars with a wider FWHM, spreading the star light further and reducing the stellar peak. The dimmest stars would be lost as they fade into the background, the images with worse seeing would always have fewer stars than the model image. In the case of night 0, where every image was dithered, all frames were fit individually. Figure 4-4 shows the best images from the z′ filter of each night.

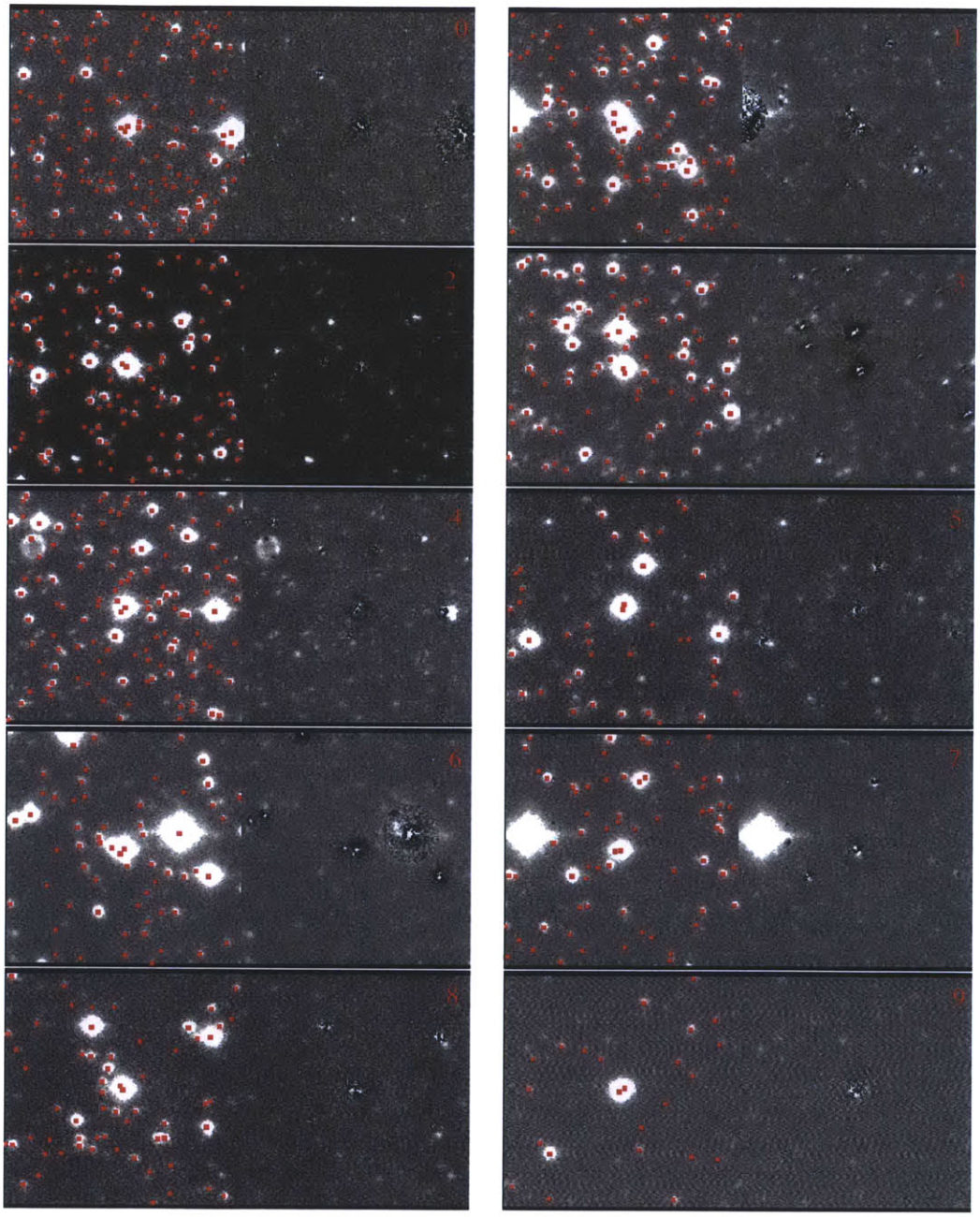

Figure 4-4: Best-seeing z′ image of Pluto as observed by LDSS-3 from each of the 10 nights. The image and every star fit is marked on the left. Residuals are at the right. Pluto is at the center of each image, and Charon's position is denoted by the small dot offset. Only nights 3, 5 and 9 are clear of major stellar interference between Pluto and Charon. Images are oriented such that north is left and east is up.

4.6.3 Data quality

At the end of the fitting process, if a PSF model was successfully subtracted for Pluto, Charon and known interfering stars, the model was considered to be "good". However, the brightness of Charon relative to Pluto was varied greatly between some images. Examination of different images fit in different manners (for example, a different value of `fitrad`), resulted in a small spread of Charon-Pluto light ratios, correlated with the distance from Charon.

The wide spread of ratios on some nights indicate that some fits were better than others, though which ones? To identify good images from outliers, for each night, a median location of Charon relative to Pluto (in pixels) was calculated. Images where Charon was located within 0.25 pixels (or 47 mas) of the median were considered good. Of 300 successfully fit images, 251 were deemed to be "good" by this metric. This elimination processes is illustrated in Figure 4-5. The spread of the points is correlated with the quality of the seeing.

A complete list of images, points and dates can be found in Appendix B. These data have not yet been corrected for solar phase (see next section).

4.6.4 Solar phase

To disentangle rotational phase effects from the changing sun-target-observer angle, we must correct for solar phase. Buie et al. (1997) found the opposition effect to differ for Pluto and Charon by 0.0572 mag/deg. Further work by Buie et al. (2010a) found a color-dependent opposition surge at low opposition angle ($< 0.5°$) for Charon. While the surge was fit for B and V data, similar opposition photometry does not exist for any other filter. Table 4.1 lists the phase angles for each night. While the 2011 observations were contained within a span of two weeks in March, the 2012 observations were made in late February and late May, making the range of phase angles seen 0.88°. Fortunately, the minimum phase angle, 0.89°, is far outside the range at which Charon's opposition surge has been spotted. Correcting any data other than the B data to zero phase angle would paint a false picture of the Charon-

Pluto magnitude difference. Instead, we calculated the phase angle for the years 2011-2012 and remove the months at which Pluto is closest to the sun and seldom observed (November-February). The average phase angle of the remaining months is 1.15°, arbitrary, but more representative of typical Pluto observations. We correct the B and g′ data to the B Pluto coefficients described in Buie et al. (2010a), while the correction for Charon follows the Hapke curve depicted in Figure 9 of the same document. The r′, i′ and z′ follow a similar process, but use the V filter coefficient and Hapke curve. While the V coefficients are probably inappropriate to use for the far infrared, correcting to 1.15° mitigates some of the wavelength dependence. The largest phase solar corrections to 1.15° is 0.017 mag; the B and V corrections differ at most by 0.003 mag. Correcting to 0.0° phase will brighten the Charon-Pluto light ratio by between 0.22 and 0.27 mag, with the *smallest* difference between the corrections between B and V at 0.017. Thus, while using V coefficients for the reddest Sloan filters is not perfect, the harm is mitigated somewhat by not correcting to an extrapolated zero phase.

4.7 Charon-Pluto light ratios

The average light ratio for each night in each filter is plotted as function of sub-Earth longitude in Figure 4-7. Night numbers are marked above, and there is a clear correlation between the seeing listed in Table 4.1, the spread of points in Figure 4-5, and the size of the error bars in Figure 4-7. With the exception of night 3, Charon is brightest in B, followed by in g′. As for r′, i′ and z′, Charon is brightest in z′, again, except for night 3. Using Magellan,Verbiscer et al. (2007) have observed resolved spectra of Charon and Pluto that cover the z′ band. Pluto has a methane absorption band at 890 nm, while Charon does not, accounting for Charon's z′ resurgence, instead of an overall dimming as Pluto gets redder. Aside from the slightly brighter z′, there is not a significant difference between the redder Sloan filters from night to night.

Because observing nights occurred when the telescope was available, and were not planned to fill in gaps in the light curve, nights 0, 4 and 6 sample a 20° degree area

on Pluto's surface. The agreement among the three nights is fantastic in all filters, including night 4, which had the B_old filter instead of B.

Night 3, where Charon is brighter in g′ than B, seems to be an outlier. Pluto may well have a very interesting surface spot. On night 3, which is near 180° longitude, we see the face of Charon that Pluto always sees, and the face of Pluto that Charon never sees. The two are also near their closet separation from each other. Night 3 is one of two nights that use the B_old filter, though Night 4's Charon-Pluto magnitude difference matches well with Night 0 and Night 6, which are nearby in rotation. We do not see a brighter Charon in blue– indeed the color difference between B and V appears constant throughout Pluto's light curve in the 2002 Buie data. Some of the previously-acquired MagIC data sample this area in the light curve. Preliminary examination of these data show that Charon is also brighter in g′, but the error bars and night quality are also suspect. A more thorough examination of the MagIC data, beyond the scope of this project, would be required.

While wavelength of the observation dominates the Charon-Pluto light ratio, we also seek to find changes in the light ratio with rotational phase. Once an average magnitude difference has been calculated for each night, and each nightly average is corrected to 1.15° solar phase. For each filter, two-term Fourier fits were applied to the light curves. A one-term fit was attempted, but the singly periodic fit produced could not match the overall double-peaked light curve seen here, making a second-order fit the simplest possible curve that represents the data. These fits are seen in Figure 4-8, and are plotted against the individual images for each night. With the exception of the g′ filter, the light curves follow the same overall pattern, and have maxima and minima that mimic that of the HST measurements of Figure 4-1. Unfortunately, the LDSS-3 data were not taken at the time of the minimum and maximum points of the Charon-Pluto magnitude difference Hubble data.

The i′ filter's Fourier fit is fairly flat with a 0.10 magnitude change overall. The B filter is the most extreme, with a 0.30 magnitude spread, a value on par with Pluto's peak to peak light curve change at equinox (Tholen & Buie, 1997). These fits could be used to interpolate the Charon-Pluto light ratio from their averages, though the

fit should be tempered with some of the earlier MagIC data.

The Fourier coefficients for each filter can be found in Table 4.2. The coefficients represent an equation of the form

$$m(x) = a_0 + a_1 \cos(x) + a_2 \cos(2x) + b_1 \sin(x) + b_2 \sin(2x), \tag{4.1}$$

where x represents the sub-Earth longitude of Pluto in degrees, and m is the magnitude difference between the two bodies.

Table 4.2: Fourier series fits to LDSS-3 Charon-Pluto magnitude difference.

Filter	a_0	a_1	b_1	a_2	b_2
B	1.85±0.02	-0.06±0.04	-0.06±0.02	0.05±0.02	0.06±0.03
g′	1.87±0.01	-0.01±0.02	-0.01±0.02	-0.03±0.02	0.02±0.02
r′	2.12±0.02	-0.03±0.02	-0.06±0.02	0.04±0.02	0.04±0.02
i′	2.12±0.02	-0.00±0.04	-0.03±0.02	0.01±0.02	0.01±0.03
z′	2.10±0.02	-0.10±0.03	-0.04±0.02	0.02±0.02	0.04±0.02

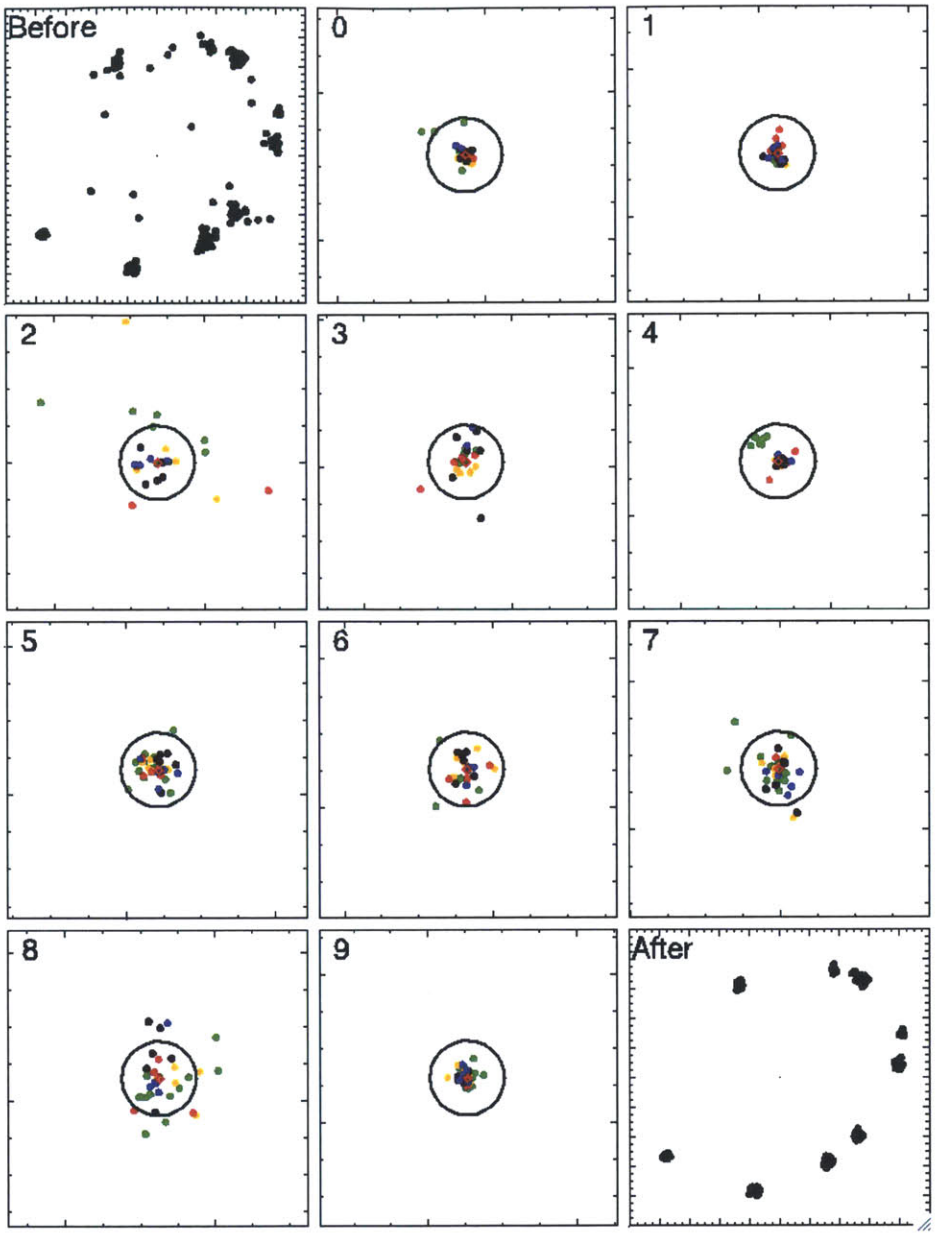

Figure 4-5: Distance-based elimination for light curve points. Colors represent the LDSS-3 filters as seen in previous figures. The first image ("Before") shows the offset of Charon in pixels relative to Pluto for all frames in which the PSF subtraction was deemed acceptable based on visual examination of the residuals. The successive frames show the location of Charon for each individual night, centered upon the median location of Charon, with night numbers are in the upper left corner (see Table 4.1 for relevant dates). The median position of Charon relative to Pluto was taken. For every plot, each major tick mark represents 1 pixel on an image, and each minor tick mark represents 0.25 pixels. All frames with a Charon offset more than 0.25 pixels away from the median position of Charon on each night were considered to be bad. The final plot (lower right, "After") show the positions of only the remaining good images.

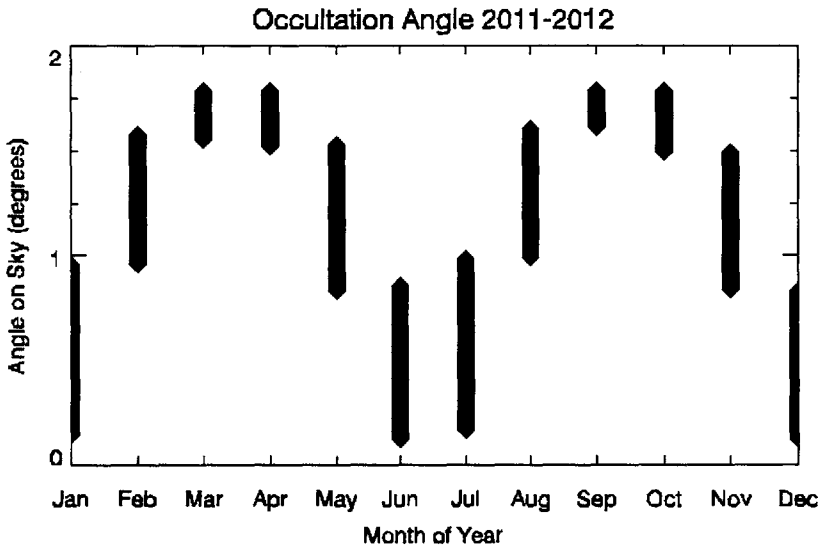

Figure 4-6: Pluto solar phase angle as a function of month of the year (3 hour resolution). The LDSS-3 observations were concentrated in March and February, where the change in Pluto's phase angle is not substantial. Two nights of data were taken in late May. Observations made in late June or early July would have had a phase angle of less than 0.5, at which point an opposition surge is seen for Charon, drastically changing the Charon-Pluto light ratio.

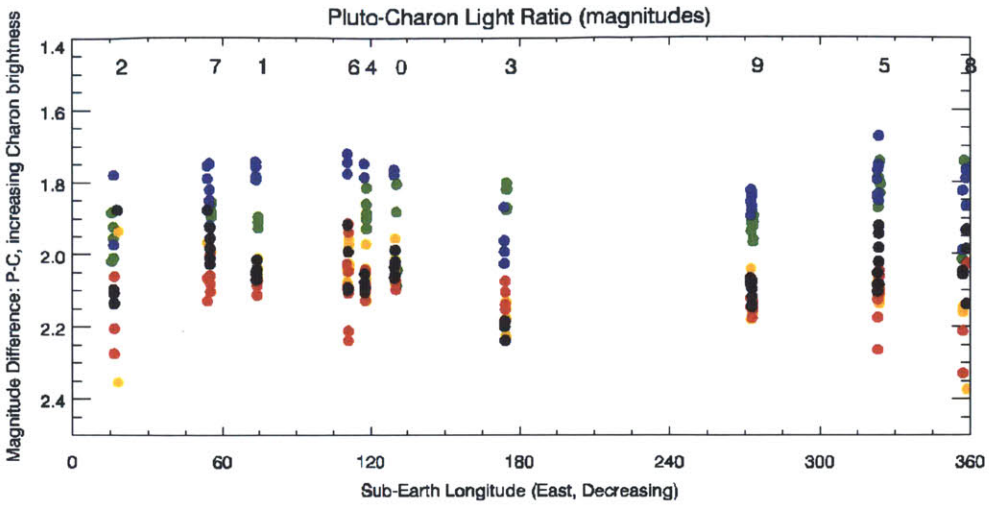

Figure 4-7: Charon-Pluto magnitude difference vs sub-Earth longitude (decreasing) for individual points. Increasing Charon brightness is up. Filters are labeled in color. Bluer Charon is naturally brightest in the B and g′ filters, while Charon is of similar brightness in the r′, i′ and z′ filters, though brightest in z′. Data have been corrected to a solar phase angle of 1.15°

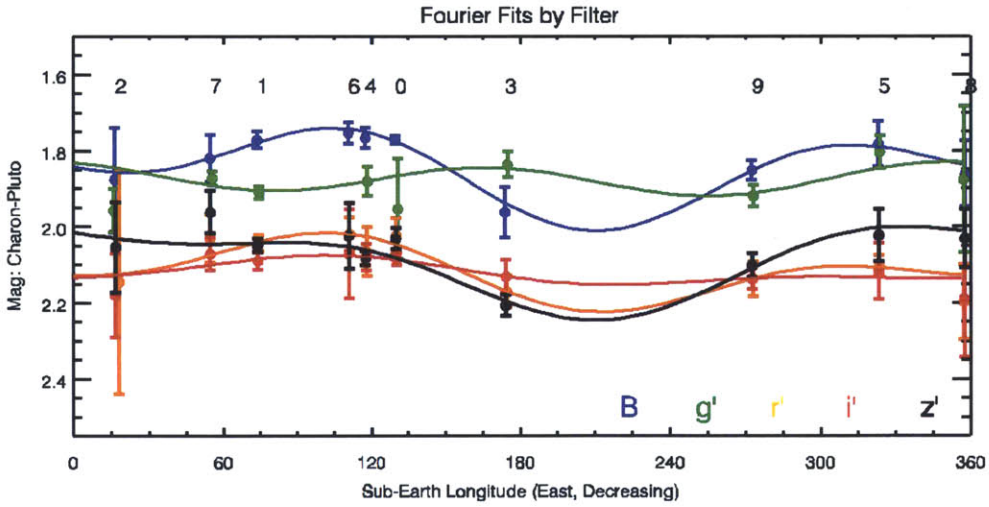

Figure 4-8: Charon-Pluto magnitude difference vs sub-Earth longitude (decreasing) for nightly averaged points. Increasing Charon brightness is up. Filters are labelled in color. Points have been corrected to a phase angle of 1.15°. A two-term Fourier series has been fit to the images in each filter. The g′ filter appears to be an outlier in that its maxima and minima do not align with the other filters' curves.

4.8 Comparisons with previous separate photometry

4.8.1 B filter HST comparisons

The presence of a B filter in the LDSS-3 filter set allows for direct comparison with the HST observations of 2002-2003. Figure 4-9 directly compares a phase-corrected F435W light curve from Figure 4-1 with that of the B light curve seen Figure 4-7, this time fully phase-corrected to 0°. The LDSS-3 light curve mimics the double peaked pattern of Pluto's light curve seen in HST.

Unlike the 2002-2003 HST measurements, the LDSS-3 data do not completely cover the light curve of Pluto, and miss the minimum Charon relative brightness at 210°, and the maximum Charon brightness at 90°. The unusually bright Charon at 90° is not an error– 90° decreasing sub-Earth longitude corresponds with Greatest Northern Elongation of Charon, which is coincidently and famously the minimum light of Pluto (see Figures 2-2 and 2-3, located on pages 38 and 39 of Chapter 2). Night 9, which sampled sub-Earth longitudes of 273° to 272° is close to southern elongation, an insignificant location in Pluto's orbit, but resulted in the best quality images, not only due to the the near-maximum separation of the two bodies, but the relative emptiness of the field, and the spectacular seeing.

For the hemisphere centered around Greatest Northern Elongation, Charon appears much dimmer in the LDSS-3 data than in the HST data set. The scant LDSS-3 data of the opposite hemisphere agree rather better with their HST counterpart.

This change in the Charon-Pluto magnitude difference has three possible explanations. The first is that there is some sort of systematic error in the calculations of the light ratio, perhaps due to stellar contamination or poor fits of some CCD images. A physical change to the light seen from either body, in this case, a dimming of Charon or brightening of Pluto provide the second and third explanations respectively. A brightening of Pluto can take two forms: physical change on Pluto's surface, or the appearance of brightening if dark regions shift out of view as Pluto's aspect changes

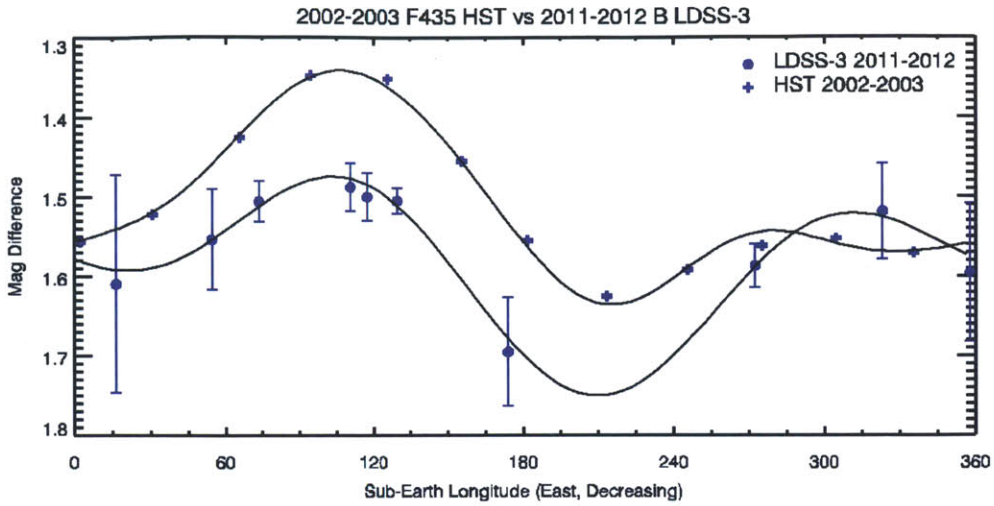

Figure 4-9: Charon-Pluto magnitude difference for 2002-2003 HST data (crosses) and LDSS-3 data (circles) as a function of sub-Earth longitude (east, decreasing). Unfortunately, the LDSS-3 data do not cover the minimum points of the light ratio curve as seen on HST. Connecting lines represent a two-term Fourier series fit to the LDSS-3 data and the four-term fit from Buie et al. (2010a). A reduction in the magnitude difference can be seen between 60 and 120 degrees sub-Earth longitude, though the (scant) data from 270 to 360 degrees sub-Earth Longitude do correlate well with the HST observations. All data have been corrected to zero phase.

from the perspective of Earth. Indeed, this latter explanation is most likely: Figure 4-10 shows the sub-Earth points for the HST and LDSS-3 images plotted atop a map from Buie et al. (2010b). Pluto's surface is broadly characterized by a dark equatorial band and bright polar caps,c while Pluto's sub-Earth point is traveling increasingly towards the north, details consistent with a brightening of Pluto. The large difference between HST and LDSS-3 ratios at 90 degrees sub-Earth longitude is consistent with a large dark spot at the same location, which should see the most drastic change as Pluto's reflectance should become both bright and more uniform with rotational phase as Pluto approaches northern hemisphere summer.

A simple preliminary average of single-scattering albedos within 90 degrees of the sub-Earth point is consistent with a global brightening of Pluto. A more-precise calculation of the expected light ratio for LDSS-3 that makes use of Hapke parameters (Hapke, 1993), phase angle and single-scattering albedo is beyond the scope of this work. However, such a calculation would allow for determination of surface changes on Pluto in the past 10 years.

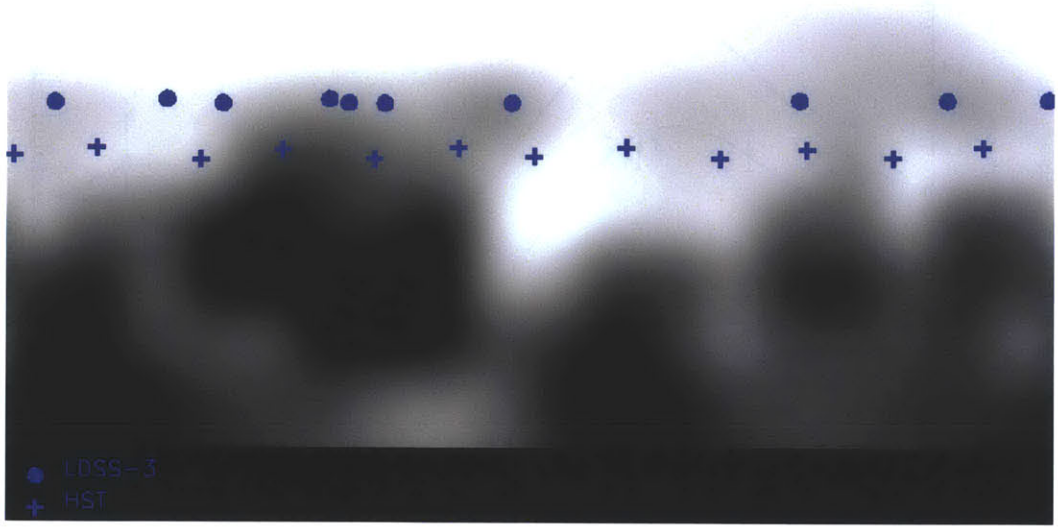

Figure 4-10: Sub-Earth points for 2002-2003 HST data (crosses) and LDSS-3 data (circles) plotted atop a B map from Buie et al. (2010b). The sub-Earth position has moved northward to a brighter region of Pluto, possibly accounting for the difference in the Charon-Pluto light ratio.

4.8.2 MagIC 2006 data

The author made a foray into the some of the backlog of MagIC data, starting with observations in 2006, that spanned 2006-05-06, 2006-06-19, 2006-06-20, 2006-06-22. On June 19 in particular, the seeing was spectacular, with FWHM reaching as low as 3.4 pixels or 0.23″! The MagIC data did not have the same sort of distortion seen with LDSS-3, so a more-straightforward non-variable PSF was used. However, there were only a very small handful of possible comparison stars available.

The MagIC images were taken in u′, g′, r′, i′, and z′. While the Johnson filter wheel was probably available at the time, no data were taken with that set. These data do not comprise enough nights to make a good phase model, but will make an excellent start when combined with the rest of the earlier MagIC data. Figure 4-11 shows the 2006 MagIC data combined with LDSS-3.

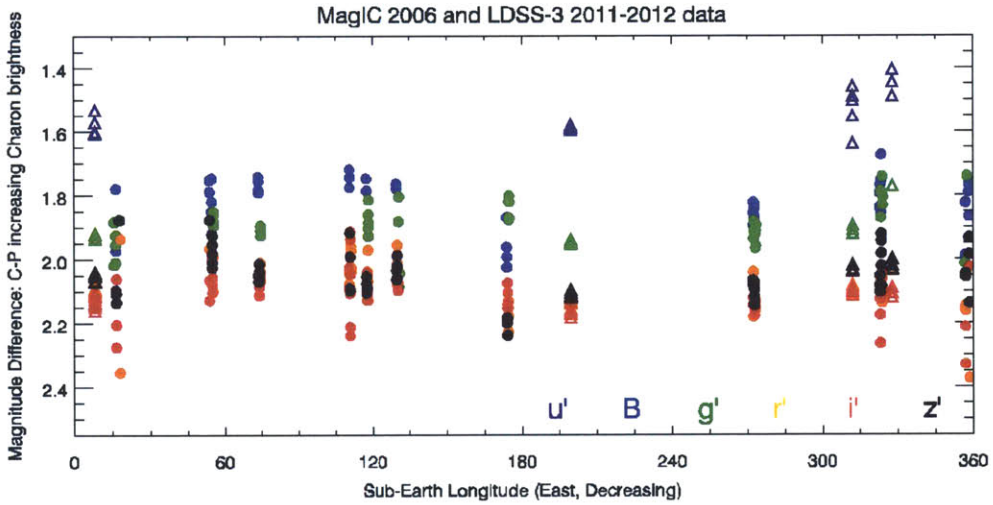

Figure 4-11: MagIC 2006 and LDSS3 2011-12 Charon-Pluto magnitude difference vs sub-Earth longitude (decreasing). Increasing Charon brightness is up. Filters are labelled in color. Bluer Charon is naturally brightest in the u′ and g′ filters, while Charon is of similar brightness in the r′, i′ and z′ filters, though brightest in z′. LDSS-3 data are overplotted. Data have been corrected to a solar phase angle of 1.15°

4.8.3 Magnitude difference vs filter

Color plays the most important role in determining the Charon-Pluto magnitude difference. Figure 4-12 shows the magnitude difference averaged for every image from Buie et al. (1997), Buie et al. (2010a), in addition to images from LDSS-3, MagIC in 2006, and the Fourier series fits presented by Clancy et al. (2005).

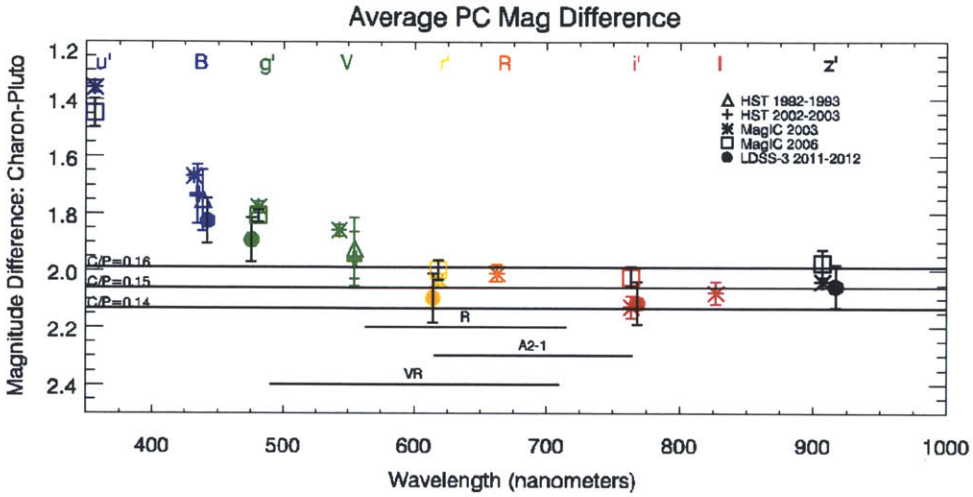

Figure 4-12: Magnitude difference versus filter, plotted as effective wavelength for LDSS-3 data, 1992-1993 HST data, 2002-2003 HST data, 2001-2003 MagIC data and 2006 MagIC data. The MagIC 2006 and LDSS-3 data were reduced by the author. The newest observations are consistently darker than their 2006 counterparts, however, the measurements herein have not been corrected for solar phase variability or unequal light-curve coverage, and thus these measurements should not be used to compare physical changes in Pluto over the years. The labeled horizontal lines mark the location of the VR filter, R filter and the A2-1 filter, three astrometric filters used to take most of the Planetary Astronomy Laboratory's Pluto occultation data. The horizontal lines represent the adopted Charon-Pluto light ratio of 0.15, plus lines at 0.14 and 0.16. The 2011-12 LDSS-3 data suggest that adopting a value of 0.142 may be more reasonable than the ratio of 0.15 proposed by Jim Elliot in 2006.

It is extraordinary difficult to recommend a single light-ratio for Charon and Pluto due to the lack of complete sampling of Pluto's rotation. Figure 4-12 shows the average magnitude difference between Charon and Pluto for each filter, and for several different sets of observations. Over-plotted are three lines representing a Charon-Pluto light ratio of 0.16, 0.15 and 0.14. The discrepancy between the different measurements can represent both real changes in the light ratio, imprecise measurements due to poor seeing, as well as a bias from the observations occurring at different times in

Pluto's rotation/Charon's revolution. In general, the new 2011-2012 measurements are dimmer than their predecessors. Unfortunately, *none* of the three filters used by MIT PAL for Pluto astrometry were used with LDSS-3. These filters, VR, a2-1, and R, are marked in Figure 4-12. The ratios for R and a2-1 filters, which fall between r′ and i′, are probably well represented by the ratio from r′. Considering the r′ filter, 0.145±0.003, not 0.15, is probably a more appropriate measurement for the a2-1 filter, and the R filter astrometric measurements. Although the VR filter has a central wavelength similar to r′, about one-third of its light overlaps with V and g′. However, VR, while centered on r′, covers enough of the V filter region that one might want to adjust the Charon-Pluto light ratio upwards by about a third of the difference between r′ and V to account for this difference. This recommendation would move the VR light ratio to 0.155.

For astrometric observations that are not made in the VR filter, the Charon-Pluto light ratio should be set to 0.142. For VR observations, the ratio should be higher, about 0.155. However, independent observations of Pluto in VR should be made and analyzed. Figure 4-13 shows the implications of at 0.8% shift in the light-ratio, which corresponds to a subsequent 150 km shift in the predicted occultation path.

4.9 Conclusions and future work

4.9.1 Recommendations for future light ratio observations

LDSS-3 has proven itself to be an adequate instrument for Charon-Pluto light ratio observations, even though the 2006 MagIC observations are superior in terms of precision. The difference light curves match in appearance to the HST data. Thus, while not ideal, LDSS-3 can effectively measure the Charon-Pluto light ratio.

It would be worthy to attempt to model the Charon-Pluto difference in the actual filters used for astrometry, such as a2, R and VR, of which only VR may be available on LDSS-3, though R and VR are available on MagIC. VR should have been used for the LDSS-3 observations, but was not. Its availability was not well-advertised, no

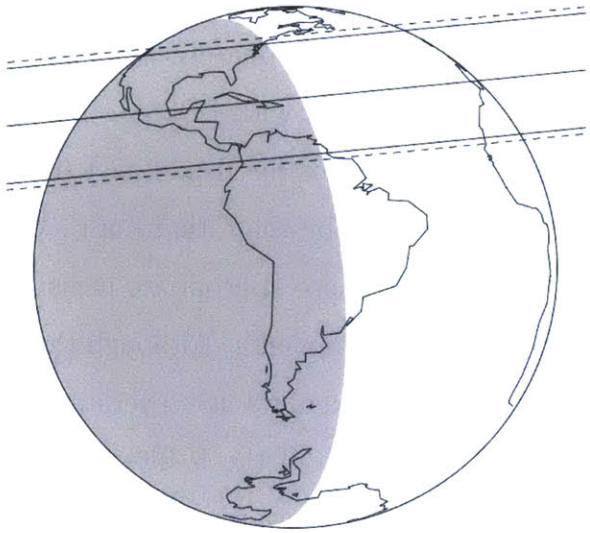

Figure 4-13: Effects of Charon-Pluto light ratio change of 0.8% on an occultation ground track. Solid lines represent Pluto occultation centerline, and the roughly 1400 km limit at which a graze would be seen. A change of 0.008% in the Charon-Pluto light ratio corresponds to a shift of this path by approximately 150 km, represented by dashed lines.

past observations had been made with it, so it did not occur to me to request this filter.

As for other filters, of great interest are B and V observations due to their comparability with historical observations. However, the redder filters should not be neglected because they are nearer in effective wavelength to an open CCD used in occultations.

Specifically, new observations should be focused on (decreasing) sub-Earth longitudes that were not well-covered or at interesting points in the magnitude difference light curve. The largest hole in the light curve is between 180° and 270° sub-Earth longitude. However, 90° and 210° probe the maximum and minimum light-ratios respectively. Longitude 180° is also of interest due to the unusual results for Night 3.

Observations are also best performed at Pluto opposition, because Pluto and Earth are at their closest annual separation, and Pluto can be observed at low-airmass. However, the solar phase correction at opposition will be made difficult due to the opposition surge of Charon. As the opposition surge has been shown to be color-

dependent based on the B and V measurements of Buie et al. (2010a), calculating a solar phase curve for red filters should be a priority. The LDSS-3 data do not probe low phase angles suitable for quantifying the opposition surge, so more measurements will be required.

Future observations and reductions should be made much easier as Pluto is entering an area of rapidly decreasing stellar density.

4.9.2 Recommendations for future reduction work

There is still a gigantic backlog of MagIC data to be reduced. The 2006 MagIC IRAF reductions yielded spectacular results, in part due to the spectacular seeing on the nights sampled. The best of the previous nights should be examined to fill in holes in the light curve and make a more complete coverage of the Charon-Pluto light ratio.

An effort should also be made to turn the B filter light ratio data into standard magnitudes for inclusion in general Pluto light curve studies.

It may be possible to examine the astrometric images themselves to find whether any images have seeing of better than 1.3″, preferably 1.0″ and attempt a PSF fit. This would be a completely new project, but may yield a more accurate light ratio estimate than taking an average from filters where light ratio measurements are already available.

The magnitudes extracted from IRAF **daophot** seem to have produced reasonable results, however, it is not the only PSF fitting program. Someone with a massive amount of time on their hands might chose to compare the **daophot** magnitudes against results from DOPHOT (Schechter et al., 1993) or Mathematica's Lorentzian fits (used for the original MagIC data).

4.9.3 Recommendations for the Charon-Pluto light ratio

We return to answer the following questions: Has the Charon-Pluto light ratio changed from previous observations? How does the ratio change with filter? How does ground-based PSF photometry compare with data from the Hubble Space Telescope? Does

the light ratio change significantly with Pluto's rotation? Does Pluto's opposition surge depend on the time of the year?

Firstly, the Charon-Pluto light ratio is very similar to previous observations. Charon may have dimmed slightly with respect to Pluto, but global change is difficult to eke out based on the enormous intranight spread, as well as the change in rotational and solar phase. A darkening of Charon in B relative to Pluto over the past 10 years may have occurred, but the most likely explanation is a brighting in Pluto's apparent brightness due to the northward wandering of Pluto's sub-Earth point, which displays the bright northern polar cap more prominently at the expense of Pluto's dark equatorial bands. The 2011-2012 data suggest a light ratio of 0.142 ± 0.003 at 1.15° solar phase, instead of the originally-assumed phase-less ratio of 0.15. Because the VR filter has an effective wavelength between that of g′ (ratio 0.179 ± 0.001) and r′, the Charon-Pluto light ratio should be between the two filters. Future light ratio observations should specifically make use of a VR filter to calculate an appropriate light ratio.

Due to Pluto's red color, and Charon's neutral color, Charon is significantly brighter in B and other green colored filters, but there is little difference in the Charon-Pluto light ratio in redder filters such as r′ and near IR filters such as i′ and z′.

The effects of solar phase should not be discounted. Observations that assume a light ratio must account for solar phase, due to the observed opposition surge of Charon below 0.5°, and the differing phase functions between the two objects. As the opposition surge occurs during the best time each year to observe Pluto (opposition), this correction is crucial.

Do the light ratio results suggest a particular filter for general astrometric imaging? I would recommend that astrometry be taken in a filter that has a recent light ratio measurement, which includes none of the three typically used by the Planetary Astronomy Laboratory at MIT. However, the A2-1 and R filters are superior to VR, as both fall somewhere on the spectrum between r′ and i′, two filters that have recent light ratio measurements. Given a choice between the V filter, historically

used to image Pluto, and R, which is used by PAL (or any other similar red filter), I would recommend R. In the northern hemisphere, Pluto fields are frequently found at high airmass, thus one would want to minimize atmospheric refraction with a higher-wavelength passband. As the best occultation predictions are made when Pluto is on the same field as its occultation star, it matters little what data were taken decades earlier, instead one should focus on getting the best images in the moment. As Pluto exits the galactic plane, its star fields will become less pathologically crowded. As most stars are brighter in R than V, more bright stars will be available for astrometric network creation in R than in V.

The ground-based PSF taken in good seeing ($< 1''$) do very well compared to the HST data. Relative to the cost of obtaining HST data, the Magellan data are a bargain.

In the case of the B filter, the Charon-Pluto light ratio is extremely variable with filter and time with a 0.2 magnitude peak to peak difference. Thus, the light ratio is better represented a Fourier series dependent on sub-Earth longitude. However, the light ratio should become less longitude-dependent as Pluto approaches the northern hemisphere summer solstice.

Monitoring the Charon-Pluto light ratio is an intensive project that requires a short amount of observing time on each night, but a large amount of different nights and different filters. While there is now a catalog of observations in Sloan filters, observations done in UBVRI filters would probably be of more scientific use. Data should be also taken in filters nearer in wavelength to the filter used for occultation astrometry. Additionally, sufficient data should be taken to calculate the solar phase correction in filters other than B and V. Lacking such resources, I recommend monitoring the performing Charon-Pluto light ratio with a frequency of every decade or so, both to adjust for Pluto's changing aspect, and to account for true surface changes. Observations should also search for an opposition surge of Pluto during its 2018 crossing of the ecliptic.

Chapter 5

Temperature asymmetries in Pluto stellar occultation light curves I: Methods

5.1 Introduction to Chapters 5 to 7

This chapter is the first in a series of three related chapters exploring asymmetries between immersion and emersion limbs of Pluto occultation light curves, and the degree to which the location probed on Pluto affects any asymmetry seen or not seen. Thus, occultation data are used to probe the geographic distribution of temperature on Pluto. As modeling of each light curve commenced, it became apparent that more detail would need to be spent on the limitations of modeling assumptions, specifically how the definition of the upper atmosphere affected temperature difference results, what signal-to-noise ratio this study is appropriate for, and finally, whether an offset in the assumed value of the impact parameter would have a confounding effect on the results. The latter examination makes use of data from all available occultation events. The first two studies use simulated idealized occultation data to set limits on the capabilities of the modeling. Based on the conclusions from this chapter, the second chapter will describe the results of the single limb models for the nine

light curves deemed fit for asymmetry analysis. The third chapter will examine these results in the context of several location-based metrics.

After fourteen years without a Pluto occultation, two occultations were predicted and observed in the summer of 2002 (Sicardy et al., 2003). The first of the two 2002 occultations, known as P126, had a large observing campaign, but weather prevented all but three small telescope from making observations (Buie et al., 2002). The second occultation was much more widely observed, from Hawaii to California, (Elliot et al., 2003b). Independent analyses of two separate observations of the second event found that Pluto's atmospheric pressure had doubled in the intervening fourteen years. Neither light curve resembled the light curve from 1988[1], which has a knee-shaped structure that clearly delineated the starting point of the upper atmosphere. Two explanations for this "knee" were provided, a thermal gradient (Hubbard et al., 1990), or haze layer (Elliot et al., 1989). In the case of the latter, fourteen years seems like plenty of time for a haze layer to dissipate, or several more to be created and dissipate again. We will not know how long it took for Pluto's atmosphere to change to its current conditions or how often such an event occurs. As part of a thorough investigation into differences between occultation light curves, location on Pluto should also be considered, given Pluto's varieagated surface.

Asymmetry in occultation light curves has been a source of some brief analysis in Sicardy et al. (2003), Young et al. (2008), Zalucha et al. (2011b) . However, each of these analyses were focused on a single light curve. Instead, for this thesis I take many light curves from many several different events and considers asymmetries anew, with references to previous studies where appropriate.

5.1.1 Pluto stellar occultation models

The first atmospheric refraction models of an occultation light curve were created by Baum & Code (1953) to model a stellar occultation by Jupiter. Due to the fact that Pluto is rather smaller than Jupiter, several modifications to Baum and Code's model

[1]These curves are plotted in Chapter 6. For the 2002 curves, see Figures 6-5 and 6-6. For the 1988 curve, see Figure 6-2.

had to be made to fit Pluto's atmosphere. Early write-ups of the 1988 event (Hubbard et al., 1988; Elliot et al., 1989) identified four major adaptations for Pluto: 1. Pluto gravity, a function of radius and mass, cannot be treated as constant. 2. "refraction shrinkage", a reduction in the apparent size of the atmosphere due to curvature of the limb 3. geometric effects from the scale height of the atmosphere being relatively large compared to Pluto's radius 4. and variation in stellar velocity relative to the limb[2]. Elliot & Young (1992) (hereafter EY92) take these four effects and create an occultation model for Pluto that also takes into account both the thermal gradient and haze layer hypotheses. EY92 assumes a power law relationship between temperature and radius.

While the EY92 model has been used extensively in modeling light curves, it is not the only stellar occultation model used for Pluto. Elliot et al. (2003a) outline a method for inverting Pluto's atmosphere that works Plutoward from an initial boundary condition above the atmosphere. These inversions create a temperature profile based on radius. Strobel et al. (1996) outline the "radiative-conductive equilibrium" model used by Zalucha et al. (2011a) to solve one-dimensional heat balance equations that recreate Pluto's vertical temperature profile. Zalucha notes the power law that provides the foundation for the EY92 model is idealized, and cannot cover every portion of the atmosphere. Zalucha et al. (2011b) update the model used in Zalucha et al. (2011a) to include eddy diffusion of temperature to make a "radiative-conductive-convective" model. Young (2012) creates an algorithm to model thin atmospheres accounting simultaneously for both refraction and diffraction.

For this analysis, I have chosen to look at Pluto occultation light curves solely through the lens of the model outlined in EY92. While EY92 is an idealized model, it is widely-used, and due to its (relative) simplicity, it is one of the first fits attempted for Pluto atmosphere. The model results are directly comparable with a previous results. Most practically, a working version of the code exists as part of the Planetary Astronomy Lab's extensive Mathematica packages. Using this code prevented the accidental introduction of errors via an attempt to re-invent a complex, previously

[2]The variation of this term,$v_\perp$, is discussed in detail in Section 5.4.3

debugged, software package.

5.1.2 Parameters of the Elliot & Young (1992) ("EY92") model

Elliot & Young (1992) ("EY92") define two sets of parameters to fit both the atmosphere and the data. A full list of parameters can be found in Table 5.1 Some parameters, exposure time (Δt), background fraction ($bkgdFrac$), slope of the baseline ($slope$), light level ($full$), and mid-time ($tMid$) define the basic shape and timing of the light curve. Others, such as closest approach in the shadow plane (ρMin) and shadow velocity (v), help determine where the occultation occurred. Most importantly, parameters such as the half-light radius (r_H), the equivalent isothermal energy parameter (λ_{Hi}, the ratio of the scale height to the half-light radius), and the isothermal exponent (b) define the shape of the light curve. Additionally, one may specify a presence or absence of haze. Used as a tool to deepen an occultation light curve model, the haze is defined by three parameters: the onset radius (r_{τ_0}), the location where opacity = 1 (r_{τ_1}), and the haze scale height (h_{τ_1}). Thus a base level of the haze is defined at one location, and its scale height denotes its thickness. The larger onset radius is to prevent a Zeno's paradox-like situation where haze is present throughout the entire atmosphere. Instead, no haze exists beyond that larger onset radius. The abrupt onset was inspired by the 1988 light curve's distinctive "knee", thought it also accommodates the idea of a layered atmosphere (Person, 2013). Lastly, a value for Pluto's surface ($rSurface$) is included in the parameter set, but it does not play a role in shaping the atmospheric model light curves as Pluto's surface has not been probed by occultation.

As our goal is to search for signs of asymmetry in Pluto's atmosphere, ultimately, we are not looking for the fit results for the individual light curve parameters, but rather the difference in temperature between the immersion and emersion limbs. The ratio of temperature to mean molecular weight as derived from an occultation light curve can be found in equation 6.13 of EY92:

$$\frac{T_0}{\mu_0} = \frac{GM_p m_{amu}}{k r_0 \lambda_{g0}} = \frac{g_0 H_{p0} m_{amu}}{k}. \tag{5.1}$$

Here, μ_0 is mean molecular weight, k is Boltzmann's constant, m_{amu} is the atomic mass unit, G, is the gravitational constant, M_p is Pluto's mass, r_0 is the half light radius, λ_g is the energy ratio, $g_0 = GM_p/r_0^2$ (eqn 6.11 of EY92) and $H_{0p} = \frac{r_0}{\lambda_0}$ is the scale height (eqn 6.12 of EY92). We assume μ_0 represents a N_2 atmosphere in all cases, and calculate the temperature alone. The N_2 assumption allows for direct temperature comparison with many recent occultation papers, including Elliot et al. (2007).

Throughout this work, we will concern ourselves with three values calculated from fits to the Pluto occultation light curves: r_H, λ_{Hi} and T_{diff}.

Table 5.1: Parameters of the Elliot & Young (1992) ("EY92") model

Parameter	Symbol	Units	Status
background fraction	$bkgdFrac$	-	fit during two-sided fit only
baseline slope	$slope$	DN/s^2	fit during two-sided fit only
baseline full flux level	$full$	DN/s	fit during two-sided fit only
occultation midtime	$tMid$	s	fit during two-sided fit only
half-light radius	r_H	km	fit for two and one-sided fits
lambdaHi "energy ratio "	λ_{Hi}	-	fit for two and one-sided fits
isothermal exponent	b	-	held as constant (0) for this work
haze onset radius	r_{τ_0}	km	set to null for this work
haze unity opacity radius	r_{τ_1}	km	set to null for this work
haze scale height	h_{τ_1}	km	set to null for this work
closest approach/impact parameter	ρ_{Min}	km	determined *a priori* from astrometry
shadow velocity	v	km s^{-1}	determined *a priori* from astrometry
image exposure time	Δt	s	known from observing logs
surface radius	$rSurface$	km	set as arbitrary constant, 800 km
occultation temperature	T	K	$\frac{r_H \times 10^3 * G * M_P * \mu_0 * m_{amu}}{(\lambda_{Hi} - \frac{5}{2}b)(r_H \times 10^3)^2 k}$
temperature difference	T_{diff}	K	$T_E - T_I$ or $T_N - T_S$

5.1.3 Model light curve fitting procedure

The light curve models were fit using a suite of Mathematica packages written and maintained by the MIT Planetary Laboratory. In particular, non-linear least squares fitting was performed using a package called "Least Squares Fitting", authored by

"Leslie Young and Friends [*sic*]" starting in February 1990, and maintained by a half-dozen PAL scientists and students throughout the years[3]. The version I used, Version 6.1.0, was last modified in August of 2008. In particular, I ran the "olcTwoLimb4ML" light curve model last updated by Jim Elliot in 2006[4].

For each light curve, three models are created for the upper atmosphere, that is, the points that fall above a particular shadow radius from Pluto's center. The first model uses both the immersion and emersion sides of the light curve and fits for parameters *slope*, $full$, $tMid$, r_H, and λ_{Hi}. These fit results form the starting parameters for the second and third fits. The second model holds the values of *slope*, $full$, $tMid$ derived from the first fit as constant, but refits for r_H and λ_{Hi} using image from the immersion side only. The third model does the same, but for the emersion side.

As λ_{Hi} and r_H are found to be correlated parameters, they were initially fit separately. My Mathematica notebooks would alternate between fitting for the slope, full light level and mid-time, then r_H, then λ_{Hi}. The pattern would repeat with increasingly stringent convergence criteria. After several iterations, all parameters would be fit simultaneously. For emersion-only and immersion-only fits, alternations were performed only between r_H and λ_{Hi}. Finally, both parameters were fit simultaneously.

A decision was made to keep b, the power law exponent and indicator of temperature gradient in Pluto's upper atmosphere, set to 0; all models assumed Pluto's

[3]Leslie A. Young, James L. Elliot Amanda S. Bosh, Cathy B. Olkin, Michael J. Person, Elisabeth R. Adams.

[4]Description of the model from Mathematica help file: olcTwoLimb4ML[{bkgdFrac, slope, full, tMid, rH, lambdaHi, b, rTau0, rTau1, hTau1, rhoMin, v, deltaT, rSurface}, coorList] and olcTwoLimb4 (with the same arguments) produce a light curve for an occultation of a small body with a possible thermal gradient, haze layer, and limb cut-off. It includes light from both limbs. The onset of the haze and the limb cut-off is integrated over the time "deltaT". The full scale is expressed in DN, which does not depend on "deltaT". Note that "deltaT" must be set accurately, or the integration over the haze and surface discontinuities will not be correct. The "bkgdFrac" parameter is the background, expressed as a fraction of the full-scale signal, and the "slope" is an additive drift to the full-scale signal (as would be caused for a variable transmission of the atmosphere). "deltaT" is an integration time, but it does not affect the "coordinates" for the light curve, which are specified by the list "lsCoor" (units of these are seconds). The units of "rTau0", "rTau1", "hTau1", "rhoMin", and "rSurface" are km. The units of "full" are DN/sec and the units of "slope" are DN/sec^2. The units of "v" are km/sec, the units of "tMid" and "deltaT" are sec. The output is a light curve level in DN (data numbers). This is the MathLink version of olcTwoLimb4.(2006-07-12 jle; rev 2006-07-14 jle)

atmosphere to be isothermal. Many fits, such those described in Elliot et al. (2007) chose several values for b and create multiple fits with this parameter held constant.

When comparing model fit-results for r_H against radially plotted occultation light curves throughout this chapter and the next, astute eyes may note that the half-flux level does not match the location of the half-light radius by several tens of kilometers. This is due to an effect known as "refraction shrinkage." Refraction of starlight around Pluto's limb causes the shadow cast on Earth by Pluto's atmosphere to appear smaller than the actual size atmosphere itself. For convenience, throughout this work, light curves will be plotted using "shadow radius", or the separation of Pluto's center and the star as seen from Earth. Distances in the shadow plane can be calculated by simple geometry using knowledge of Pluto's velocity, the closest approach distance to Pluto, and time of closest approach. Upper atmosphere cut-off points are also defined in terms of the shadow radius. The half-light radius, however, reflects the actual atmospheric size as calculated by the model. More detail about refraction shrinkage can be found in Elliot et al. (1989).

5.2 Purpose of the methods chapter

This chapter is designed to be a companion to Chapter 6. While the next chapter will discuss temperature asymmetries in Pluto's upper atmosphere, this chapter will deal with the reliability of such measurements, and explain the subjective choices made during modeling. I hope to answer whether measurement asymmetry is even possible to measure with the data and how accurate such results might be.

Six major questions needed to be answered to ensure the accuracy of the results:

1. Stellar occultations vary greatly in signal-to-noise ratio due to a large range in telescope size, stellar brightness, sky conditions and camera sensitivity. What is the minimum signal-to-noise ratio for light curves in this study?

2. For simulated occultation light curves with known parameters, can models of the upper atmosphere reproduce the model parameters? Can a temperature

asymmetry be identified from a group of light curves?

3. What is the optimal cut-off to determine the extent of the upper atmosphere? What are the effects of including too much of the lower atmosphere or too little of the upper atmosphere on the fit results? How does the presence of haze affect the measured temperature difference in a light curve?

4. Do the errors that result from the model fits accurately reflect random noise?

5. Will an inaccurate determination of the closest approach of observing station to Pluto's centerline bias the temperature difference result?

6. How do atmospheric spikes bias light curve results?

Questions 1-4 are the subject of two experiments with simulated light curves. Question 5 will be answered using all occultation light curves available to me in Section 5.6. Question 6 will be discussed briefly in Chapter 6.

5.3 Occultation light curve asymmetry simulation experiments

5.3.1 Why concern ourselves with upper atmospheric cut-offs?

In the list of questions above, by far the most complicated question involved the definition of the onset location of the lower atmosphere. While the upper atmosphere is readily modeled by refraction, the lower atmosphere remains a mystery. In 1988, the KAO light curve was discontinuous between the upper and lower atmosphere. Both a haze layer and/or a thermal gradient was proposed to to make up for the change in slope in Pluto's atmosphere (Elliot & Young, 1992). Future occultations did not have such an obvious discontinuity. The disappearance of the knee does not indicate an absence of a haze layer/thermal gradient. Rather something is still

present, albeit with a less dramatic onset (see Figure 5-1). The upper atmosphere matches a refraction-only paradigm, but to what degree, it is hard to tell without an obvious knee. Thus one must fit for the lower atmosphere or remain agnostic on the haze/thermal gradient equations, simply chopping off the lower atmosphere.

In the EY92 model, the parameter r_{τ_0} defines a sharp onset of a lower-atmospheric haze layer implemented as the boundary of a piecewise function for the upper and lower atmosphere. With fits that include a haze layer, the output for points at radii above r_{τ_0} should be mathematically equivalent to simply excluding points below r_{τ_0} from the atmospheric model and leaving all three haze parameters as null. The parameter r_{τ_0} will be referred to throughout this document as the **cut-off**. The first models showed that temperature difference was not consistent with changing cut-off level. As the cut-off was not included in the non-linear least squares fit, this chapter outlines how cutoffs were chosen.

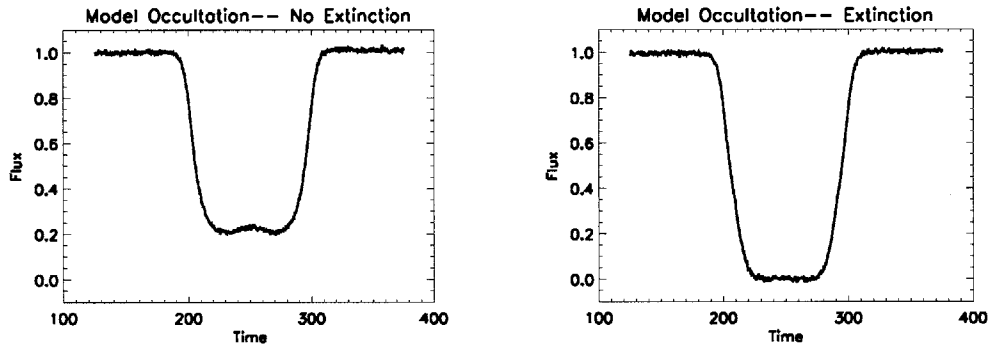

Figure 5-1: Left: Model light curve created using only refraction. Note that the light curve does not reach the zero flux, and contains the beginnings of a central flash. Right: Model light curve that includes extinction in the form of haze. This light curve reaches the zero flux level and has a flat bottom. Both light curves are 500 km from the center of their imaginary Pluto-like body. Non-graze Pluto light curves typically resemble the light curve on the right.

5.3.2 Synthetic light curve creation and fits

To help understand the effects that cut-offs have on the temperature difference results, identify a minimum S/N, verify accuracy of the modeling techniques, and investigate the model accuracy with respect to noise, two experiments involving synthetic data

were run.

The first experiment concerned five synthetic light curve models at varying levels of noise. Each light curve had Gaussian noise S/N per point of 25, 50, 100 and 150 added to it, for a total of 20 light curves. Each light curve was given a designation, A through E, and simulated a different type of atmosphere, i.e. with and without haze, thermal gradients and asymmetry. Following the experiments with light curves A-E, a second series was generated, denoted F. This series featured an asymmetric light curve with haze, with Gaussian S/N per point of 50 added, not once, but 100 times in an effort to compare internal and external errors for light curve modeling. Table 5.2 lists the different light curve models simulated and their parameter types.

Table 5.2: Overview of synthetic light curve models

Model ID	Haze	Thermal Gradient	Asymmetry	S/N per point	Versions
A	no	b=0.0	no	25	1
A	no	b=0.0	no	50	1
A	no	b=0.0	no	100	1
A	no	b=0.0	no	150	1
B	yes	b=0.0	no	25	1
B	yes	b=0.0	no	50	1
B	yes	b=0.0	no	100	1
B	yes	b=0.0	no	150	1
C	no	b=-2.0	no	25	1
C	no	b=-2.0	no	50	1
C	no	b=-2.0	no	100	1
C	no	b=-2.0	no	150	1
D	yes	b=-2.0	no	25	1
D	yes	b=-2.0	no	50	1
D	yes	b=-2.0	no	100	1
D	yes	b=-2.0	no	150	1
E	no	b=0.0	yes	25	1
E	no	b=0.0	yes	50	1
E	no	b=0.0	yes	100	1
E	no	b=0.0	yes	150	1
F	yes	b=0.0	yes	50	100

All synthetic light curves were created by Michael J. Person and provided to the author. MJP supplied the impact parameter (ρ_{Min}=500 km), background fraction ($bkgdFrac$=0), exposure time (Δt=0.5 s), and shadow velocity (v=25 km/s). These parameters were common to all synthetic light curves, and represent information

essential to the fit, but always known *a priori*, from astrometry, ephemerides or a multi-chord occultation fit.

However, the rest of the parameters were not disclosed, allowing the variables that would be true unknowns when fitting actual occultation data to be tested in manner that resembled an attempt at a blind experiment. While r_H and λ_{Hi} were unknown parameters, it was obvious from visible inspection that curves B and D contained a haze layer, while curves A, C and E did not. It was also visually obvious that curve E was asymmetric, as bottom of the light curve had a small slope. Thus, unfortunately, it was also obvious that A, B, C, and D were not designed to have a temperature difference. In the case of light curve F, I requested that MJP create a light curve that was both asymmetric and contained a haze layer. The parameters remained unknown until after examination of the fit results as a function of cut-off. Then an optimal cut-off was chosen, and best fit parameters and their errors were recorded. Only then did MJP reveal the parameters used to make the light curve.

Each light curve was fit to the EY92 model using a non-linear least squares in Mathematica (see Section 5.1.3). The same Mathematica notebook and fitting methods were later used for fitting the observational data analyzed in Chapter 6. Using the astrometric information provided by MJP, and a rough estimate of the occultation mid time, the mid times for each "image" were transformed into distance from the body's center, or the *shadow radius*. Any points with a radial distance smaller than a specific cut-off shadow radius were not included in the symmetric fit. Since a more robust value of $tMid$ was calculated during the symmetric fit, the shadow radius was recalculated for the immersion-only and emersion-only fits. For A-E, cut-offs ranging from 835 km to 1390 km in 15 km from the center of the imaginary body were tested. At 15 km resolution, each cut-off represented the addition of 1-2 points per curve. For light curve F, cut-offs were performed in a similar fashion, but ranged from 1000 km to 1300 km, due to the determination that modeling the atmosphere below 1000 km was far beyond the range of data that would include the upper atmosphere.

For this experiment (and fits for the data covered in Chapter 6), the thermal gradient parameter b was held constant. Direct fitting of b had proved unreliable,

and adding multiple versions of b would add another dimension to the parameter space which already included cut-off and S/N.

The next two sections present the synthetic light curve model results, first for light curves A-E, then for the 100 versions of light curve F. In Section 5.4.1 and Section 5.5.1, I will present the effects that different cut-offs have on the determination of the best fit model. In Section 5.4.2 and Section 5.5.2, I will compare the parameters found using the chosen cut-off with the parameters as revealed by MJP. Section 5.4.3 will discuss limitations on the signal to noise ratio, while Section 5.5.3 will examine internal and external errors.

5.3.3 A guide to cut-off figures

Figures 5-2 through 5-6, and 5-7 display the same four basic plots for each major light curve type. Instead of wasting caption space (and paper) writing the same description of all four axes and symbol key five times over, I will describe these figures in detail here, and leave the figure caption space to highlight what is out-of-the-ordinary about the model and cut-off results.

For Figures 5-2 through 5-6:

- The **top figure** displays the two of the four **light curves**, plotted as a function of shadow radius. It would be impossible to distinguish between light curves, if all four were plotted on the same axis. Therefore, only the light curves with an S/N per point of 25 (in black) and S/N of 150 (in red) were plotted. The light curves are folded over, so both immersion and emersion are plotted for each light curve. The black vertical lines represent the maximum and minimum cut-offs modeled, and the red vertical line represents the cut-off value that was eventually chosen (repeated in all four plots). To the left is a key that that matches the four S/N with the appropriate symbol for the three figures below.

- The **second from the top** figure shows the **temperature difference** as a function of shadow radius cut-off choice (km). Error bars are not included, otherwise the graph would not be legible. Instead, to the left, between 600 and

700 km, there are four points that represent the temperature difference and error bar of the temperature difference at the chosen cut-offs. A horizontal bar represents the actual light curve temperature difference.

- The **second from the bottom** figure shows the **half-light radius** as a function of shadow radius cut-off choice (km). While the half-light radius represents the actual distance in Pluto's atmosphere, the cut-offs are in units of shadow radius. In the shadow plane, Pluto's atmosphere appears smaller due to a phenomenon called refraction shrinkage. Error bars are not included, otherwise the graph would not be legible. Instead, to the left, between 600 and 700 km, there are four points that represent the half-light radius and error bar of the at the chosen cut-offs.

- The **bottom** figure shows the λ_{Hi} as a function of cut-off choice (in units of shadow radius). Error bars are not included, otherwise the graph would not be legible. Instead, to the left, between 600 and 700 km, there are four points that represent the λ_{Hi} and error bar of the half-light radius for at the chosen cut-offs.

The figure for Data Set F (Figure 5-7) has the same basic categories as the figures for A-E, except for a few basic changes:

- As there is only one noise level, the immersion side is plotted in black, while immersion is plotted in red. Only one light curve out of the one-hundred light-curves is plotted.

- For each cut-off level, all 100 points are plotted in the graphs for temperature difference, r_H and λ_{Hi}. No error bars are shown, as the point spread illustrates the dispersion of the points.

- For the plots that show r_H and λ_{Hi}, the immersion fit values are plotted in black, while the emersion fit values plotted in red. The parameter values used to create the immersion and emersion light curves are represented by black and red horizontal lines respectively.

5.4 Synthetic light curves tests, models A-E (S/N threshold test)

5.4.1 Model fit results vs cut-off

For each S/N version of light curves A-E, non-linear least squares fits were run to calculate r_H, λ_{Hi}. From these parameters and their errors, T for immersion and emersion and ΔT were calculated, along with their respective errors. In Figures 5-2 through 5-6, we present model results for each light curve type, arranged by cut-off. We look at ΔT, r_H, λ_{Hi}, and compare the shapes of the light curves with the greatest (S/N per point = 25) and least noise (S/N per point =150).

Figures 5-2 and 5-4 represent the refraction-only case. The entire light curve conforms to the upper atmospheric model, and as a result, the fits reproduce the parameters of the models that created them. Thus, the deeper the light curve cut-off, the smaller the error bar: more points are available to pin down the fit. Increasingly shallow cut offs have increasing larger error bars. At some point, each light curve breaks away from the "best" fit and the results are dominated by some piece of noise that is capable of systematically biasing the fit of the few remaining points. For example, in Figure 5-2, at an S/N of 25, the temperature difference breaks off from its known input of no difference at about 1135 km, while the curves with higher S/N do not exhibit such a break until 1255 km.

Figures 5-3 and 5-5 represent the cases with haze. As seen in Figure 5-1, the presence of haze increases the slope of the light curve. When the lower atmosphere is cut off, no haze parameters are specified in the model. Thus, the parts of the light curves used to model could still contain some haze. What effects would such haze have? While the ΔT and r_H show no drastic changes due to haze, the onset of haze becomes very clear due to the discontinuous slope of the λ_{Hi} parameter. For cut-offs above about 1120 km, λ_{Hi} for light curves B and D remains stable, but if the curve is cut off below 1120 km, the fit for λ_{Hi} increases strongly as haze forces the model to fit a drastically different slope, with a much less noticeable response in

rH. This increase can be seen with all S/N levels. Thus, it is highly likely that any λ_{Hi} in the range that increases drastically with decreasing cut-offs is systematically wrong. Throughout this paper, I shall refer to the cut-off as point where λ_{Hi} stops decreasing sharply with increasing cut-off as the λ **turn-off**. At the opposite end, the effects of fewer points making up a model become apparent: errors will get bigger and light curve model results will go haywire. Thus, any cut-off choice must be a balance avoiding points with haze versus including as many points as possible to have a more reliable fit.

The fit results for the final light curve are shown in Figure 5-6. For this light curve a temperature difference between immersion and emersion was built into the model. Below 1200 km, models of every S/N agreed that the emersion side had a warmer temperature than the immersion side. However, in the case of S/N=25, while the fits predict a warmer temperature, the error bar on the measurement is not precise enough to confidently report an asymmetric temperature.

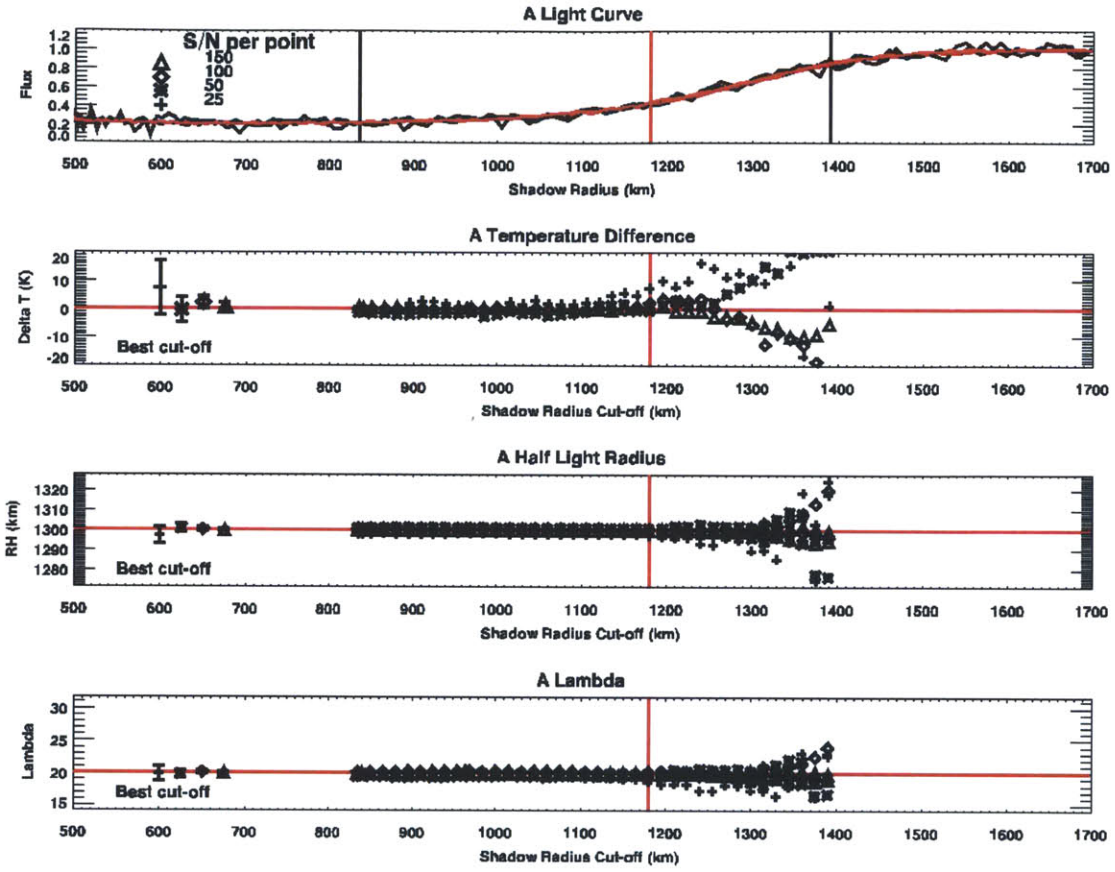

Figure 5-2: **Data Set A** cut-off experiment. See Section 5.3.3 for a description of each plot.
Top: This synthetic data set is a **refraction-only** model with a closest approach of 500 km from an imaginary Pluto.
Second from top: For the S/N 25 light curve, the temperature difference calculation begins to deviate at 1135 km while all other light curves begin to deviate at 1255 km.
Second from bottom: Deviations in r_H correlate with a change in temperature difference and λ_{Hi}, thus r_H remains constant until about 1255 km for the high S/N curves, with deviations for the S/N 25 curve at slightly earlier.
Bottom: Save for the variability when the number of points available to fit becomes reduced due to shallow cut-offs, there is no change inλ_{Hi} with cut-off depth.

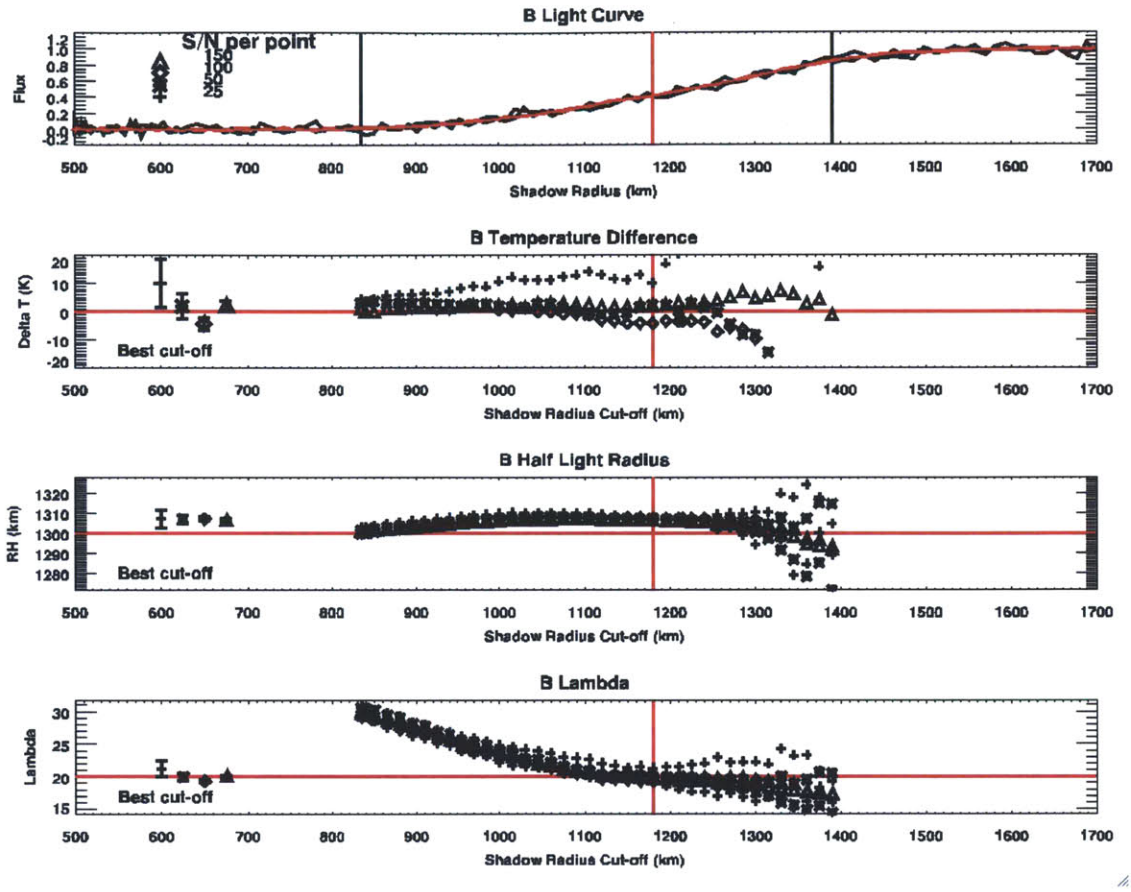

Figure 5-3: **Data Set B** cut-off experiment. See Section 5.3.3 for a description of each plot.

Top: This synthetic data set is a **refraction plus haze** model with a closest approach of 500 km from an imaginary Pluto.

Second from top: Despite the haze layer, the temperature difference is maintained across all cut-offs with a few exceptions. For the S/N 25 light curve, the temperature difference calculation begins to deviate at 1135 km, while all other light curves begin to deviate at 1255 km.

Second from bottom: The effects of including points below the haze onset are much less drastic for r_H than λ_{Hi}. The presence of haze causes a consistent overestimation of the half-light radius.

Bottom: There is a clear slope difference between the models that include points below and above 1150 km.

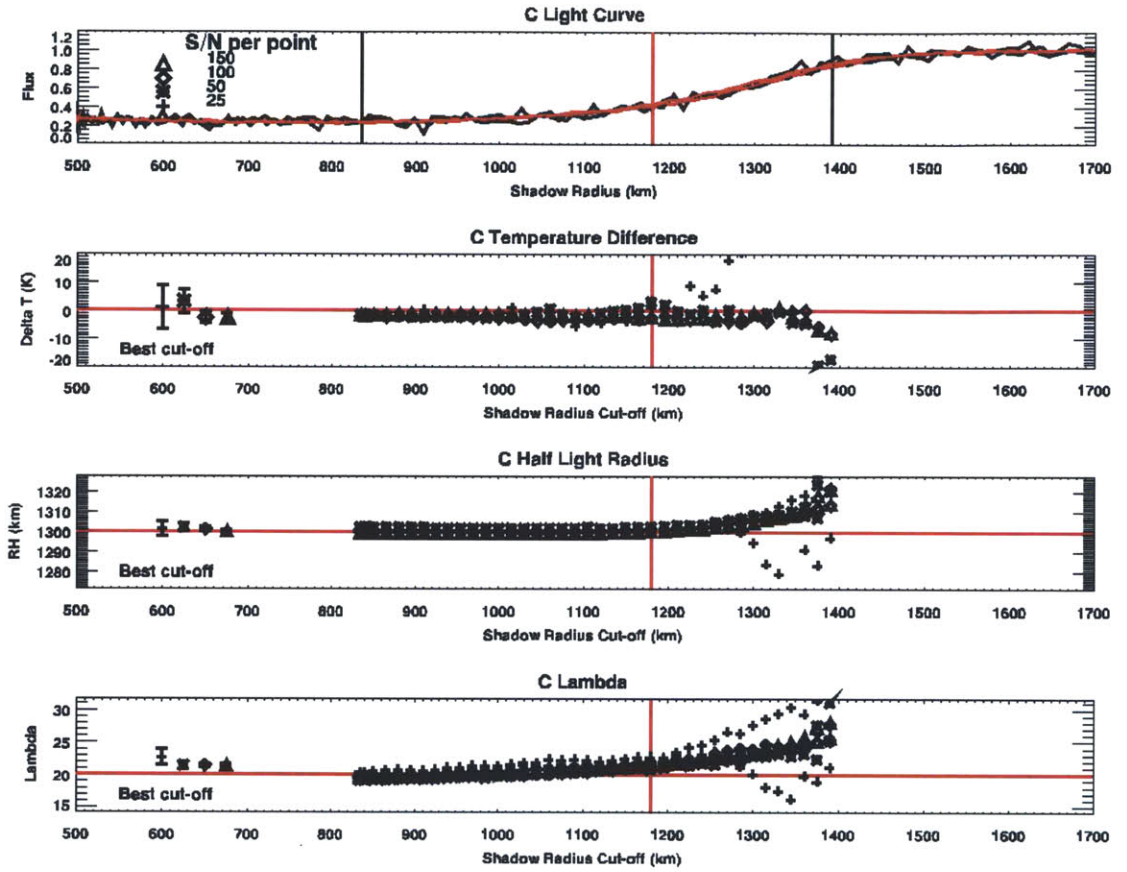

Figure 5-4: **Data Set C cut-off experiment**. See Section 5.3.3 for a description of each plot.

Top: This synthetic data set is a **refraction and thermal gradient** model with a closest approach of 500 km from an imaginary Pluto.

Second from top: For the S/N 25 light curve, the temperature difference calculation begins to deviate at 1210 km.

Second from bottom: Though subtle, the half-light radius fit output is not completely linear with cut-off radius.

Bottom: Like Data Set A, shown in Figure 5-2, which does not contain haze, there is no slope change in the values of λ_{Hi} vs cut-off. Unlike Data Set A, λ_{Hi} is not constant with time, but instead has an slight upward slope that persists until systematic effects take over, due to a smaller number of points included in the fit.

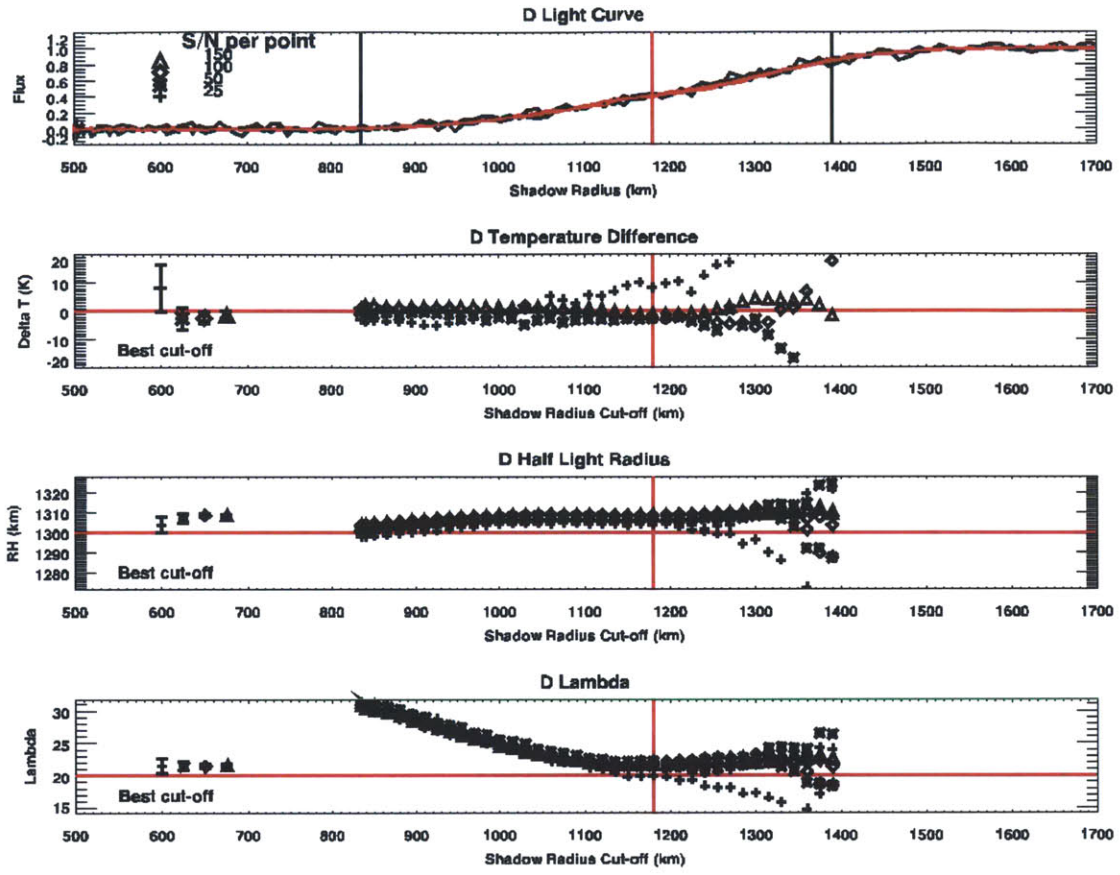

Figure 5-5: **Data Set D** cut-off experiment. See Section 5.3.3 for a description of each plot.

Top: This synthetic data set is a **refraction, haze and thermal gradient** model with a closest approach of 500 km from an imaginary Pluto.

Second from top: The temperature difference measurement reliably finds that that light curve has no temperature difference until the data divert in the low 1200s km, with the exception of S/N=25, which diverts in the 1000s km.

Second from bottom: The effects of including points below the haze onset are much less drastic for r_H than λ_{Hi}. The presence of haze causes a consistent overestimation of the half-light radius.

Bottom: There is a clear slope difference between the data that include points before and after 1150 km. The upward trend of λ_{Hi} seen in Figure 5-4 is still visible, but harder to see.

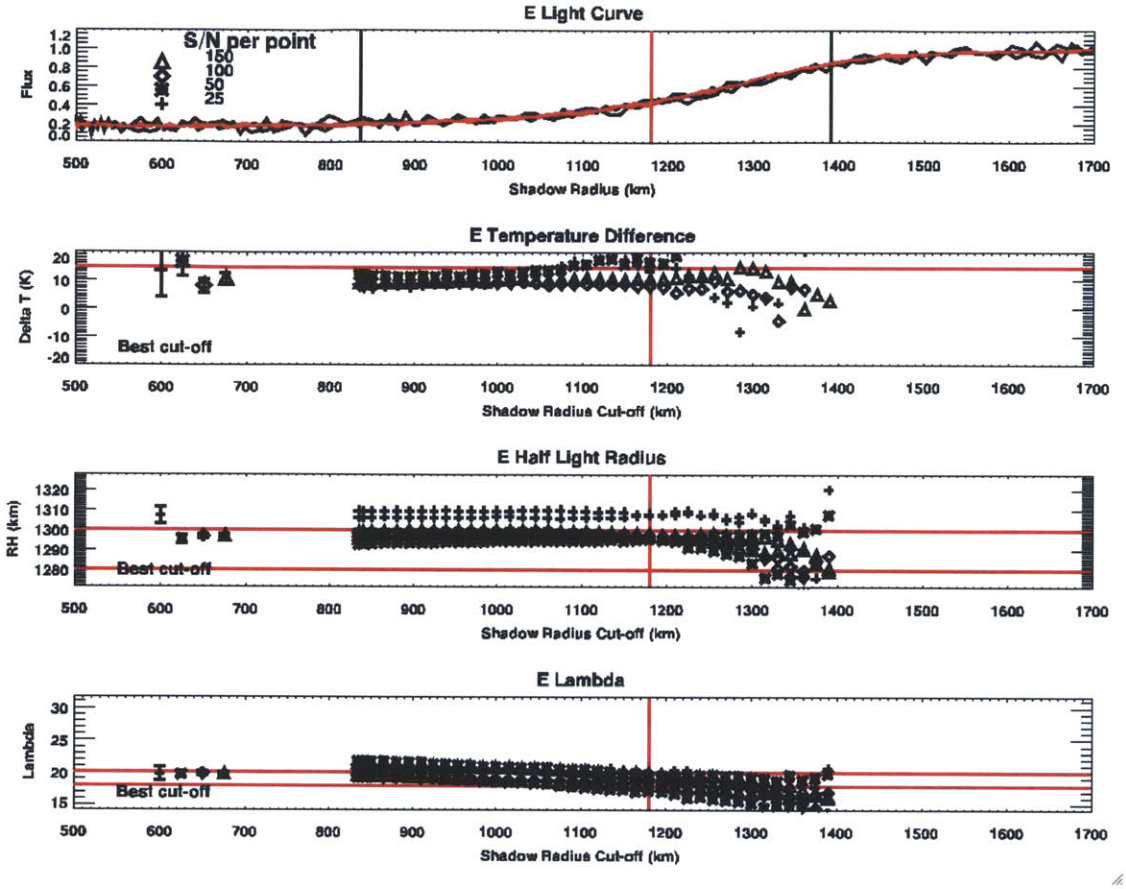

Figure 5-6: **Data Set E** cut-off experiment. See Section 5.3.3 for a description of each plot.

Top: This synthetic data set is an **asymmetric refraction-only** model with a closest approach of 500 km from an imaginary Pluto. As is true for all figures in this set, both the immersion and emersion limbs are plotted in this figure. Despite a built-in 14.5 K temperature difference, when folded, the immersion and emersion sides visually appear very similar.

Second from top: For the S/N 25 light curve, the temperature difference calculation begins to deviate at 1210 km.

Second from bottom: It is unknown why the S/N 25 curve has a larger r_H than the other light curves.

Bottom: Unlike with Data Set A, λ_{Hi} shows a slight downward slope with increasing cut-off.

Table 5.3: Chosen cut-offs versus synthetic atmosphere parameters for light curves A, B, C, D and E.

Light Curve	mid-time (s)	slope $\times 10^5$	*imm.* r_H (km)	*em.* r_H (km)	*imm.* λ_{Hi}	*em.* λ_{Hi}	*imm.* T (K)	*em.* T (K)	T_{diff} (K)
A	250.0	0.5	1300	1300	20	20	112.8	112.8	0
A25 1180	250.1±0.1	0.6±0.1	1297±4	1297±5	20±1	19±1	114±6	121±7	7±10
A50 1180	250.05±0.07	0.58±0.07	1301±2	1301±2	19.8±0.5	19.8±0.6	114±3	114±3	0±5
A100 1180	249.93±0.03	0.49±0.03	1300±1	1300±1	20.1±0.3	19.7±0.3	112±2	114±2	2±2
A150 1180	249.98±0.02	0.51±0.02	1299.8±0.6	1299.8±0.7	20.0±0.2	19.8±0.2	113.0±0.9	114±1	1±1
B	250	0.5	1300	1300	20	20	112.8	112.8	0
B25 1180	250.1±0.1	0.4±0.1	1307±4	1308±4	21±1	19.3±1.0	106±6	116±6	10±8
B50 1180	249.99±0.07	0.64±0.07	1307±2	1307±2	20.0±0.6	19.7±0.5	112±3	114±3	2±5
B100 1180	250.05±0.03	0.52±0.03	1307±1	1307±1	19.3±0.3	20.0±0.3	116±2	112±2	-4±2
B150 1180	249.98±0.02	0.46±0.02	1306.4±0.7	1306.5±0.8	20.1±0.2	19.7±0.2	112±1	114±1	2±2
C	250	0.5	1300	1300	20	20	90.3	90.3	0
C25 1180	249.7±0.1	0.5±0.1	1302±4	1301±4	23±1	22±1	99±5	101±6	1±8
C50 1180	249.90±0.07	0.49±0.07	1302±2	1302±2	21.5±0.6	20.8±0.6	105±3	108±3	3±4
C100 1180	249.98±0.03	0.49±0.04	1301±1	1301±1	21.4±0.3	21.9±0.3	105±1	103±2	-2±2
C150 1180	250.02±0.02	0.50±0.02	1300.1±0.7	1300.0±0.8	21.4±0.2	21.9±0.2	105±1	103±1	-2±2
D	250	0.5	1300	1300	20	20	90.3	90.3	0
D25 1180	249.7±0.1	0.4±0.1	1304±4	1304±4	21±1	20±1	105±6	113±6	8±8
D50 1180	249.91±0.06	0.41±0.07	1307±2	1307±2	21.5±0.6	22.1±0.6	104±3	102±3	-3±4
D100 1180	250.04±0.03	0.53±0.03	1308.6±1.0	1308±1	21.5±0.3	22.0±0.3	104±1	102±1	-2±2
D150 1180	250.02±0.02	0.48±0.02	1308.4±0.7	1308.3±0.7	21.6±0.2	21.9±0.2	103.7±1.0	102.4±1.0	-1±1
E	250	0.5	1300	1280	20	18	112.8	127.3	14.5
E25 1180	249.7±0.1	0.0±0.1	1307±4	1308±5	20±1	17.7±1.0	114±6	127±7	13±9
E50 1180	249.52±0.07	-0.11±0.07	1295±2	1296±2	19.7±0.5	17.2±0.5	115±3	132±4	17±5
E100 1180	249.55±0.04	-0.01±0.04	1297±1	1297±1	19.9±0.3	18.6±0.3	114±2	122±2	8±2
E150 1180	249.58±0.03	-0.03±0.03	1297.1±0.8	1297.7±0.8	19.8±0.2	18.1±0.2	114±1	125±1	11±2

5.4.2 Model choice vs synthetic light curve parameters

In the previous section, we have described the effects of cut-off on the occultation model outputs for five types of light curves at four different signal-to-noise ratios. Once I picked a cut-off, and recorded the fit results, MJP revealed the parameters that went into each light curve model. This section will discuss my cut-off choices, and how well the chosen model compared with the input model parameters. I will also discuss the reliability of the fits.

For light curves A-E, I chose a cut-off of 1180 km. At 1180 km, the cut-off seemed to be above the haze layer break in λ_{Hi}, or λ turn-off, described in Section 5.4.1, but still deep enough to have occurred before the noise took over (at least for light curves that had an S/N per point greater than 25, which had become unstable much lower). The three haze-less light curves did not have a clear turn-off or any sort of lower bounds, so 1180 km was chosen to be consistent with the light curves that did contain haze. The exact flux depth was not constant between curves, but ranged from 0.39 to 0.46.

Table 5.3 compares best fit results with the answers for each light curve. Overall, the models for light curves terminated at 1180 km did a reasonable job of reproducing r_H, λ_{Hi}, and ΔT, with some exceptions, which will be discussed here.

While not necessarily inaccurate thanks to large error bars, it is clear from the figures that a S/N of 25 per point is inadequate to have a reliable fit. With a few exceptions, the results for each light curve are consistent with each other, regardless of signal-to-noise ratio. For instance, it is unknown why in light curve E that the r_H values are systematically 10 km greater than other measurements.

While light curves A and B had an isothermal atmosphere, light curves C and D had a non-zero temperature exponent, revealed to be b=-2.0. For this test, the possibility of a temperature gradient was simply not considered in the modeling. Fitting the temperature gradient in non-linear least squares turns out to be an extremely unstable process with large error bars. In previous occultation fits for Pluto, such as those described by Elliot et al. (2007), several static values were chosen for b, and each set of fit results was presented. To compensate for the missing temperature gradient, the non-linear least squares fits tended to overestimate λ_{Hi} as 21 to 22, instead of 20. The gentle slope of λ_{Hi} with cut-off seen for Data Set C, shown in Figure 5-4, may be a general indicator of the presence of a thermal gradient. While I am not concerned with absolute temperature, the atmospheres with thermal gradients were measured as systematically warmer.

For light curves A and C, there is no haze component, while light curves B and D do contain a haze component. Both light curves B and D overestimate r_H. Once the λ turn-off is located, the haze does not affect the fitted value: λ_{Hi} is fit accurately for isothermal curve B, but overestimated for D, which does have a thermal gradient.

Both B and D had haze parameters (r_{τ_0}, r_{τ_1} and h_{τ_1}) of 1260 km, 1220 km and 20 km respectively. The haze onset radius of 1260 km is well below the half-light radius at 1300 km. In the shadow plane, inspection reveals the half-light radius to be at roughly 1210-1220 km, suggesting that 1180 km is at or near haze onset.

For asymmetric light curve E, the r_H value for a fit of occultation points cut-off at 1180 km is identical for both immersion and emersion. Both values hover at just under 1300 km, while one side measures 1300 km and the other measures 1280 km. In a perfect scenario, the immersion radius should be found to be larger than the emersion radius. Instead, radii are larger than the average radius of 1290

km. Interestingly enough, below about 1100 km, one radius is larger than the other. Unfortunately, the larger radius is not the immersion radius, but rather the emersion radius. This crossover is true for all S/Ns, even the oddly behaved S/N=25. The equal radii output may be explained by a shift in mid-time in the direction of the larger r_H. The relationship between r_H, and occultation mid time is discussed in greater detail in Section 5.5.2. Unlike its isothermal cousin, Data Set A, the λ_{Hi} fit for light curve E is not constant with cut-off, but instead slopes downwards with increasing cut-off. Mere chance allows the λ_{Hi} output from the 1180 km cut-off fit to match the input parameters. However, the measurements of every light-curve cut-off below about 1250 km identified the immersion side as having a larger λ_{Hi}, which translated into each model correctly predicting the emersion side as warmer. Thus, the temperature difference was at least reliably identified.

One surprise after the true numbers were revealed was the presence of a slope in the baseline equivalent to 0.00005 DN/s^2 (0.5 if the baseline is adjusted to 10,000 for fitting purposes). While not consciously considered in the design of the experiment, the baseline slope was (and always has been) an open parameter in the initial two-limb fit. The slope was accurately fit for light curves A-D, but fits for light curve E erroneously reported slopes consistent with 0 (see Table 5.3).

Always assuming one does not cut off the light curve too high in the atmosphere, fits of the synthetic light curves show clear trends in the reproduction of the input parameters, with the exception of the curves of S/N per point of 25. For a symmetric isothermal, haze-free light curve, the input parameters can be recovered at any lower depth. Light-curves with haze must be cut-off above the point at which the change in the energy ratio, λ_{Hi}, begins to level off with increasing cut-off depth. From that point, λ_{Hi} will be reproduced accurately, but the half-light radius will be slightly over-estimated with an atmosphere containing haze. For atmospheres with a temperature gradient of b=-2.0, λ_{Hi} and absolute temperature are not measured accurately when an isothermal atmosphere is assumed. For asymmetric light-light curves, the mid-time, and baseline slope are never properly fitted. Despite these problems, temperature asymmetries (or lack thereof) are consistently identified.

5.4.3 S/N threshold for asymmetry measurements

As seen in Figures 5-2 through 5-6, and Table 5.3, an S/N of 25 is simply not enough to determine a temperature difference or have a good cut off above the haze threshold. Of the five light curves with the lowest S/N, two diverge almost completely from the group solution at very low-cutoffs. Thus, any data set with a similar S/N cannot be trusted.

However, the S/N used denote the amount of Gaussian noise in these models reflects S/N per point. The signal-to-noise variation is based on the calculating the standard deviation of points that make up the occultation baseline, with no regard to the resolution of the light curve. More images may make up the same distance in the atmosphere when comparing one occultation light curve to another, due to differences in cycle time or Pluto velocity. The *signal-to-noise per scale height*, or S/N per scale height is considered a "figure of merit" for occultation light curves (Harrington & French, 2010). It takes into account exposure time, object velocity, location in the atmosphere and scale height. Defined as ϵ_ϕ^{-1}, it takes the form

$$\epsilon_\phi = \epsilon\sqrt{v_\perp / H} \tag{5.2}$$

where ϵ is the "standard deviation of the unocculted stellar flux in one-second bins divided by its mean", H is the scale height and $v_\perp$ is the component of the shadow velocity perpendicular to Pluto's surface (Harrington & French, 2010; French et al., 1978). One should not confuse $v_\perp$ with the velocity of the occulting body in the sky plane (v). Rather, $v_\perp$ is the component of this velocity that points toward the center of the planet or vertically in Pluto's atmosphere. Its companion, $v_\parallel$, represents the horizontal component. As the component velocities are constantly changing, we choose the half light radius in the shadow plane (ρ_H) to calculate $v_\perp$ as

$$v_\perp = v\cos\left(\sin^{-1}\left(\frac{\rho_{min}}{\rho_H}\right)\right) \tag{5.3}$$

where ρ_{min} is the closest approach. A graze occultation will have a larger horizontal component in the atmosphere compared to an occultation that is observed at the

centerline. While centerline observers may see a scientifically desirable central flash, those who observe a graze (or other non-central chord) get a higher resolution peek into Pluto's atmosphere.

Table 5.4 calculates the three types of S/N for each light-curve, (S/N per point, ϵ^{-1}, and ϵ_{ϕ}^{-1}) for each of the synthetic light curves (including light curve F, which will be discussed in the following section). The S/N levels used to name the light curves reflect nominal noise added to each light curve during creation. The actual noise measured from the baseline may differ slightly. Because ϵ_{ϕ}^{-1} relies on the scale height, itself a function of λ_{IIi} and r_{II}, it is highly dependent on the fit that created those numbers, and may vary from fit to fit (and noise addition to noise addition). Thus the numbers in Table 5.4 represent values calculated using the results from the chosen cut-off fits. In any case, it is safe to generalize that an S/N per scale height of 50 corresponds to a light curve similar in quality to the curves with an S/N per point of 25, and an S/N per scale height of 100 corresponds to a light curve similar in quality to the curves with an S/N per point of 50. In any event, curves $\epsilon_{\phi}^{-1} < 50$ should be treated as suspect and $\epsilon_{\phi}^{-1} < 100$ treated with caution.

In Table 5.5 we present the S/N measurements for all light curves included in this study, as well as some that were disbanded. These light curves are described in the next chapter. Using our criterion of $\epsilon_{\phi}^{-1} < 50$, we have eliminated the Black Springs, ATOM, and Aloe Ridge light curves. Our stricter criterion, $\epsilon_{\phi}^{-1} < 100$, calls the results for the SOFIA Blue light curve, USNO, Siding Springs and UH 2.2-m into suspicion. While the SOFIA Blue, Black Springs and Siding Springs light curves appear at first considered to be higher quality than the data taken at the USNO for P445.3, the slow velocity and graze status boost the USNO curve to have a much higher ϵ_{ϕ}^{-1}. Thus, I have decided to keep the USNO light-curve in the study, but remove the others.

Table 5.4: S/N for synthetic light curves

Model	S/N Added	S/N per point	ϵ^{-1}	ϵ_ϕ^{-1}
A	25	24	33	57
	50	45	58	98
	100	85	102	173
	150	106	122	206
B	25	25	35	61
	50	44	56	96
	100	85	108	185
	150	113	132	226
C	25	25	37	59
	50	46	61	99
	100	82	101	163
	150	101	116	187
D	25	25	347	56
	50	48	69	112
	100	85	103	167
	150	108	124	201
E	25	25	38	65
	50	50	68	121
	100	102	147	256
	150	149	213	371
F	50	49	70	122

Table 5.5: S/N for observed light curves

Event	Telescope	S/N per point	ϵ^{-1}	ϵ_ϕ^{-1}	In Ch. 6
P8	KAOss	30	72	155	yes
P131.1	CFHT	61	61	185	yes
	UH2.2m	26	32	104	yes
P384.2	AAT	63	143	251	yes
	BS	16	20	33	no
	SS	14	31	52	no
P445.3	MMT	60	88	-‡	no
	Hall	24	24	114	yes
	USNO	16	20	87	yes
	USNO†	14	17	73	no
PC20110623	MORIS	46	74	231	yes
	SOFIAfdc	48	89	153	yes
	SOFIAred	61	84	144	yes
	SOFIAred†	50	68	118	no
	SOFIAblue	36	37	64	no
	SOFIAblue†	31	35	59	no

† Alternate reduction.

‡ ϵ_ϕ^{-1} is calculated at the half flux shadow radius. For this curve, the flux level simply does not reach that low.

5.5 Synthetic light curves tests, models F (model consistency test)

5.5.1 Model fit results vs cut-off

While illuminating, the analysis of light-curves A-E lacked two major components. Firstly, as it is likely all our occultation light curves have some sort of haze or thermal gradient, failing to consider an asymmetric light curve with a haze layer would be a serious oversight. Secondly, each light curve/S/N type had only one version. What variation would exist between two light curves of the same atmospheric type? Thus light curve F represents an asymmetric light curve with a haze layer. A full 100 versions were made and fit based on the parameters of Data Set F. Noise of S/N per point of 50 was added for each light curve.

The model results as a function of cut-off are displayed in Figure 5-7. As with models B and D, there is a λ turn off at a lower cut-offs. As with all the other models, there are increasingly large errors (in the form of greater scatter) as the cut-off becomes more shallow. The temperature difference is near zero at low cut-offs, then favors a warmer emersion temperature as the cut-off escapes the haze layer. With more points, we can see a clearer correlation between changes in r_H with the presence of haze than in previous light curves. However, λ_{Hi} is still the most reliable indicator of the cut-off choice. Here, the choice of cut-off is extremely important. The temperature difference calculated from a light curve that includes haze, is not only different from one that does not, but inaccurately reflects the upper atmosphere.

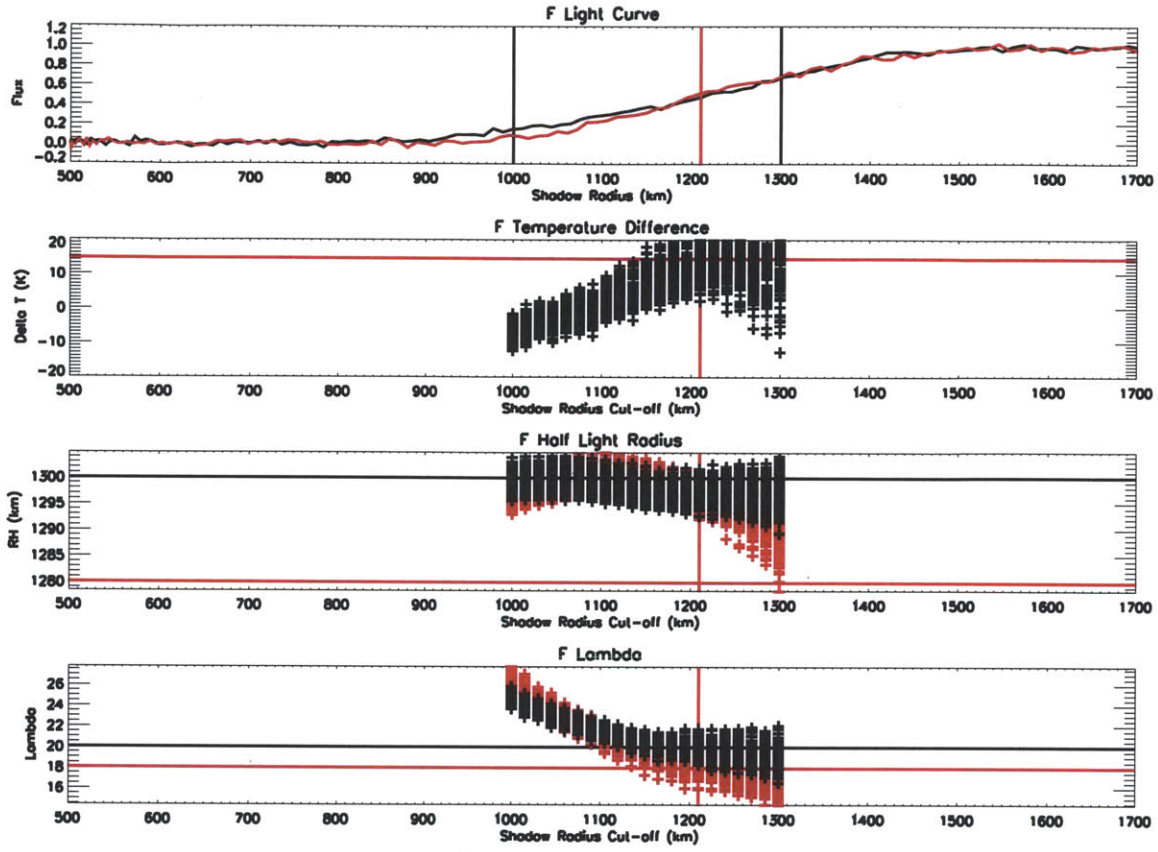

Figure 5-7: **Data Set F** cut-off experiment.
Top: This synthetic data set is an **isothermal, asymmetric haze model** with a closest approach of 500 km from an imaginary Pluto. This is only one of 100 curves with noise of S/N 50 per point added. The immersion is plotted in black, while emersion is plotted in red. The difference between the two curves us most apparent in the lower atmosphere.
Second from top: The temperature difference is highly dependent on cut-off, showing a warmer immersion while a more shallow cut-offs show a cooler immersion.
Second from bottom: The half-light radii both converge to a value that is slightly smaller than the larger immersion radius.
Bottom: Below about 1200 km, the value for λ_{Hi} rapidly increases, while it levels off above that level, as the haze disappears in the model light curve.

5.5.2 Model choice vs synthetic light curve parameters

Based on the stabilization of λ_{Hi} after about 1200 km, the cut-off level of 1210 km was chosen as the "good" cut-off for light curve F. The flux level for the immersion side was 0.47, while the emersion flux level was 0.52. A simple arithmetic mean of the 100 results of r_H, λ_{Hi}, T, and T_{diff} and their standard deviations were taken. Having chosen a cut-off, we seek the input values that generated the light curve, which were previously unknown. In Table 5.6, I compare the chosen cut-off's average model results against the revealed input model parameters. We find that the average model fits do an excellent job of reproducing the model parameters, save for the half light-radius (typical for both a case with haze, and a case with asymmetry), confirming 1210 km as an excellent choice of cut-off. At 1210 km, the temperature difference of 13.7±5.6 K accurately and significantly predicts the temperature difference of 14.5 K. This temperature difference is based on the determination of the difference in λ_{Hi} between the two halves of the light curve, not r_H, which was fit to be identical between the two curves.

Table 5.6: Mean model output values Light Curve F

Light Curve	mid-time	imm. r_H	em. r_H	imm. λ_{Hi}	em. λ_{Hi}	imm. T	em. T	T_{diff}
Model Input	250	1300	1280	20	18	112.8	127.3	14.5
F results at 1210 km	249.6	1298 ± 2	1297 ± 3	19.9 ± 0.6	17.8± 0.6	113.8 ± 3.6	127.6 ± 4.3	13.7± 5.6

What about the half-light radius? For the immersion, the model accurately measures the 1300 km half-light radius, albeit with a slight under-measurement. The emersion model over-measures the 1280 km half light radius, and not slightly, though the inflation may be a result of the haze, as both fits for the two other light curves with haze (B and D) over-estimated the half-light radius. Additionally, the light curve models are not designed to be discontinuous. To make the asymmetric light curves, two separate symmetric models were created. Each light curve was split and one side from each curve was joined at the mid time. During fitting, the mid time that was initially calculated using both curves, and fixed for the single-sided fits is not accurate. Instead of the highly symmetric 250 s mid time, the single-sided fits were locked into a mid time of 249.6 s. With a velocity of 25 km/s, this 0.4 s difference translates

into a 10 km offset, exactly sufficient to be the average mid time of an occultation of r_H 1280 km on one side and 1300 km on the other, with an average r_H of 1290 km. A run with the fixed proper mid-point was not performed.

While Data Set F shares all the issues that plagued the data-sets with asymmetry and haze, and fails to fit r_H or the mid-time, an accurate temperature difference is found at the chosen cut-off. The 100 light curves fit show the full range of fits betray an underlying pattern that show the best fit is just above any haze.

5.5.3 Internal vs external errors

With Pluto occultation data, we do not have the luxury of 100 light curves for a single event. Would another telescope observing the same occultation on the same day see the same temperature difference? Rather, we must rely on the errors provided from the covariance matrices on the non-linear least squares fits, or the *internal error*. The internal errors are calculated using the covariance matrix produced by the final iteration of the non-least squares fit[5]. The errors quoted in Table 5.6 are average of the internal errors. The *external errors* are calculated by taking the standard deviation of several measurements of a quantity, in this case the temperature output. At the 1210 km cut-off, the standard deviation of all 100 model outputs for the important light curve parameters was taken and compared against the average model error output. See Table 5.7 for a comparison of internal and external errors. For all r_H, λ_{Hi}, T and T_{diff}, the internal and external errors match well.

Table 5.7: External error vs internal error for light curve F and a cut-off value of 1210 km.

Parameter	Mean model output	Average internal error (mean output model error)	Average external error (stdev of model output for 1210 km)
$imm.\ r_H$	1298	2.2	1.8
$em.\ r_H$	1297	2.5	1.9
$imm.\ \lambda_{Hi}$	19.9	0.62	0.72
$em.\ \lambda_{Hi}$	17.8	0.59	0.64
$imm.\ T$	113.8	3.6	4.1
$em.\ T$	127.6	4.3	4.6
T_{diff}	13.7	5.6	5.5

[5]Providing errors for the covariance matrix is another reason why all parameters are left free during the last iteration, as described in 5.1.3.

Do these errors, especially the temperature error calculation, match what is predicted by analytical methods? Beginning with the light curve equation of Baum & Code (1953):

$$v_\perp(t - t_0)/H = (1/\phi - 2) + \ln(1/\phi - 1) \tag{5.4}$$

where ϕ is the normalized and calibrated flux, French et al. (1978) predict the error of scale height, H for a fit to an isothermal light curve with no cut-off. The fractional error in scale height is

$$\frac{\sigma(H)}{H} = \frac{(c_{t_0}/d)^{1/2}}{H} \tag{5.5}$$

where

$$d = c_H c_{t_0} - c_{Ht_0}^2, \tag{5.6}$$

$$c_{t_0} = [v_\perp/(H\epsilon^2(\phi))] \int_0^1 \phi^2(1-\phi)d\phi, \tag{5.7}$$

$$c_H = [1/(v_\perp H\epsilon^2(\phi))]^2 \int_0^1 [(1/\phi - 2) + \ln(1/\phi - 1)]^2\phi^2(1-\phi)d\phi, \tag{5.8}$$

$$c_{Ht_0} = [1/(H\epsilon^2(\phi))]^2 \int_0^1 [(1/\phi - 2) + \ln(1/\phi - 1)]\phi^2(1-\phi)d\phi. \tag{5.9}$$

Thus, the fractional scale height is

$$\frac{\sigma(H)}{H} = 1.54(v_\perp/H)^{1/2}\epsilon(\phi). \tag{5.10}$$

As seen in Section 5.4.3, $(v_\perp/H)^{1/2}\epsilon(\phi)$ is the inverse of S/N per scale height. Thus, if light curve has a S/N per scale height of 100, then $(v_\perp/H)^{1/2}\epsilon(\phi) = 0.01$, then the fractional error in scale height should equal 0.0154. Assuming that the error from the Pluto's gravity g does not contribute to the error of the temperature calculation (see Equation 5.1), then the error in an individual temperature measurement is simply proportional to the fractional error in scale height. Thus, the temperature

measurement error for a 100 K light curve should be 1.54 K, and the error on a temperature difference should be $1.54\sqrt{2}$ K .

However, these error figures assume that the entire light curve is fit. To replicate the cut-off, the lower limit of 0 flux for each integral in equations 5.7 to 5.9 is replaced with the minimum flux of the cut-off. Figure 5-8 shows the fractional error for each cut-off level. As seen with the synthetic data, the fractional error increases with increasingly shallower cut-offs.

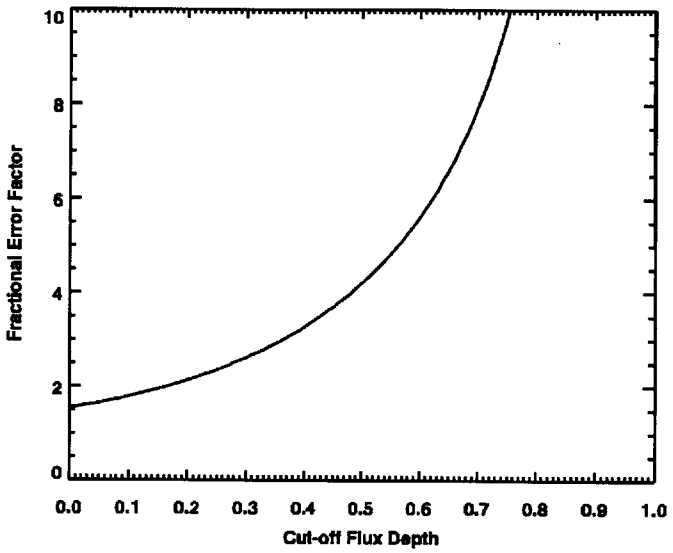

Figure 5-8: Change in fractional analytic error in scale height based on minimum flux of a light curve cut-off. To calculate the fractional analytic scale height error, divide by the S/N per scale height.

How do the temperature errors compare with the internal and external errors? For light curve F, the model flux of the chosen cut-off at 1210 km terminates at 0.47 for the immersion limb and 0.52 for the emersion limb. The average S/N per scale height is 122. Based on the curve in Figure 5-8, the immersion limb has fractional error of 3.8 divided by the S/N per scale height, while the emersion limb's fractional error is 4.4 divided by the S/N per scale height. Combined with respective mean temperature outputs of 113.8 K and 127.6 K, the predicted temperature difference error is 6.0 K. This internal error is comparable to, though slightly larger than, the average internal temperature difference error of 5.6 K and the average external error of 5.5 K. Thus, our reported errors do not disagree substantially from theoretical estimates.

5.6 Impact parameter offset analysis

While I will only discuss a single light curve from some occultation events in Chapter 6, every occultation in this paper was successfully observed from more than one station. As big telescopes are in short supply and usually located under the occultation shadow tracks by sheer luck, not portability, there are usually only 1-2 excellent light curves per event, even though many more light-curves may have been observed. The other light curves, while carefully measured and observed, have a lower signal-to-noise ratio, and were not included in the study. See Section 5.4.3 for a rigorous determination of appropriate S/N for this study. However, despite being found to have inadequate S/N to make a definitive declaration of whether a temperature asymmetry could be measured, the timings derived from lower S/N light curves are essential to reconstructing the astrometry of the event to determine the closest approach radius of Pluto's center for each station.

While every measurement has its error bar, the accuracy of impact parameter measurement is affected by the location of successful observing stations for each event (Person, 2012). For example, observations of the PC20100704 were limited to the north side of the occultation centerline, while observations of the P445.3 were limited to the south of the centerline. In addition to ground-based biases, the impact parameter for the KAO observations was not initially well-constrained due to equipment issues. It was estimated that the impact parameter had a systematic error as large as 20 km (Elliot et al., 1989). No other occultation light curve is suspected to have errors as large as P8.

During fitting, the occultation station impact parameter was assumed to be constant, known *a priori*, and treated as a quantity without an error bar. Identified as a cause for concern, the temperature difference as related to impact parameter was examined in detail. Thus, I aim to answer the question, "What happens to the temperature difference between immersion and emersion if another impact parameter is substituted?"

For this analysis, the observed occultation light curves (and some alternate reduc-

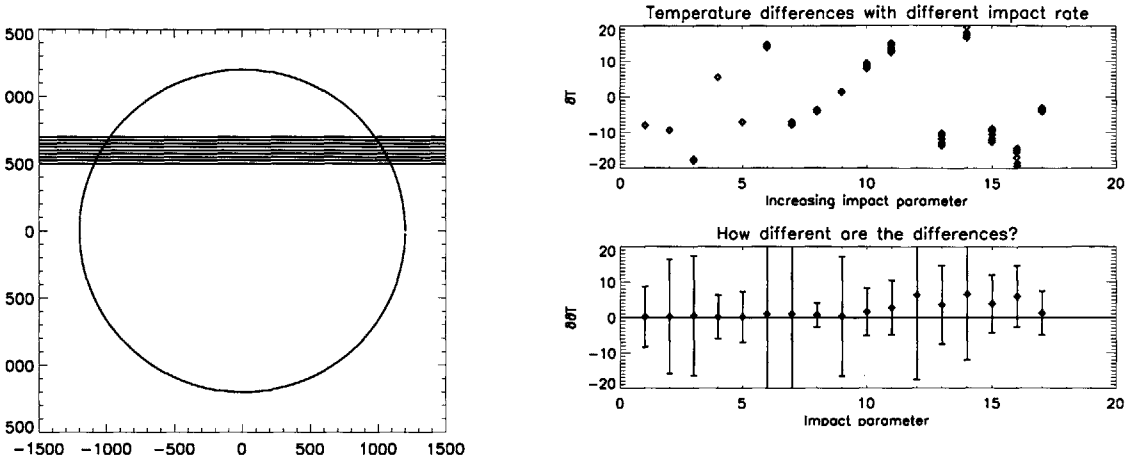

Figure 5-9: This analysis seeks to study the effects of a false impact parameter on the derived temperature difference.
Left: Schematic of runs made to check errors in impact parameter. Each occultation light curve was fit at a differing closest approach level.
Right Top: Temperature difference versus event. Scatter plot of 17 different curves' temperature *differences* for 0 $\pm$50, $\pm$75 and $\pm$100 km from its original *a priori* closest approach value. Error bars are omitted for clarity. In the perfect situation, each of the 17 curves would appear to have a single point, and the seven different points per event would not be scattered.
Right Bottom: Difference between the calculated temperature difference with a 100 km offset from the known closest approach and the temperature difference with a -100 km offset. Error bars corresponding to 1σ propagated from this difference of differences have been included. The independent axis refers to an individual light curve, ordered in the same manner as above. If an offset in closest approach had no effect on the temperature difference, then this difference of differences should be zero. Each difference of temperature differences has no significant deviation from zero. Thus, an error in the closest approach should not significantly alter the conclusions for each light curve.

tions) from each event were used. Each value of closest approach was adjusted both north and south by 50, 75 and 100 km, for total a range of 200 km. See Figure 5-9 for an explanation. A single cut-off, 1210 km, was chosen for each light curve and an isothermal fits were performed. Each light curve was fit using the non-linear least squares method described in Section 5.1.3.

In absolute terms, atmosphere temperatures became colder as an occultation chord is shifted away from its centerline. Here, we care only for the temperature difference between immersion and emersion. The differences in temperature at different impact parameters are plotted atop each other for each event in Figure 5-9. While the temperature differences are scattered for each event, they display a remarkable consistency not shown by any cut-off test. Figure 5-9 also shows the difference between the temperature difference at +100 km and the temperature difference at -100 km with error. For every light curve, the two extreme shifts have a temperature difference that agrees with zero within the error bars. Light curves that were more graze-like had less consistent temperature differences between the +100 km and -100 km offsets. A measurement with a 1-σ error bar should agree with its true value approximately 68% of the time. Here, the 1-σ error bars match with no change 100% of the time.

In general, any temperature difference would become stronger as the impact parameter was moved toward the centerline (possibly a mathematical consequence of the temperature increasing as the light curve was marked as closer to the centerline.). Overall, due to the agreement between the -100 km and 100 km offsets for all actual light curves, it is safe to discount what would be much much smaller errors in the reckoning of the closest approach. While a closest approach measurement could be inaccurate for some unknown reason, I do not predict that it will bias the determination of whether one limb of Pluto has a warmer temperature than the other.

5.7 Conclusions

Fits of the EY92 model were carried on out six different light curve simulations, and varied signal-to-noise ratios. Additionally, the data discussed in the next Chapter

were used to test the importance of an accurately determined impact parameter. A summary of the conclusions is as follows:

1. The light curves with S/N *per point* of 25 are too noisy to make reliable measurements of the occultation parameters, above an S/N per point of 50 the measurements are precise enough. Using S/N *per scale height* as the standard, a reliable S/N per scale height limit is somewhere between 50 and 100. I have identified light curves below this limit, and excluded them from the analysis in the following chapters.

2. In a haze-less, symmetric, isothermal atmosphere, the fits to synthetic occultation light curves can accurately reproduce the parameters used to create them. However, modeling a non-isothermal atmosphere as isothermal will fail to reproduce λ_{Hi} and T, while excluding haze in atmosphere with haze will over-estimate r_H. For an asymmetric model, an atmosphere with a extended radius on one side will not be recognized by the modeling process. Nor will the baseline slope or mid time be properly fit. However, the modeling process does reliably identify temperature asymmetries (or lacks thereof) in the models.

3. When determining the temperature, an accurate determination of λ_{Hi} has larger influence on results than an accurate determination of the half light radius. An optimal cut-off occurs above the λ turn-off, the point at which λ_{Hi} no longer decreases with increasing cut-off. Cutting off a light curve too high in the upper atmosphere will result in an imprecise fit. For an asymmetric light curve with haze, a poor choice of cut-off will not reproduce the temperature asymmetry.

4. The internal errors for the EY92 derived from covariance matrices match well with the external errors derived from sampling many model light curves.

5. While important to the absolute temperature results for an occultation light curve, a 200 km error in the measurement of an observing station's impact parameter does not have a significant effect on the temperature difference results.

The tests of synthetic light curves A-F have given interesting insight into the process of occultation fitting. In an idealized world, the cut-off choice would not affect the results of the occultation light curve. Instead we find that the appropriate cut-off range has both a lower and upper bounds– the lower the cut-off, the lower the error, however, cut-offs must be above any significant haze.

For asymmetric curves, the best fit did not properly measure the (rather large) asymmetry in r_H. The mid-time was found to be an average of two unequally-sized curves, instead of the true mid-time. In data where the midpoint is unknown, it will be difficult to spot a bulge on one side of one light curve of Pluto. This light curve may be slightly off the best fit circle, or in the case of very few light curves, dominate the determination of the best fit circle. The 20 km difference in half light radius, altered the mid time by less than one frame. Errors in timing are very easily attributed in the scientist's mind to faulty camera start times. Additionally, a start time error of one frame was found in the P445.3 USNO light curve (see Section 6.5). Thus, an asymmetric r_H may never be detected. In any event, a change in λ_{Hi} has a far greater effect on temperature than r_H, and is consequently more useful in determining the temperature difference. Fortunately, the model fits are much more reliable at determining differences in λ_{Hi}!

These tests do not cover every possible scenario. For instance, non-isothermal light curves were not considered as part of testing, even though they were included for curves C and D.

The experiments using light curve F inspire confidence in the methods used for fitting the light curve. Even though the temperature difference jumps from one side being warmer to the other as the cut-off increases, the model at the chosen cut-off accurately predicts the 14.5 K difference built into the model at a greater than 2 sigma level. Thus, the λ turn-off can be sought after to find the proper cut-off.

Thus, if we use λ_{Hi} as a vehicle to determine the cut-off, and a temperature difference measurement of 13±5 K is found, one can assert that that value reflects a temperature asymmetry in the light curve.

Chapter 6

Temperature asymmetries in Pluto stellar occultation light curves II: Best fit modeling

6.1 Introduction

This chapter is the second of three related chapters exploring asymmetries between immersion and emersion limbs of Pluto occultation light curves, and the degree to which the location probed on Pluto affects any temperature asymmetry seen or not seen. Using the methodology derived in the previous chapter, this chapter takes nine Pluto occultation light curves, spanning a range in years from 1988 to 2011 and examines separate fits of the immersion and emersion limb to determine whether a significant temperature difference exists between the two limbs. This chapter will focus on the light curves themselves and the reliability of each light curve fit. The third and final asymmetry chapter will focus on the physical significance of any light curve temperature differences.

6.1.1 Occultation light curve selection

To be considered for inclusion in this study, a Pluto occultation light curve had to meet all of the following criteria:

- Most importantly, the light curve had to be available for use in this study. While I have access to every Pluto occultation light curve observed by the MIT's Planetary Astronomy Laboratory, I do not necessarily have access to light curves obtained by other groups. For some occultations, I was able to obtain high-quality light curves from competing groups that had already been published. In other cases, I was able to obtain unpublished light curves of comparatively lower quality in hopes that they would see scientific use. There are several light curves that would have been extremely suitable for this study, but were unable to be obtained because these observations are awaiting further studies by the people who observed them. A full list of potentially useful light curves can be found in Section 6.8.

- The impact parameter of the light curve relative to Pluto's center in the shadow path had to be previously known. In the case of where a light curve was provided by an outside group, the closest approach to Pluto's center was recalculated relative to the solution published by MIT PAL. The precision of these events was on the order of a few kilometers. The effects of an inaccurate determination of the impact parameter of up to 100 km in either direction was found to be irrelevant for asymmetrical analyses in Section 5.6. Nevertheless, events with single-chord observations, or incomplete global astrometric solutions were not considered.

- An event had to be fully observed. Pasachoff et al. (2005) and Person et al. (2008) display tantalizingly high signal-to-noise occultation observations from the 3.67-m AEOS telescope and the 8.4-m LBTO that have only one limb of the planet observed. These observations are simply unsuitable for a study that compares immersion and emersion limbs of an occultation.

- The occultation light curve had to be of reasonably good quality. When I began to collect light curves from MIT PAL's archives, I had hoped to include every light curve in the backlog, poor quality or not. Attempts to model the low signal-to-noise P131.1 UH 0.6-m light curve were met with several repeated program crashes, so this light curve and the paradigm of including every possible light curve were abandoned.[1] Several less well-studied observations were added to the program and modeled successfully. However, these light curves were later removed based on the minimum S/N per scale height recommendations laid out in Section 5.4.3. Light curves successfully modeled but later removed due to signal-to-noise will be mentioned below to differentiate between light curves that were not included in this study, and light curves that were overlooked or not initially considered.

- A graze occultation light curve had to penetrate deeply enough into Pluto's atmosphere such that an optimal upper atmosphere observation cut-off determination could be made. See Chapter 5 for an in depth discussion of cut-offs.

If an observation met all of the above criteria, the light curve was included in the study. In the end, 18 light curves were selected for preliminary fits. Table 5.5 lists these light curves and their signal-to-noise ratios. Of these 18 light curves, three light curves were lower signal-to-noise alternate reductions (see Section 6.9 for more detail), one (MMT) was eliminated because it was too shallow, and five (Black Springs, Siding Springs, ATOM, Aloe Ridge and SOFIA blue) were eliminated due to inadequate S/N per scale height as outlined in Section 5.4.3. The nine remaining light curves span five events, and will be referred to as P8 KAO, P131.1 UH2.2-m, P131.1 CFHT, P384.2 AAT, P445.3 USNO, P445.3 Hall, PC20110623 MORIS, PC20110623 FDC and PC20110623 SOFIA red.

[1]While several other rejected light curves will appear in this text from time to time, the 0.6-m light curve was discarded too early in the fitting processes to be included elsewhere in the text, specifically the impact parameter study described in Section 5.6, which made use of several other rejected light curves. These light curves have sets of fits nearly equal in scope to their fully analyzed brethren.

6.1.2 Occultation light curve formatting and fixed parameters

The light curves to be analyzed were transformed into a file containing only modified Julian date, and normalized, calibrated flux. An occultation light curve is said to be *normalized* if its baseline, that is the flux from Pluto and the unocculted star together, is set to 1. Normalization is usually accomplished by dividing the entire light curve by the occultation baseline. An occultation light curve is said to *calibrated* when an occultation flux of 0 represents complete extinction of the occulted star, which will not occur with a grazing occultation. The contribution of light from Pluto is subtracted from both the regular flux and the normalized baseline. Calibration usually requires observations of Pluto or the occultation star with enough separation between them so that aperture photometry can be performed, ideally a few hours before the event. From separate photometry, a *background fraction* can be determined. The background fraction is equal to

$$bf = \frac{F_{Pluto}}{F_* + F_{Pluto}} \tag{6.1}$$

where F is the separate flux of Pluto and the occultation star. After the background fraction is calculated, normalized and calibrated flux ("normcalflux") of each image (denoted with i) is calculated from the uncalibrated, unnormalized light curve flux ("flux") by the following formula:

$$normCalFlux_i = \frac{(flux_i - bf * mean(flux[doesNotContainOccultation])}{(1 - bf) * mean(flux[doesNotContainOccultation]))} \tag{6.2}$$

Some light curves were previously normalized and calibrated; for others, this process was performed on the provided light curve. Table 6.1 lists the background fractions and their source.

The MJD exposure mid-time was transformed to seconds since the lowest hour of the first exposure. That is to say if the first image had a mid-time of 11:10:15, the first image's timing would be 615 s (seconds since 11:00). Based on an approximate

Table 6.1: Background Fractions.

Event	Background Fraction
P8 KAO	previously normalized
P131.1 UH 2.2-m	previously normalized
P131.1 CFHT	0.79 (B. Sicardy)
P384.2 BS	0.6796
P384.2 SS	0.6880
P384.2 AAT	previously normalized
P445.3 USNO	0.6869
P445.3 Hall	0.6869
P445.3 MMT	0.6932
PC20100704 AR	0.52
PC20100704 ATOM	0.649
PC20110623 MORIS	previously normalized
PC20110623 SOFIAred	previously normalized
PC20110623 SOFIAfdc	previously normalized
PC20110623 SOFIAblue	previously normalized

mid-time, the closest approach of the star to Pluto's center, and the event velocity, the distance of the star from Pluto's center in kilometers was calculated for each point. Only points with a distance from Pluto's center greater than a particular minimum, labeled in this chapter as the **cut-off** were considered. The mid-times used for this initial calculation are approximations based on prior fit results. However, the distance from Pluto's center in shadow radius space was re-calculated with the newly fit mid-time for the two-limb fits, and the light curve cut-offs points were re-defined. The closest approach to Pluto and event velocity were taken from previously performed fits and calculations, and were treated as perfectly known quantities. Effects of uncertainty in the former is discussed in detail in Section 5.6, while the latter are calculated directly from ephemerides and do not change with distance from Pluto's center. Table 6.2 lists the closest approaches and event velocities used. For each light curve, the starting point and duration of the occultation (in camera images) were designated by hand. The number of points that comprised the occultation baseline varied immensely among the light curves, from very little (KAO, CFHT) to extensive observations before and after the event (USNO, MMT). As the baseline level varies with the separation between Pluto and the occultation star, an overly-long baseline will not improve an occultation fit. Thus long occultation baselines were trimmed

to be equal in points on either side to the number of images comprised the occultation. For each light curve, a file listing the light curve, event velocity, location of the event, exposure time and identification data was created along with a list of starting parameters. From there, the best-fit model light curve based on the model described EY92 was found using non-linear least squares fits.

Table 6.2: Fixed closest approach and event velocity values used for each event.

Event	Closest Approach	CA Source	Event Velocity	EV Source
P8 KAO	865.69 km	Elliot et al. (2003a)	18.45 km s^{-1}	Elliot et al. (1989)
P131.1 UH 2.2-m	597 km	Elliot et al. (2003b)	6.8489 km s^{-1}	Elliot et al. (2003b)
P131.1 CFHT	597 km	set to UH 2.2-m CA	6.8489 km s^{-1}	set to UH 2.2-m EV
P384.2 BS	414.74 km	PAL fitting notebook	24.0157 km s^{-1}	PAL fitting notebook
P384.2 SS	570.094 km	PAL fitting notebook	23.9964 km s^{-1}	PAL fitting notebook
P384.2 AAT	570.094 km	set to SS	23.9903 km s^{-1}	provided in light curve file
P445.3 USNO	-1102.0 km	Person et al. (2008)	6.78 km s^{-1}	Zuluaga (2007)
P445.3 Hall	-1108.0 km	Zuluaga (2012)	6.78 km s^{-1}	set to USNO.
P445.3 MMT	-1319.0 km	Person et al. (2008)	6.77 km s^{-1}	Zuluaga (2007)
PC20100704 AR	141 km	Person (2012)	23.78 km s^{-1}	provided in light curve file
PC20100704 ATOM	775.349 km	PAL fitting notebook	23.89 km s^{-1}	Zuluaga (2010)
PC20110623 MORIS	1135.73 km	Person (2012)	24.2 km s^{-1}	Person (2012)
PC20110623 SOFIAred	104.33 km	Person (2012)	24.03 km s^{-1}	Person (2012)
PC20110623 SOFIAfdc	"	"	"	"
PC20110623 SOFIAblue	"	"	"	"

6.1.3 Light curve modeling procedure

Using the procedure described in detail in Section 5.1.3, separate best fit model light curves for the immersion and emersion side were created for each light curve. Light curve models were run with the upper atmosphere cut-off points ranging from 1000 km to 1300 km from Pluto's center with a resolution of 15 kilometers. A single, "best" atmospheric depth was chosen based on combination of four factors:

- The atmospheric cut-off should be at least 15 km above "λ turn-off' described in Chapter 5. If one includes an increasingly deeper fraction of the light curve in the model, there becomes a point where the model parameter λ_{Hi} increases as the depth of the light curve modeled increases. This increase occurs because the light curve is no longer well-described by the an isothermal upper atmospheric model if portions of the lower atmosphere are included in the light curve. Above this turn-off, if only the upper atmosphere is included, λ_{Hi} becomes relatively stable. The clearest illustration of this phenomenon can be seen in Figure 6-1.

- Visual examination of the light curve model should not reveal a model that is pulled in the direction of a spike in the light curve.

- Visual examination of the light curve residuals should not reveal any systematic trend.

- The chosen model should be optimized to have a better χ^2 per degree of freedom relative to other models. It often came to pass that the best model depth for the immersion side was not the best model depth for emersion based on χ^2 per degree of freedom. For one, χ^2 per degree of freedom was highly sensitive to the presence of spikes. For instance, the MORIS light curve has a large spike on the immersion side seen at approximately 1360 s since 2011-06-23 11:00 (see Figure 6-18), which had a large negative affect on the χ^2 per degree of freedom for any fits that included that spike. In general, I tried to choose a cut-off level that minimized the χ^2 per degree of freedom for both sides, with a slight preference to the light curve with the weaker fit.

In the end, all chosen light curve cut-offs were greater than 1150 km. The remainder of this chapter will look at each of the nine selected events. It will discuss the choice of cut-off, the quality of fit, and relevant temperature asymmetries. For each light curve, an identical suite of figures and tables are presented. Firstly, there is a table of parameters for each light curve: input parameters such as closest approach, event velocity, location of each site, model outputs[2] such as r_H, λ_{Hi}, b, χ^2 per degree of freedom, and calculated quantities such as S/N per scale height, and temperature[3]. Temperature difference is provided twice: first as the difference between emersion and immersion, and second as the difference between north and south. The first difference allows for comparison of the fit results against the appearance of the light curve. The second difference allows for comparison of the fit results against location, to be discussed in further detail in Chapter 7. It is not necessarily the case, for instance, that immersion will always correspond to the more southern limb. The cut-off choice

[2]See Section 5.1.2 for a description of the EY92 light curve model parameters.
[3]The temperature calculation assumes an atmosphere fully comprised of N_2.

figures are nearly identical in content to figures from Chapter 5. The top panel contains the light curve plotted in units of shadow radius with minimum and maximum cut-offs marked. The immersion limb is plotted in black while emersion is plotted in red. The second panel contains emersion-immersion temperature difference as a function of cutoff. The lower two panels show the effects of cut-off choice on the the best fit half-light radius (r_H) and energy ratio at half-light (λ_H). Immersion points are plotted as diamonds while emersion points are plotted as xes. The cut-off choice is marked in red for all four figures. The third figure shows the occultation light curve, model fit using the chosen cut-off, and its residuals. The residuals are only plotted for points used in modeling.

6.1.4 A note on spikes

Spikes are flashes of light in an occultation light curve. Spikes have two causes. The first is mere out-sized noise, the second indicates an non-isothermal atmosphere. Spikes were commonly seen in Jovian planet atmosphere occultations and indicate fine structure in the atmosphere, turbulent cells or atmospheric density waves (Elliot & Veverka, 1976). Toigo et al. (2010) suggests that occultation spikes are caused by diurnal sublimation and "breathing."

While the 1988 light curve contained only a few minor spikes, (Elliot & Young, 1992), several major spikes are clearly visible in later occultation light curves, such as P131.1 CFHT, P384.2 AAT and P445.3 MMT light curves. Pasachoff et al. (2005) provide an in-depth analysis of the spikes seen during the P131.1 occultation using the CFHT telescope and the emersion-only data set taken on Maui. In theory, the upward bump in light caused by a spike should be compensated for by slightly lower fluxes right around it, and would simply disappear in low resolution data. However, when part of the light curve is cut off during the fitting process, a spike can bias a light curve fit upwards. Averaging, smoothing and model fitting can mitigate the spikes somewhat.

In an attempt to look directly at the effect of spikes on the modeling results, a full set of models were rerun for versions of each light curve that were binned

in both 15 and 40 kilometer increments. It was found that binning smoothed the difference between models that used consecutive cut-offs, but the fundamental conclusions, namely, which side was warmer, and by how much, were not significantly altered. Thus I present only results for unbinned occultation light curves.

6.2 1988-06-09 P8

On June 9, 1988, Pluto occulted a 12.8 magnitude star (Bosh et al., 1986) in an event called "P8". The occultation gets its name because it was the eighth occultation star catalogued by Mink & Klemola (1985). Successive occultation prediction efforts (Dunham et al., 1991; Mink et al., 1991; McDonald & Elliot, 1996, 2000) continued numbering occultations successively, inserting decimals to add extra stars that were initially skipped, but maintain chronological order. After 2009, the last year of predictions included in McDonald & Elliot (2000), Pluto occultations were denoted by their date, with an initial added for a potential event including another of Pluto's moons.

While P8 was not the first stellar occultation observed by Pluto (Brosch, 1995), it was the first unambiguous detection of a Pluto occultation, and was widely observed. The most famous observation of P8 was from the Kuiper Airborne Observatory (865.69 km North of the centerline) (see Figure 6-2), however, observations were also taken at Auckland, Toowoomba, Mt. Tambourine, Charters Towers (985 km North), Black Birch, Hobart and Mt. John. The KAO light curve was by far the cleanest, with a S/N per scale height of about 150. The light curve features an obvious discontinuity between the upper and lower atmosphere, very clearly present in some of the other occultations of the same event (Millis et al., 1993).

For the KAO occultation, there was a systematic error with the inertial navigation system of 15 km, but in an unspecified direction. Thus the placement of the radius scale from the occultation was $\pm$ 20 km (Elliot et al., 1989). This error, the largest post-occultation fitting error, inspired the analysis performed in the methods section. That analysis found that a shift of 100 km affects absolute temperature, but does not

substantially change the final conclusion of whether a particular side is warmer than the other (see Section 5.6). In any event, by 2007, a new variable position analysis method was able to work around the large KAO uncertainty (Elliot et al., 2007).

For this occultation, choosing a cut-off was rather straight-forward. As the occultation light curve sharply changed slope above 1120 km, fits that considered points at lower depths along Pluto's shadow radius became increasingly poorly fit at an alarming rate. Visual inspection of the fit revealed that 1135 km seemed a bit close to the edge, so 1150 km was chosen as a cut-off (see Figure 6-1 for the effects of cut-off on model results). Table 6.3 lists the best fit parameters for an isothermal fit with a 1150 km cut-off.

The P8 KAO occultation light curve was initially written up by Elliot et al. (1989) and Millis et al. (1993), but was revisited after P384.2 (Elliot et al., 2007). The latter paper, which was written after the creation of the olcTwoLimbModel used in this analysis (see Chapter 5) gives a global half light radius of 1233 ± 4, and a λ_H of 22 ± 2[4], and an unspecified thermal gradient parameter, b. These results are comparable the with the parameters for the KAO occultation in Table 6.3. Elliot et al. (2003a) use the KAO light curve as a test case for the inversion methodology laid out in the paper. The authors find a warmer emersion side, though not significantly so.

The asymmetric EY92 fits find that there is no significant temperature difference between emersion and immersion (4 ± 5 K).

[4]Calculated from pressure scale height at half light.

Table 6.3: Fit results for P8 data taken from the KAO.

Quantity	Fit Value
Pluto Closest Approach	865.69 km
Pluto Velocity	18.450 km s^{-1}
Upper Atmosphere Fit Cutoff	1150 km
Imm. Lat	40°
Imm. Long	219°
Em. Lat	-50°
Em. Long	219°
Midtime (from lowest hour)	2246.9±0.1 s
Normalized Unocculted Flux (x10000)	9930±20 DN
Occultation Slope (x10000)	-0.1±0.2 DN/s^2
Imm. r_H	1240±2 km
Em. r_H	1240±2 km
Imm. λ_{Hi}	22.1±0.7
Em. λ_{Hi}	21.3±0.7
b	0.0
$Temp_I$	107±3 K
$Temp_E$	111±3 K
Tdiff (E-I)	4±5 K
Tdiff (N-S)	-4±5 K
Imm. χ^2 per DOF	1.428
Em. χ^2 per DOF	1.315
Imm. SNR per SH	149
Em. SNR per SH	152

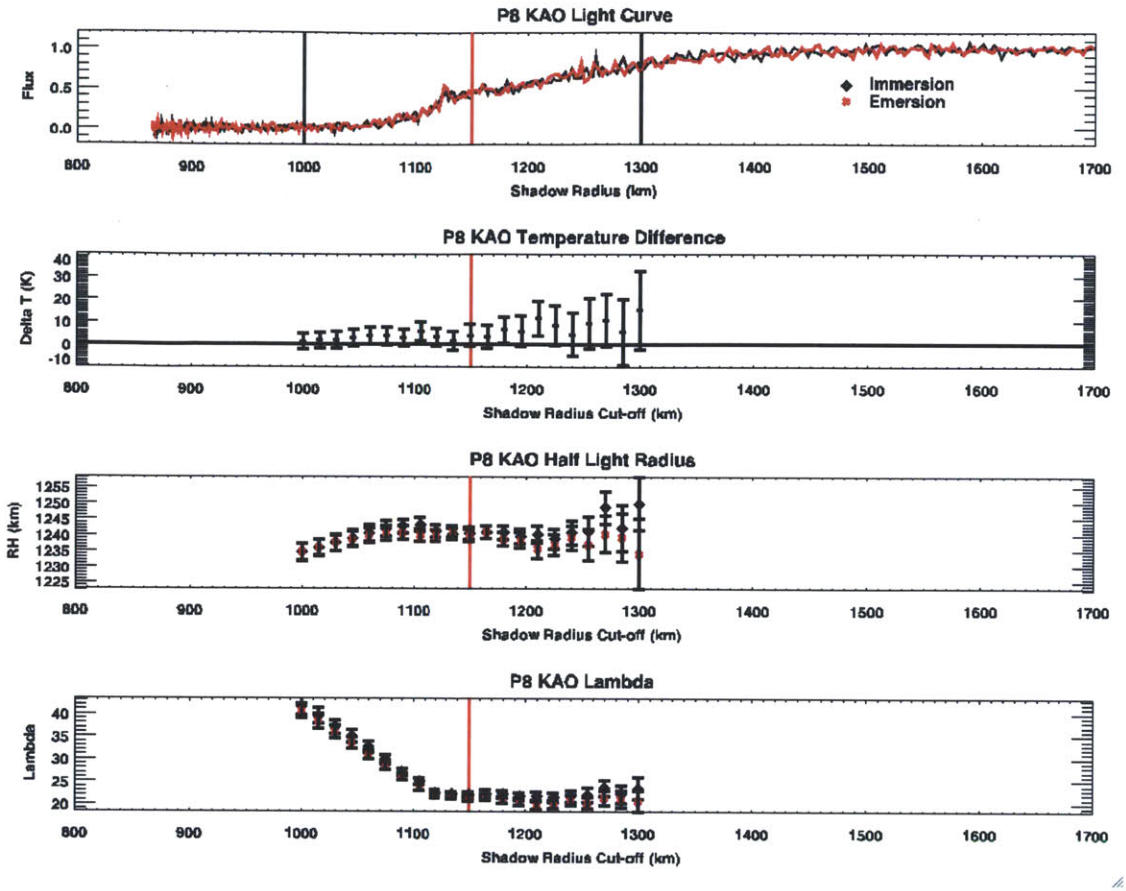

Figure 6-1: **P8 KAO** cut-off choices.
Top: Plot of immersion (black) and emersion (red) for P8 KAO light curve. Vertical lines show the upper and lower points of cut-offs analyzed. The KAO light curve features a sharp change in slope between the upper and lower atmosphere.
Second from top: Temperature difference versus cut-off. Note that each cut-off consistently reports an insignificantly warmer emersion.
Second from bottom: Half-light radius versus cut-off.
Bottom: λ_{Hi} versus cut-off. Note the sharp λ turn-off, just above 1100 km.
A cut-off of 1150 km was chosen.

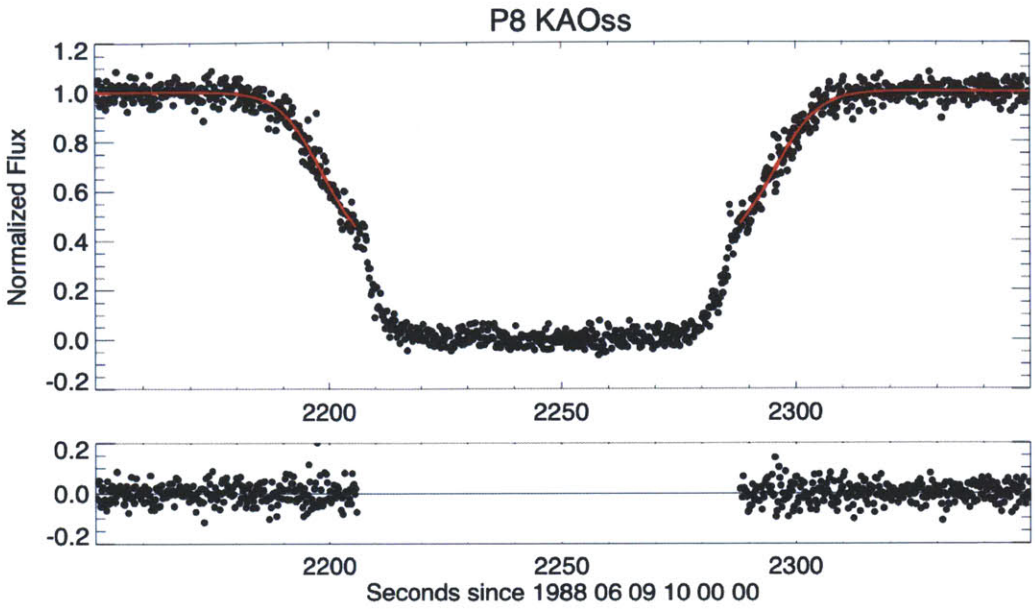

Figure 6-2: Light curve, fit and residuals for P8 occultation as observed by the KAO. Up until the "knee", the model provides an excellent fit for the upper atmosphere.

6.3 2002-08-21 P131.1

After a fourteen-year-long drought of Pluto occultations due to a relatively "star poor" area of the sky, two Pluto occultations were observed in the summer of 2002. In spite of a large observing campaign, the first occultation, P126 (mag=12, 2002 July 21), resulted in only in observations from small telescopes (Buie et al., 2002). The second occultation, P131.1 (mag=14.9, 2002 August 21)) was more successful, yielding two high-quality light curves from Mauna Kea, at the 3.6-m Canada-France-Hawaii Telescope (McDonald & Elliot, 2000; Sicardy et al., 2003), and the University of Hawaii 2.2-m Telescope (Elliot et al., 2003b; Pasachoff et al., 2005). Observations were conducted by Bruno Sicardy's team and the Planetary Science Lab at MIT, respectively. The MIT team also successfully observed P131.1 in the visible from the University of Hawaii 24-inch telescope, and Lick Observatory's 3.0-m Shane Telescope, though at a significantly reduced signal-to-noise (in the case of these last two telescopes, the data were too noisy to make successful individual models). Thus we will consider the two light curves from the CFHT and the UH 2.2-m, and these two light curves will be designated P131.1 CFHT and P131.1 UH-2.2m respectively.

The first thing to note is that Pluto's light curve has changed drastically over those 14 years. The half-light radius increased, atmospheric pressure had doubled, and the curve transitioned to the lower atmosphere more smoothly, albeit with some strong spikes. Gone were the "knees" at immersion and emersion. As shown in Figure 5-1 on page 117, the absence of a hard slope change does not indicate that the upper atmospheric model can apply to the whole light curve. Indeed, below 1120 km, the model output for λ_H still varies strongly with cut-off. However, a much more conservative cut-off at 1240 km from Pluto's center was chosen to avoid some spikes (see Figure 6-3, 6-4). The resulting model is plotted in Figure 6-5 and 6-6. Additionally the χ^2 per degree of freedom was smallest for both occultations when the model contained only points above 1240 km.

Table 6.4 shows the fit results for a cut-off of 1240 km. While the two sides do not agree on absolute temperature (the UH 2.2-m data suggests a warmer temperature),

both light curves agree that the immersion light curve has a warmer temperature. The UH light curve has a much smaller S/N per scale height, and is at the borderline of good light curves.

Previous model fits agree with the diagnosis of the immersion limb as warmer: inversion of CFHT light curve shows that the emersion is warmer from 1350 to 1260 km, while immersion is warmer below 1260 km (Sicardy et al., 2003). For the UH 2.2-m, inversion shows a consistently warmer immersion (Elliot et al., 2003b). In 2007, the UH light curve was refit and an r_H of 1279 $\pm$ 5 and a λ_H of 21.0 $\pm$ 1.4 were found (Elliot et al., 2007), both of which agree with the results of Table 6.4.

Table 6.4: Fit results for P131.1 data taken from the CFHT and the UH 2.2-m.

Quantity	**CFHT** Fit Value	**UH 2.2-m** Fit Value
Pluto Closest Approach	597.00 km	597.00 km
Pluto Velocity	6.849 km s^{-1}	6.849 km s^{-1}
Upper Atmosphere Fit Cutoff	1240 km	1240 km
Imm. Lat	55°	55°
Imm. Long	106°	106°
Em. Lat	-12°	-12°
Em. Long	240°	240°
Midtime (from lowest hour)	3034.5±0.2 s	3034.0±0.3 s
Normalized Unocculted Flux (x10000)	9950±20 DN	9935±10 DN
Occultation Slope (x10000)	0.03±0.06 DN/s^2	-0.31±0.02 DN/s^2
Imm. r_H	1286±2 km	1281±3 km
Em. r_H	1287±2 km	1284±3 km
Imm. λ_{Hi}	22.2±0.9	1284±3
Em. λ_{Hi}	24.0±0.9	21.8±0.9
b	0.0	0.0
$Temp_I$	103±4 K	119±5 K
$Temp_E$	95±3 K	105±5 K
Tdiff (E-I)	-8±6 K	-15±7 K
Tdiff (N-S)	8±6 K	15±7 K
Imm. χ^2 per DOF	1.911	0.895
Em. χ^2 per DOF	1.148	0.982
Imm. SNR per SH	188	106
Em. SNR per SH	181	100

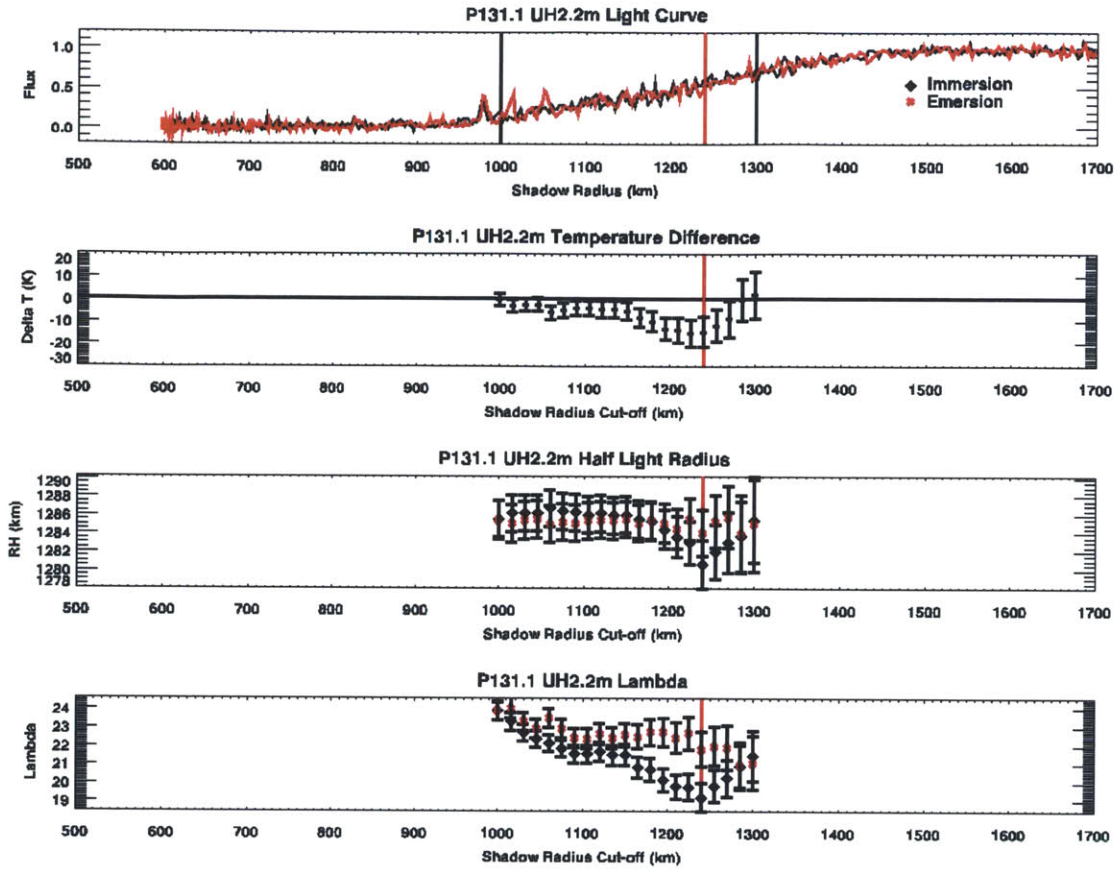

Figure 6-3: **P131.1 UH 2.2-m** cut-off choices.
Top: Plot of immersion (black) and emersion (red) for P131.1 UH 2.2-m light curve. Vertical lines show the upper and lower points of cut-offs analyzed.
Second from top: Temperature difference versus cut-off. Inversion is warmer for almost all cut-offs and significantly so for points between 1150 and 1255 km.
Second from bottom: Half-light radius versus cut-off.
Bottom: λ_{Hi} versus cut-off. The λ turn-off seems to have completed by 1120 km for immersion, but not emersion.
A cut-off of 1240 km was chosen.

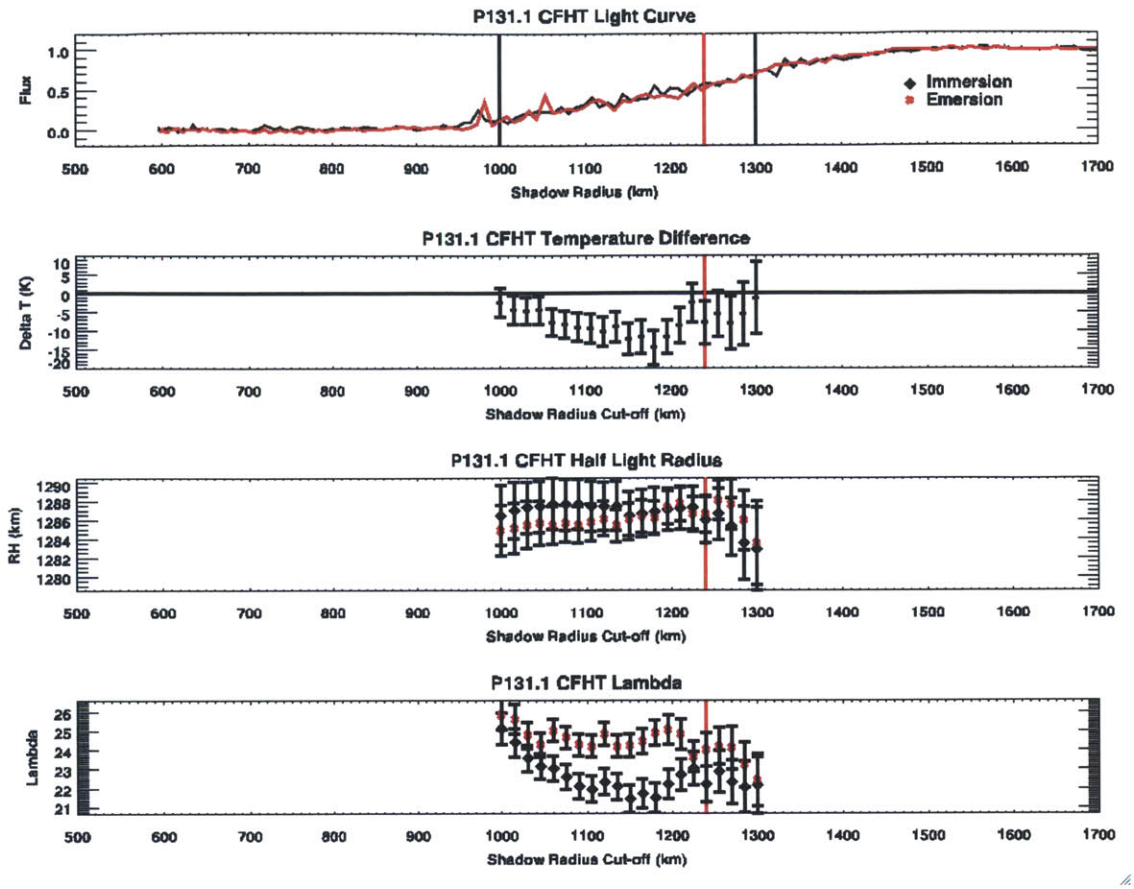

Figure 6-4: **P131.1 CFHT** cut-off choices.
Top: Plot of immersion (black) and emersion (red) for P131.1 CFHT light curve. Vertical lines show the upper and lower points of cut-offs analyzed.
Second from top: Temperature difference versus cut-off. Note that each cut-off reports a warmer immersion.
Second from bottom: Half-light radius versus cut-off.
Bottom: λ_{Hi} versus cut-off.
A cut-off of 1240 km was chosen.

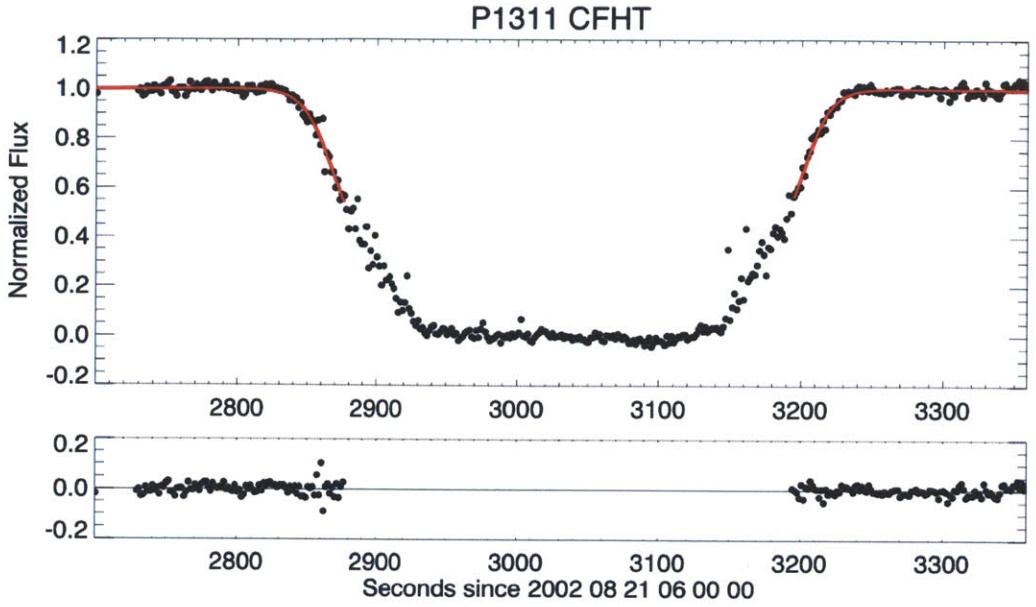

Figure 6-5: Light curve, fit and residuals for P131.1 occultation as observed by the CFHT.

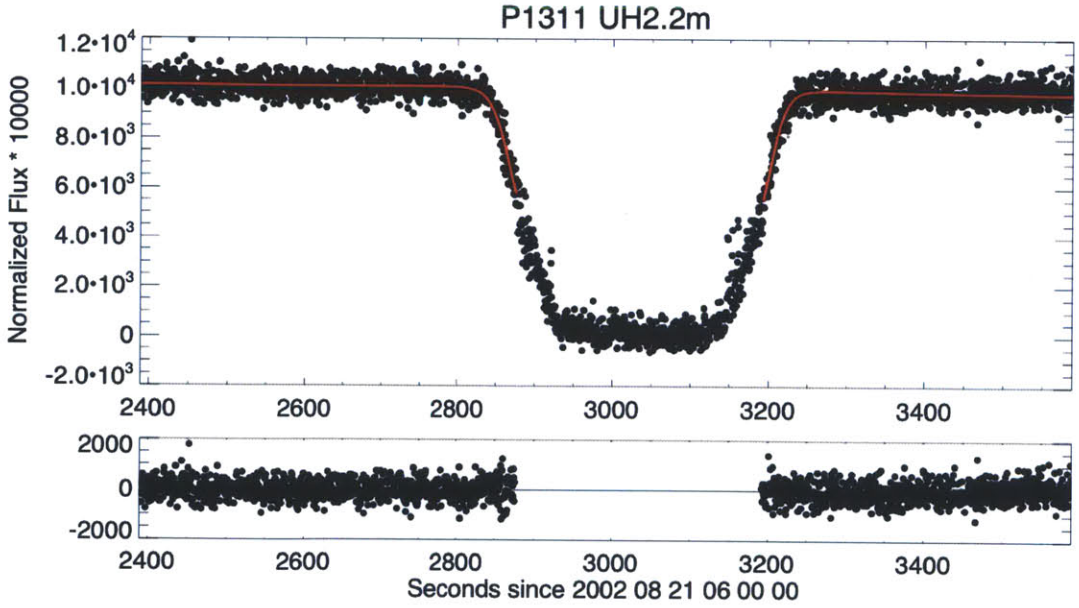

Figure 6-6: Light curve, fit and residuals for P131.1 occultation as observed by the UH 2.2-m telescope.

6.4 2006-06-12 P384.2

On June 12, 2006, Pluto occulted a UCAC=14.8 magnitude[5] star, as seen from Australia and New Zealand. Teams from SwRI and MIT both acquired several occultation light curves. Three good light curves, Siding Springs (2.3-m), Black Springs (0.8-m), the AAT (3.9-m)[6], came out of the 384.2 observations. The first two light curves were discussed in Elliot et al. (2007), though they will not be discussed here due to low S/N per scale height (about 50 and 30 respectively), which translated to errors of 12 and 17 K on the temperature difference. The AAT had a S/N per scale height of approximately 250, making it the finest and most detailed light curve used in this analysis. The unusually poor signal-to-noise of the Siding Springs light curve, relative to telescope size is well-explained by Pluto's approximately 15° separation from a full moon. While telescopes suffered from the moonlight, baffling quality and optical elements made some telescopes worse than others.

Table 6.5 lists the results for the best AAT occultation model, with a cut-off of 1225 km. This model cut-off was chosen due to the clear evidence of a turn-off in λ_{Hi} values around 1210 km, as seen in Figure 6-7. Every model light curve predicts a warmer emersion limb, and the temperature difference of 7±3 K is significant with respect to the noise of the model. The residuals in Figure 6-8 show a light curve with many spikes.

The choice of the emersion as the warmer side for the AAT seem to agree with previously published results. Young et al. (2008) performed a two-sided fit to the upper atmosphere, and report an immersion temperature of 100.0 ± 4.2 and an emersion temperature of 106 ± 4.6. The reason for the larger error bars is unknown.

Zalucha et al. (2011b) performed separate fits on the Siding Springs light curve and found the temperature difference to be negligible within the error bars of the event measurement. Before elimination, preliminary models showed that the two

[5]UCAC bandpass: 579-642 nm.

[6]The AAT ("Anglo-Australian Telescope") and ATT ("Advanced Technology Telescope") are both located at Siding Springs Observatory. The AAT 3.9-m data were referred to as AAT in the original paper (Young et al., 2008), while the ATT 2.3-m telescope was referred to as Siding Springs (Elliot et al., 2007). These conventions will be kept in this paper.

sides of Siding Springs agreed with each other within their error bars. These error bars were naturally rather larger than the error bars on higher-quality observations of that event, such as the one with the AAT (about 8 K as opposed 3 K).

Nevertheless, the AAT's temperature difference is one of the strongest in this study.

Table 6.5: Fit results for P384.2 data taken from the AAT.

Quantity	Fit Value
Pluto Closest Approach	570.09 km
Pluto Velocity	23.990 km s^{-1}
Upper Atmosphere Fit Cutoff	1225 km
Imm. Lat	32°
Imm. Long	253°
Em. Lat	-51°
Em. Long	3°
Midtime (from lowest hour)	1399.67±0.03 s
Normalized Unocculted Flux (x10000)	9993±3 DN
Occultation Slope (x10000)	0.14±0.02 DN/s^2
Imm. r_H	1284.1±1.0 km
Em. r_H	1283.1±1.0 km
Imm. λ_{Hi}	20.2±0.3
Em. λ_{Hi}	19.0±0.3
b	0.0
$Temp_I$	113±2 K
$Temp_E$	120±2 K
Tdiff (E-I)	7±3 K
Tdiff (N-S)	-7±3 K
Imm. χ^2 per DOF	1.254
Em. χ^2 per DOF	1.100
Imm. SNR per SH	245
Em. SNR per SH	253

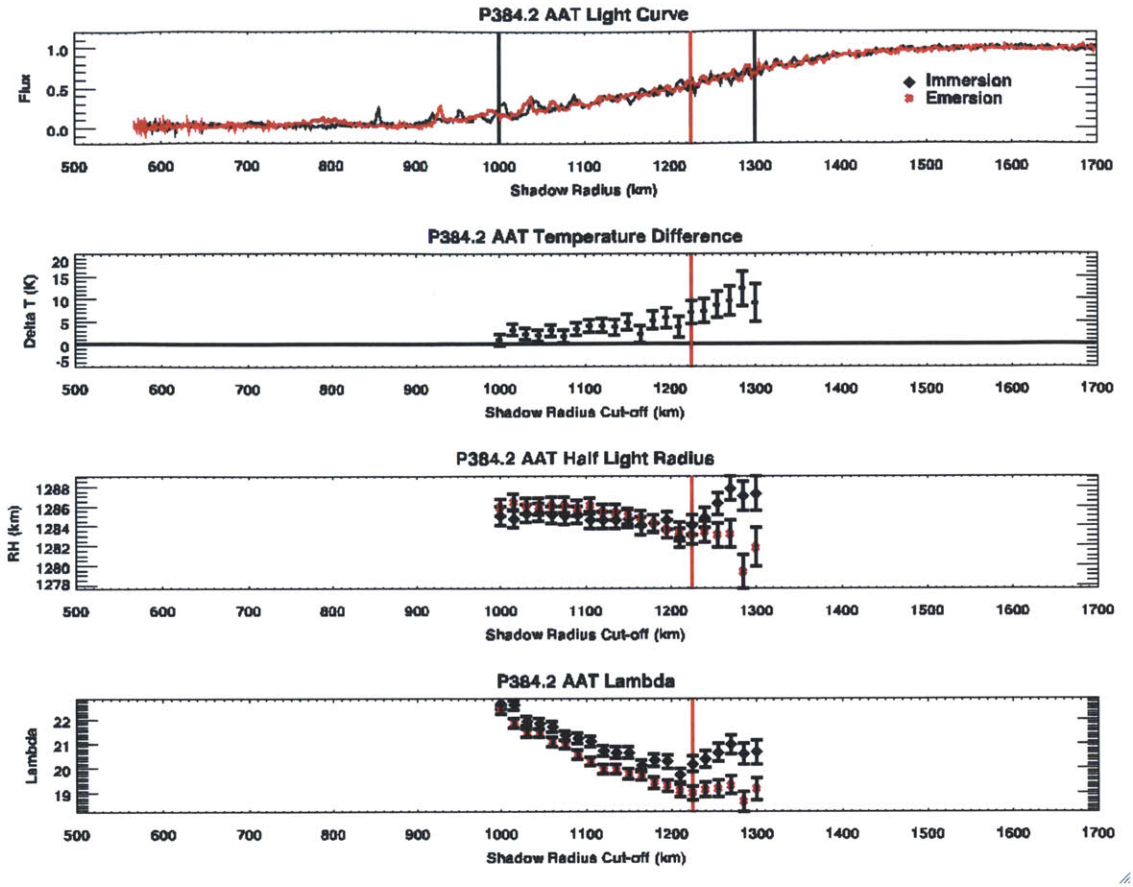

Figure 6-7: **P384.2 AAT** cut-off choices.
Top: Plot of immersion (black) and emersion (red) for P384.2 AAT light curve. Vertical lines show the upper and lower points of cut-offs analyzed.
Second from top: Temperature difference versus cut-off. Note that each cut-off consistently reports a warmer emersion.
Second from bottom: Half-light radius versus cut-off.
Bottom: λ_{Hi} versus cut-off.
A cut-off of 1225 km was chosen.

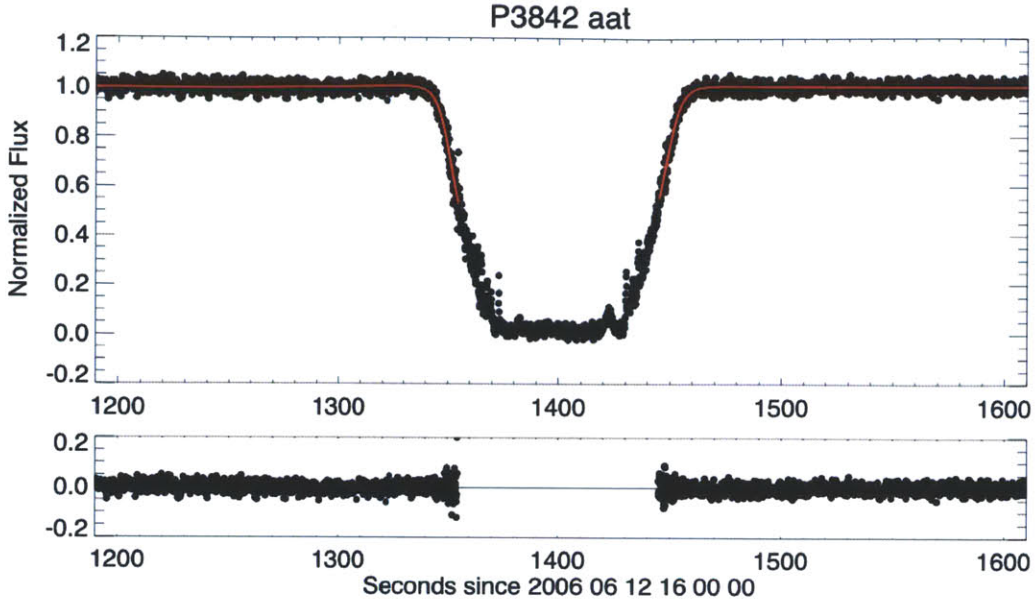

Figure 6-8: Light curve, fit and residuals for P384.2 occultation as observed by the AAT.

6.5 2007-03-18 P445.3

On March 18 2007, Pluto occulted a R=15.3 magnitude star, this time over the western United States. The MIT Planetary Astronomy Laboratory obtained five light curves from the event– from Fremont Peak Observatory, the U.S. Naval Observatory, the MMT Observatory, Magdalena Ridge Observatory and the Large Binocular Telescope. Of these light curves, the MRO and LBTO light curves do not have complete coverage of the event. While the Fremont Peak Observatory light curve is the only full occultation (the others are grazes), it is highly noisy (Person et al., 2008). The remaining two light curves, the USNO and MMT light curves were analyzed in some detail, though the MMT light curve was later discarded from the analysis. Its closest approach distance of 1319 km south was greater than 1300 km, the highest cut-off tested for every other light curve. While the USNO 61-inch light curve had a low S/N per scale height of 85, it was left in to compare against its Lowell counterpart. At -1102 km from the centerline, the light curve did not reach the zero level, but it was deep enough to fit, so P4453USNO is in this study.

The author was part of an effort led by Southwest Research Institute, observing at Apache Point Observatory's 1-m telescope. While the weather had been clear on the days leading up to the event, clouds rolled in shortly before the occultation, and no good data were obtained. However, there were several other telescopes that had successes at Red Buttes Observatory, Lick Observatory, Lowell Observatory, Palomar, Mount Lemmon, Table Mountain, Kitt Peak and San Pedro Martir (Young et al., 2007). Of these light curves, the SwRI team was generous enough to provide a light curve taken using the 42-inch Hall telescope at Lowell Observatory's Anderson Mesa station for comparison (P445.3 Hall). While not at the same site, Lowell Observatory and the US Naval Observatory are both near Flagstaff, Arizona. Lowell Observatory's distance from the centerline was recalculated based on the MIT centerline and found to be -1108 km (Zuluaga, 2012). The error on the distances is expected to be about ± 4 km (Person et al., 2008).

While the observations from the USNO were included in all formal write-ups of

the event, that light curve differs from the one used in this document in two respects. Firstly, the published USNO light curve used was based on photometry without a comparison star. An earlier light curve, created by Steve Levine and located in PAL's archives along with the published, comparison star-less light curve, did feature a comparison star, the use of which improved the signal-to-noise ratio, and created a much flatter baseline. While preparing these data, I discovered that the observation mid-time for each image was improperly calculated.[7] Both light curves were run in preliminary experiments (see Section 6.9). The results of my fits are in Table 6.6. Figures 6-9 and 6-10 report the outcomes for a variety of cut-off levels. The cut-off was chosen to be 1150 km for each light curve, because that level had the best χ^2 per degree of freedom per side.

Figures 6-11 and 6-12 show the light curves and their models. Superficially, the resemblance between the Hall and USNO light curves is quite striking, though the two light curves disagree with each other which limb has the warmer temperature. The USNO light curve has a temperature difference of -12±4 (and is consistent in favor of a warmer immersion for all other cut-offs). The Hall light curve has a temperature difference of 8±7 (and is consistent in favor of a warmer emersion for all other cut-offs). What could be responsible for the difference? For the Hall and the USNO, the S/N per scale heights are 114 and 84, at and below the border of the S/N per scale height minimum determined from Section 5.4.3. For the USNO light curve, the original light curve was available and was ran (see Section 6.9). The USNO difference for that light curve was even more extreme in favor of immersion. While the Hall light curve is more or less consistent with 0 (as a 1 σ result should appear 1/3 of the time), the USNO light curve is a 3σ result.

[7]When operating the GPS on POETS, the user sets a start time. The readout of the first image will occur at the start time, thus the mid-time of the first image is half an exposure time *before* the set time, not after.

Table 6.6: Fit results for P445.3 data taken from the Hall Telescope at Lowell Observatory, and the USNO 61-inch.

Quantity	**Hall** Fit Value	**USNO** Fit Value
Pluto Closest Approach	-1108.00 km	-1108.00 km
Pluto Velocity	6.780 km s^{-1}	6.780 km s^{-1}
Upper Atmosphere Fit Cutoff	1150 km	1150 km
Imm. Lat	-18°	-18°
Imm. Long	213°	213°
Em. Lat	28°	28°
Em. Long	258°	258°
Midtime (from lowest hour)	3248.7±0.9 s	3251.4±0.5 s
Normalized Unocculted Flux (x10000)	9980±30 DN	9940±20 DN
Occultation Slope (x10000)	-0.11±0.07 DN/s^2	0.22±0.04 DN/s^2
Imm. r_H	1305±4 km	1310±3 km
Em. r_H	1307±5 km	1308±2 km
Imm. λ_{Hi}	21.2±0.9	21.0±0.6
Em. λ_{Hi}	20±1	23.7±0.7
b	0.0	0.0
$Temp_I$	106±5 K	106±3 K
$Temp_E$	114±6 K	95±3 K
Tdiff (E-I)	8± K7	-12±4 K
Tdiff (N-S)	8± K7	-12±4 K
Imm. χ^2 per DOF	0.912	0.884
Em. χ^2 per DOF	1.188	0.832
Imm. SNR per SH	101	82
Em. SNR per SH	105	78

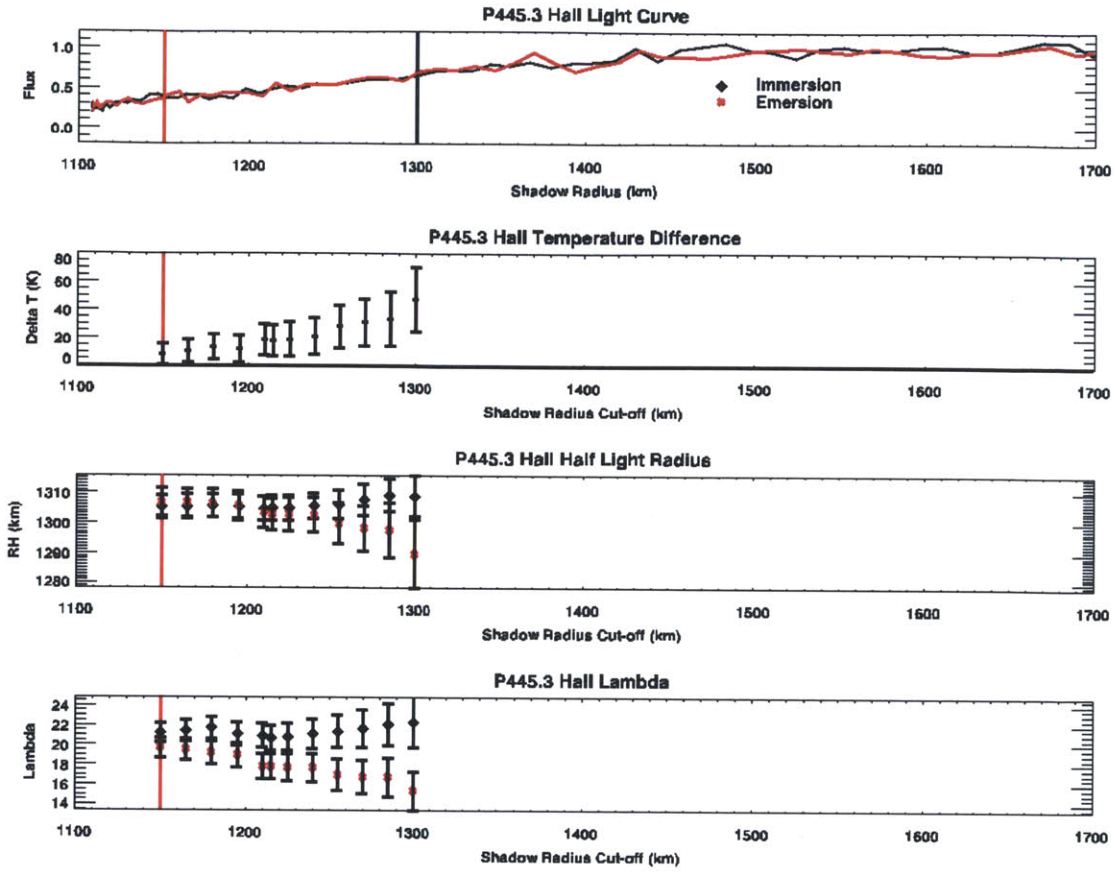

Figure 6-9: **P445.3 Hall** cut-off choices.
Top: Plot of immersion (black) and emersion (red) for P445.3 Hall light curve. Vertical lines show the upper and lower points of cut-offs analyzed.
Second from top: Temperature difference versus cut-off. Note each cut-off reports a warmer emersion, opposite of the USNO results.
Second from bottom: Half-light radius versus cut-off.
Bottom: λ_{Hi} versus cut-off.
A cut-off of 1150 km was chosen.

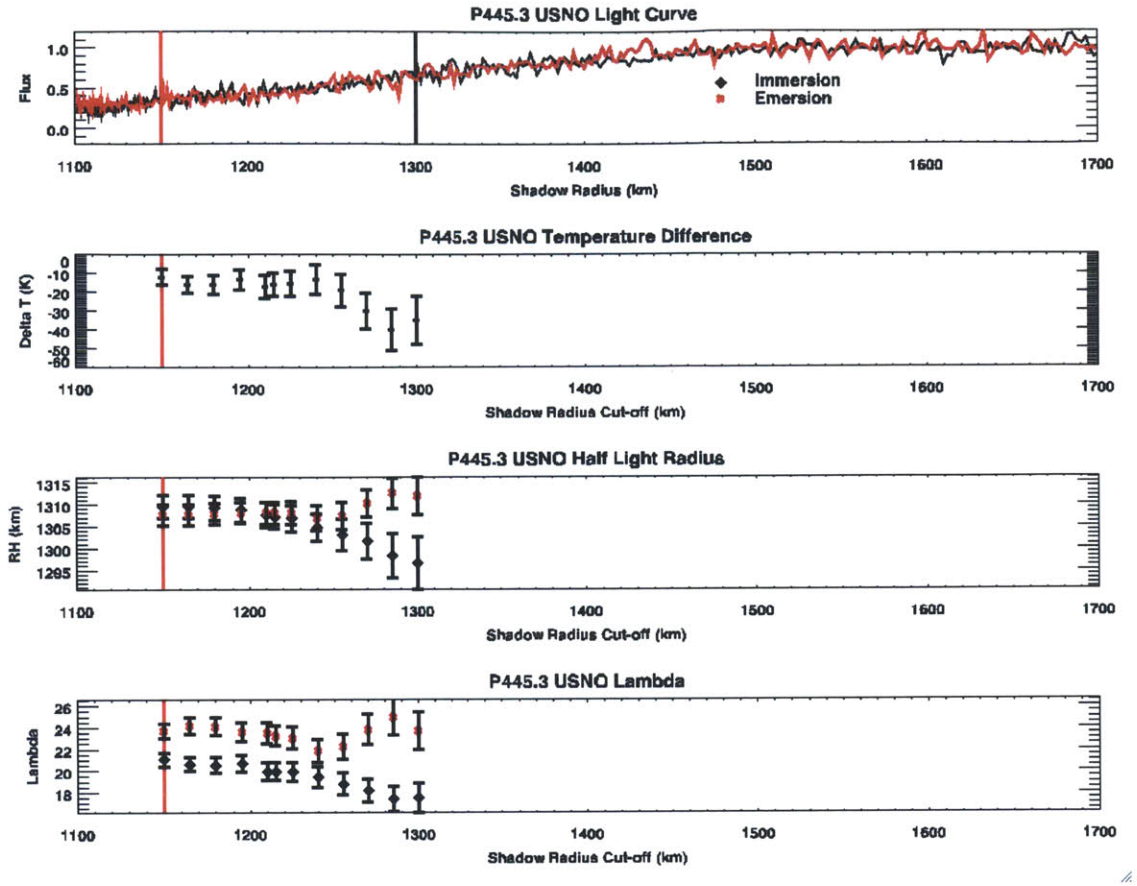

Figure 6-10: **P445.3 USNO** cut-off choices.
Top: Plot of immersion (black) and emersion (red) for P445.3 USNO light curve. Vertical lines show the upper and lower points of cut-offs analyzed.
Second from top: Temperature difference versus cut-off. Note that each cut-off shows a significantly warmer immersion, the opposite of the Hall results.
Second from bottom: Half-light radius versus cut-off.
Bottom: λ_{Hi} versus cut-off.
A cut-off of 1150 km was chosen.

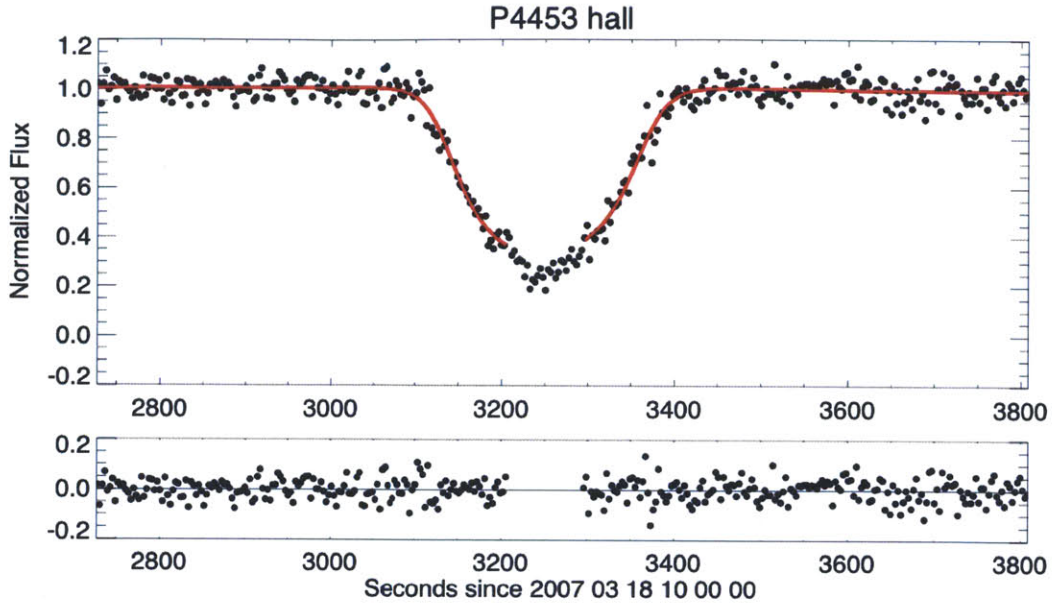

Figure 6-11: Light curve, fit and residuals for P445.3 occultation as observed by the Hall Telescope.

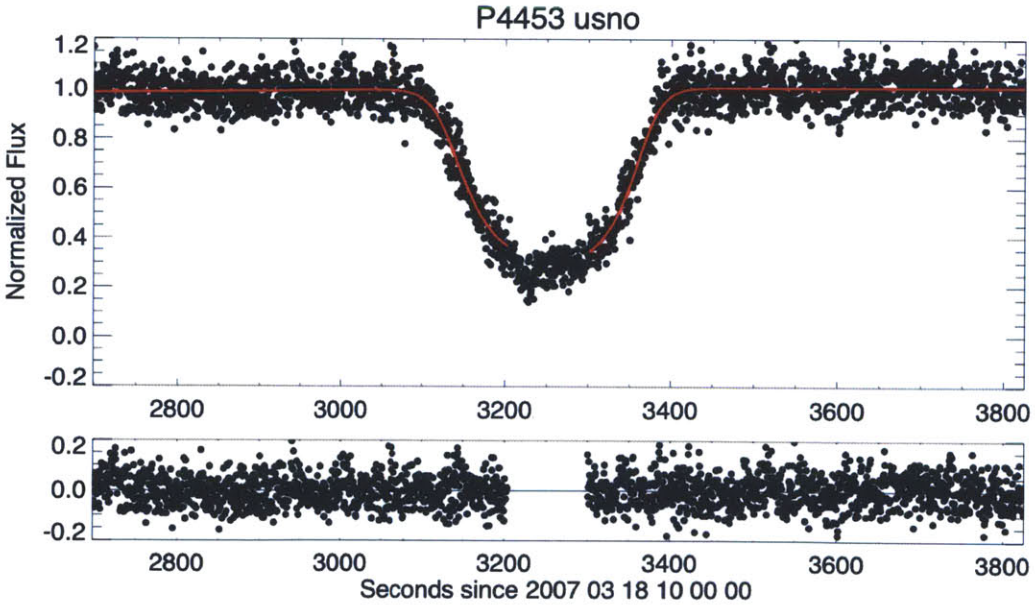

Figure 6-12: Light curve, fit and residuals for P445.3 occultation as observed by the USNO 61" telescope.

6.6 P20100704

On July 4, 2010, Pluto occulted a UCAC=15.3 magnitude star (Zuluaga, 2013). This event was observed from various locations in South America and Africa. The author and Jim Elliot attempted to observe this event from the Clay telescope at Las Campanas observatory. High winds prevented opening of the telescope. The best, successful observations were made with the ATOM telescope in Namibia by Michael Person and Rebecca Jensen-Clem (Person et al., 2010) and at Aloe Ridge by Bob Howell and Kate Lonergan (Young et al., 2010) (light curve kindly provided by Leslie Young). Neither light curve had adequate S/N per scale height to be considered in this study.

6.7 PC20110623

Fifteen years after the decommissioning of the Kuiper Airborne Observatory, the Stratospheric Observatory For Infrared Astronomy ("SOFIA") started science flights in Fall 2010. The MIT Planetary Astronomy Laboratory, represented by Michael Person, was fortunate enough to fly to the centerline to observe Pluto occult a 14.43 UCAC2 magnitude star from SOFIA, along with other ground sites that included the IRTF, USNO-Flagstaff and Leeward Community College. The IRTF and sites north also saw an occultation by Charon (Gulbis et al., 2012; Person et al., 2012).

The author attempted to observe PC20110623 in Cairns, Australia. Cairns suffered intermittent clouds during the occultation time, but the site was too far south to have seen an occultation. Thanks to in-flight astrometry, not only was SOFIA within the occultation path, it was close enough to see a central flash (Person et al., 2013)!

During the occultation, both the High-speed Imaging Photometer for Occultations ("HIPO") instrument and the Fast Diagnostic Camera ("FDC") were running on SOFIA, making three simultaneous light curves through the same telescope. HIPO is described in detail in Chapter 3. The FDC is an instrument designed to help with

pointing, and receives light from tertiary mirror (Wolf et al., 2010). Because the occultation flights occurred during commissioning, a special tertiary mirror was used, and an unusually large amount of light was directed to the FDC, rather than HIPO, whose dichroic directed light to unfiltered red and blue chips. As a result, the FDC had the highest S/N per scale height, 150, while the red side had an S/N per scale height of 143, and the blue, only 47. Thus, we will not examine the blue light curve here. At 104 km $\pm$ 3 km from the centerline, a small central flash can be seen from each light curve (Person et al., 2013).

We will also consider visible light curve from MORIS on the IRTF. Observed at 1135 km above Pluto's center, Pluto did not fully occult the star as seen from Mauna Kea. While this light curve and the FDC have similar S/N per point, the IRTF occultation has a higher S/N per scale height due to its higher $v_\perp$ as a graze.

The fit results can be found in Tables 6.7 and 6.8, while a broader selection of fit results using other cut-offs can be found in Figures 6-13, 6-14, and 6-15. In the case of MORIS, the λ_{Hi} cut-off is above 1180 km, but a cut-off of 1210 km was chosen to avoid the large spikes on immersion. For the FDC and SOFIA red light curves, a turn-off of 1210 km was chosen based on the first point after the λ turn-off. The chosen fits' light curves can be seen in Figures 6-16, 6-17 and 6-18.

The most disturbing result is the mismatch between the SOFIA red and FDC light curves. The FDC light curve has a temperature difference of -6 $\pm$ 4 K, while the SOFIA red light curve has a difference of 7 $\pm$ 5 K. Both differences are not terribly inconsistent with no difference, but their disagreement is disturbing due to the fact that both light curves are of decent quality and taken through the same telescope.

There were some differences in the creation of the light curves. While both light curves were created by the author, the process was not identical. The FDC light curve was bias-corrected, while the SOFIA red light curve was overscan-corrected. The SOFIA red light curve was also corrected by flats created after the fact. These flats did not have the same binning as the science data, and thus were binned 3×3 to match. The FDC field of view used was considerable smaller than the HIPO field, and thus used three comparison stars to HIPO's eleven. Alternate reductions of

both HIPO light curves using the sub-optimal conditions of the FDC were created to account for the discrepancy, but the conclusions of the SOFIA red light curve models were not changed. Alternate light curves are described in more detail in Section 6.9. Table 6.7 shows a small slope in the baseline of the FDC light curve. Perhaps a re-reduction of the FDC light curve could eliminate it.

Table 6.7: Fit results for PC20110623 data taken from SOFIA's Fast Diagnostic Camera and SOFIA red chip.

Quantity	**FDC** Fit Value	**SOFIA red** FIt Value
Pluto Closest Approach	104.33 km	104.33 km
Pluto Velocity	24.030 km s^{-1}	24.030 km s^{-1}
Upper Atmosphere Fit Cutoff	1210 km	1210 km
Imm. Lat	36°	36°
Imm. Long	16°	16°
Em. Lat	-40°	-40°
Em. Long	185°	185°
Midtime (from lowest hour)	1300.65±0.06 s	1300.77±0.06 s
Normalized Unocculted Flux (x10000)	10106±5 DN	9983±6 DN
Occultation Slope (x10000)	0.23±0.03 DN/s^2	-0.02±0.03 DN/s^2
Imm. r_H	1295±2 km	1297±2 km
Em. r_H	1296±2 km	1297±2 km
Imm. λ_{Hi}	17.9±0.4	18.5±0.5
Em. λ_{Hi}	18.7±0.5	17.5±0.5
b	0.0	0.0
$Temp_I$	127±3 K	122±3 K
$Temp_E$	121±3 K	129±4 K
Tdiff (E-I)	-6±4 K	7±5 K
Tdiff (N-S)	6±4 K	-7±5 K
Imm. χ^2 per DOF	0.714	0.921
Em. χ^2 per DOF	0.671	1.019
Imm. SNR per SH	154	143
Em. SNR per SH	150	147

Table 6.8: Fit results for PC20110623 data taken from 3-m NASA IRTF.

Quantity	Fit Value
Pluto Closest Approach	1135.73 km
Pluto Velocity	24.200 km s^{-1}
Upper Atmosphere Fit Cutoff	1210 km
Imm. Lat	2°
Imm. Long	65°
Em. Lat	-34°
Em. Long	112°
Midtime (from lowest hour)	1383.0±0.1 s
Normalized Unocculted Flux (x10000)	9882±9 DN
Occultation Slope (x10000)	-0.29±0.08 DN/s^2
Imm. r_H	1297±2 km
Em. r_H	1297±2 km
Imm. λ_{Hi}	18.2±0.5
Em. λ_{Hi}	17.7±0.4
b	0.0
$Temp_I$	124±3 K
$Temp_E$	127±3 K
Tdiff (E-I)	3±4 K
Tdiff (N-S)	-3±4 K
Imm. χ^2 per DOF	1.540
Em. χ^2 per DOF	1.115
Imm. SNR per SH	182
Em. SNR per SH	185

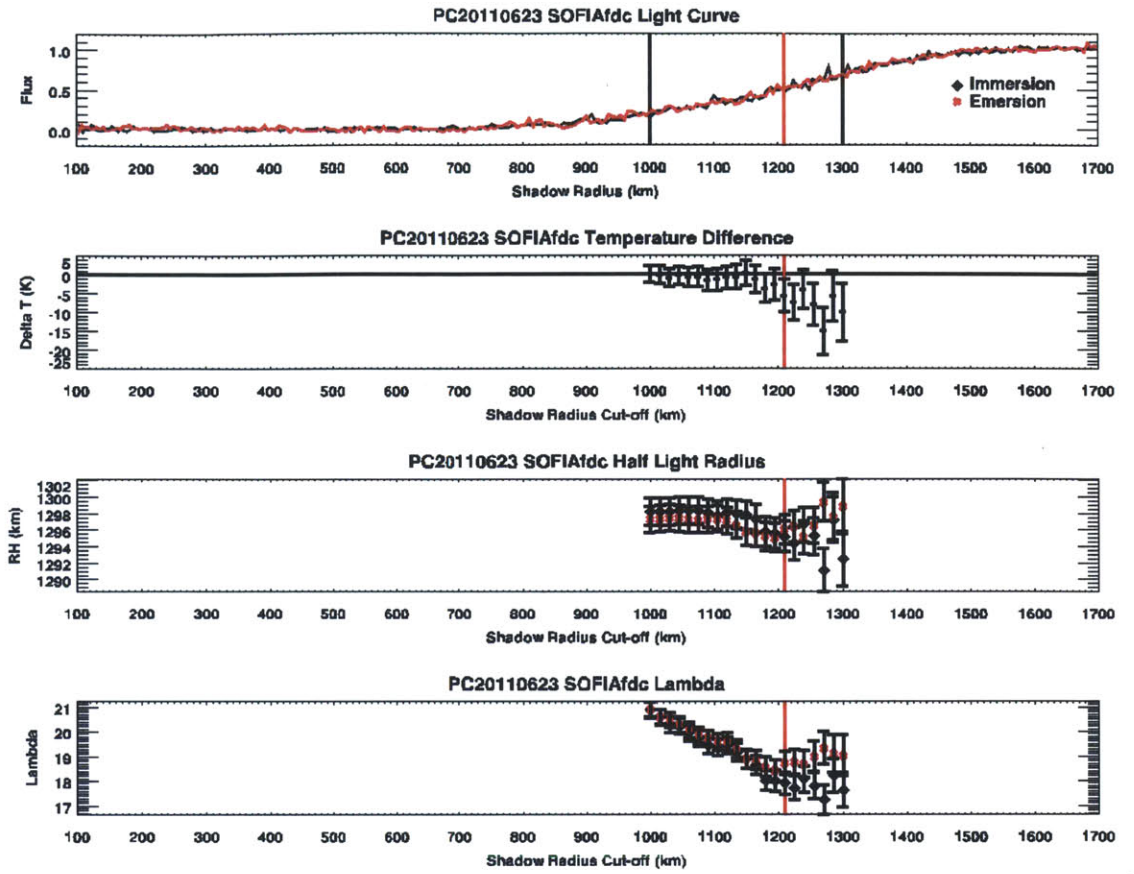

Figure 6-13: SOFIA FDC cut-off choices.
Top: Plot of immersion (black) and emersion (red) for PC20110623 FDC light curve. Vertical lines show the upper and lower points of cut-offs analyzed.
Second from top: Temperature difference versus cut-off. Temperature difference versus cut-off. The temperature difference is consistent with zero before the λ turn-off, at 1200 km, at which point immersion becomes warmer.
Second from bottom: Half-light radius versus cut-off.
Bottom: λ_{Hi} versus cut-off.
A cut-off of 1210 km was chosen.

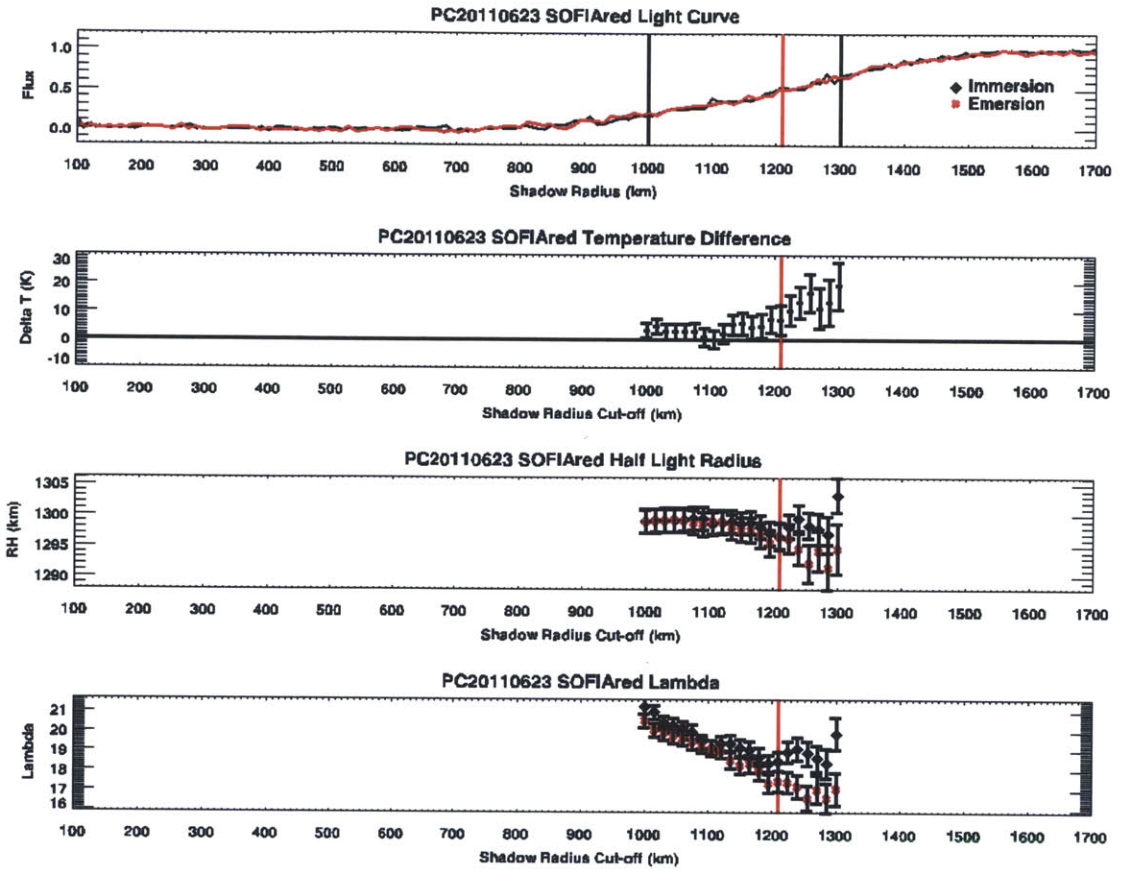

Figure 6-14: **SOFIA red** cut-off choices.
Top: Plot of immersion (black) and emersion (red) for PC20110623 HIPO light curve. Vertical lines show the upper and lower points of cut-offs analyzed.
Second from top: Temperature difference versus cut-off. The temperature difference is consistent with zero before the λ turn-off, at 1200 km, at which point emersion becomes warmer.
Second from bottom: Half-light radius versus cut-off.
Bottom: λ_{Hi} versus cut-off.
A cut-off of 1210 km was chosen.

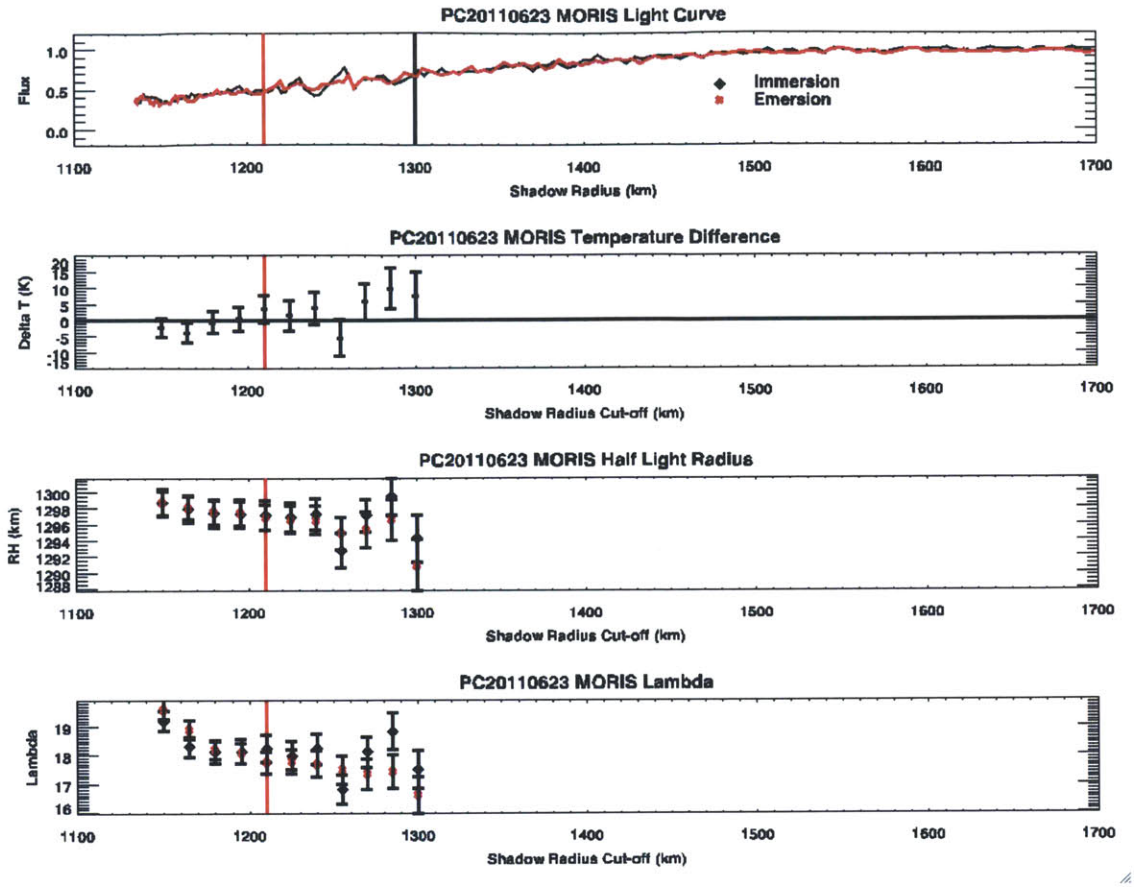

Figure 6-15: MORIS cut-off choices.
Top: Plot of immersion (black) and emersion (red) for PC20110623 MORIS light curve. Vertical lines show the upper and lower points of cut-offs analyzed. Note the spike at approximately 1250 km.
Second from top: Temperature difference versus cut-off.
Second from bottom: Half-light radius versus cut-off.
Bottom: λ_{Hi} versus cut-off.
A cut-off of 1210 km was chosen.

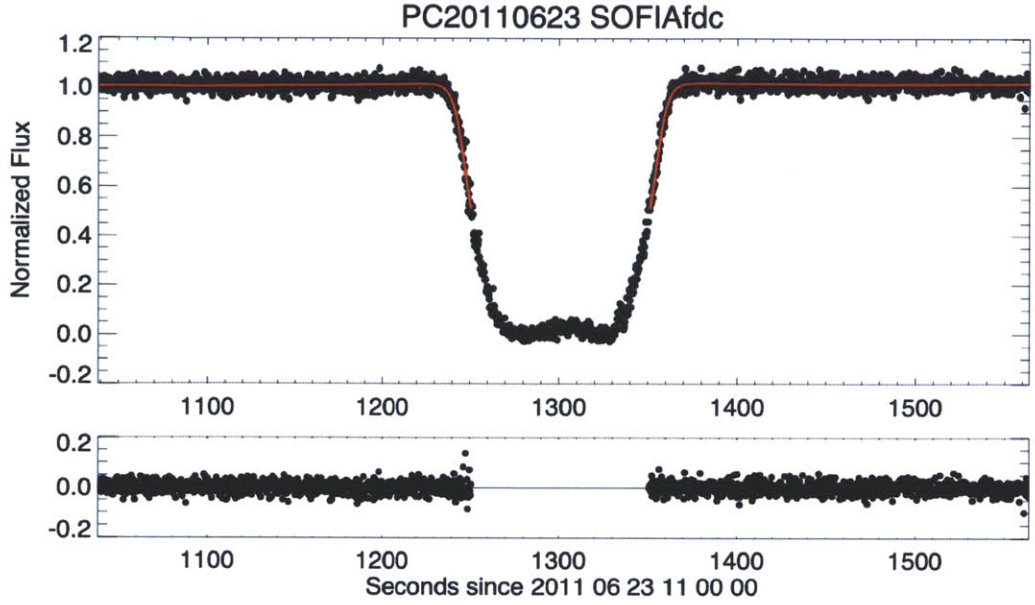

Figure 6-16: Light curve, fit and residuals for PC20110623 occultation as observed by from SOFIA's Fast Diagnostic Camera.

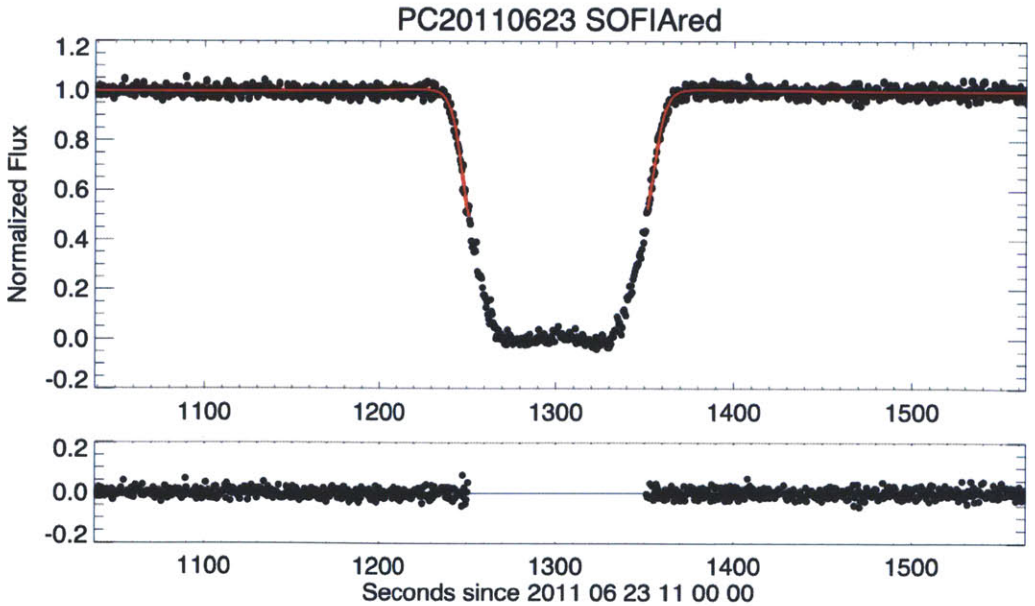

Figure 6-17: Light curve, fit and residuals for PC20110623 occultation as observed by SOFIA's SOFIA red chip.

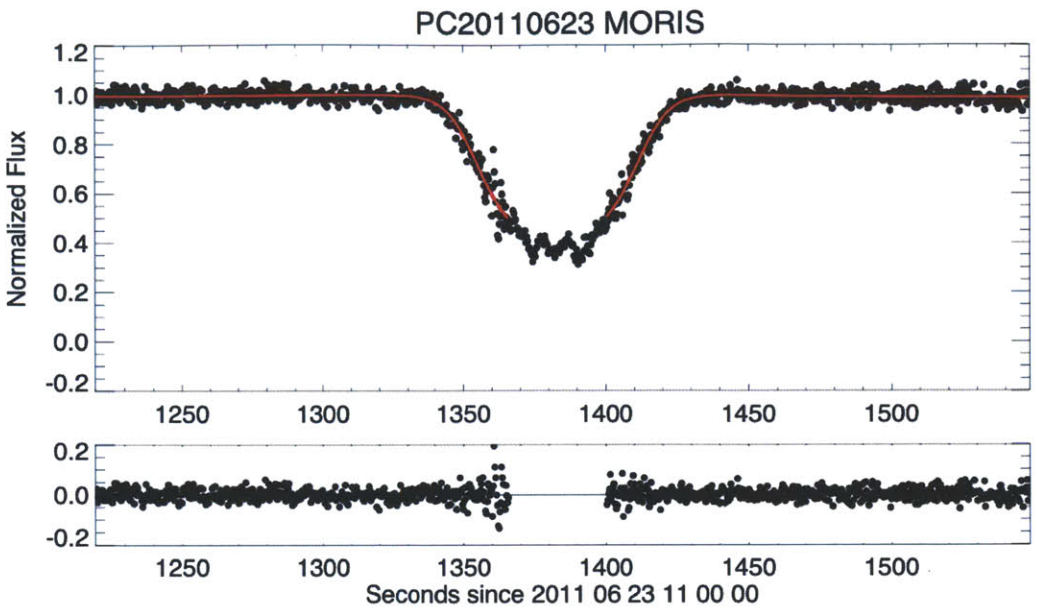

Figure 6-18: Light curve, fit and residuals for PC20110623 occultation as observed by MORIS on the IRTF.

6.8 Omitted light curves

While many light curves were considered in this study, not every Pluto occultation light curve was included. While there are many Pluto occultation light curves out there, not every light curve will have the signal to noise appropriate to even consider looking for temperature differences. Light curves such as the AAT, and CFHT light curve had been previously published, but used with their observer's permission. The following is a list of light curves that did not get incorporated into this study due to unavailability, but have the potential to be useful:

- In addition to the Hall, the SwRI team received light curves from Palomar and WIRO. However, no full paper has been written up on that event.

- In July 2007, a central flash occultation was observed and discussed by Olkin et al. (2007, 2011, 2012). Analyses so far focus mainly on the central flash, not the state of the upper atmosphere. A wind analysis for this light curve has been published by Zalucha & Gulbis (2012).

- Sicardy et al. (2012) mention a good occultation observed in June 2011, distinct from PC20110623. This light curve may be useful to probe short time-scale atmospheric changes, when compared with PC20110623.

- Sicardy et al. (2011b) write up an occultation observed on 22 Jun 2008. This occultation may have one or two stations that may have adequate signal-to-noise, but would need to be examined in detail.

- Most excitingly, Sicardy (2012) has observed an occultation with a signal-to-noise rivaling the AAT. This occultation has not yet been published.

- Finally, occultations of Pluto by PAL were observed on 2012 September 09 and 2012 October 02. However, no astrometric solution has been performed with either data set, nor has a determination been made whether these data would be suitable for this project.

6.9 Alternative light curves

During the creation of the fits for this chapter, several additional light curves were run.

For P445.3, experiments were also performed using the USNO light curve that was part of Person et al. (2008). The temperature difference between the two sides was found to be more extreme. This result is not to be trusted as no comparison stars were used in the creation of the light curve. The addition of a comparison star reduced the slope of the baseline by a factor of five.

As part of the effort to understand the disagreement between the HIPO and FDC light curves, the red and blue light curves were re-created from non-flattened images (no flats exist for the FDC) and the number of comparison stars were reduced to include only those that are part of the much-smaller FDC field of view. The elimination of several comparison stars resulted in a noisier light curve for each station.

For SOFIA blue (which was later discarded due to inadequate S/N per scale height), the alternate reduction resulted in near-identical emersion results, but a 10

K drop in immersion temperature. The red light curve did not change appreciably.

The alternate light curves were used for the impact parameter study described in Section 5.6.

6.10 Conclusions

Separate immersion and emersion upper atmosphere models were created for nine Pluto occultation light curves that met the S/N per scale height requirements outlined in Section 5.4.3. Choosing a fit that adequately represented the upper atmosphere was quite difficult, making interpreting the asymmetry results for each light curve to be a challenge. However, I found that the temperature difference of the 1988 P8 observations is consistent with zero. Both 2002 August observations of P131.1 agree that the immersion limb is warmer than the emersion limb. However, the UH 2.2-m results suggest a much stronger temperature difference than the CFHT results. Both light curves disagree on the absolute temperature. For the June 2006 P384.2 occultations, the AAT shows a small but firm temperature difference in favor of a warmer emersion. Unfortunately, two additional light curves from P384.2, including one taken at the same observing site, did not meet the minimum S/N per scale height requirement, and were discarded. As for the 2007 March P445.3 event, the Hall and USNO observations completely contradict each other. These light curves are among the noisier light curves in the study. In 2011 June, SOFIA observations of PC20110623 yielded three light curves: SOFIA blue, SOFIA red and FDC. The blue light curve was too noisy for analysis. While the red light curve suggests a warmer emersion, the FDC suggests a warmer immersion.

Overall, if prior temperature asymmetry measurements had been published, such as was the case with the AAT, CFHT, UH 2.2-m and KAO, the new results presented here agreed with the general conclusion about which side was warmer. These agreements show that the *light curves* have a temperature asymmetry. The disagreement between two light curves that should boast the same temperature difference raises the question of whether the temperature asymmetries in the light curves reflect the state

of the atmosphere or random noise greater than the minimum suggested by the error bars, and systematic effects introduced during the light curve's creation. It is difficult to tell because only a few occultation observations in an already small sample set have redundant observations. In the case of the USNO and the Hall, these telescopes are still a few kilometers apart in Pluto's atmosphere. Variations of a few Kelvin may be plausible over small areas. In all cases, the temperature asymmetries seen were not very strong. These temperature differences (and lack thereof) will be considered in the context of occultation location in the following chapter.

Chapter 7

Temperature asymmetries in Pluto stellar occultation light curves III: Discussion

7.1 Introduction

This chapter is the third of three related chapters exploring asymmetries between immersion and emersion limbs of Pluto occultation light curves, and the degree to which the location probed on Pluto affects any temperature asymmetry seen or not seen. The first chapter derived methodologies for determining the reliability of occultation temperature asymmetry measurements. The second chapter examined nine Pluto occultation light curves to determine whether a significant temperature difference exists between the two limbs. This final asymmetry chapter will focus on the temperature differences themselves and examine them in the context of light curve circumstances, discussing average daily insolation (season), immediate insolation (time of day), and terrain surrounding the occultation area.

7.1.1 Pluto's atmosphere in time and space

Quite possibly the most important question about Pluto's atmosphere is how long will Pluto even have an atmosphere? As Pluto travels further away from the sun's warmth, there have been several predictions that Pluto will no longer be capable of supporting an atmosphere. For example, Hansen & Paige (1996) predict collapse starting in 2020, while Young (2013) posits three different scenarios all dependent on the thermal inertia. In the first scenario, a high thermal inertia provides for a permanent atmosphere, and volatile caps with reduced exchange between the two poles. The second and third scenarios, based on middle and low thermal inertias do predict atmospheric collapse, in the most extreme scenarios, collapse will occur before 2015.

Aside from the obvious scientific merits of sending a spacecraft to Pluto, one of the big drivers of getting New Horizons approved in its current time frame has been to reach Pluto before a possible atmospheric collapse happens (Stern, 1993). So far, stellar occultations have shown that neither Eris (Sicardy et al., 2011a), nor Makemake (Ortiz et al., 2012), has an atmosphere, making Pluto unique among dwarf planets in that regard. The authors find high albedos in both cases, perhaps from collapsed volatiles on the surface that could have once been an atmosphere.

When attempting to distinguish atmospheric models, it is important to know whether atmospheric temperature results are a product of their locations. By the time of the 2013 occultations, it should be apparent whether or not Pluto's atmosphere is doomed to an early collapse (Young, 2013).

However, atmospheric models are not perfect. Both Hansen & Paige (1996) and Young (2013) have had difficulties re-creating the south polar cap that persists all the way until the end of southern summer at Pluto's perihelion, and does not fully sublimate. Sublimation of nitrogen ice is an important process in Pluto's atmosphere. For example, diurnal sublimation causes "breathing" of frost surfaces, which may be responsible for vertical structure in the atmosphere (Toigo et al., 2010). However, using time constants supplied by Strobel et al. (1996), Toigo et al. (2010) suggest

that diurnal atmosphere variations should be no more than 0.2 K, a temperature much more precise than the error bars on the best occultation temperature difference in this study.

Pluto's surface, however, has been seen not to be so isothermal. Lellouch et al. (2000) report 60, 100, 150 and 200 μm thermal observations of Pluto's light curve. They find that surface temperatures are anti-correlated with the light curve, though these temperature differences are shifted about 25 $\pm$ 15° in longitude due to thermal inertia. Roughly, Pluto's surface is made up of three components: N_2 ice, CH_4 ice, and tholins[1]. Lellouch et al. (2011) find the majority of the variations in temperature of the thermal light curve are due to tholins, while the surface N_2 ice is isothermal. Tryka et al. (1994) analyze surface temperature as a function of time, and create a model called THERMOD. Like Lellouch et al. (2011), the authors find that maximum temperature occurs not at noon, but at 2 pm. Sunset and sunrise surface temperatures are expected to differ by about 4 K. However, Tryka considered Pluto at equinox, and not today's extreme tilt.

Thus models have predicted temperature asymmetries of the atmosphere ranging from 0 K (Zalucha et al., 2011b) to 0.2 K (Toigo et al., 2010) and surface asymmetries ranging from 4 K (Tryka et al., 1994) to 20 K+ (Lellouch et al., 2000).

7.1.2 Asymmetry data set

In this chapter, my goals are simple: I will take a group of occultation light curves and identify which light curves would be the most likely to exhibit diurnal, seasonal or compositional differences. Then I compare these differences to observed temperature differences or lack thereof.

In Chapter 6, nine Pluto stellar occultation light curves were fit using equations derived in Elliot & Young (1992) and the methods outlined in Chapter 5. After the whole curve was used to establish the occultation baseline and mid-time, separate fits were performed on the immersion and emersion limbs for each chord. Upper atmospheric cut-offs were chosen for each event. Assuming a pure nitrogen atmo-

[1]For details on the reddish-brown compounds described as "tholins", see Sagan & Khare (1979).

sphere, I calculated the difference between atmospheric temperature at the half-light radius for immersion and emersion limbs. Now we will look at the circumstances for each of those light curves. Table 7.1 summarizes the cut-offs, temperature differences (northern hemisphere - southern hemisphere; emersion-immersion), Pluto longitudes and latitudes for both immersion and emersion, ratios of insolation, and whether the curve represented immersion or emersion. These nine light curves represent six different observing stations, as two light curves were taken from each of Mauna Kea in 2002, Flagstaff, AZ in 2007 and SOFIA in 2011.

As the accuracy of the asymmetry fits is discussed in depth in Chapter 6, let us make the following working assumptions without questioning their strength: the P8 (1988) light curve does not have a temperature difference, the P131.1 (2002) light curve models show a warmer immersion (north) side, the P384.2 (2006) light curve has a warmer the emersion (south) side, the P445.3 (2007) and PC20110623 light curves (both SOFIA and the IRTF) do not favor either side. We will compare them against several considerations: average daily insolation (season), immediate insolation (time of day), and terrain surrounding the occultation area.

7.1.3 Surface location calculation method

Before any comparisons between observing sites were made, the locations of immersion and emersion half-light on Pluto were calculated using the following method. First, the sub-Earth point (longitude, latitude and rotation of the pole) of Pluto is interpolated from a PLU022/DE405 JPL ephemeris with three-hour resolution[2]. The velocity of Pluto is converted from arcseconds per hour to kilometers per second, based on the Pluto-Earth distance. This velocity vector determines the direction of the occultation path. A globe of size equal to the half-light radius is drawn. The occultation path is offset from the center of the light curve by the known closest approach[3] to the shadow radius. The (two) intersection points of the circle and the

[2]The pole coordinates for PLU022 are α=6.1764, δ=313.052032, W=237.1753, $\dot{W}$=-56.362478504433917, and can be found at `http://naif.jpl.nasa.gov/pub/naif/generic_kernels/spk/satellites/a_old_versions/plu022.cmt`.

[3]See Table 6.2 for a list of closest approach values for each occultation.

Table 7.1. Summary of occultation light curve circumstances.

Event	Cut-off	Tdiff (E-I)	Tdiff (N-S)	Imm. Long	Imm. Lat	Em. Long	Em. Lat	Imm. TOD	Em. TOD	Imm. Solar Alt.	Em. Solar Alt.	N/S insol
P8 KAO	1150 km	4±5 K	-4±5 K	219°	41°	220°	-51°	sunrise	sunrise	1.29	-0.17	1.3
P131.1 CFHT	1240 km	-8±6 K	8±6 K	106°	55°	241°	-13°	sunset	sunrise	1.31	0.29	2.0
P131.1 UH2.2m	1240 km	-15±7 K	15±7 K	107°	55°	241°	-12°	sunset	sunrise	1.32	0.30	2.0
P384.2 AAT	1225 km	7±3 K	-7±3 K	254°	33°	4°	-52°	sunrise	sunrise	-0.02	0.24	607.9
P445.3 Hall	1150 km	8±7 K	8±7 K	213°	-18°	258°	29°	sunset	sunset	1.37	-0.48	2.7
P445.3 USNO	1150 km	-12±4 K	-12±4 K	213°	-19°	258°	29°	sunset	sunset	1.38	-0.50	2.7
PC20110623 SOFIAfdc	1210 km	-6±4 K	6±4 K	16°	37°	185°	-40°	sunrise	sunset	-0.15	0.17	67.1
PC20110623 SOFIAred	1210 km	7±5 K	-7±5 K	16°	37°	186°	-40°	sunrise	sunset	-0.15	0.17	67.1
PC20110623 MORIS	1210 km	3±4 K	-3±4 K	65°	3°	113°	-34°	sunrise	sunrise	0.04	0.19	8.1

occultation path are considered to be points on a sphere that are then de-rotated in longitude, latitude and north pole angle. The longitude and latitude are then calculated based on the assumption Pluto is perfect sphere. Finally, the coordinates are converted from JPL's "ecliptic north" system to the right-hand rule (see Chapter 2 which discusses these systems in detail).

7.2 Average daily insolation

First, we consider the relative daily insolation between immersion and emersion. Pluto's high inclination and high axial tilt cause Pluto to have rather extreme seasons. For this exercise, I will not take into account surface albedo.

When P8 occurred in June 1988, Pluto was just past equinox and still in the midst of mutual events. Its axial tilt was less than one degree, and its equatorial regions received more light than the poles. Fourteen years later, in 2002, Pluto had tilted to a sub-Earth latitude of 29°. Once an object tilts beyond 21°, its pole will receive more light than the equator, and after 25°, insolation increases monotonically with latitude, allowing more northern latitudes to receive more sunlight. By 2011, Pluto's sub-Solar point had become circumpolar. No occultation can probe at a latitude greater than the circumpolar latitude, nor below the latitude that remains in constant darkness. Thus, the maximum latitude range probable by occultations will decrease until 2031 (Stern & Mitton, 2005b), when Pluto reaches its greatest pole-on configuration.

The amount of daily insolation received is simply the cosine of the angular distance between Pluto and its sub-Solar point. For each occultation, I have estimated the relative insolation by rotating a single meridian throughout one Pluto day, summing the insolation received at each latitude throughout the day. The relative daily insolation is simply the ratio of the cumulative insolation at the latitudes of immersion and emersion sites. Table 7.1 shows the the insolation ratios, comparing not immersion and emersion, but sorth (more light) versus south (less light). By mere chance, the immersion limb of the KAO occultation, located in the northern hemisphere, is at 41°N and receives more light than the emersion limb at 51°S. In every case I shall

examine in this chapter, the more northern occultation site receives more light from the sun each day.

We would expect that temperature differences would correlate with relative insolation received. The smallest insolation ratio (1.3) belongs to P8, an occultation with no significant temperature difference. For P131.1, which favors the warmer northern inversion limb in temperature, the northern limb receives twice as much light as its southern counterpart. While such an insolation difference seems adequate to account for the P131.1 temperature difference, it is actually the second-smallest insolation difference seen between two immersion and emersion sites. The largest insolation ratio belongs to AAT observations of P384.2. With a sub-Solar longitude of 37.8 N, Plutonians at the emersion site of 51.6°S see the sun peak at 0.6° altitude and see light for 5.5% of a Plutonian day. The emersion site is as close to eternal night as possible– hence the more-northern immersion site receives 608 times more light per day. However, the light-starved emersion side was found to be warmer!

In the case of the inconclusive P445.3 and PC20110623 SOFIA occultations, the former's immersion sides have a modest insolation ratio of 2.7, while SOFIA has a ratio of 67.1, due in part to the extreme southern immersion. At 40°S with a sub-Solar latitude of 46°, the SOFIA site sees a noon-time solar peak of 4° altitude and sees sunlight for 16.5% of a Pluto day (which works out to be about an Earth day).

The PC20110623 MORIS light curve shows no temperature difference, despite an insolation ratio of 8.

Figure 7-1 (top) compiles these temperature differences and insolation ratios. A linear least squares fit finds a non-zero but not significantly different from zero, slope of -2.3 $\pm$ 1.9 with a correlation coefficient of -0.33. Such a correlation will be exceeded by random data 39% of the time, meaning that this correlation does not carry any statistical significance. Clearly, no firm connection can be made between relative insolation and temperature difference.

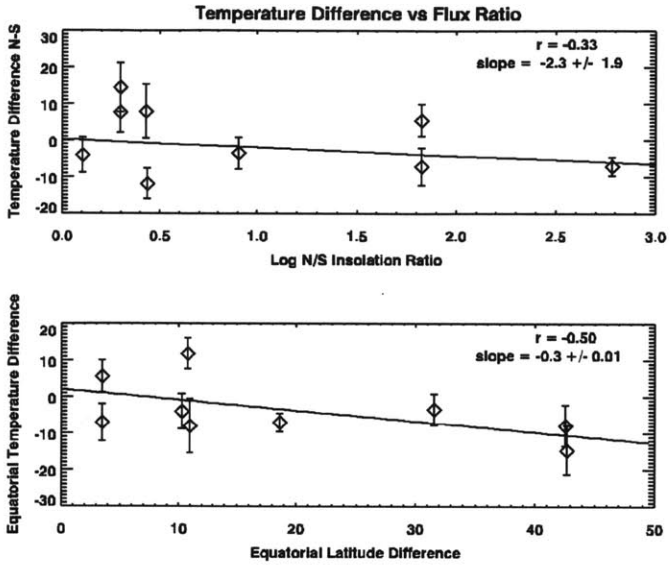

Figure 7-1: Temperature difference versus insolation and equatorial latitude.
Top: North-south temperature difference versus log(insolation ratio) for each occultation site. All northern occultation sites receive more sunlight than their southern counterparts. For all but the P8 KAO observations, the north receives more light because it is northern hemisphere summer on Pluto. For the KAO observations, the northern hemisphere site was coincidently closer to the equator at equinox. The temperature difference should become increasingly positive with increasing insolation ratio. Instead, there is no strong correlation between points. See Section 7.2 for more details.
Bottom: Equatorial temperature difference vs equatorial latitude difference. The difference of the distance of each site from the equator has been calculated, that is to say ||Imm. Lat| − |Em. Lat||. The temperature differences have been similarly recast such the calculated temperature of the site furthest from the equator is subtracted from the site nearest to the equator. These temperature and latitude differences test the predictions of the Zalucha & Gulbis (2012) simple Pluto Global Circulation models described in Section 7.5. The 2-D GCM predictions hypothesize that atmospheric temperatures are warmest closest to the equator, independent of whether a site probes summer or winter hemisphere. To match the GCM predictions, there should be a positive correlation with equatorial latitude difference. Again, there is no correlation.

7.3 Time of day

Second, I consider the time of day of the occultation.

The consensus in the astronomical community is that there should not be strong diurnal effects on Pluto's atmosphere. Trafton & Stern (1983) consider a scenario where the sun's insolation is simply shut off. The authors calculate that it would take 93 days for half of Pluto's atmosphere to freeze out.

Due to Pluto's extreme distance, the immersion and emersion points of an occultation are always somewhere within about a degree of the terminator. Table 7.1 notes whether the immersion or emersion site occurs at sunrise or sunset. Does Pluto's thermal inertia make occultation temperatures colder in the morning, but warmer in the evening? Does the length of the long night make a difference? Arguably, one can only answer these questions for occultation light curves that probe both sunrise and sunset.

In the case of P8, not only are both sides on the sunrise limb, but both sides are at nearly the same longitude. The P384.2 and P20110623 MORIS occultation curves also probe sunrise on both sides. The P445.3 light-curves both probe sunset. Thus, for these four sites, time of day can be discounted relative to insolation as a factor.

What about curves that probe sunset on one side and sunrise on the other? That the emersion side of PC20110623 SOFIA was probed at the end of short winter day while its immersion side probed a summer morning, may not make a substantial difference due the relative lack of sun in the winter hemisphere. In absolute time, the low-latitude's day is shorter than the summer night. As this light curve did not show a clear temperature difference, the implication for this light curve is ambiguous.

The case with P131.1 is more straightforward. The winter morning probed on emersion is in fact colder than the summer evening probed on immersion, as would be expected. However, one positive point is not sufficient to make a clear statement about diurnal effects.

To make a stronger case, we would need at least two more occultations that probe winter sunrise and summer sunset. To probe winter sunrise, and summer

sunset, Pluto must move in a north-south direction in the sky (see Figure 7-2). Pluto generally travels in the east-west direction, but the angle of its motion will change when it reaches a stationary point. In August 2002, when P131.1 was observed, Pluto's occultation angle was in the north-south direction, as Pluto had reached its stationary point. As the time of opposition has shifted to slightly later in the year over the past decade, this time has shifted from August to September. Figure 7-2 also shows the occultation angle for 2013 to 2015 as a function of year. North-south occultations now occur in the months of April and September.

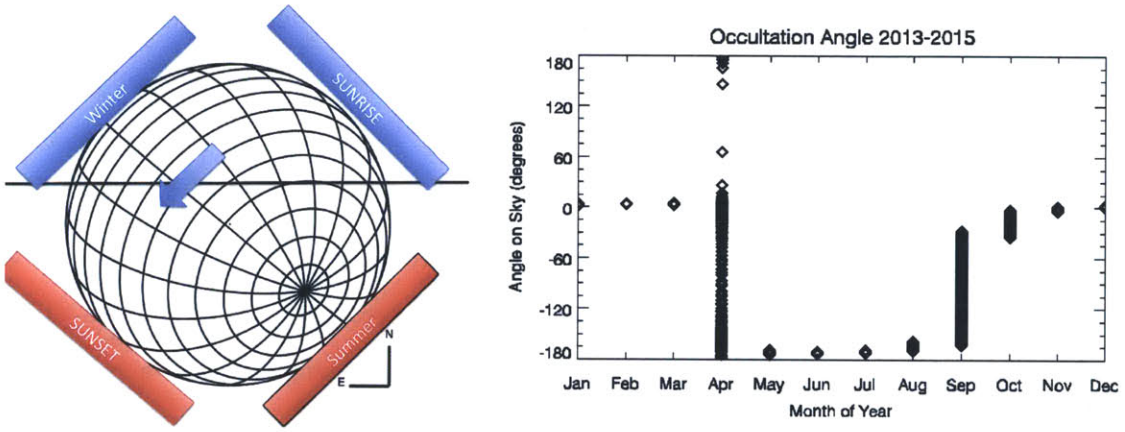

Figure 7-2: Left: Pluto globe with winter hemisphere, summer hemisphere, sunrise, sunset and Pluto rotation marked. A 180° line, similar to the most common occultation angle, has been drawn. To probe summer sunset and winter sunrise, one would need to observe when Pluto is at a stationary point or changing directions on the sky. Right: Occultation angle on the sky versus month of the year for the years 2013-2015 for an ephemeris of resolution 3 hour (PLU022/DE405). Pluto is observable at night from roughly late February to early October. An angle of $\pm 90°$ would result in the north-south motion that would allow for probing summer sunset and winter sunrise. Pluto spends most of the year traveling in the east-west direction, however, it changes from prograde motion to retrograde in April, and returns to prograde motion in September-October. Pluto's angle on the sky is dominated by reflex motion on the Earth. Thus, the best chance to see a slow event with a north-south occultation is in either April or September in 2013 to 2015.

7.4 Comparison with surface maps

7.4.1 A brief history of maps

The earliest attempts to map Pluto's surface were primitive two-spot models (Marcialis, 1988). The first real mapping opportunities were provided by the mutual events: Buie et al. (1992) and Young & Binzel (1993) created maps by mapping Pluto's surface as Charon transited increasingly souther latitudes of Pluto. The original Young & Binzel (1993) maps were later improved upon by Young et al. (1999, 2001), while Grundy & Fink (1996) and Lellouch et al. (2000) created a composition map from Buie et al. (1992).

The most well-known maps are the single-scattering albedo maps created by Stern et al. (1997) based on 1994 HST observations of Pluto. From these maps, composition maps were created by Grundy & Buie (2001) , while Toigo et al. (2010) derived a frost map. In 2010, new versions of the HST maps were published by Buie et al. (2010b). These maps supersede the old HST maps, and are to be the final maps published before New Horizons arrives at Pluto in 2015.

Several less well-known maps were created by Drish et al. (1995) using light curves from the 1950s to the 1980s.

From the myriad of options, I have chosen to compare the occultation site locations against the composition map by Grundy & Buie (2001) and a single scattering albedo map by Buie et al. (2010b). I have chosen the Grundy & Buie (2001) maps due to their inclusion, along with the maps from Stern et al. (1997) in the GEOVIZ New Horizons encounter planning tool. The composition map divides Pluto's surface into three types of terrain: tholins/H_2O, CH_4 and N_2. The average geometric albedo of Pluto's light curve ranges from approximately 0.4 to 0.66 (Lellouch et al., 2000). Based on the distribution of surface types, the authors offer a handful of geometric albedos that reproduce the Pluto visible light curve (0.04-0.23, 0.55-0.66 and 0.72-0.75), but similar measurements do not exist for the newer map of Grundy & Buie (2001). This map allows the identification of terrain differences, and we should take the difference between tholins and methane as more extreme than methane and nitrogen. The Buie

maps were chosen because they were the most up-to-date of any map of Pluto. Buie et al. (2010b) actually features several maps, a false color UV map, and a synthesized true-color map. However, in the case of the latter, the true color map also contained synthesized tholin component in addition to the B and V equivalent HST filters. Here, I will only look at the V maps re-created using the software available online as part of the journal article's supplemental materials. While B maps are directly comparable to photometric data in Chapter 4, the V maps were chosen because their redder wavelength is closer to the typical unfiltered CCD observation, used for most occultations studied here.

The composition map and single-scattering maps are both similar and different. Though both maps feature a dark equatorial band, and brighter poles, when comparing the two maps, it is not immediately apparent that the maps depict the same object. In the case of the Buie maps, the south pole is not as bright as the currently-visible north pole. On the other, hand Lellouch et al. (2000) describe the south polar region as "bright, extended" while the northern region is "somewhat smaller and dimmer". The dissimilarity in physical features between the two (and all other previously published Pluto maps) is somewhat due to the fact that the maps are dependent on the scarce data that make them up. Stern et al. (1997) note that the max entropy models from the mutual events disagree with the Hubble observations, but they "do not yet have enough confidence in the polar regions of our map to attempt to settle this discrepancy, so we stress the fact that the equatorial regions are similar and leave the issue of a polar discrepancy to a future paper". With some of the earlier mutual event maps, some of the albedo features were thought to be due to limb effects (Grundy & Buie, 2001), though such effects are eliminated in later reductions (Buie et al., 2010b). Thus while one map predicts a patch on Pluto's surface may be dark, the other may predict it may be light.

Pluto is known to have the second largest albedo differences in the Solar system, after Iapetus. While the V magnitude of Pluto's light-curve ranges from 15.8 to 16.1 (Tholen & Buie, 1997), a large portion of the differences are due to north-south changes– by nature, a light curve averages areas from north to south.

There are several reasons why these two maps could disagree. Whether by noise, differences in measurement technique or physical changes on Pluto's surface, I will not claim that one map supersedes the other (though arguably the albedo map from 2010 superseded the albedo map the composition map was based upon). Rather I will use each map as a check on the other. If the two maps agree that one occultation location has darker terrain than the other, I will identify that occultation as probing two different areas. If not, then the maps will be considered inconclusive.

7.4.2 My occultation maps

Figures 7-3 and 7-4 show Pluto's surface at the time of the occultation for six of the nine occultations discussed herein. Due to duplicate site coverage, maps from P131.1, P445.3 and SOFIA have been omitted (P131.1 UH2.2-m, P445.3 Hall, PC20110623 SOFIA FDC). A square marks the emersion point and an "x" marks the immersion point. Day/night, sunrise, sunset and the sub-Solar points are labeled. In addition, the numerical average of the pixels that make up surrounding 5° area of each site has been labeled. For composition map in Figure 7-3, an average of 0 represents tholins, an average of 1 represents methane and an average of 2 represents nitrogen. The nitrogen areas should be the most reflective. The single-scattering albedo map of Figure 7-4 contains values from 0 to 1, where 1 represents the most reflective. In all cases, for the single scattering map, the more northern site has a higher albedo. Table 7.2 contains a qualitative description of each sites' composition, the extent of their relative composition differences, and the difference of the single-scattering albedo between the two sites.

In Figure 7-5, the temperature and albedo/composition differences are compared for each individual map. Considering the albedo map alone, a completely insignificant slope of -6 $\pm$ 63 is found. The correlation coefficient of -0.16 is surpassed by random data 68% of the time, also without statistical significance. The composition map fares little better. A slope of 2.7 $\pm$ 2.8 is found. The correlation coefficient of 0.33 is surpassed by random data 39% of the time. Thus there is no statistically significant linear correlation between map depiction and temperature difference.

Table 7.2: Occultation local surface features and map agreement.

Event	North comp.	South comp.	Comp. diff.	Alb. diff.	Maps agree?
P8 KAO	N_2	mostly tholin	large	0.76	Yes
P131.1 CFHT	CH_4	almost CH_4	similar	0.30	Yes
P3842 AAT	mostly CH_4	N_2	small	0.42	No
P4453 USNO	mix CH_4/tholin	almost N_2	moderate	0.58	No
PC20110623 MORIS	tholin	CH_4	moderate	0.09	No
PC20110623 red	mostly tholin	tholin	similar	0.60	Yes

As mentioned in the introduction, areas with tholins have been shown to be more important than nitrogen for determining the surface temperature of Pluto. Thus an occultation that probes an area with tholins and methane compares more varied terrain than occultation sites that compare methane and nitrogen.

In the next section, I will take each occultation event and compare it to both maps.

7.4.3 Individual site analyses

P8 KAO

Of the six occultation sites, the P8 KAO site appears to have the most significantly different terrains and the best agreement between the maps shown in Figures 7-3 and 7-4. The northern emersion site consists of highly reflective nitrogen, and the area surrounding the southern immersion site is made of mostly of dark red tholins. The albedo map show a highly reflective northern site, and the southern site is well-placed within one of the equatorial dark spots, the darkest of any occultation site. The ratio of the two single-scattering albedos is the largest of any of the occultations in Table 7.2, and this event is the only one in which the albedo differences are significantly stronger than the insolation differences. It is curious that the darkest albedo site is not the darkest composition site. Due to the general agreement between maps, it is safe to assume that the occultation sites are indeed sampling two different types of surface on Pluto, the north is bright and reflective, while the south is dark. Arguably, if there were to be any terrain-based differences between occultation limbs, they should occur

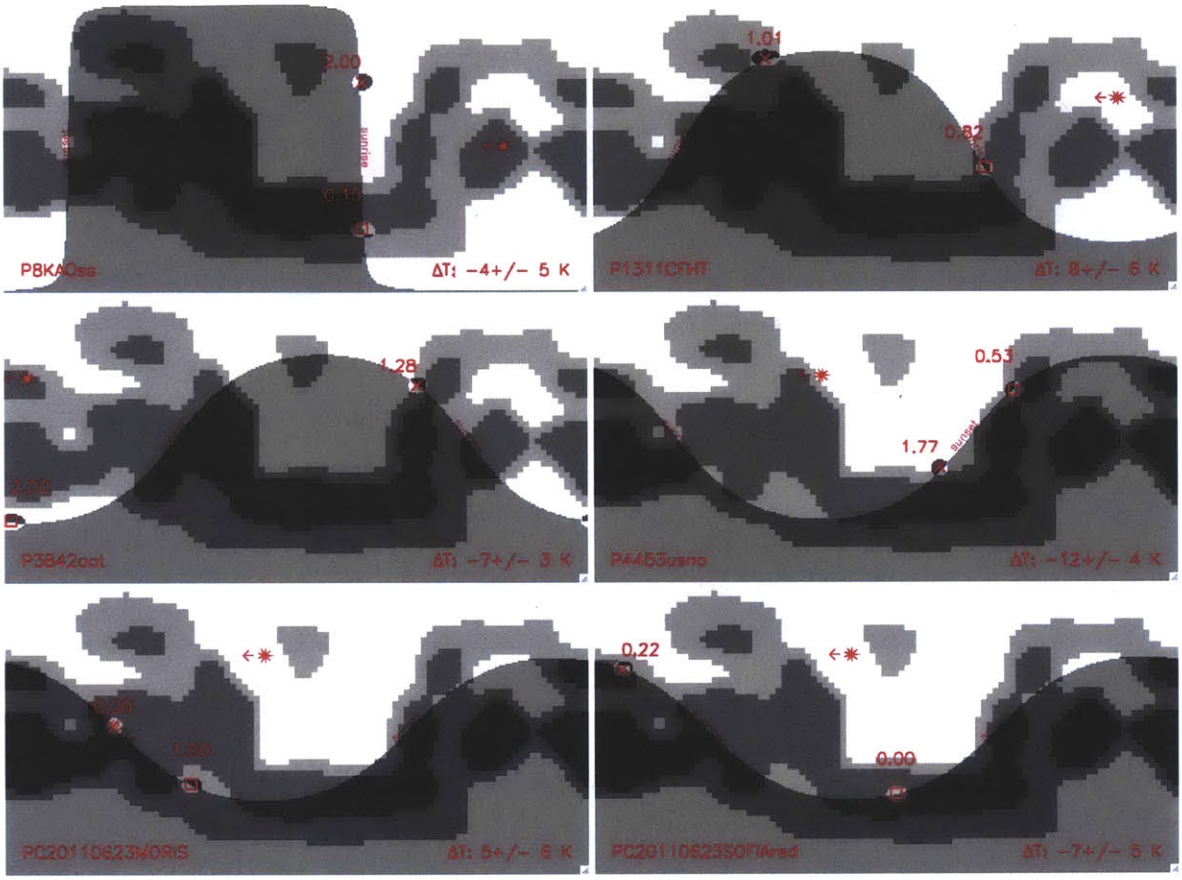

Figure 7-3: Composition maps for P8 KAO, P131.1 CFHT, P384.2 AAT, P445.3 USNO, PC20110623 MORIS and PC20110623 SOFIAred after Grundy & Buie (2001), Figure 10 "Sliced HST Map". This map was generated based on HST albedo maps (Stern et al., 1997), where black designates tholin regions, gray is CH_4 and white is N_2. This map is also part of the GEOVIZ encounter planning tool. Shaded regions denote night, and the nine-point star and arrow mark the sub-Solar point and the motion of the sun across Pluto's surface; the sunrise and sunset limbs are also labeled. The sub-Earth point is omitted for clarity. The Immersion point is indicated by an x while emersion is indicated by a square. The 5° area around each occultation site has been averaged, and the mean surface composition has been labeled. An average value of 2 represents pure nitrogen, a value of 1 represents pure methane, and 0 represents tholins. For these maps, a more northern occultation site, does not necessarily correspond with landing in more reflective area.

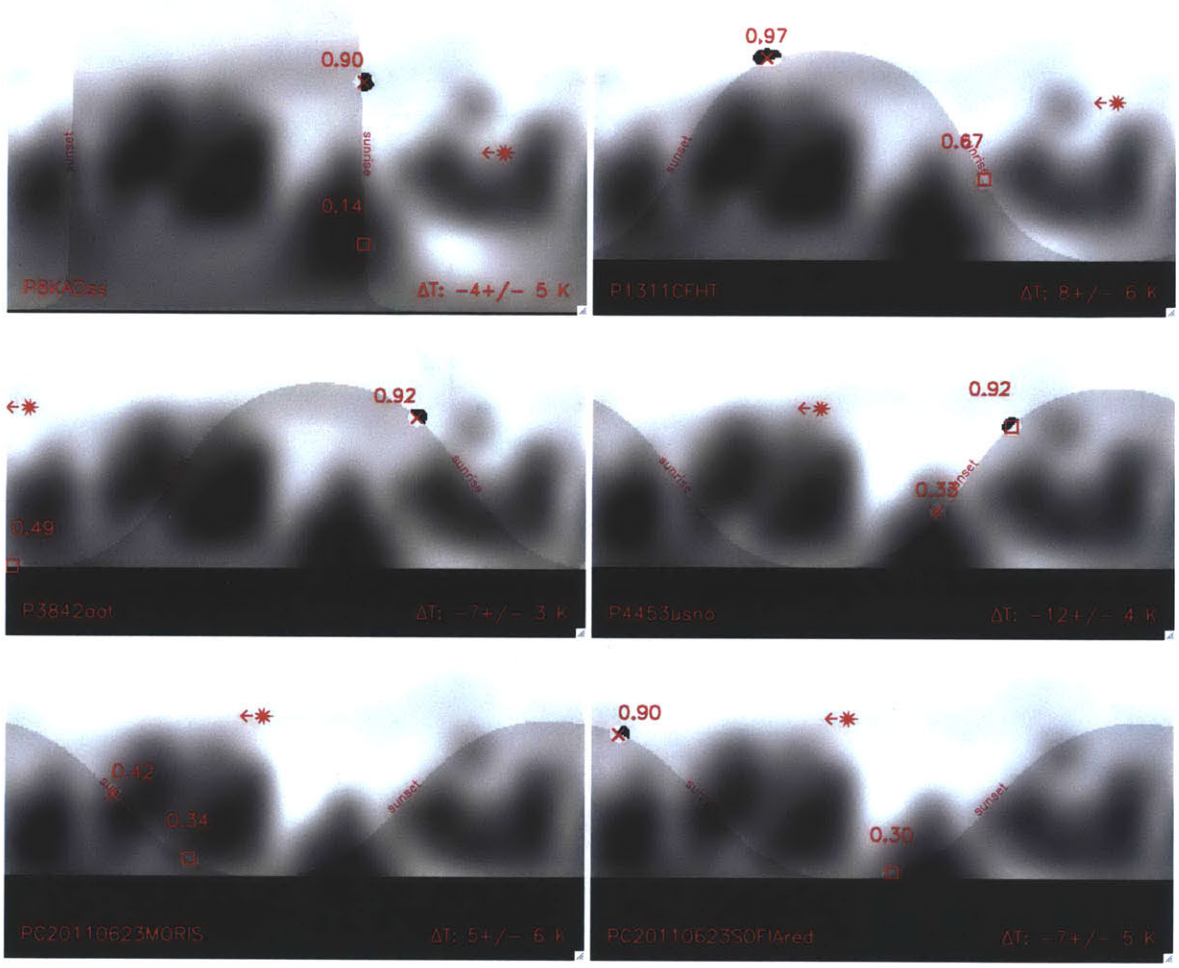

Figure 7-4: Single Scattering albedo maps in V for P8 KAO, P131.1 CFHT, P384.2 AAT, P445.3 USNO, PC20110623 MORIS and PC20110623 SOFIAred, generated from supplemental software published in Buie et al. (2010b). Shaded regions denote night, and star marks sub-Solar point and motion of the sun across Pluto's surface, and sunrise and sunset limbs are labeled. The sub-Earth point is omitted for clarity. Immersion point is indicated by an x while Emersion is indicated by a square. The 5° area around each occultation site has been averaged, and the mean single-scattering albedo for each site has been labeled. For these maps, northern areas have a higher single-scattering albedo than more southern areas. Maps have been orientated in such that the north pole aligns with the angular momentum vector and sub-Earth longitude decreases with increasing time.

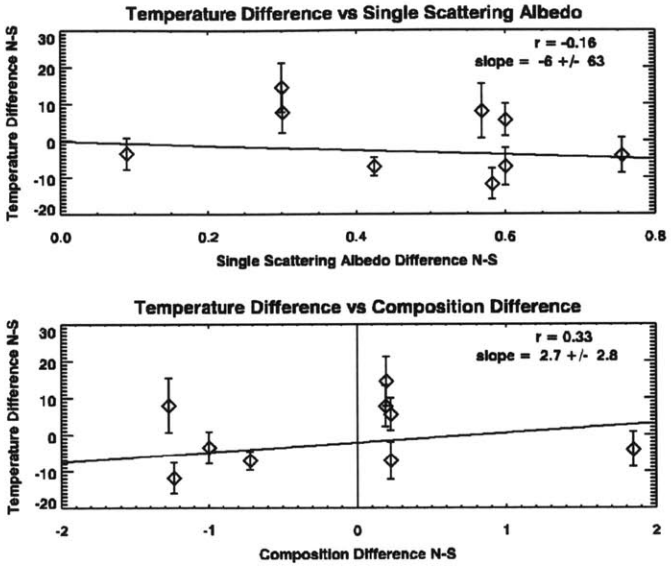

Figure 7-5: Temperature difference versus albedo and composition differences.
Top: North-south temperature difference versus north-south single scattering albedo differences for each occultation site. The single scattering albedo difference is based on the average of pixels within a 5° area surrounding each limb based on the V albdeo maps of Buie et al. (2010b), and pictured in Figure 7-4. By coincidence. northern occultation sites are brighter than their southern counterparts, and thus should be colder based on albedo difference. While the data do show a negative trend with albedo difference, there is no correlation between the data points and albedo difference.
Bottom: North-south temperature difference versus north-south composition differences for each occultation site. The composition differences is based on the average of pixels within a 5° area surrounding each limb based on the composition maps of Grundy & Buie (2001) and pictured in Figure 7-3. The compositions map is divided into three constituents: tholins (0), CH_4 (1) and N_2 (2). Unlike the albedo map, on the composition map, the northernmost sites are not necessarily the brightest. Thus, three of the six occultation sites (P384.2 AAT, P445.3 USNO/Hall, 20110623 MORIS) have conclusions that differ with albedo map, and have negative composition differences. However, the data should still show a negative trend with increasing composition difference if the atmosphere is warmer over darker areas. Treating the composition map independently, we see there is no correlation between temperature and composition difference.

at this site; the two sites receive the most-similar insolation, and the occultation occurs at the same time of day for each site. Furthermore, if any southern site should be warmer based on contributions due to the surface, it should be this one. Instead, the most-unique occultation pattern, with its large knee, is repeated on both limbs, and the scant warmness seen on the more southern site has no statistical significance.

P131.1 CFHT (and UH 2.2-m)

For the P131.1 occultation, two light curves probe winter sunrise and summer sunset. According to the composition map, the northern immersion site is made up of moderately reflective methane, while the immersion site is made up of almost all methane, with a small amount of tholins. Thus, while not completely identical, the sites are very similar in terms of makeup. The albedo maps also points to a marginally brighter north pole, and a still fairly bright southern site. The albedo maps disagree with the composition map, in that the albedo maps suggest that the northern site is the brightest of all northern sites sampled by these occultations, and the southern site is the brightest site sampled by all occultations. However, methane regions are not as bright as nitrogen ice regions seen at other sites. For either map, the difference between the two sites is not as extreme as other sites, nor should it be extreme enough to outdo the contributions from insolation and time of day. Thus the map predicts that the site location should not bias the difference in the direction of a cooler southern area. Indeed, the difference seen is in the direction of the higher insolation.

P384.2 AAT

For P384.2, the composition map and single scattering albedo map disagree about the relative surface compositions. The albedo map, like all other events, shows a brighter northern area and a darker southern area, though the southern area is at the edge of, not a part of the dark equatorial bands. With the composition map, the southern emersion side is fully below the dark equatorial band, and, because of the imprecision of the map, represents an area of nitrogen as bright as the North polar regions. The northern immersion site composition is a mix of methane and

nitrogen, darker by the composition map's standards, but not by much. Thus the composition map predicts a very cold, reflective southern site. The single-scattering albedo, which is not quite twice as strong at the pole, is not nearly enough to overcome the massive insolation ratio between the two sites. Thus these maps, which disagree with each other, cannot explain slightly warmer southern occultation site for the AAT measurements of P384.2.

P453.3 USNO (and Hall)

Like the two light curves disagree on temperature, the two Pluto maps disagree on which surface is more reflective. The single scattering albedo ratio is higher than that of the AAT or CFHT, but not nearly as extreme as the KAO. The composition map shows a darker northern emersion site comprised of a nearly equal mix of tholin and methane, while the southern immersion site is a mix of methane and nitrogen, mostly bright nitrogen. To be fair, both sites are located on an area with all three terrain types in relatively close proximity. Thus, this site is inconclusive.

PC20110623 MORIS

The maps disagree for this observation, in which both points lie around the darker mid-latitude regions. The single-scattering albedo map shows only a very small disagreement between north and south. Indeed the MORIS north emersion observation site is the darkest northern albedo site, and is the only northern site that does not have an albedo greater than 0.9. At 0.42, it is also darker than the albedos of the AAT and the CFHT. The barely darker southern region does not account for the near-equal temperatures in spite of the insolation differences. However, the composition map shows a dark pure tholin region for the north, and bright, methane-only region in the south. An albedo difference between a methane and tholin region is more profound than the methane and nitrogen regions.

PC20110623 SOFIA Red (and FDC)

For the SOFIA sites, the two maps agree with the fundamental conclusion that the north site is more reflective, but disagree about how much. The albedo map shows a very bright northern immersion and a dark, but not extremely dark southern emersion. The composition map shows a mostly dark tholin with some methane northern immersion, but a pure, dark, tholin emersion. As the two occultation light-curves prove inconclusive about which site is warmer, the point is moot.

7.4.4 Maps conclusion

Of the six occultation sites considered, only half (KAO, CFHT and SOFIA) have maps that agree that the same site has a higher albedo than the other. Even then, those sites disagree on the character of such a site. The most extreme (and consistent) site difference occurs with the P8 KAO occultation, a site which boasts a non-significant temperature difference. Additionally, two edges of the light-curve are cosmetically not different.

Currently, we cannot correlate temperature difference with site-location. When New Horizons arrives at Pluto, detailed maps will be made of the surface, and a solar occultation will be observed. While New Horizon's maps could be considered definitive guides to Pluto's surface, if Pluto is found to be undergoing rapid surface changes (or atmospheric collapse), any maps created will be useful only for the few short years sandwiching the Pluto encounter.

7.5 Comparison with Global Circulation Models

Zalucha & Gulbis (2012) provide an extremely detailed picture of the contents of Pluto's atmosphere using a *simple 2-D Pluto Global Circulation Model (GCM).* The best fit GCM results are provided for the 1988, 2002 and 2006 occultations discussed herein[4].

[4]The original GCM papers follow the ecliptic north convention. All latitudes reported in this chapter have been adjusted to match the right hand rule convention.

The 2D global circulation models make the following general predictions:

1. Below ±60° latitude, the temperature of Pluto's atmosphere warms rapidly with altitude above Pluto's surface until it reaches a maximum temperature of 90-120 K. This warmest area rests between 100-200 km altitude above Pluto's surface (assumed in the GCM to be 1180 km). The atmosphere then begins to cool with altitude, but the atmospheric temperature at 500 km (where the model output stops) is still much warmer at 80-90 K than Pluto's surface, which has a temperature of about 40 K. As we measure the half-light radius to range from 1240 km (P8) to 1310 km (P445.3), our model correspond to an altitude range of 60 to 130 km above the surface.

2. The temperature of Pluto's atmosphere decreases towards the poles. Thus equatorial regions are warmer predicted to be warmest. A temperature gradient can be seen starting at latitudes greater than ±50°, even in 2002 and 2006 where Pluto has a non-zero sub-Earth longitude.

Thus the GCM predicts that occultation sites closer to the equator should be warmer, in spite of a large insolation difference between the northern and southern hemispheres. Typically, the atmospheric temperature at ±60° latitude is 10-20 K warmer than the equatorial temperature. We shall compare these GCM predictions with the three occultations modeled. A list of latitudes for each site can be found in Table 7.1:

- For P8, the GCM predicts a slightly warmer temperature for the side of the occultation closest to the equator, in this case the northern immersion site, which does see more insolation. While the actual temperature difference will be altitude dependent, the northern immersion site should be no more than 5 K warmer than the southern site. This is the only occultation that occurs near equinox, and for which insolation received does not monotonically increase with latitude. However, the temperature difference (N-S) of -4±5 found is not significant.

- For P131.1, the GCM predicts a 5-15 K warmer temperature for the southern hemisphere site, which is closest to the equator. However, the northern hemisphere was found to be warmer by 8±6 K and 15 ± 7 K for the CFHT and UH 2.2-m.

- For P384.2, the northern site was closest to the equator, while the southern site was nearly at the southern limit of latitude range probable by occultations at the time. The GCM predicts that the northern site should be warmer by 10 K. Instead, our data result finds the opposite: the winter site, which is also further from the equator than the summer site, is warmer by 7± 3 K.

- There are no GCM fits for P445.3 or PC20110623.

Thus, in both cases where the data indicate a possible temperature difference, the simplified Pluto GCM predicts a temperature difference *opposite* of what is seen with the asymmetric fits. Expanding these predictions to the full set, a linear fit of for all temperatures and latitude differences is shown in Figure 7-1 (bottom). There is a significant slope of 0.30 ± 0.01 K°, and the correlation coefficient of -0.5 is beat by random data 17% of the time. However, this weak correlation is the wrong direction.

GCMs for Pluto are in a constant state of improvement. Recently, Zalucha & Michaels (2013) expanded the 2D GCM to a 3D model. The 3D GCM temperature distribution predicts that the atmosphere temperature between 100 km and 200 km above Pluto's surface constant is with latitude. Future improvements, which include frost cycles and methane transport are planned.

7.6 Discussion: an isothermal atmosphere for Pluto

We have considered the temperature differences calculated in the previous chapter against three metrics: insolation, time of day and map location. In most cases, the temperature differences cannot be explained by location on Pluto. While the P131.1 occultation matches insolation and time of day predictions, occultations with stronger insolation differences, such as those with the P384.2 AAT occultation do not

follow that metric. As for differences with maps, P8, the occultation that samples the two most-different surfaces is one with statistically identical temperatures. Once Pluto occultations are subdivided into so many categories, we find ourselves making conclusions based on just one or two data points, when perhaps three to five light-curves are needed before a conclusion beyond "not enough information" can be made. With evidence of contradictory light curves, such as SOFIA red and FDC, and USNO and Hall, it may be wisest to concentrate efforts on acquiring high signal-to-noise Pluto occultation light-curves with fantastic localized agreement.

In the absence of any compelling trend that explains temperature difference with respect to the location of the immersion and emersion sites, we consider three plausible explanations:

The first explanation is that we simply do not have enough data to make a compelling conclusion. Our nine excellent stellar occultation light curves reduce themselves to six stellar occultation observing sites, only four of which do not have conflicting difference measurements. From these four, only one event (P131.1) had immersion and emersion sites that were arranged to probe diurnal variations. As each temperature difference is not extremely significant within the error bars, only many repeated measurements can confirm such specific hypotheses against expected measurement error due to noise.

The second explanation is that there could be as-yet-unaccounted-for systematic effects that alter the temperature difference results. In addition to an inappropriate cut-off choice and light curve spikes, camera problems, a poor choice of comparison star, and scattered background light are just a few of many things that could cause a light curve to display a false temperature difference. Re-reduction of light-curves could provide different temperature results.

The final explanation is that Pluto's atmosphere may be isothermal with longitude and latitude. At the beginning of this chapter, we noted that we would assume that the temperature differences calculated in Chapter 6 and summarized in Table 7.1 would be treated as an absolute measurement. However, even the most extreme temperature difference (USNO) has a result no greater than 3-σ. Thus, there are no

truly extreme temperature differences measured, and what we see is noise centered about a measurement of an isothermal atmosphere.

We calculate a weighted mean and standard error for each north-south temperature difference:

$$\Delta T_{N-S} = -3.0 \pm 1.5K. \tag{7.1}$$

This temperature difference, while favoring Pluto's southern pole, which is darker in both insolation and albedo, is not significant relative to the error bar. Given that surface temperature differences are clearly seen in Pluto's thermal light curve (Lellouch et al., 2000, 2011), a lack of a strong temperature difference in the atmosphere suggests that Pluto's atmosphere and surface are not strongly coupled. Instead, some sort of equalizing force must efficiently redistribute heat from warmer regions to colder regions. Both 2D and 3D GCMs (Zalucha & Gulbis, 2012; Zalucha & Michaels, 2013) predict that Pluto should have winds of greater than 100 ms^{-1} blowing in the prograde direction. While the 2D GCM models do predict a non-uniform temperature distribution with latitude, an isothermal atmosphere is consistent with the output of the 3D GCM model.

A lack of change in Pluto's atmospheric temperature based on season or immediate insolation is consistent with high thermal inertia. While calculating a precise thermal inertia is beyond the scope of this work, a low thermal inertia atmosphere will be more prone to early collapse. In any event, a single calculation of thermal inertia is not enough to give Pluto's atmosphere a complete reprieve, as its fate is degenerate with the amount of N_2, albedo and emissivity (Young, 2013).

In addition to an optimistic outlook on continued employment, a lack of strong temperature asymmetries in Pluto's atmosphere also spells good news for those attempting to monitor the atmosphere via stellar occultation. It confirms the reliability of using a single atmospheric measurement as representative of global, time-based atmospheric trends. This work is timely because as Pluto tilts to a more pole-on orientation, the range of latitudes probe-able by stellar occultation is shrinking with each passing year. Whether bright or not, the polar regions will become increasingly

inaccessible to stellar occultation.

Chapter 8

Conclusions

Over the past six chapters, I have discussed several projects, related directly or tangentially to stellar occultations by Pluto:

- In Chapter 2, I discussed the results of a survey that catalogued the use of longitude and latitude on Pluto in almost all published research papers on Pluto from the late 1970s until 2012. Clear descriptions of Pluto coordinates can reduce confusion between the systems.

- In Chapter 3, I report several tests of the HIPO instrument in the laboratory. Despite disturbances, under laboratory conditions, HIPO is capable of producing photometry as good as one part in 10^4, stable over about a 10 minute period. In 2011, HIPO was mounted on SOFIA and used to observe an occultation by Pluto.

- In Chapter 4, the Charon-Pluto light ratio was calculated for the B, g′, r′, i′, and z′ filters using LDSS-3 data from 2011 and 2012. While Charon is brightest relative to Pluto when observed in shorter wavelengths, an average light ratio of 0.142 ± 0.003 was found for the r′ filter at a phase angle of 1.15°, a result that is significantly different from the previous 0.15 magnitude estimate. The dimmer ratio should shift stellar occultation prediction paths by about 150 km. Although our data set did not sample the sub-Earth longitudes of minima or maxima seen with previous HST measurements, there is evidence of periodic

variations in the light ratio for some filters. In sub-arcsecond seeing, reasonable results can be derived from ground-based data when compared to HST. Charon's solar phase has a strong impact on the light ratio, especially for data taken a low phase angle.

- Chapter 5 contains several tests to determine the reliability of stellar occultation asymmetry measurements, using simulated occultation light curves. The value of λ_{Hi} for an occultation fits changes with altitude in situations with haze, and can be used to determine an occultation cut-off. Light curves with a signal-to-noise per scale height of 100 or greater can be used to accurately compare temperatures.

- In Chapter 5, it was also determined that an occultation impact parameter error of 100 km should have no bearing on the ability of a light curve model to probe an occultation asymmetry.

- In Chaper 6, nine light curves were modeled to determine temperature differences between immersion and emersion limbs. Occultation temperature differences can be found for the P384.2 AAT light curve and the P131.1 CFHT light curves. Dual observations of P445.3 and PC20110623 provide contradictory asymmetry information.

- In Chapter 7, the occultation light curve immersion-emersion differences (or lack thereof) were considered with respect to location on Pluto. No meaningful correlations between temperature difference, insolation, season or surface features were found. Thus, on average, Pluto's north-south atmospheric temperature difference is -3.0 $\pm$ 1.5 K. This null results confirms several prior predictions of a spatially isothermal atmosphere for Pluto, and suggests a high thermal inertia.

THE END.

Appendix A

IRAF PSF fitting procedure

The following instructions detail the process for fitting a variable PSF to images from LDSS-3 using **daophot** in IRAF and several custom packages written by AMZ. These instructions assume that the image name is of the format ccd.xxxx.fits.

Daophot setup

Datapars entries for LDSS3:

keyword	input
fwhmpsf	4[a]
datamin	10
sigma	15[a]
gain	egain
ccdread	enoise
exposur	exptime
filter	filter
airmass	airmass
obsttime	ut-time

a. Typical value. Will be changed for each image

DAOPARS entries for LDSS3

keyword	input
function	gauss,moffat15,moffat25,penny1,penny2
varorder	2
nclean	3
matchrad	3
psfrad	21[a]
fitrad	3.4[b]

a. Set to reflect minimum Pluto-Charon separation. Or FWHM +0.1 per each image

b. Typical value. Will be changed for each image or left to a value large enough to include all light above background for the brightest non-saturated star on the image with the largest FWHM.

other entries for LDSS3

task	keyword	input
photpars	apertur	10
fitskypars	annulus	45
fitskypars	dannulus	10

Plate scale =0.1889

PSF fitting steps

1. `IRAF> disp ccd.xxxx 1`

2. `IRAF> imexam "" 1` Locate target star and strike `a` key. Use "moffat" as FWHM. Strike `m` key on patch of blank sky near target, let "median" be SKY value.

3. `IRAF> epar datapars` Update: `fwhmpsf`=FWHM, `sigma`=$(\sqrt{(SKY * 0.64 + 5.44^2)}/0.64) - 1$ (round to nearest whole number)

4. `IRAF> epar daopars` Update: `fitrad=FWHM+0.1`

5. `IRAF> daofind ccd.xxxx` Find stars in image. If noise has been identified as stars, increase `sigma` in **datapars**. If more stars are needed, decrease `sigma`.

6. `IRAF> tvmark 1 ccd.xxxx.coo.1` Manually inspect pertinent parts of the image for missing, but known objects (e.g. Charon). Add by including rerunning with `inter+` and pressing an `a` over each missing object with `q` to quit. The `l` command will display all stars currently in the `.coo` file.

7. `IRAF> phot ccd.xxxx` Makes photometry list with contents of `.coo` file.

8. `IRAF> pstselect ccd.xxxx` Selects 170 candidate PSF stars with no sources brighter than target star within `fitrad` + `psfrad` pixels.

9. `IDL> repst,'ccd.xxxx',1,1` AMZ custom package. Looks at files `ccd.xxxx.mag.1` and `ccd.xxxx.pst.1`. Removes sources from `ccd.xxxx.pst.1` that have ANY stars within 3.1 *`fitrad`. Adjust numerals to latest `.mag` and `.pst.` numbers respectively. From 70-100 stars should be eliminated.

10. `IRAF> psf ccd.xxxx default default inter+` Use `a` and `d` keys to accept and reject candidate PSF stars. Reject stars that appear to have more than one star in the radial profile, or large neighbors in the wings.

11. `IDL> killneighbor,'ccd.xxxx.psg.1'` AMZ custom package. Determines minimum distance of any neighbor star and offers that distance minus `fitrad` to be used as X in `nstar` and `substar` steps as an adjustment for `psfrad`. If a psf star contains a member of its group closer than 3.1*`fitrad`, a new `pst` file is created without those stars and the program asks the user to rerun PSF.

12. `IRAF> nstar ccd.xxxx ccd.xxxx.psg.1 psfrad=X` Models but does not subtract stars selected as part of the PSF model and their "neighbors" and "friends of neighbors".

13. `IRAF> substar ccd.xxxx default "" psfrad=X` Subtracts stars selected as part of the PSF model and their "neighbors" and "friends of neighbors".

14. `IDL> examcompstar,'ccd.xxxx',1,1` AMZ custom package. Creates a `.cl` file that will create a small image of each compstar juxtaposed with its subtracted version in its own folder. File makes "chi" output from **nstar** be the header value for the `OBJECT` field (will show up in DS9). If necessary, adjust numerals to latest `.nst` and `.sub.` numbers respectively.

15. `IRAF> cl < ccd.xxxx.nst.1.check.cl` AMZ custom `.cl` file. Performs actions from **examcompstar** and starts **imexam** with a log file open. Page through stars using `n` and `p` keys. Using `x` add unfound neighbor stars. Eliminate bad PSF stars entirely with `y`. Recommended: make concentric circles of size psfrad and 1.5*psfrad+4.0*fitrad to identify how far out neighbors SHOULD have been found. The program is robust enough to handle multiple visits to the same image and SINGLE accidental strikes of the `a` and `m` keys.

    Press `q` to quit.

16. `IDL> addneighbor,'ccd.xxxx',1,1,1,3` AMZ custom IDL package. Takes result from **imexam** log file and adjusts `.coo` and `.pst` files accordingly, *i.e.* adds missed neighbor stars to photometry file and removes bad star from psf file. The package can handle multiple designations of a star as bad, but multiple identifications of the same star will be added multiple times. They should be deleted from the **imexam** log file by hand. If new stars have been identified on a star that is also bad, they will STILL be added to the new `.coo` file. The location of the **imexam** log file is specified in the last line of the `.cl` file, but it should be ccd.xxxx.nst.1.checkstar/ccd.xxxx.sub.1.check.txt. If necessary, adjust numerals to latest `.nst`, `.sub`, `.coo` and `.pst` numbers respectively.

17. `IRAF> phot` Performs photometry on ccd.xxxx and its new `.coo` file which contains all the old stars and ALL the new stars. Making a routine that simply perform the new photometry, then concatenate the two files is under consideration.

18. `IDL> repst,'ccd.xxxx',2,4` AMZ custom IDL package. Run repst again, this

time removing stars who have newly ID'd neighbors that are a little too close. Hopefully there will not be too few neighbors. If needed, adjust numerals to latest `.mag` and `.pst.` numbers respectively.

19. `IRAF> psf` Makes a new PSF star model with pesky neighbors included and bad stars gone. Default file names and settings all filled out as described above make no input required.

20. `IDL> killneighbor,'ccd.xxxx.psg.2'` AMZ custom IDL package. Run to get new PSFRAD as Y below.

21. `IRAF> nstar ccd.xxxx ccd.xxxx.psg.1 psfrad=Y` Models but does not subtract stars selected as part of the PSF model and their "neighbors" and "friends of neighbors".

22. `IRAF> substar ccd.xxxx default default psfrad=Y` Subtracts stars selected as "neighbors" and "friends of neighbors" of PSF model stars, but not the model stars themselves. (Hence the second default– omitted in Davis and Massy '92).

23. `IRAF> psf ccd.xxxx.sub.2 ccd.xxxx.mag.2 ccd.xxxx.pst.6` Remake PSF without neighbor stars at all! Note all files have to be typed in. Numbers assume that procedures were followed exactly, otherwise, adjust accordingly.

24. `IRAF> allstar ccd.xxxx default ccd.xxxx.sub.2.psf.1` PSF fit ALL THE STARS!

25. `IRAF> disp ccd.xxxx 2` Use "match frames physical" and blink to examine fits. If dissatisfied with PSF model, make a new one.

26. If more stars need to be added, do so either by rerunning daofind and concatenating the new photometry. You may rerun **allstar** using the same command as above.

27. You may need to "aperture correct', but I've never done this.

28. Organize your results in a useable form. I like to make a note of the best `.als` file and move all the files associated with a completed image to their own directory, often all.ccd.xxxx

Appendix B

LDSS-3 2011-2012 Charon-Pluto differential magnitudes

This appendix contains a Table of the full list of images that make up the LDSS-3 data set. The purpose of the table is to have a written record of which images make up the plots in Chapter 4. The first several columns, which cover the image number (the first of which is the night number), filter, full width half maximum for Pluto, Pluto X coordinate, Pluto Y coordinate, Charon X and Y offsets, Pluto Instrumental Magnitude, Charon Magnitude difference and its error, are self-explanatory. The second to last column indicates whether the image's results were eliminated via the method described in Section 4.6.3 and illustrated in Figure 4-5 on page 95. The final column indicates how many fits were attempted before the final fit was arrived at, essential for reconstruction of these fits by another person.

Table B.1. Charon-Pluto magnitude difference for LDSS-3, all finished images

Image	JD midtime	Filter	FWHM	Pluto X	Pluto Y	Ch X off	Ch Y off	Pl Inst. Mag.	Ch Mag	Diff	Diff. Err	IsGood	Fit Number
0129	2455627.86034	g	5.12	1050.44	689.28	1.86	3.79	12.16	2.06	0.02	0	1	
0130	2455627.86350	g	5.27	1050.89	691.19	1.58	3.73	12.13	1.77	0.02	1	2	
0131	2455627.86502	g	5.34	1103.93	638.41	1.67	3.73	12.16	1.74	0.01	1	1	
0132	2455627.86575	g	5.67	1104.31	638.33	1.90	3.52	12.17	1.82	0.02	0	1	
0133	2455627.86649	g	5.32	1156.69	585.80	1.85	3.46	12.08	2.10	0.03	0	1	
0134	2455627.86722	g	5.63	1209.85	533.20	1.83	3.60	12.14	1.89	0.01	0	2	
0136	2455627.87110	i	3.67	1315.05	430.91	1.86	3.57	11.33	2.09	0.02	0	1	
0137	2455627.87177	i	3.78	1367.59	377.99	1.93	3.55	11.35	2.11	0.02	0	3	
0138	2455627.87243	i	3.51	1390.69	474.89	4.30	9.21	11.05	6.20	0.15	1	1	
0139	2455627.87309	i	3.80	1364.22	501.36	15.46	5.58	10.94	5.52	0.02	1	1	
0140	2455627.87388	r	3.39	1045.54	704.01	1.87	3.52	11.35	2.03	0.02	0	1	
0141	2455627.87466	r	3.24	1019.04	730.11	1.89	3.57	11.30	2.10	0.01	0	1	
0142	2455627.87534	r	3.27	992.08	757.59	1.83	3.55	11.28	2.06	0.01	0	2	
0143	2455627.87601	r	3.80	965.58	783.47	1.92	3.51	11.30	1.97	0.02	0	1	
0144	2455627.87667	r	3.02	939.20	811.14	1.85	3.56	11.22	2.05	0.01	0	1	
0145	2455627.87737	z	2.70	1045.09	707.75	1.88	3.53	12.21	2.03	0.03	0	2	
0146	2455627.87820	z	3.00	1018.60	734.38	1.84	3.55	12.38	2.00	0.02	0	2	
0147	2455627.87887	z	3.06	991.76	761.28	1.85	3.61	12.37	2.07	0.02	0	1	
0148	2455627.87955	z	3.23	965.10	788.33	1.87	3.59	12.35	2.05	0.02	0	1	
0149	2455627.88023	z	2.86	937.84	815.15	1.92	3.60	12.28	2.08	0.02	0	1	
0150	2455627.88091	z	2.45	912.24	840.94	1.84	3.61	12.30	2.05	0.02	0	2	
0152	2455627.88250	B	3.76	1071.02	680.01	3.22	1.75	12.81	4.73	0.39	1	1	
0153	2455627.88324	B	3.87	1097.25	653.35	3.21	2.55	12.80	4.72	0.45	1	2	
0154	2455627.88397	B	3.72	1124.14	627.27	1.85	3.61	12.78	1.79	0.02	0	1	
0155	2455627.88471	B	4.04	1150.73	600.52	1.81	3.63	12.79	1.78	0.02	0	2	
1118	2455628.85940	g	5.16	663.95	1038.56	0.57	3.62	12.12	3.53	0.09	1	1	
1119	2455628.86023	g	5.24	984.22	1039.58	-0.20	2.93	12.20	2.69	0.05	1	2	
1120	2455628.86292	g	5.10	984.11	1040.49	1.50	4.03	12.22	3.57	0.08	1	1	
1121	2455628.86424	g	5.23	983.71	1041.07	0.41	3.37	12.23	3.26	0.07	1	1	
1122	2455628.86492	g	4.95	983.76	1041.82	4.14	1.46	12.19	1.91	0.01	0	1	
1123	2455628.86560	g	5.13	983.45	1040.83	4.14	1.47	12.19	1.94	0.02	0	1	
1124	2455628.86630	g	5.54	983.77	1042.50	4.12	1.53	12.20	1.92	0.02	0	1	
1125	2455628.86737	r	4.73	983.42	1046.01	4.08	1.44	11.39	2.03	0.02	0	1	
1126	2455628.86819	r	4.46	982.63	1046.05	4.16	1.47	11.36	2.06	0.01	0	1	
1127	2455628.86887	r	5.17	982.66	1045.56	4.14	1.58	11.35	2.08	0.02	0	1	
1128	2455628.86954	r	4.71	982.65	1045.75	4.11	1.47	11.32	2.05	0.02	0	1	
1129	2455628.87021	r	4.45	983.53	1045.40	4.10	1.42	11.32	2.07	0.01	0	1	

Table B.1 (cont'd)

Image	JD midtime	Filter	FWHM	Pluto X	Pluto Y	Ch X off	Ch Y off	Pl Inst. Mag.	Ch Mag	Diff Diff. Err	IsGood	Fit Number
1130	2455628.87094	i	4.00	982.62	1047.67	4.14	1.43	11.42	2.09	0.02	0	1
1131	2455628.87178	i	3.99	982.48	1048.40	4.12	1.42	11.44	2.10	0.01	0	1
1132	2455628.87247	i	4.03	981.82	1048.07	4.18	1.35	11.42	2.13	0.02	0	1
1133	2455628.87314	i	3.97	982.34	1049.06	4.17	1.38	11.44	2.13	0.02	0	1
1134	2455628.87380	i	4.10	981.93	1048.60	4.13	1.39	11.42	2.08	0.02	0	1
1135	2455628.87453	z	4.56	982.64	1049.26	4.03	1.40	12.36	2.03	0.02	0	1
1136	2455628.87554	z	3.41	983.09	1049.07	4.11	1.42	12.26	2.06	0.02	0	1
1137	2455628.87641	z	3.46	982.84	1049.97	4.16	1.36	12.27	2.08	0.02	0	1
1138	2455628.87710	z	3.07	982.49	1050.80	4.15	1.35	12.27	2.07	0.01	0	1
1139	2455628.87781	z	3.04	982.82	1050.29	4.12	1.41	12.28	2.06	0.02	0	2
1140	2455628.87850	z	3.50	983.08	1049.97	4.15	1.38	12.27	2.09	0.02	0	1
1141	2455628.87921	z	10.86	982.69	1050.82	4.13	1.48	12.22	2.07	0.02	0	1
1142	2455628.88007	B	4.38	984.11	1047.41	4.10	1.46	12.84	1.80	0.01	0	1
1143	2455628.88087	B	4.82	984.04	1047.53	4.10	1.44	12.82	1.81	0.01	0	1
1144	2455628.88160	B	4.65	983.90	1047.98	4.12	1.35	12.83	1.80	0.01	0	1
1145	2455628.88234	B	4.05	983.91	1048.08	4.11	1.38	12.85	1.77	0.01	0	1
1146	2455628.88307	B	4.22	983.92	1048.70	4.07	1.39	12.84	1.76	0.01	0	1
2110	2455629.85802	g	5.89	960.28	1346.07	3.00	-1.85	12.16	2.10	0.03	1	1
2113	2455629.86019	g	6.11	961.10	1345.15	3.01	-1.93	12.09	2.41	0.03	1	1
2114	2455629.86088	g	5.75	960.90	1346.72	2.52	-1.66	12.19	1.79	0.03	1	1
2115	2455629.86157	g	6.04	960.64	1346.64	2.68	-1.68	12.19	1.86	0.02	1	1
2116	2455629.86240	r	5.56	959.86	1350.21	2.65	-1.76	11.46	1.95	0.04	0	1
2117	2455629.86306	r	5.78	959.84	1349.47	1.91	-1.60	11.48	1.35	0.02	1	1
2118	2455629.86373	r	6.68	959.94	1348.47	3.43	-2.19	11.46	2.63	0.06	1	1
2119	2455629.86440	r	6.17	959.48	1349.59	3.83	-2.17	11.35	3.15	0.06	1	1
2120	2455629.86507	r	5.79	958.15	1350.86	2.55	-2.03	11.38	2.37	0.04	0	2
2121	2455629.86583	i	5.46	958.47	1350.90	2.52	-2.29	11.48	2.24	0.03	1	2
2125	2455629.86851	i	5.47	959.75	1353.89	3.09	-2.25	11.31	2.54	0.03	1	1
2127	2455629.87005	z	6.10	960.33	1354.59	2.47	-1.05	12.48	1.40	0.04	1	2
2128	2455629.87076	z	6.06	959.48	1354.75	2.54	-2.05	12.40	1.89	0.02	0	2
2152	2455629.89039	i	4.14	969.11	1374.95	2.81	-2.00	11.39	2.22	0.03	0	1
2153	2455629.89106	i	4.70	970.49	1374.82	2.74	-1.91	11.34	2.08	0.03	0	1
2154	2455629.89172	i	4.36	969.20	1374.74	2.72	-2.10	11.26	2.29	0.02	0	1
2155	2455629.89251	z	4.03	970.11	1375.69	2.60	-2.15	12.31	2.15	0.04	0	1
2156	2455629.89321	z	4.06	969.58	1375.51	2.76	-1.99	12.28	2.12	0.03	0	1
2157	2455629.89391	z	3.65	970.24	1375.99	2.72	-2.00	12.29	2.11	0.02	0	1
2158	2455629.89483	B	5.16	970.91	1372.65	2.68	-2.13	12.79	1.98	0.02	0	1

Table B.1 (cont'd)

Image	JD midtime	Filter	FWHM	Pluto X	Pluto Y	Ch X off	Ch Y off	Pl Inst. Mag.	Ch Mag	Diff	Diff. Err	IsGood	Fit Number
2159	2455629.89564	B	5.02	971.14	1373.04	2.57	-1.90	12.83	1.79	0.02	0	1	
2160	2455629.89640	B	5.82	971.02	1373.52	1.39	-3.24	13.20	0.20	0.06	1	1	
2161	2455629.89719	g	4.54	969.96	1372.81	2.57	-2.02	12.07	1.94	0.03	0	1	
2162	2455629.89788	g	4.59	969.71	1373.38	2.64	-1.98	12.09	1.97	0.03	0	1	
2163	2455629.89858	g	4.75	969.86	1373.22	2.75	-1.99	12.08	2.02	0.02	0	1	
2173	2455629.90880	g	4.11	975.21	1390.49	2.68	-2.01	12.05	2.03	0.02	0	1	
2174	2455629.90993	g	4.56	975.29	1390.93	2.53	-2.02	12.11	1.90	0.02	0	1	
3029	2455639.85475	g	4.10	1026.21	713.10	-1.31	3.03	11.88	1.83	0.02	0	1	
3030	2455639.85551	g	4.06	1026.19	712.71	-1.31	3.11	11.91	1.88	0.02	0	1	
3031	2455639.85619	g	4.50	1026.46	712.87	-1.38	3.03	11.90	1.81	0.02	0	1	
3032	2455639.85688	g	4.03	1026.04	713.92	-1.32	3.08	11.88	1.89	0.03	0	1	
3033	2455639.85756	g	3.92	1026.31	713.31	-1.34	3.02	11.86	1.83	0.02	0	1	
3034	2455639.85914	r	3.44	1025.22	716.14	-1.23	3.11	11.22	2.15	0.03	0	1	
3035	2455639.85979	r	3.96	1025.45	716.36	-1.24	3.08	11.28	2.17	0.03	0	1	
3036	2455639.86043	r	3.74	1025.16	717.16	-1.38	3.03	11.25	2.19	0.03	0	1	
3037	2455639.86108	r	3.91	1025.17	717.06	-1.33	3.06	11.15	2.24	0.03	0	1	
3038	2455639.86173	r	4.70	1025.69	715.55	-1.61	2.85	11.28	2.09	0.03	1	1	
3039	2455639.86322	i	3.45	1024.88	717.54	-1.28	2.96	11.26	2.12	0.03	0	1	
3040	2455639.86388	i	3.65	1025.02	717.99	-1.36	2.98	11.28	2.17	0.03	0	1	
3041	2455639.86454	i	3.45	1024.39	719.02	-1.34	2.95	11.27	2.16	0.03	0	1	
3042	2455639.86521	i	3.53	1024.73	718.47	-1.27	2.96	11.23	2.09	0.03	0	1	
3043	2455639.86587	i	3.38	1024.99	718.71	-1.23	3.00	11.21	2.20	0.03	0	1	
3044	2455639.86666	z	4.35	1025.87	718.80	-1.39	2.92	12.17	2.26	0.03	0	1	
3046	2455639.86806	z	4.88	1025.38	719.39	-1.29	3.11	12.24	2.20	0.03	0	1	
3047	2455639.86876	z	4.04	1025.93	719.46	-1.21	3.11	12.23	2.22	0.05	0	1	
3049	2455639.87028	B	5.72	1024.88	716.54	-1.20	2.65	13.28	1.51	0.03	1	1	
3050	2455639.87101	B	5.44	1024.64	717.28	-1.23	3.24	13.18	2.01	0.03	0	1	
3051	2455639.87174	B	4.82	1024.72	717.04	-1.36	3.20	13.17	2.04	0.03	0	1	
3052	2455639.87248	B	4.47	1024.91	717.25	-1.26	3.27	13.18	1.97	0.02	0	1	
3053	2455639.87321	B	4.86	1024.61	717.15	-1.30	3.14	13.19	1.88	0.02	0	1	
4037	2455640.86083	g	5.29	1037.33	954.11	2.53	3.49	12.07	1.91	0.03	0	1	
4038	2455640.86162	g	4.97	1037.76	954.53	2.54	3.48	12.03	1.83	0.02	0	1	
4039	2455640.86230	g	5.54	1037.20	954.14	2.47	3.47	12.04	1.90	0.02	0	1	
4040	2455640.86299	g	5.65	1037.37	954.32	2.50	3.53	12.00	1.94	0.02	0	1	
4041	2455640.86367	g	5.69	1037.56	954.61	2.55	3.52	12.03	1.91	0.02	0	1	
4042	2455640.86436	g	5.13	1037.61	955.44	2.58	3.54	12.04	1.87	0.02	0	1	
4043	2455640.86510	r	4.77	1037.23	957.04	2.59	3.24	11.40	1.99	0.02	0	1	

Table B.1 (cont'd)

Image	JD midtime	Filter	FWHM	Pluto X	Pluto Y	Ch X off	Ch Y off	Pl Inst. Mag.	Ch Mag	Diff Diff. Err	IsGood	Fit Number
4044	2455640.86576	r	4.96	1037.08	956.90	2.77	3.43	11.38	2.15	0.02	0	1
4045	2455640.86644	r	3.96	1037.08	957.12	2.69	3.36	11.37	2.08	0.02	0	1
4046	2455640.86709	r	4.79	1036.67	957.97	2.73	3.36	11.35	2.14	0.02	0	1
4047	2455640.86777	r	4.75	1037.88	957.81	2.65	3.36	11.39	2.06	0.02	0	1
4048	2455640.86854	i	4.17	1037.57	958.91	2.64	3.37	11.37	2.10	0.01	0	1
4049	2455640.86922	i	3.36	1037.10	959.03	2.65	3.39	11.35	2.12	0.02	0	1
4050	2455640.86989	i	3.62	1036.18	959.16	2.64	3.38	11.33	2.14	0.01	0	1
4051	2455640.87057	i	3.93	1036.34	959.25	2.66	3.33	11.38	2.07	0.02	0	1
4052	2455640.87126	i	4.18	1036.76	959.39	2.64	3.33	11.39	2.06	0.01	0	1
4053	2455640.87202	z	4.37	1037.41	959.76	2.66	3.39	12.27	2.11	0.02	0	1
4054	2455640.87271	z	3.30	1037.81	959.96	2.68	3.38	12.25	2.10	0.02	0	1
4055	2455640.87342	z	3.98	1037.66	959.82	2.69	3.34	12.22	2.12	0.02	0	1
4056	2455640.87411	z	2.95	1037.15	960.78	2.65	3.37	12.23	2.07	0.02	0	1
4057	2455640.87482	z	4.03	1037.63	960.10	2.70	3.36	12.24	2.09	0.02	0	1
4058	2455640.87563	B	6.14	1036.47	957.71	-2.16	-1.21	13.25	4.41	0.22	1	1
4059	2455640.87637	B	5.47	1036.32	957.27	-0.58	-2.12	13.29	2.80	0.07	1	1
4060	2455640.87709	B	5.20	1036.28	957.94	2.65	3.41	13.23	1.80	0.02	0	2
4061	2455640.87782	B	5.93	1036.05	957.22	-0.77	-1.33	13.48	1.21	0.05	1	1
4062	2455640.87856	B	6.62	1036.41	957.85	2.74	3.37	13.30	1.76	0.02	0	1
5118	2456077.89065	g	6.66	972.91	888.47	-0.94	-3.78	12.23	1.79	0.02	0	1
5120	2456077.89175	g	6.06	973.25	889.17	-0.68	-3.56	11.97	1.59	0.02	1	1
5121	2456077.89226	g	5.75	973.48	889.25	-0.82	-3.74	11.98	1.82	0.02	0	1
5122	2456077.89276	g	5.36	972.81	888.68	-0.74	-3.90	12.01	1.73	0.02	0	1
5123	2456077.89347	r	5.06	972.83	887.96	-0.88	-3.88	11.28	2.11	0.02	0	1
5124	2456077.89396	r	4.70	973.28	887.72	-0.76	-3.83	11.26	2.08	0.02	0	1
5125	2456077.89446	r	4.19	972.52	887.28	-0.83	-3.85	11.21	2.10	0.02	0	1
5126	2456077.89496	r	4.53	972.41	886.73	-0.78	-3.84	11.23	2.08	0.02	0	1
5127	2456077.89546	r	4.87	972.88	887.49	-0.77	-3.87	11.20	2.12	0.02	0	1
5128	2456077.89602	i	4.89	972.48	885.20	-0.89	-3.76	11.37	2.05	0.02	0	1
5129	2456077.89652	i	5.14	972.03	885.89	-0.84	-3.84	11.39	2.08	0.02	0	1
5130	2456077.89702	i	4.31	971.71	886.49	-0.79	-3.83	11.25	2.09	0.01	0	1
5131	2456077.89752	i	4.58	971.92	885.96	-0.84	-3.76	11.29	2.03	0.02	0	1
5132	2456077.89802	i	4.62	972.72	885.08	-0.89	-3.78	11.31	2.04	0.02	0	1
5133	2456077.89862	z	4.04	973.41	884.41	-0.82	-3.84	12.24	2.07	0.01	0	1
5134	2456077.89911	z	4.69	972.47	884.38	-0.77	-3.73	12.34	1.93	0.03	0	1
5135	2456077.89961	z	4.22	972.86	883.66	-0.80	-3.76	12.33	1.97	0.02	0	1
5136	2456077.90011	z	4.75	971.77	882.65	-0.72	-3.72	12.28	1.91	0.02	0	1

Table B.1 (cont'd)

Image	JD midtime	Filter	FWHM	Pluto X	Pluto Y	Ch X off	Ch Y off	Pl Inst. Mag.	Ch Mag	Diff	Diff. Err	IsGood	Fit Number
5137	2456077.90061	z	4.20	973.70	883.26	-0.67	-3.80	12.28	2.01	0.02	0	1	
5138	2456077.90119	B	6.04	974.14	887.96	-0.77	-3.99	12.75	1.82	0.02	0	1	
5139	2456077.90181	B	5.71	973.96	888.12	-0.78	-3.78	12.82	1.66	0.02	0	1	
5140	2456077.90236	B	5.20	974.38	887.93	-0.79	-3.96	12.74	1.84	0.02	0	1	
5141	2456077.90293	B	5.20	974.23	887.47	-0.75	-3.83	12.76	1.74	0.02	0	1	
5142	2456077.90348	B	5.13	974.78	887.73	-0.79	-3.85	12.75	1.74	0.01	0	1	
5143	2456077.90409	g	4.99	973.12	885.08	-0.91	-3.76	12.04	1.78	0.02	0	1	
5144	2456077.90459	g	5.27	973.75	884.40	-0.88	-3.72	11.99	1.77	0.02	0	1	
5145	2456077.90509	g	4.90	972.98	884.14	-0.70	-3.99	11.99	1.86	0.03	0	1	
5146	2456077.90564	r	4.26	973.12	882.74	-0.81	-3.82	11.16	2.04	0.02	0	1	
5147	2456077.90614	r	4.35	972.50	882.95	-0.88	-3.78	11.15	2.06	0.02	0	1	
5148	2456077.90664	r	4.26	973.44	884.19	-0.92	-3.84	11.11	2.10	0.03	0	1	
5149	2456077.90721	i	3.86	972.53	881.40	-0.77	-3.86	11.21	2.16	0.02	0	1	
5150	2456077.90770	i	4.44	972.87	881.50	-0.99	-3.96	11.22	2.25	0.03	0	1	
5151	2456077.90818	i	3.86	972.68	880.74	-0.72	-3.83	11.25	2.11	0.02	0	1	
5152	2456077.90884	z	4.13	972.96	879.39	-0.82	-3.84	12.12	2.04	0.03	0	1	
5153	2456077.90933	z	4.07	973.21	879.33	-0.85	-3.82	12.13	2.09	0.02	0	1	
5154	2456077.90983	z	3.99	973.96	881.44	-0.79	-3.83	12.12	2.07	0.02	0	1	
5155	2456077.91043	B	5.28	974.55	884.70	-0.78	-3.79	12.61	1.75	0.01	0	1	
5156	2456077.91098	B	5.43	974.77	884.52	-0.89	-3.87	12.64	1.78	0.02	0	1	
5157	2456077.91154	B	5.70	975.47	884.70	-0.66	-3.85	12.67	1.82	0.02	0	1	
6237	2455985.86244	r	5.39	696.79	546.47	2.84	3.25	11.41	2.05	0.02	0	1	
6238	2455985.86303	r	4.32	696.17	547.28	2.91	3.11	11.31	2.04	0.02	0	1	
6239	2455985.86354	r	4.35	696.67	547.72	2.79	3.19	11.39	1.99	0.02	0	1	
6240	2455985.86405	r	4.75	696.48	546.83	2.77	3.17	11.40	1.97	0.01	0	1	
6241	2455985.86454	r	5.29	695.92	548.20	2.62	3.00	11.46	1.82	0.02	1	1	
6243	2455985.86595	i	5.49	694.82	549.87	2.65	3.45	11.57	2.28	0.03	1	1	
6244	2455985.86646	i	6.36	695.20	550.07	2.71	3.19	11.63	1.95	0.02	0	1	
6245	2455985.86696	i	5.75	696.22	550.19	2.83	3.19	11.58	2.06	0.02	0	1	
6246	2455985.86747	i	4.96	695.46	549.22	2.98	3.28	11.55	2.23	0.02	0	1	
6247	2455985.86810	i	5.84	695.89	550.78	2.82	3.03	11.66	1.93	0.02	0	1	
6248	2455985.86859	i	5.09	695.08	549.78	3.01	3.26	11.58	2.25	0.02	0	1	
6249	2455985.86910	i	4.93	695.43	550.49	2.81	3.30	11.60	2.12	0.02	0	1	
6250	2455985.86986	z	4.75	696.47	551.76	2.74	3.20	12.39	2.01	0.02	0	1	
6251	2455985.87049	z	5.55	695.98	552.95	2.90	3.39	12.37	2.10	0.02	0	1	
6252	2455985.87102	z	4.26	696.40	552.55	2.76	3.33	12.33	2.11	0.02	0	2	
6253	2455985.87155	z	4.77	696.40	552.69	2.75	3.16	12.39	1.93	0.02	0	1	

Table B.1 (cont'd)

Image	JD midtime	Filter	FWHM	Pluto X	Pluto Y	Ch X off	Ch Y off	Pl Inst. Mag.	Ch Mag Diff	Diff. Err	IsGood	Fit Number
6256	2455985.87345	B	5.59	698.77	549.14	2.77	3.37	12.97	1.75	0.01	0	1
6257	2455985.87413	B	6.16	698.61	549.34	2.80	3.35	13.00	1.79	0.01	0	1
6258	2455985.87471	B	5.62	698.56	549.76	2.83	3.37	12.99	1.79	0.01	0	1
6259	2455985.87530	B	5.53	698.50	550.18	2.81	3.31	13.01	1.73	0.01	0	2
6260	2455985.87592	r	4.60	696.62	552.43	2.88	3.21	11.19	2.06	0.02	0	1
6261	2455985.87645	r	4.40	696.12	552.90	2.87	3.27	11.25	2.09	0.01	0	1
6262	2455985.87709	i	4.53	696.04	553.17	2.84	3.27	11.42	2.10	0.02	0	1
6263	2455985.87762	i	3.87	695.30	554.42	2.82	3.14	11.38	2.04	0.01	0	1
7090	2455986.85052	g	5.27	675.07	918.01	3.95	0.42	12.28	1.86	0.01	0	2
7091	2455986.85111	g	6.27	675.41	918.56	4.00	0.26	12.30	1.90	0.02	0	1
7092	2455986.85166	g	6.01	674.83	918.76	4.04	0.38	12.27	1.89	0.02	0	1
7093	2455986.85225	g	6.38	675.07	918.78	3.70	0.72	12.31	1.75	0.02	1	1
7094	2455986.85278	g	6.17	674.73	919.52	4.08	0.63	12.28	1.87	0.02	0	1
7095	2455986.85337	r	5.00	673.37	923.86	3.98	0.32	11.40	2.01	0.02	0	1
7096	2455986.85399	r	5.15	673.24	924.20	3.97	0.48	11.35	2.12	0.02	0	1
7097	2455986.85450	r	5.25	672.99	923.94	-1.69	1.35	11.49	3.82	0.14	1	1
7098	2455986.85499	r	4.09	674.03	923.85	-2.06	2.71	11.46	5.47	0.40	1	1
7099	2455986.85550	r	4.91	673.74	924.19	-1.19	3.47	11.45	5.11	0.23	1	1
7100	2455986.85611	i	3.98	672.50	926.55	4.03	0.49	11.47	2.09	0.02	0	1
7101	2455986.85670	i	4.86	672.99	925.98	4.09	0.08	11.56	2.28	0.02	1	1
7102	2455986.85720	i	3.83	672.77	926.18	3.97	0.41	11.44	2.12	0.01	0	1
7103	2455986.85770	i	3.66	671.74	926.84	4.00	0.43	11.48	2.07	0.02	0	1
7104	2455986.85821	i	3.99	672.37	927.14	3.88	0.45	11.41	2.01	0.03	0	1
7105	2455986.85874	z	3.76	672.41	927.96	3.91	0.27	12.28	1.97	0.03	0	1
7106	2455986.85939	z	3.61	672.77	928.37	3.98	0.30	12.28	2.02	0.02	0	2
7107	2455986.85989	z	4.14	672.28	928.76	4.03	0.46	12.34	1.94	0.03	0	1
7108	2455986.86040	z	4.08	672.80	928.64	3.99	0.54	12.37	1.99	0.03	0	1
7109	2455986.86090	z	4.89	673.25	928.84	4.04	0.44	12.42	2.04	0.03	0	1
7110	2455986.86141	z	5.34	672.11	928.41	4.12	0.11	12.33	2.24	0.04	1	1
7111	2455986.86218	B	5.98	675.12	924.02	4.08	0.29	13.11	1.87	0.02	0	1
7112	2455986.86284	B	5.76	674.67	924.13	4.13	0.38	13.11	1.93	0.02	0	1
7113	2455986.86340	B	5.85	675.07	924.42	3.91	0.39	13.15	1.76	0.02	0	1
7114	2455986.86396	B	5.75	675.43	924.61	4.05	0.23	13.11	1.83	0.02	0	1
7115	2455986.86453	B	5.22	675.05	925.02	4.01	0.43	13.11	1.86	0.02	0	1
7135	2455986.87674	r	3.84	670.89	936.76	3.99	0.44	11.21	2.08	0.02	0	1
7136	2455986.87725	r	3.64	670.21	936.71	3.91	0.33	11.31	1.98	0.02	0	1
7137	2455986.87782	i	3.96	668.92	937.43	4.03	0.33	11.46	2.14	0.02	0	1

Table B.1 (cont'd)

Image	JD midtime	Filter	FWHM	Pluto X	Pluto Y	Ch X off	Ch Y off	Pl Inst. Mag.	Ch Mag	Diff	Diff. Err	IsGood	Fit Number
7138	2455986.87832	i	4.04	669.59	938.75	4.01	0.39	11.46	2.08	0.02	0	1	
7139	2455986.87891	z	4.74	670.53	938.88	3.87	0.49	12.42	1.89	0.04	0	1	
7140	2455986.87940	z	4.69	670.56	939.68	3.65	0.39	12.44	1.71	0.04	1	1	
7141	2455986.88003	B	4.80	672.30	935.33	3.97	0.36	12.84	1.80	0.01	0	1	
7142	2455986.88060	B	5.22	672.34	935.55	3.99	0.36	12.93	1.76	0.02	0	1	
8177	2455987.85630	r	5.31	1050.48	858.70	1.20	0.95	11.62	1.89	0.05	1	1	
8178	2455987.85690	r	5.37	1050.23	859.54	1.67	-3.15	11.38	2.63	0.03	1	1	
8180	2455987.85791	r	5.21	1049.96	859.89	1.76	-2.92	11.39	2.39	0.03	0	1	
8181	2455987.85842	i	4.92	1049.29	862.09	1.53	-3.22	11.38	2.70	0.05	1	1	
8182	2455987.85906	i	4.84	1048.75	861.62	2.03	-2.80	11.42	2.40	0.03	1	1	
8183	2455987.85957	i	5.26	1049.59	862.00	2.01	-2.57	11.45	2.22	0.03	1	1	
8184	2455987.86006	i	5.39	1048.77	862.70	1.46	-3.07	11.49	2.21	0.02	1	1	
8185	2455987.86057	i	4.94	1049.30	861.97	1.62	-2.72	11.45	2.04	0.03	0	1	
8186	2455987.86112	r	5.44	1049.47	861.34	1.86	-3.08	11.35	2.62	0.03	1	1	
8187	2455987.86167	z	4.88	1049.97	864.14	1.59	-2.81	12.33	1.95	0.03	0	1	
8188	2455987.86224	z	4.69	1050.40	864.21	1.87	-3.10	12.20	2.38	0.03	1	1	
8189	2455987.86275	z	4.59	1050.33	864.33	1.61	-2.85	12.32	2.00	0.03	0	1	
8190	2455987.86325	z	4.82	1050.07	865.30	1.73	-2.88	12.27	2.15	0.03	0	1	
8191	2455987.86376	z	4.51	1050.02	865.23	1.90	-2.81	12.28	2.12	0.03	1	1	
8192	2455987.86449	B	5.73	1051.51	860.14	1.73	-2.78	12.99	1.88	0.02	0	1	
8193	2455987.86514	B	6.01	1051.49	860.44	1.55	-2.47	13.06	1.45	0.02	1	1	
8194	2455987.86571	B	6.09	1051.51	860.45	1.54	-2.79	12.97	1.78	0.03	0	1	
8195	2455987.86626	B	6.45	1051.89	860.26	1.71	-2.72	12.99	1.80	0.03	0	1	
8196	2455987.86682	B	6.44	1051.51	861.03	1.60	-3.08	12.98	1.95	0.02	0	1	
8213	2455987.87743	g	5.73	1041.94	864.44	1.63	-2.51	12.18	1.72	0.03	1	1	
8214	2455987.87821	g	5.80	1041.99	865.11	1.58	-2.68	12.23	1.75	0.02	0	1	
8215	2455987.87875	g	5.51	1042.31	865.87	1.68	-2.48	12.20	1.71	0.03	1	1	
8223	2455987.88533	r	3.90	1041.54	975.01	1.61	-2.88	11.32	2.17	0.01	0	1	
8224	2455987.88592	r	4.21	1042.15	974.06	1.60	-2.88	11.29	2.16	0.02	0	1	
8225	2455987.88643	r	4.44	1041.53	975.66	1.62	-2.95	11.34	2.17	0.02	0	1	
8226	2455987.88693	r	4.41	1041.73	975.06	1.54	-2.83	11.30	2.16	0.02	0	1	
8227	2455987.88755	i	4.88	1041.36	976.57	1.53	-2.98	11.34	2.34	0.03	0	1	
8228	2455987.88806	i	4.36	1041.16	977.23	1.49	-2.98	11.35	2.23	0.02	0	2	
8229	2455987.88870	z	4.49	1041.21	978.17	1.57	-2.96	12.16	2.07	0.02	0	1	
8230	2455987.88930	z	4.14	1042.31	977.98	1.83	-2.84	12.19	2.06	0.03	0	1	
8231	2455987.88998	B	5.14	1043.31	974.31	1.63	-2.84	12.93	1.84	0.02	0	1	
8232	2455987.89054	B	5.18	1043.20	975.07	1.70	-2.97	12.90	2.00	0.02	0	1	

Table B.1 (cont'd)

Image	JD midtime	Filter	FWHM	Pluto X	Pluto Y	Ch X off	Ch Y off	Pl Inst. Mag.	Ch Mag	Diff	Diff. Err	IsGood	Fit Number
8234	2455987.89170	g	4.75	1042.23	974.61	1.56	-2.91	12.16	2.02	0.02	0	1	
9044	2456078.78746	g	4.03	929.22	951.61	-3.70	-2.76	11.84	1.88	0.02	0	1	
9045	2456078.78811	g	4.05	929.27	951.50	-3.70	-2.70	11.79	1.94	0.02	0	1	
9046	2456078.78858	g	3.60	928.98	951.11	-3.73	-2.77	11.81	1.90	0.02	0	1	
9047	2456078.78906	g	3.73	929.41	950.84	-3.74	-2.77	11.83	1.95	0.02	0	1	
9048	2456078.78962	g	4.00	928.96	950.88	-3.73	-2.70	11.86	1.90	0.02	0	1	
9049	2456078.79010	g	3.89	928.79	950.73	-3.68	-2.67	11.81	1.89	0.03	0	1	
9050	2456078.79062	r	3.97	928.42	950.55	-3.73	-2.72	11.06	2.14	0.01	0	1	
9051	2456078.79109	r	3.13	928.95	950.64	-3.74	-2.76	11.07	2.14	0.02	0	1	
9052	2456078.79157	r	3.63	928.89	950.83	-3.77	-2.69	11.04	2.14	0.02	0	1	
9053	2456078.79204	r	3.30	929.14	950.48	-3.73	-2.72	11.05	2.11	0.02	0	1	
9054	2456078.79252	r	2.85	928.89	950.13	-3.76	-2.73	11.03	2.15	0.02	0	1	
9055	2456078.79305	i	3.15	928.29	949.76	-3.72	-2.71	11.08	2.14	0.02	0	1	
9056	2456078.79352	i	3.15	928.65	949.83	-3.71	-2.74	11.07	2.12	0.02	0	1	
9057	2456078.79400	i	3.13	928.10	949.15	-3.72	-2.68	11.10	2.13	0.02	0	1	
9058	2456078.79447	i	2.98	928.54	948.98	-3.74	-2.74	11.04	2.16	0.02	0	2	
9059	2456078.79495	i	3.54	928.91	949.54	-3.72	-2.66	11.06	2.11	0.02	0	1	
9060	2456078.79548	z	3.61	929.54	948.66	-3.79	-2.69	12.14	2.08	0.02	0	1	
9061	2456078.79595	z	3.74	929.52	948.72	-3.73	-2.67	12.14	2.06	0.02	0	1	
9062	2456078.79643	z	3.18	930.10	948.54	-3.76	-2.74	12.11	2.10	0.02	0	1	
9063	2456078.79690	z	3.02	929.35	947.78	-3.79	-2.72	12.14	2.12	0.03	0	1	
9064	2456078.79738	z	2.72	929.69	948.27	-3.78	-2.69	12.09	2.13	0.02	0	1	
9065	2456078.79819	B	4.14	930.35	949.23	-3.72	-2.73	12.52	1.82	0.02	0	1	
9066	2456078.79868	B	3.79	930.21	949.41	-3.76	-2.68	12.49	1.85	0.02	0	1	
9067	2456078.79917	B	3.80	930.15	948.20	-3.74	-2.65	12.50	1.83	0.02	0	1	
9068	2456078.79965	B	3.80	930.31	948.83	-3.78	-2.72	12.52	1.86	0.02	0	1	
9069	2456078.80014	B	4.02	930.59	948.48	-3.71	-2.68	12.51	1.81	0.02	0	1	
9070	2456078.80070	g	4.39	930.14	946.36	-3.78	-2.64	11.85	1.87	0.02	0	1	
9071	2456078.80117	g	4.24	930.13	946.39	-3.74	-2.70	11.82	1.90	0.02	0	1	
9072	2456078.80165	g	4.31	929.81	946.43	-3.75	-2.64	11.83	1.92	0.02	0	1	
9073	2456078.80217	r	4.00	930.36	946.71	-3.74	-2.76	11.07	2.16	0.02	0	1	
9075	2456078.80312	r	5.26	929.65	945.73	-3.62	-2.68	11.15	2.02	0.02	0	1	
9076	2456078.80373	i	4.50	928.82	945.80	-3.69	-2.57	11.18	2.06	0.02	0	1	
9077	2456078.80421	i	3.90	929.69	945.32	-3.76	-2.66	11.12	2.13	0.02	0	1	
9078	2456078.80468	i	3.70	929.29	945.47	-3.75	-2.69	11.11	2.10	0.02	0	1	
9079	2456078.80523	B	4.98	930.70	946.97	-3.79	-2.62	12.45	1.81	0.03	0	1	
9080	2456078.80570	B	4.68	930.55	946.96	-3.72	-2.75	12.42	1.84	0.02	0	1	

Table B.1 (cont'd)

Image	JD midtime	Filter	FWHM	Pluto X	Pluto Y	Ch X off	Ch Y off	Pl Inst. Mag.	Ch Mag	Diff	Diff. Err	IsGood	Fit Number
9081	2456078.80617	B	4.93	930.52	946.44	-3.86	-2.70	12.43	1.88	0.03	0	1	
9082	2456078.80672	z	2.95	930.06	944.85	-3.77	-2.70	12.10	2.06	0.02	0	1	
9083	2456078.80719	z	3.04	930.92	944.34	-3.74	-2.66	12.12	2.05	0.02	0	1	
9084	2456078.80767	z	2.94	930.42	944.19	-3.76	-2.61	12.10	2.08	0.02	1	1	

Bibliography

Andersson, L. E., & Fix, J. D. 1973, Icarus, 20, 279

Archinal, B. A., A'Hearn, M. F., Conrad, A., et al. 2011a, Celestial Mechanics and Dynamical Astronomy, 110, 401

Archinal, B. A., A'Hearn, M. F., Bowell, E., et al. 2011b, Celestial Mechanics and Dynamical Astronomy, 109, 101

Assafin, M., Camargo, J. I. B., Vieira Martins, R., et al. 2010, A&A, 515, A32

Baade, W. 1934, PASP, 46, 218

Baum, W. A., & Code, A. D. 1953, AJ, 58, 108

Binzel, R. 2012, personal communication

Binzel, R. P. 1988, Science (ISSN 0036-8075), vol. 241, Aug. 26, 1988, p. 1070-1072., 241, 1070

Binzel, R. P., & Frueh, M. L. 1986, in Bulletin of the American Astronomical Society, Vol. 18, Bulletin of the American Astronomical Society, 937

Binzel, R. P., Tholen, D. J., Tedesco, E. F., Buratti, B. J., & Nelson, R. M. 1985, Science, 228, 1193

Bosh, A. S., Elliot, J. L., Kruse, S. E., Baron, R. L., & Dunham, E. W. 1986, Icarus, 66, 556

Bosh, A. S., Young, L. A., Elliot, J. L., Hammel, H. B., & Baron, R. L. 1992, Icarus, 95, 319

Brosch, N. 1995, MNRAS, 276, 571

Buie, M. W., Grundy, W. M., Young, E. F., Young, L. A., & Stern, S. A. 2006, AJ, 132, 290

—. 2010a, AJ, 139, 1117

—. 2010b, AJ, 139, 1128

Buie, M. W., Tholen, D. J., & Grundy, W. M. 2012, AJ, 144, 15

Buie, M. W., Tholen, D. J., & Horne, K. 1992, Icarus, 97, 211

Buie, M. W., Tholen, D. J., & Wasserman, L. H. 1997, Icarus, 125, 233

Buie, M. W., Millis, R. L., Wasserman, L. W., et al. 1993, in Bulletin of the American Astronomical Society, Vol. 25, AAS/Division for Planetary Sciences Meeting Abstracts #25, 1115–+

Buie, M. W., Elliot, J. L., Kidger, M. R., et al. 2002, in Bulletin of the American Astronomical Society, Vol. 34, AAS/Division for Planetary Sciences Meeting Abstracts #34, 877

Buie, M. W., Young, L. A., Young, E. F., et al. 2009, in Bulletin of the American Astronomical Society, Vol. 41, AAS/Division for Planetary Sciences Meeting Abstracts, 562

Christy, J. W., & Harrington, R. S. 1978, AJ, 83, 1005

Clancy, K. B., Elliot, J. L., & Person, M. J. 2005, Highlights of Astronomy, 13, 916

Collins, P. L. 2011, Personal Communication

Davies, M. E., Abalakin, V. K., Bursa, M., Hunt, G. E., & Lieske, J. H. 1989, Celestial Mechanics and Dynamical Astronomy, 46, 187

Davies, M. E., Abalakin, V. K., Bursa, M., Lederle, T., & Lieske, J. H. 1986, Celestial Mechanics, 39, 103

Davies, M. E., Abalakin, V. K., Lieske, J. H., et al. 1983, Celestial Mechanics, 29, 309

Davies, M. E., Abalakin, V. K., Brahic, A., et al. 1992, Celestial Mechanics and Dynamical Astronomy, 53, 377

Davies, M. E., Abalakin, V. K., Bursa, M., et al. 1996, Celestial Mechanics and Dynamical Astronomy, 63, 127

Davies, M. F., Abalakin, V. K., Duncombe, R. L., et al. 1980, Celestial Mechanics, 22, 205

Davis, L. E. 1994, A Reference Guide to the IRAF/DAOPHOT Package, `http://iraf.noao.edu/iraf/docs/daorefman.ps.Z`, accessed 17/03/2013

Derral Mulholland, J. 1978, Science, 201, 867

Dessler, A. J., & Russell, C. T. 1980, Eos, Transactions American Geophysical Union, 61, 690

Dobrovolskis, A. R., Peale, S. J., & Harris, A. W. 1997, Dynamics of the Pluto-Charon Binary, ed. S. A. Stern & D. J. Tholen, 159

Drish, Jr., W. F., Harmon, R., Marcialis, R. L., & Wild, W. J. 1995, Icarus, 113, 360

Dunham, E. W. 2003, in Society of Photo-Optical Instrumentation Engineers (SPIE) Conference Series, Vol. 4857, Society of Photo-Optical Instrumentation Engineers (SPIE) Conference Series, ed. R. K. Melugin & H.-P. Roeser, 62–72

Dunham, E. W. 2011, Personal Communication

—. 2013, Personal Communication

Dunham, E. W., Baron, R. L., Elliot, J. L., Vallerga, J. V., & Doty, J. P. 1985, PASP, 97, 1196

Dunham, E. W., & Elliot, J. L. 1983, PASP, 95, 325

Dunham, E. W., Elliot, J. L., Bida, T. A., et al. 2008, in Society of Photo-Optical Instrumentation Engineers (SPIE) Conference Series, Vol. 7014, Society of Photo-Optical Instrumentation Engineers (SPIE) Conference Series

Dunham, E. W., Elliot, J. L., Bida, T. A., & Taylor, B. W. 2004, in Society of Photo-Optical Instrumentation Engineers (SPIE) Conference Series, Vol. 5492, Society of Photo-Optical Instrumentation Engineers (SPIE) Conference Series, ed. A. F. M. Moorwood & M. Iye, 592–603

Dunham, E. W., Elliot, J. L., Bosh, A. S., Cordella, L. L., & Young, L. A. 1989, in Bulletin of the American Astronomical Society, Vol. 21, Bulletin of the American Astronomical Society, 932–+

Dunham, E. W., McDonald, S. W., & Elliot, J. L. 1991, AJ, 102, 1464

Elliot, J. L. 2009, Personal Communication

Elliot, J. L., Dunham, E., Wasserman, L. H., & Millis, R. L. 1978, AJ, 83, 980

Elliot, J. L., Dunham, E. W., Bosh, A. S., et al. 1988, in Bulletin of the American Astronomical Society, Vol. 20, Bulletin of the American Astronomical Society, 805–+

Elliot, J. L., Dunham, E. W., Bosh, A. S., et al. 1989, Icarus, 77, 148

Elliot, J. L., Dunham, E. W., & Olkin, C. B. 1993, in Bulletin of the American Astronomical Society, Vol. 25, AAS/Division for Planetary Sciences Meeting Abstracts #25, 1106–+

Elliot, J. L., French, R. G., Dunham, E., et al. 1977a, Science, 195, 485

—. 1977b, APJ, 217, 661

Elliot, J. L., Person, M. J., & Qu, S. 2003a, AJ, 126, 1041

Elliot, J. L., & Veverka, J. 1976, Icarus, 27, 359

Elliot, J. L., Veverka, J., & Goguen, J. 1975, icarus, 26, 387

Elliot, J. L., & Young, L. A. 1992, AJ, 103, 991

Elliot, J. L., Olkin, C. B., Dunham, E. W., et al. 1995, Nature, 373, 46

Elliot, J. L., Ates, A., Babcock, B. A., et al. 2003b, Nature, 424, 165

Elliot, J. L., Person, M. J., Gulbis, A. A. S., et al. 2007, AJ, 134, 1

Elliot, J. L., Person, M. J., Zuluaga, C. A., et al. 2010, Nature, 465, 897

Fink, U., Smith, B. A., Johnson, J. R., et al. 1980, Icarus, 44, 62

French, R. G., Elliot, J. L., & Gierasch, P. J. 1978, Icarus, 33, 186

Gehrz, R. D., Angerhausen, D., Becklin, E. E., et al. 2010, in Astronomical Society of the Pacific Conference Series, Vol. 430, Pathways Towards Habitable Planets, ed. V. Coudé Du Foresto, D. M. Gelino, & I. Ribas, 201–+

Grundy, W. M., & Buie, M. W. 2001, Icarus, 153, 248

Grundy, W. M., & Fink, U. 1996, Icarus, 124, 329

Gulbis, A. A. S., Emery, J. P., Person, M. J., et al. 2012, in AAS/Division for Planetary Sciences Meeting Abstracts, Vol. 44, AAS/Division for Planetary Sciences Meeting Abstracts, 304.03

Gulbis, A. A. S., Bus, S. J., Elliot, J. L., et al. 2011, PASP, 123, 461

Haas, M. 1995, NASA Quest: Live from the Stratosphere Questions and Answers, `http://quest.nasa.gov/lfs/QA/Big_technological_difficul.txt`, [Online; accessed 31-Oct-2011]

Hansen, C. J., & Paige, D. A. 1996, Icarus, 120, 247

Hapke, B. 1993, Theory of reflectance and emittance spectroscopy

Harrington, J., & French, R. G. 2010, ApJ, 716, 398

Hubbard, W. B., Hunten, D. M., Dieters, S. W., Hill, K. M., & Watson, R. D. 1988, Nature, 336, 452

Hubbard, W. B., Yelle, R. V., & Lunine, J. I. 1990, Icarus, 84, 1

Jensen-Clem, R., Elliot, J. L., Person, M. J., et al. 2011, in Bulletin of the American Astronomical Society, Vol. 43, American Astronomical Society Meeting Abstracts #217, 306.05

Jones, J. H., Christian, C. A., & Waddell, P. 1988, PASP, 100, 489

Kern, S., Rojas, F., Lockhart, M., et al. 2008, GENERAL USER MANUAL FOR MAGIC II, http://www.lco.cl/telescopes-information/magellan/instruments/magic/MagIC_Manual.LCO.30.pdf, accessed 16/03/2013

Las Campanas Observatory. 2007, LDSS-3 Filters Data, http://www.lco.cl/telescopes-information/magellan/operations-homepage/instruments/ldss3/ldss3-filters/filters-data, accessed 25/02/2013

Leach, R. W., Beale, F. L., & Eriksen, J. E. 1998, in Society of Photo-Optical Instrumentation Engineers (SPIE) Conference Series, Vol. 3355, Society of Photo-Optical Instrumentation Engineers (SPIE) Conference Series, ed. S. D'Odorico, 512–519

Lellouch, E., Laureijs, R., Schmitt, B., et al. 2000, Icarus, 147, 220

Lellouch, E., Stansberry, J., Emery, J., Grundy, W., & Cruikshank, D. P. 2011, Icarus, 214, 701

Levine, S. E. 2010, Personal Communication

Lockhart, M., Person, M. J., Elliot, J. L., & Souza, S. P. 2010, PASP, 122, 1207

Marcialis, R. L. 1988, AJ, 95, 941

—. 1997, The First 50 Years of Pluto-Charon Research, ed. S. A. Stern & D. J. Tholen, 27

Marsden, B. G. 1986, IAU Circ., 4157, 3

McDonald, S. W., & Elliot, J. L. 1996, AJ, 112, 788

—. 2000, AJ, 119, 1999

Millis, R. L., Wasserman, L. H., Franz, O. G., et al. 1993, Icarus, 105, 282

Mink, D. J., & Klemola, A. 1985, AJ, 90, 1894

Mink, D. J., Klemola, A. R., & Buie, M. W. 1991, AJ, 101, 2255

Muchaey, J., & Gladders, M. 2011, LDSS-3 Users Guide, http://www.lco.cl/telescopes-information/magellan/instruments/ldss-3/ldss-3-users-guide/users-guide, accessed 18/12/2012

Nicholson, P. D., & Gladman, B. J. 2006, Icarus, 181, 218

Olkin, C. B., Young, E., & Young, L. 2012, in AAS/Division for Planetary Sciences Meeting Abstracts, Vol. 44, AAS/Division for Planetary Sciences Meeting Abstracts, 310.01

Olkin, C. B., Young, L. A., French, R. G., Buie, M. W., & Young, E. F. 2011, in EPSC-DPS Joint Meeting 2011, 334

Olkin, C. B., Young, L., Young, E. F., et al. 2007, in Bulletin of the American Astronomical Society, Vol. 39, AAS/Division for Planetary Sciences Meeting Abstracts #39, 520

Ortiz, J. L., Sicardy, B., Braga-Ribas, F., et al. 2012, Nature, 491, 566

Osip, D. J., Floyd, D., & Covarrubias, R. 2008, in Presented at the Society of Photo-Optical Instrumentation Engineers (SPIE) Conference, Vol. 7014, Society of Photo-Optical Instrumentation Engineers (SPIE) Conference Series, 9

Osip, D. J., Phillips, M. M., Bernstein, R., et al. 2004, in Society of Photo-Optical Instrumentation Engineers (SPIE) Conference Series, Vol. 5492, Society of Photo-Optical Instrumentation Engineers (SPIE) Conference Series, ed. A. F. M. Moorwood & M. Iye, 49–59

Pasachoff, J. M., Souza, S. P., Babcock, B. A., et al. 2005, AJ, 129, 1718

Pasachoff, J. M., Souza, S. P., Babcock, B. A., et al. 2011, in EPSC-DPS Joint Meeting 2011, 1784

Person, M. 2012, personal communication

—. 2013, personal communication

Person, M. J., Elliot, J. L., Gulbis, A. A. S., et al. 2008, AJ, 136, 1510

Person, M. J., Elliot, J. L., Bosh, A. S., et al. 2010, in Bulletin of the American Astronomical Society, Vol. 42, AAS/Division for Planetary Sciences Meeting Abstracts #42, 983

Person, M. J., Bosh, A. S., Levine, S. E., et al. 2012, in AAS/Division for Planetary Sciences Meeting Abstracts, Vol. 44, AAS/Division for Planetary Sciences Meeting Abstracts, 304.02

Person, M. J., Bosh, A. S., Levine, S. E., et al. 2013, AJ, submitted

Rayner, J. T., Toomey, D. W., Onaka, P. M., et al. 2003, PASP, 115, 362

Riley, W. J. 2008, NIST Special Publication 1065: Handbook of Frequency Stability Analysis., `http://tf.nist.gov/timefreq/general/pdf/2220.pdf`, [Online; accessed 31-Oct-2011]

Ruprecht, J. D. 2013, PhD thesis, MASSACHUSETTS INSTITUTE OF TECHNOLOGY..

Sagan, C., & Khare, B. N. 1979, Nature, 277, 102

Sawyer, S. R., Barker, E. S., Cochran, A. L., & Cochran, W. D. 1987, Science, 238, 1560

Schechter, P. L., Mateo, M., & Saha, A. 1993, PASP, 105, 1342

Seidelmann, P. K., Abalakin, V. K., Bursa, M., et al. 2002, Celestial Mechanics and Dynamical Astronomy, 82, 83

Seidelmann, P. K., Archinal, B. A., A'Hearn, M. F., et al. 2005, Celestial Mechanics and Dynamical Astronomy, 91, 203

—. 2007, Celestial Mechanics and Dynamical Astronomy, 98, 155

Showalter, M. R., Hamilton, D. P., Stern, S. A., et al. 2011, Central Bureau Electronic Telegrams, 2769, 1

Showalter, M. R., Weaver, H. A., Stern, S. A., et al. 2012, IAU Circ., 9253, 1

Sicardy, B. 2012, personal communication

Sicardy, B., Widemann, T., Lellouch, E., et al. 2003, Nature, 424, 168

Sicardy, B., Ortiz, J. L., Assafin, M., et al. 2011a, Nature, 478, 493

Sicardy, B., Bolt, G., Broughton, J., et al. 2011b, AJ, 141, 67

Sicardy, B., Braga-Ribas, F., Widemann, T., et al. 2012, in AAS/Division for Planetary Sciences Meeting Abstracts, Vol. 44, AAS/Division for Planetary Sciences Meeting Abstracts, 304.01

Sooknah, M. 2011, mIT Astronomy Field Camp (12.411)

Souza, S. P., Babcock, B. A., Pasachoff, J. M., et al. 2006, PASP, 118, 1550

Stern, A. 1993, EOS Transactions, 74, 73

Stern, A., & Mitton, J. 2005a, Pluto and Charon: Ice Worlds on the Ragged Edge of the Solar System

Stern, S. A. 2003, in Lunar and Planetary Inst. Technical Report, Vol. 34, Lunar and Planetary Institute Science Conference Abstracts, ed. S. Mackwell & E. Stansbery, 1106

Stern, S. A., Buie, M. W., & Trafton, L. M. 1997, AJ, 113, 827

Stern, S. A., & Mitton, J. 2005b, Pluto and Charon: Ice Worlds on the Ragged Edge of the Solar System, Second Edition

Stern, S. A., Parker, J. W., Fesen, R. A., Barker, E. S., & Trafton, L. M. 1991, Icarus, 94, 246

Stetson, P. B., Davis, L. E., & Crabtree, D. R. 1990, in Astronomical Society of the Pacific Conference Series, Vol. 8, CCDs in astronomy, ed. G. H. Jacoby, 289–304

Strobel, D. F., Zhu, X., Summers, M. E., & Stevens, M. H. 1996, Icarus, 120, 266

Terrile, R. J., Stern, S. A., Staehle, R. L., et al. 1997, Spacecraft Missions to Pluto and Charon, ed. S. A. Stern & D. J. Tholen, 103

Tholen, D. J., & Buie, M. W. 1997, Bulk Properties of Pluto and Charon, ed. S. A. Stern & D. J. Tholen, 193

Throop, H. 2012, personal communication

Toigo, A. D., Gierasch, P. J., Sicardy, B., & Lellouch, E. 2010, Icarus, 208, 402

Trafton, L., & Stern, S. A. 1983, ApJ, 267, 872

Tryka, K. A., Brown, R. H., Chruikshank, D. P., et al. 1994, Icarus, 112, 513

Verbiscer, A. J., Peterson, D. E., Skrutskie, M. F., et al. 2007, in Lunar and Planetary Inst. Technical Report, Vol. 38, Lunar and Planetary Institute Science Conference Abstracts, 2318

Walker, A. R. 1980, MNRAS, 192, 47P

Walker, M. F., & Hardie, R. 1955, PASP, 67, 224

Weaver, H. A., Stern, S. A., Mutchler, M. J., et al. 2006, Nature, 439, 943

Witteborn, F., Koch, D., Jenkins, J., et al. 2000, final Report on the Kepler Technology Demonstration

Wolf, J., Röser, H.-P., Krabbe, A., & Pfüller, E. 2010, in Society of Photo-Optical Instrumentation Engineers (SPIE) Conference Series, Vol. 7733, Society of Photo-Optical Instrumentation Engineers (SPIE) Conference Series

Young, E. F. 2012, AJ, 144, 32

Young, E. F., & Binzel, R. P. 1993, Icarus, 102, 134

Young, E. F., Binzel, R. P., & Crane, K. 2001, AJ, 121, 552

Young, E. F., Galdamez, K., Buie, M. W., Binzel, R. P., & Tholen, D. J. 1999, AJ, 117, 1063

Young, E. F., Young, L. A., Olkin, C. B., et al. 2011, PASP, 123, 735

Young, E. F., French, R. G., Young, L. A., et al. 2008, AJ, 136, 1757

Young, L. 2013, personal communication

Young, L., Bally, J., Bauer, J. M., et al. 2007, in Bulletin of the American Astronomical Society, Vol. 39, AAS/Division for Planetary Sciences Meeting Abstracts #39, 541

Young, L., Buie, M. W., Olkin, C. B., et al. 2009, in AAS/Division for Planetary Sciences Meeting Abstracts, Vol. 41, AAS/Division for Planetary Sciences Meeting Abstracts #41, 06.05

Young, L., Sicardy, B., Widemann, T., et al. 2010, in Bulletin of the American Astronomical Society, Vol. 42, AAS/Division for Planetary Sciences Meeting Abstracts #42, 982

Young, L. A. 2011, Personal Communication

—. 2013, ApJ, 766, L22

Young, L. A., Olkin, C. B., Elliot, J. L., Tholen, D. J., & Buie, M. W. 1994, Icarus, 108, 186

Zalucha, A. M., & Gulbis, A. A. S. 2012, Journal of Geophysical Research (Planets), 117, 5002

Zalucha, A. M., Gulbis, A. A. S., Zhu, X., Strobel, D. F., & Elliot, J. L. 2011a, Icarus, 211, 804

Zalucha, A. M., & Michaels, T. I. 2013, Icarus, 223, 819

Zalucha, A. M., Zhu, X., Gulbis, A. A. S., Strobel, D. F., & Elliot, J. L. 2011b, Icarus, 214, 685

Zangari, A. 2011, full Report on HIPO Imaging Tests: October - December 2010

Zangari, A. M., Dunham, E., Mandushev, G., et al. 2011, in EPSC-DPS Joint Meeting 2011, 1378

Zuluaga, C. 2007, P445.3 Pluto Occultation Prediction; March 18, 2007, `http://occult.mit.edu/research/occultations/Pluto/P445.3/index.html`, accessed 21/03/2013

—. 2010, PC20100704; July 4, 2010, `http://occult.mit.edu/research/occultations/Pluto/PC20100704-preds/index.html`, accessed 21/03/2013

Zuluaga, C. 2012, personal communication

Zuluaga, C. 2013, PC20100704; July 4, 2010, `http://occult.mit.edu/research/occultations/Pluto/PC20100704-preds/index.html`, accessed 01/02/2013